Development of an *In Silico* Methodology for the Multiscale Modelling of Atherosclerosis

Giulia Di Tomaso

Department of Mechanical Engineering

University College London

A thesis submitted for the degree of

Doctor of Philosophy

23 September 2014

I, Giulia Di Tomaso, confirm that the work presented in this thesis is my own. Where information has been derived from other sources, I confirm that this has been indicated in the thesis.

Giulia Di Tomaso

September 2014

Ai miei genitori

Acknowledgements

These are possibly the two most important pages of them all, as without the priceless help and support of all the people that will be mentioned here, the work presented in this thesis would have never been possible.

I feel that this PhD is the product of the love and support of two families, my work family and my real family.

First and foremost, I would like to thank my work "parents", my supervisors Vanessa and Cesar. You have been extremely important in this journey. Without your guidance, your help, your support, your chats, your shouts and your hugs, I would have never managed to complete this PhD journey. A journey that I was doing together with my work "siblings": Kevin, thanks for the red pen and for the jokes. Gaelle, thanks for all your love and the chats on the steps. Ben, thanks for always making me smile. Lydia, thanks for always being there for me and for sharing the love for the model! Gregorio, thanks for being my work-desk neighbour, the best I could have ever wished for! Neil, thanks for the great afternoon teas. Mona, thanks for the tears you shared with me over ScanIP. Jina thank you so much for your advices. Husher and Yiannis, thanks for welcoming me in your office and for the great life-work chats. Tristan, thank you so much for being my cluster-master. Sarah, thanks for the sweet cappuccino breaks and lastly Abu, thank you, your morning welcomes made the office feel like a real home.

A special thanks goes to Obi, my clinical supervisor. Thank you for all your help and your kindness, for sitting patiently with me in front of the MSCT images hunting for plaques, and thanks for making my "clinical experience" so special and rewarding.

Another very special thank you goes to my under-cover office mate Nick, you LaTeX genius! Thanks for initiating me and for making this possible!

Now to my real family. Thank you Mum for all your love and for believing my wings were strong enough to fly, you gave me the strength when I could not find my own anymore. Thank you Dad for all the technical and psychological support. I know you got to love the model as your grandchild! Thank you Alessandro "mitico fratello", the best brother and friend ever. When I could not make it, you would give me the extra shake (literally!) to make me go further. Even if you are not here anymore, thank you Grandad, you believed in my UK dream from the start and without your support, I would have possibly never left Italy. Thank you Grandma – without you I would have not managed to stay so far away from home but yet so close!

And at last but not the least I'd like to thank a "new" family member, my fiancé Ruslan. I would not know what else to say but that we made it! Thank you!

Abstract

Atherosclerosis is the main cause of mortality and morbidity in Western World, causing more death and disability than all the types of cancer. Given its high potential danger it is of major importance to better understand the causes of atherosclerosis, which are linked to both the lipoprotein metabolism and haemodynamics in arteries. Together with *in vivo* and *in vitro* experiments, *in silico* models and simulations allow for a better insight and understanding of the mechanisms of atherosclerosis formation.

A multiscale model coming from the integration of a fluid dynamics model, and a biochemical model is here presented for the modelling of atherosclerosis at its early stage. An artery-specific approach was used in the fluid dynamics model for modelling the interaction between arterial endothelium and blood flow. The low density lipoprotein (LDL) oxidation leading to immune-response (cytokines-monocytes/macrophages) and foam cell formation and accumulation at the basis of plaque formation was described in the biochemical model. Integration of these modelling approaches led to the creation of an effective tool for the modelling of atherosclerosis plaque development, the *atherosclerosis remodelling cycle*.

The impact on the disease development of different mean blood LDL concentrations and arterial geometries was analysed. The *atherosclerosis remodelling cycle* was applied for patient-specific simulation of plaque formations in a patient presenting with atherosclerosis formations in the aorta and peripheral arteries. When compared with the multi-slice computed tomography (MSCT) images, the model highlighted atherosclerosis-prone areas, where plaques were found *in vivo*, with 91.7% accuracy and replicated 41.7% of the plaques presenting in the patients.

Contents

Contents vi

List of Figures x

List of Tables xv

Acronyms xvi

1 Literature Review 1

1.1 Biological background 2

1.1.1 Overview of the arterial structure 2

1.1.1.1 Tunica intima 2

1.1.1.2 Tunica media 3

1.1.1.3 Tunica adventitia 4

1.1.2 Atherosclerosis 4

1.1.2.1 Early lesion formation 6

1.1.3 Haemodynamic Wall Parameters for the identification of atherosclerosis-prone areas 11

1.2 Computational Modelling 14

1.2.1 Transport models 15

1.2.1.1 Lumen modelling 16

1.2.1.2 Endothelial modelling 18

1.2.1.3 Arterial wall modelling 22

1.2.2 Biochemical models 24

1.2.3 Multiscale modelling 28

1.3 Conclusion and key advantages of the proposed model 29

2 Atherosclerosis Model 31

2.1 Model description 31

2.1.1 Arterial Lumen Model 34

2.1.1.1 Haemodynamics 34

2.1.1.2 Description of the Lumen-Free Approach 36

2.1.2 Endothelium Model 37

2.1.2.1 Correlation between Endothelial Shape Index and Wall shear stress (WSS) 37

2.1.2.2 Membrane Transport Model 42

2.1.3 Arterial Wall Model 46

2.1.3.1 LDL Transport 47

2.1.3.2 LDL Oxidation 48

2.1.3.3 Monocytes Transport 50

2.1.3.4 Foam cell formation and accumulations 51

2.2 Multiscale Modelling 53

2.2.1 Spatial Scales 54

2.2.2 Temporal scale 56

2.3 Summary of model assumptions and limitations 57

2.4 Conclusion 59

3 Atherosclerosis Remodelling Cycle 61

3.1 Theoretical workflow 61

3.2 Computational Workflow 68

3.2.1 Atherosclerosis remodelling initialisation cycle 68

3.2.2 Atherosclerosis remodelling cycle 74

3.3 Discussion 76

3.4 Conclusion 78

4 Atherosclerosis Modelling On Idealised Arterial Geometries 79

4.1 Methods 80

4.1.1 Steady-state model 80

4.1.1.1 Idealised geometry of a coronary arterial stenosis 80

4.1.2 Transient Model 83
4.1.2.1 Idealised Geometry of a Common Femoral Artery Stenosis 83
4.1.2.2 Idealised Geometry of an S-shaped Common Femoral Artery 85
4.2 Results 86
4.2.1 Steady-state Model 86
4.2.2 Transient Model 95
4.2.2.1 Idealised geometry of a common femoral artery stenosis 95
4.2.2.2 Idealised geometry of S-shaped common femoral artery 100
4.3 Discussion 104
4.4 Conclusion 107

5 Patient Specific Modeling of Atherosclerosis Formation 109
5.1 Methods 112
5.1.1 Image acquisition and processing 112
5.1.1.1 Image processing 113
5.1.1.2 Image segmentation 115
5.1.1.3 Generation of a Computational Mesh for a Real Patient Geometry 116
5.1.1.4 Plaque scoring and segmentation 118
5.1.1.5 Velocity data acquisition and processing 119
5.1.2 Case 1: Model of the Descending Abdominal Aorta with the two common iliac arteries (CIAs), the external iliac arteries (EIAs) and internal iliac arteries (IIAs) 123
5.1.2.1 Geometry specifications and computational implementation 123
5.1.2.2 Fluid domain discretisation 124
5.1.3 Case 2: Model of the Right Common Femoral Artery (CFA), with the Deep Femoral Artery (DFA) and the Superficial Femoral Artery (SFA) 127

5.1.3.1 Geometry specifications and computational implementation 127
5.1.3.2 Fluid domain discretisation 128
5.1.4 Case 3: Model of the Left Common Femoral Artery (CFA), with the Deep Femoral Artery (DFA) and the Superficial Femoral Artery (SFA) 130
5.1.4.1 Geometry specifications and computational implementation 130
5.1.4.2 Fluid domain discretisation 131
5.2 Results 133
5.2.1 Case 1: Simulation Results 133
5.2.2 Case 2: Simulation Results 143
5.2.3 Case 3: Simulation Results 147
5.3 Discussion 151
5.4 Conclusion 156

6 Conclusion and Future Work 158
6.1 Atherosclerosis Model 158
6.2 Atherosclerosis Remodelling Cycle 160
6.3 Atherosclerosis Modelling on Idealised Arterial Geometries 162
6.4 Patient Specific Modelling of Atherosclerosis Formation 163

Appendix A 181

Appendix B 184

Appendix C 190

List of Figures

1.1 Arterial structure. 2
1.2 Sketch of the endothelial cell monolayer arrangement 4
1.3 Atherosclerosis timeline. 5
1.4 LDL Particle. 7
1.5 LDL Particle with vitamin E. 9
1.6 Fatty streak formation 10
1.7 Wall Shear Stress. 11
1.8 Transverse section of the computational domain considered. . . . 16
1.9 Three pores model 21

2.1 Graphical representation of the transverse section of modelled artery 32
2.2 Control volume definition 36
2.3 Detail of Figure 2.1 showing the model specifications for the arterial lumen. 36
2.4 Light micrographs of endothelial cells in areas of low 38
2.5 Flow direction. 39
2.6 Variation of wall shear stress 40
2.7 Shape Index as function of WSS 40
2.8 Normalised Shape Index as function of WSS 41
2.9 Arterial endothelium model specifications 43
2.10 Arterial endothelium model specifications 46
2.11 Macromolecule transport through the artery wall and endothelium 48
2.12 Electron micrograph of sub-endothelial fatty streak 52
2.13 The biological domain as a function of time 54
2.14 Slice of the model artery 56

3.1 Theoretical workflow of the atherosclerosis model. 63
3.2 Theoretical workflow of the atherosclerosis model. 67
3.3 Computational workflow of the atherosclerosis model. 69
3.4 Mesh deformation technique 73

4.1 Axisymmetric straight idealised geometry 81
4.2 Geometry of an S-shaped femoral artery 86
4.3 Local value of WSS as a function of the axial location z. 87
4.4 Velocity streamlines in the stenotic areas. 87
4.5 Apparent permeability (P_{app}) of endothelium as a function of the axial location z. 88
4.6 LDL arterial concentration profiles taken at point z_0 along the vessel length. 89
4.7 Wall Shear Stress contour plot and pattern along the vessel length 92
4.8 Atherosclerotic formation with percentage of maximum normalised radial reduction (R) 93
4.9 LDL endothelial apparent permeability (P_{app}) as a function of the axial location z. 94
4.10 Local value of WSS as a function of the axial location z. 95
4.11 Apparent permeability (P_{app}) of endothelium as a function of the axial location z. 96
4.12 Temporal profile of the LDL oxidation cascade and foam cell formation 97
4.13 Contour plot of a total mesh displacement showing the plaque formation after 6 years. 99
4.14 Velocity contour plot for a middle plane. 100
4.15 Apparent endothelial permeability (P_{app}). 101
4.16 Contour plot of a total mesh displacement showing the plaque formation after 17 years. 102
4.17 Contour plot of a total mesh displacement showing the plaque formation after 17 years and 6 months. 103

5.1 Diagram of the human circulatory system, with the three arterial segments considered in the modelled cases highlighted. 111

5.2 MSCT angiogram transverse slice 113
5.3 Computer tomography 114
5.4 MSCT angiogram transverse slice showing the two CIA lumen . . 117
5.5 MSCT angiogram transverse slice showing the two CIA lumen . . 119
5.6 Plaque scoring. Detail of a MSCT slice of the descending aorta (already shown in Figure 5.2). 121
5.7 Velocity profile acquisition from Doppler echocardiography images. 122
5.8 Geometry of the descending aorta with the two common iliac arteries, the external iliac and internal iliac arteries. 123
5.9 MSCT segmented geometry of the Model of the descending aorta with the two common iliac arteries, the external iliac and internal iliac arteries. 126
5.10 Geometry of the right common femoral artery, with the deep femoral artery and the superficial femoral artery. 127
5.11 MSCT segmented geometry of the model of the right common femoral artery, with the deep femoral artery and the superficial femoral artery. 129
5.12 Geometry of the left common femoral artery, with the deep femoral artery and the superficial femoral artery. 130
5.13 Geometry of the model of the left common femoral artery, with the deep femoral artery and the superficial femoral artery. 132
5.14 Model of the descending aorta with the two common iliac arteries, the external iliac and internal iliac arteries global WSS contour plot. 135
5.15 Re-scaled WSS contour plot of the descending aorta. The plot maximum WSS detectable is the Poiseuille WSS for the descending aorta $\tau_0 = 0.3554$ Pa. 136
5.16 Re-scaled WSS contour plot of the left common iliac artery. The plot maximum WSS detectable is the Poiseuille WSS for the right common iliac artery $\tau_0 = 0.68$ Pa. 137
5.17 Re-scaled WSS contour plot of the right common iliac artery. The plot maximum WSS detectable is the Poiseuille WSS for the left common iliac artery $\tau_0 = 0.88$ Pa 138

5.18 Mesh deformation contour plot for the descending aorta with the two common iliac arteries, the external iliac and internal iliac arteries. 139
5.19 Mesh deformation contour plot for the descending aorta with the two common iliac arteries, the external iliac and internal iliac arteries. 140
5.20 Mesh deformation contour plot for the descending aorta with the two common iliac arteries, the external iliac and internal iliac arteries. 141
5.21 Surface velocity contour plots at the location of plaque development for the descending aorta with the two common iliac arteries, the external iliac and internal iliac arteries. 142
5.22 Velocity streamlines for the model of the right common femoral artery, with the deep femoral artery and the superficial femoral artery. 144
5.23 Global WSS contour plot for the model of the right common femoral artery, with the deep femoral artery and the superficial femoral artery. 145
5.24 Re-scaled WSS contour plot of the right deep femoral artery. The plot maximum WSS detectable is the Poiseuille WSS for the right deep femoral artery $\tau_0 = 0.724$ Pa 145
5.25 Mesh deformation contour plot for the right common femoral artery, with the deep femoral artery and the superficial femoral artery. . . 146
5.26 Velocity streamlines for the model of the left common femoral artery, with the deep femoral artery and the superficial femoral artery. 148
5.27 Re-scaled WSS contour plot of the left common femoral artery. The plot maximum WSS detectable is the Poiseuille WSS for the left common femoral artery $\tau_0 = 0.6572$ Pa 149
5.28 Mesh deformation contour plot for the left common femoral artery, with the deep femoral artery and the superficial femoral artery. . . 150

A.1 Local value of WSS as a function of the axial location z for three different grids. 182
A.2 Global minima of WSS as a function of grid elements number. . . 183

B.1 Impact of the change in k_m and K_5 on the time of growth. 186

B.2 Impact of the change in k_m and K_5 on the time of growth. 187
B.3 Impact of the change in k_m and K_5 on the time of growth. 188
B.4 Impact of the change in k_m and K_5 on the time of growth. 189

C.1 Local value of WSS as a function of the axial location z for four different grids 191
C.2 Local value of WSS as a function of the axial location z for the three different grids considered for case 2 191
C.3 Local value of WSS as a function of the axial location z for the three different grids considered for case 2. 192

List of Tables

2.1 List of variables used in the governing equations of the atherosclerosis model. 33

3.1 Workflow (3.1, 3.2) entries with the corresponding set of equations or quantities that they represent 64

4.1 Simulation Results 91

5.1 Case 1 Summary 134
5.2 Case 2 Summary 143
5.3 Case 3 Summary 147
5.4 Summary of the *in vivo* observed plaques together with the model diagnostic indices. 152

Acronyms

3D three-dimensional.

ABPI Ankle Brachial Pressure Index.

ApoB apolipoprotein B.

CFA common femoral artery.

CFD computational fluid dynamics.

CIA common iliac artery.

CT Angiography Computed Tomography Angiography.

DFA deep femoral artery.

EEL external elastic lamina.

EIA external iliac artery.

FSI fluid-structure interaction model.

HWP Haemodynamic Wall Parameter.

IEL internal elastic lamina.

IIA internal iliac artery.

IMT intima-media thickness.

LC leaky cell.

LDL low density lipoprotein.

LFTA lumen-free time-averaged.

lipoprotein plasma lipid.

MC mitotic cells.

MCP-1 monocyte chemotactic protein 1.

MRA Magnetic Resonance Angiography.

MSCT multi-slice computed tomography.

ODE ordinary differential equation.

OSI oscillatory shear index.

oxLDL oxidised LDL.

PAD peripheral artery disease.

PDE partial differential equation.

ROS reactive oxygen species.

SFA superficial femoral artery.

SI Shape Index.

SMC smooth muscle cell.

TAWSS time-averaged WSS.

UCLH University College London Hospital.

VCAM-1 vascular-adhesion molecule 1.

WSS wall shear stress.

WSSG Wall Shear Stress Gradient.

Chapter 1

Literature Review

This chapter is a brief review of the various aspects related to the modelling of atherosclerosis.

Atherosclerosis is a pathology of the cardiovascular system that affects the arteries. A brief background about the pathophysiology of the disease will be provided in the first section of this chapter; describing the structure of the artery, followed by an overview of the disease development and progression. As the subject of this thesis is the modelling of the initial state of atherosclerosis, a more detailed description of this phase, known as fatty streak development, will be given. A review of the haemodynamic parameters involved in atherosclerosis formation introduces the next section of this chapter which is devoted to the description of the mathematical modelling of atherosclerosis. The different approaches used to model the transport of macromolecules inside the artery and the biochemical interactions that are the basis of atherosclerosis formation will be explained in the second part of this chapter. A conclusion will be presented at the end.

1.1 Biological background

1.1.1 Overview of the arterial structure

Arteries are a type of blood vessel that transports oxygenated blood away from the heart, to the cells, tissues and organs of the whole body (except the pulmonary and umbilical arteries). An artery (Figure 1.1) can be divided into two main parts, the lumen (the hollow core of the vessel where blood circulates), and the wall. The arterial wall is formed by three layers: (1) tunica intima, (2) tunica media and (3) tunica adventitia.

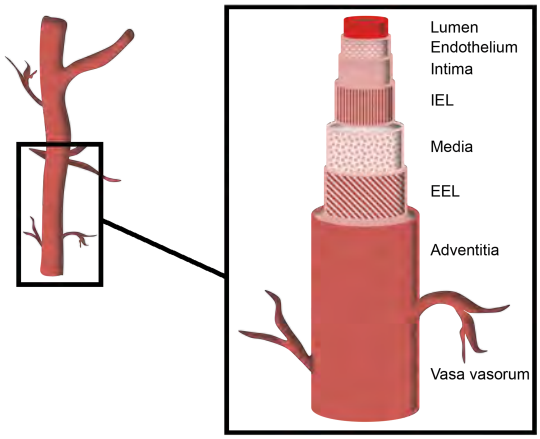

Figure 1.1: Arterial structure.

1.1.1.1 Tunica intima

The tunica intima is the "coating" of the lumen. It is comprised of the endothelium, the subendothelial connective tissue and the internal elastic lamina (IEL) [1]. The main functions of the intima layer are to prevent the blood plasma from filtering through the walls and to secrete vaso-active substances into the vessel lumen and through the vessel wall. This is mostly done by the endothelial cells (endothelium), the vaso-active cells. The endothelium is the innermost part of the arterial wall and it has a critical role in regulating the blood/tissue interaction inside the artery. It consists of a paved monolayer of endothelial cells (0.2 – 0.3 μm thick)[2]. These cells have three distinct surfaces, the luminal surface

(apical), the subluminal surface (basal) and the intercellular surface. The luminal surface of the endothelium is lined with a carbohydrate-rich layer, the endothelial glycocalyx[3]. The endothelial glycocalyx is the layer separating the arterial wall from the blood flow. Among its various functions, it serves as a mechanotransducer of haemodynamic forces to the endothelium and reduces the permeability of the endothelial layer to the plasma macromolecules.

The endothelium forms a semipermeable lining for the arterial lumen that serves to limit the passage of flowing macromolecules from the blood into the arterial tissue. Water, and some small solutes, are absorbed by the glycocalyx and pass through the endothelium via intercellular clefts (20 nm wide)[4]. The intercellular clefts are the spaces between the intercellular surfaces. Junctional strands (rows of protein molecules) form several tight junctions across the intercellular clefts, blocking the macromolecules pathway (Figure 1.2). The tightness of these clefts together with the thickness of glycocalyx defines the permeability of the endothelium. Besides their blood-borne macromolecule retaining role, endothelial cells also have the power to release vaso-regulative substances such as vasoactive agents (i.e. Nitric Oxide), anti-haemostatic agents and pro-inflammatory agents (i.e. Cytokines)[2] into the arterial lumen. As part of the body defence against pathogens, endothelial cells produce adhesion molecules that capture circulating leukocytes (i.e. monocytes) and lead them to migrate into the affected tissue. Abnormalities in endothelial function, such as increased endothelial permeability and overproduction of pro-inflammatory agents, are pro-atherogenic factors of major importance, as will be explained later.

1.1.1.2 Tunica media

The tunica media supplies the mechanical strength of the vessel wall. Its tissue is made up of a matrix of collagen fibres and elastin, in which smooth muscle cells are embedded[5]. Smooth muscle cells contribute to the compliance of the arterial wall. By contracting or relaxing, they control the calibre of the blood vessel and the local blood pressure. This portion of smooth muscle-rich tissue lies in-between two sheets of elastin, the IEL and the external elastic lamina (EEL) (Figure 1.1). Both of these consist of a thin layer of fenestrated elastic tissue.

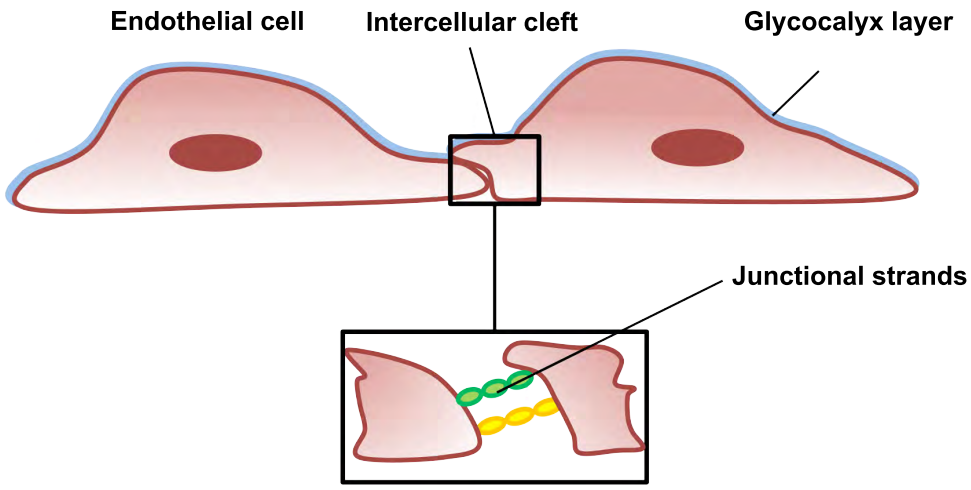

Figure 1.2: Sketch of the endothelial cell monolayer arrangement showing the glycolyx, intercellular clefts and junctional strands between cells.

1.1.1.3 Tunica adventitia

The outermost portion of the wall is the tunica adventitia. This layer is made of connective tissue and has the primary purpose of anchoring the vessel to the surrounding organs. In the case of large arteries, it can contain small blood vessels called *vasa vasorum*, which serve to nourish the media[5].

1.1.2 Atherosclerosis

Atherosclerosis is a chronic inflammatory disease of the subendothelial region of the artery. Formation of atherosclerotic plaque leads to thickening and hardening of the arterial wall, and may cause tissue ischemia and thrombosis. From histological examination of atherosclerotic plaques[6, 7], it has emerged that there are six main stages of plaque development (Figure 1.3). The first stage is represented by type I (foam cell formation) and type II (fatty streak) lesions[6]. Fatty streaks are lipid-laden lesions having the appearance of yellow streaks of $1 - 2$ mm in width and up to 10 mm in lenght. These are the earliest visible lesions at the beginning of the inflammatory process, where the blood-monocytes have already migrated into the arterial wall becoming lipid-laden foam cells and have started accumulating in the arterial wall. The type III lesion is the intermediate stage or

pre-atheroma[7]. This is a crucial step towards the formation of a more complex type of lesion. An initial formation of an extra-cellular lipid pool can be detected underneath the layer of macrophages and foam cells inside the intima. These extracellular lipids are the result of cholesterol released from dying foam cells. The growth in size of the extra-cellular lipid pool is a characteristic of type IV lesion, also known as atheroma. Atheroma is the first type of advanced lesion and is characterised by a deep structural change in the intima caused by the presence of the lipid pool, also known as the lipid core of the plaque[7]. Around this lipid core, new fibrous connective tissue is formed, and calcification of the lipid core can occur. At this stage, the plaque is defined as type V. New tissue is formed by smooth muscle cells(SMCs) migrating from the media[8] and collagen, and it contributes to increasing the size of the plaque.

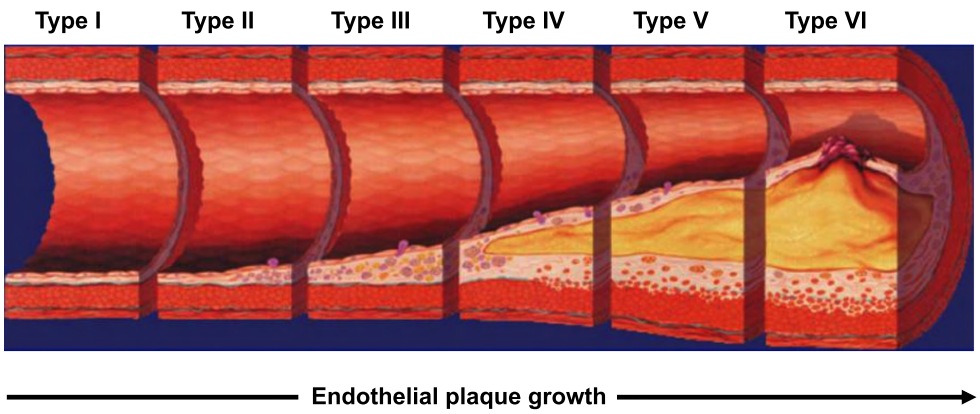

Figure 1.3: Atherosclerosis timeline. Representation of a typical atherosclerotic plaque development starting from foam cells migration (Type I) and ending with lesion rupture (Type VI). (Modification of open-source image from `http://en.wikipedia.org/wiki/Atherosclerosis`)

When a lesion surface or a thrombotic deposit develops in a lesion of type IV or V this becomes a complicated lesion (defined as a type VI lesion). This type of plaque is highly unstable, and it is clinically the most dangerous type as its rupture could lead to sudden death of the patient, due to thrombotic stroke. The different stages of atherosclerotic lesion development are shown in Figure 1.3.

The main objective of the present work is the development of a multiscale computational framework for atherosclerosis. Pre-atheroma lesions have been chosen as an exemplar application for this framework. A more detailed description of the biological processes that form the basis of type I–II lesions will be given in the following section.

1.1.2.1 Early lesion formation

LDL and its role in atherosclerosis

Plasma lipids, such as cholesterol and triglycerides, are essential to life. For example, cholesterol is a precursor to hormones and bile acids and is needed for cellular membrane synthesis, whilst triglycerides are an energy source for both cardiac and skeletal muscle. Among the different carriers of plasma lipids(lipoproteins), low density lipoprotein (LDL) is the one with the highest concentration of lipids in its core[9]. LDL is composed of 20 – 40% phospholipids, 9 – 10% free cholesterol, 40 – 44% of cholesteryl esters, 3 – 5% triglycerides, and 21 – 26% protein (Figure 1.4)[9]. The core is formed by the neutral lipids (cholesteryl esters, triglycerides), whilst the surface consist of a monolayer of phospholipids and cholesterol. Within the monolayer, a large protein, apolipoprotein B (ApoB) is embedded, which is used for receptor-dependent catabolism by the body tissues. The surface monolayer contains other substances among which α-tocopherol (vitamin E), believed to be the main protector of LDL against oxidation[10]. The quantity of vitamin E can be approximated to about 6 molecules per LDL particle[11]. Cox et al.[12] investigated the role of vitamin E in the development of atherosclerosis, showing that treating cholesterol fed rabbits with α-tocopherol protected them from showing the typical endothelial dysfunction coming from such a diet[12].

LDL is delivered as a nutrient to the arterial tissues by means of two main

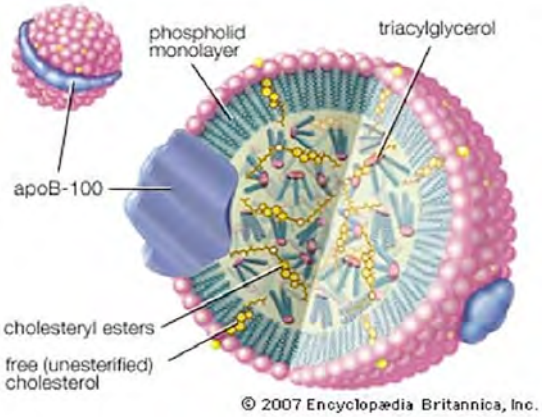

Figure 1.4: LDL particle, the inner core of the macromolecule is shown together with the apolipoprotein B. (Image after: lipoprotein : LDL complex. In Britannica Online for Kids. Retrieved from `http://kids.britannica.com/comptons/art-149526`)

receptor-dependent pathways through which LDL gets internalised by endothelial cells, nameli; endocytosis and transcytosis[13]:

- Endocytosis is the processing of the LDL particle by the endothelial cell lysosomes in the nucleus, where the LDL particle is degraded and the cholesterol released into the cell[14]. Through endocytosis the endothelium gets the amount of cholesterol required for its cellular membrane synthesis [15].

- Transcytosis is the transport of a macromolecule across the interior of a cell. The LDL macromolecule is taken up by a vesicle that travels across the endothelial cell layer and discharges the macromolecule at the sub-endothelial side of the cell.

The main native LDL (the LDL contained in plasma) receptor expressed by the endothelial cells is LDL-R, this binds to ApoB and lets the internalisation processes previously described happen[16]. The expression of the LDL receptors on the surface of a cell is controlled by intracellular cholesterol levels. When a cell has enough sterols for its needs, transcription of the receptor protein is down-regulated and the LDL uptake diminishes. Inhibition of lipid synthesis or promoting its conversion (and excretion via the liver) stimulates expression of LDL receptors boosting the uptake and diminishing the main blood LDL level.

From experiments, it has emerged that the bulk of uptake by the arterial wall of LDL is not receptor-dependent[17]. Especially in areas of altered haemodynamics (such as high intraluminal pressure or low wall shear stress (WSS)) that are detected as atherosclerosis-prone sites, it has been found that the receptor-dependent pathway contributes to only 10% of the overall transport of LDL inside the arterial wall[18]. The remaining 90% is due to the penetration of LDL macromolecules through endothelial intra-cellular clefts that are "leaky" and allow the passage of macromolecules through them (Figure 1.9).

Once inside the arterial wall, it is believed that LDL is oxidised by reactive oxygen species (ROS) (Figure 1.5)[19]. These ROS or free radicals are generated by the normal metabolic processes of cells or molecules contained in the arterial wall, such as macrophages and endothelial cells [19]. Interaction between LDL and free radicals leads to the modification of LDL into a highly cytotoxic lipoprotein [20]. Free radicals have a high affinity to react with the vitamin E contained in the LDL particles, having five orders of magnitude more affinity with this than with other components of the LDL core[21]. Prolonged residency of LDL in a "highly reactive" environment such as the arterial wall, can lead to the total depletion of antioxidant vitamin E molecules by the free-radicals from the outside layer of LDL.[22] LDL without its protective vitamin E layer is exposed to oxidation[10], leading to its degradation into the cytotoxic lipoprotein oxidised LDL (oxLDL) and stimulating the body's immune system to react (cytokine production activation and migration of plasma monocytes inside the arterial wall) (Figure 1.6 A). *In vitro* experiments performed with oxLDL incubated with cultured endothelial cells have shown that oxLDL particles stimulate the endothelial cells to release the chemoattractant peptide-1 and macrophage colony stimulating factor (activation of the immunological response of the body)[12]. Cells such as monocytes-macrophages belong to the so called receptor-independent LDL catabolism. Native plasma LDL is not taken up by macrophages, rather, it is sensed by macrophages receptors only when it is fully oxidised[23] (that is, when the ApoB protein is fragmented). OxLDL ApoB is modified in a form that is recognisable by the scavenger receptors present in macrophages and the oxLDL macromolecule is taken up [23].

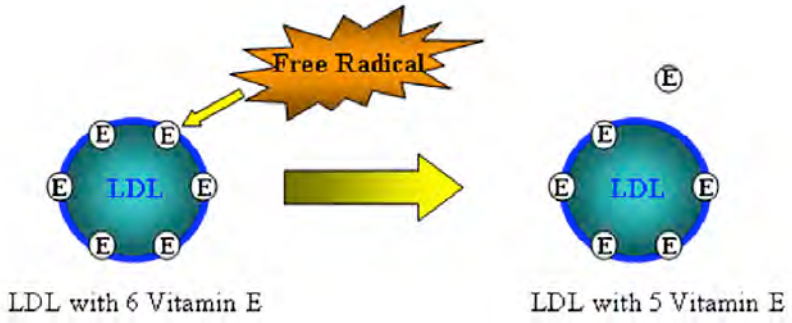

Figure 1.5: LDL particle with six vitamin E molecules on its outside layer loses a vitamin E as consequence of free radical interaction.

From Monocytes to Foam Cells - The immune response to oxidised LDL

Monocytes are a type of leukocyte (immune cell) that are produced by myeloid multipotential stem cells in the bone marrow. They travel in the blood where they reside for approximately eight hours before entering the connective tissue to mature into macrophages[24]. In atherosclerotic lesion sites, rolling interactions between plasma monocytes and endothelial cells layer are mediated by selectins, and their attachment to these cells to penetrate inside the arterial wall is mediated by integrins[25]; once attached they migrate towards the subendothelial area (Figure 1.6 B) attracted by cytokines (small cell-signalling protein molecules that are secreted by endothelial cells and tissue macrophages as a reaction to oxLDL particles). From *in vitro* experiments, it has been observed that oxLDL stimulates the recruitment of plasma monocytes to the atherosclerotic site by increasing the endothelial production of the vascular-adhesion molecule 1 (VCAM-1) and stimulating the secretion of monocyte chemotactic protein 1 (MCP-1)[25].

The arterial wall macrophages take up oxidised LDL, storing their cholesterol in cellular lipid droplets (Figure 1.6 B)[26]. Although such uptake is initially beneficial as it eliminates pro-inflammatory oxidised LDL from the arterial wall, the accumulation of these lipids eventually leads to a modification in the macrophage cellular structure. Macrophages become lipid laden foam cells with an impaired efflux from the arterial wall, and accumulate in the intima to form fatty streaks.

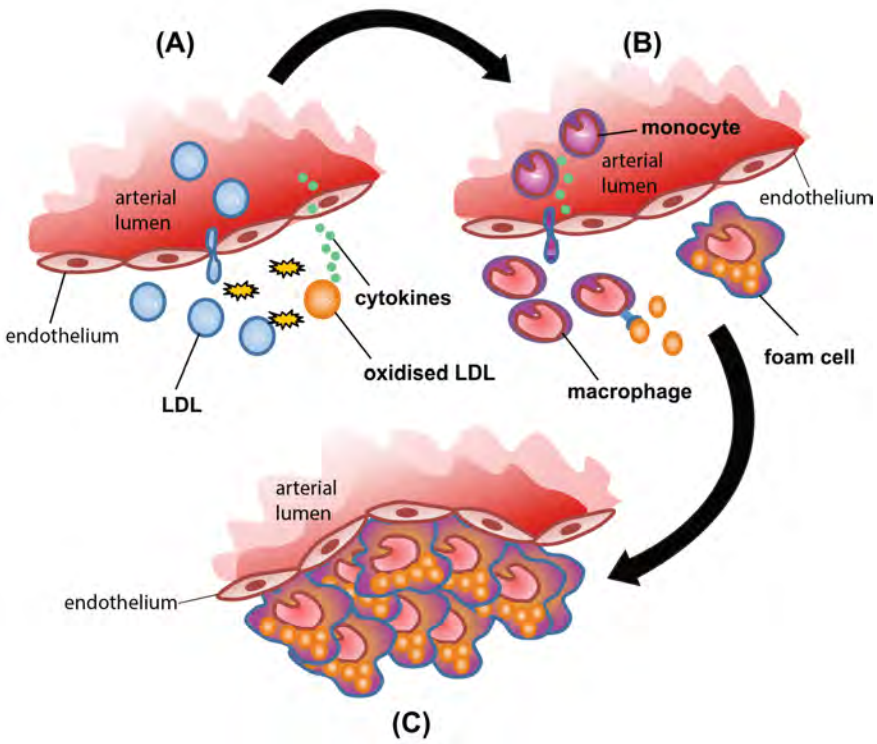

Figure 1.6: Fatty streak formation. From (a) LDL penetration inside the arterial wall and oxidation to (b) foam cell formation and (c) accumulation leading to intimal swelling.

Foam cells stratify in adjacent layers; this leads to the initial arterial intima thickening that is typical of fatty streak formation (Figure 1.6 C).

Atherosclerosis formation is associated with several systemic factors such as genetic predisposition (i.e. hypercholesterolaemia), hypertension and behavioural factors like sedentary lifestyle and smoking[27, 28]. From *in vivo* observation it has emerged that, despite these risk factors, atherosclerosis tends to develop in specific regions of the vasculature, such as curvatures and bifurcations of the artery[29], suggesting a role played by local haemodynamics in the creation of atherosclerosis-prone areas.

1.1.3 Haemodynamic Wall Parameters for the identification of atherosclerosis-prone areas

Experimental evidence indicates that some properties of the endothelium such as cell geometry[30], orientation[31] and permeability to macromolecules[32] are influenced by haemodynamic forces. The blood flow produces a frictional force on the endothelial glycocalyx known as haemodynamic shear stress. This frictional force is dependent on both the blood viscosity and the blood velocity. There are different parameters derived from the haemodynamic shear stress that can be used as markers of the impact of the haemodynamics on the arterial wall, they are called Haemodynamic Wall Parameters(HWPs)[33].

The frictional force exerted by blood on the arterial wall is proportional to the velocity gradient at the wall and the fluid viscosity, and it is defined as the wall shear stress (WSS):

$$\tau_w = \mu \frac{\partial \nu}{\partial r}\bigg|_{wall} \tag{1.1}$$

where τ_w is the WSS, μ is the dynamic viscosity of the fluid, ν is the fluid velocity along the boundary and r is the radial distance from the boundary (the wall). WSS is mechanically transduced from the glycocalyx to the endothelium underneath, and serves as a regulator of the endothelial cell activity (Figure 1.7).

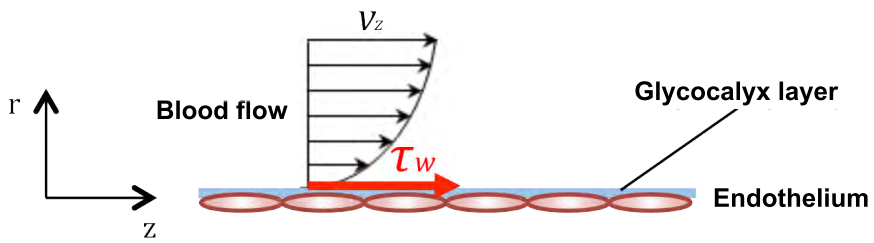

Figure 1.7: WSS induced by blood flow on the glycocalyx layer and endothelium.

In the main human arterial vessels, WSS typically varies between 5 and 20 dyn/cm^2 (0.5 and 2.0 Pa)[34]. This large range of WSS levels leads each artery to respond differently to various stimuli of WSS[35]. According to different studies[34, 36–39], atherosclerosis is more likely to develop in areas where the local WSS is low (less than 5 dyn/cm^2) (atherosclerosis-prone areas). WSS is able to

influence the endothelial structure and disrupt the glycocalyx layer[40], and it might be a key player in the development of vascular pathologies such atherosclerosis[41]. *In vitro* findings[32] show that the endothelial cell shape is changed, and permeability is enhanced in areas of low WSS. The structural change in endothelial cell alignment and shape was found to be particularly severe distal to a stenosis, where an area of high WSS would be followed by an area of low WSS[32]. The spatial change in the WSS vector is defined as the Wall Shear Stress Gradient (WSSG)[42].

$$WSSG = \sqrt{\left(\frac{\partial \tau_x}{\partial x}\right)^2 + \left(\frac{\partial \tau_y}{\partial y}\right)^2 + \left(\frac{\partial \tau_z}{\partial z}\right)^2} \tag{1.2}$$

A study by Lei et al.[43] linked increased vascular permeability to a combination of high WSSG and low WSS. These two HWPs are time-independent indicators of the onset of atherosclerosis. Time variations in the local haemodynamic stimuli also affect the endothelial function[44]. In transient environments, with a pulsatile time-dependent flow, the HWPs used to characterise the haemodynamics include time-averaged WSS (TAWSS) and oscillatory shear index (OSI) [33].

$$TAWSS = \frac{1}{T}\int_0^T |\tau_w| dt \tag{1.3}$$

where T is the period of time over which the shear stress is averaged. There is a strong correlation between WSSG and TAWSS and monocyte adhesion patterns, suggesting that these two indices are of major importance when identifying atherosclerosis in peripheral arteries [33, 41].

The prevalence of atherosclerotic lesions in both the human carotid bifurcation and the abdominal aorta strongly correlate with low shear regions with an almost purely oscillatory flow[44, 45]. The OSI is a measure of the degree of deviation of the WSS from its average direction during pulsatile flow, and it is expressed as[46]:

$$OSI = \frac{1}{2}\left(1 - \frac{\left|\frac{1}{T}\int_0^T |\tau_w| dt\right|}{\frac{1}{T}\int_0^T |\tau_w| dt}\right) \tag{1.4}$$

OSI has been associated with vascular cell rearrangement and increased endothelial permeability[47] especially in arteries with extensive curvature like the carotid artery[39]. In the descending abdominal aorta and sub-umbilical peripheral arteries, flow patterns are not strongly disturbed by flow pulsatility, in contrast to other arteries such as the thoracic aorta, the coronary arteries and the carotid arteries[41].

A study by Niwa et al.[48] on bovine cocultured endothelial cells and SMCs, showed that the number of intimal SMC is inversely proportional to the local level of WSS, suggesting a role played by WSS even in the later stages of atherosclerosis development.

Although largely accepted, the theory of low and oscillatory shear as pro-atherogenic is still subject of study and debate [49]. Investigations are trying to estabilish the most significant for atherogenesis development among the different HWPs presented in this section, and to individuate HWPs that could be atheroprotective [50, 51].

Some studies failed to find a correlation between TAWSS [52], WSS [53], and OSI [54] and atherosclerosis formations. As there is lack in a generalized methodology for analysing this phenomenon, Pfeiffer et al. [49] argue that the difference in the analysis methods used could be leading to contrasting results [49]. Whilst the studies using visual comparison maps [33], and axial [55] and circumferencial [56, 57] avereging to compare disease location with local HWPs agreed with the low shear theory, the majority of studies using the point-by-point comparison[53, 54] failed to report a connection between observed lesions and HWPs.

Together with data processing methods, techniques used to individuate disease location and to reproduce the disease-free environment for haemodynamic simulations have to be considered [49]. Measurements of intima thickness [53] can not alone identify atherosclerosis locations [49], and calcium scoring is a good assesment criterion, but only for atherosclerosis at a later stage [49]. Blood flow assessment is usually done either on subject specific geometries, or on multiple group studies. The latter one, would consider the same artery in a population of diseased and healthy individuals and perform a comparison between the two. However, of more interest are individual studies, where the specific arte-

rial anatomy of the subject is considered, before and after the disease formation, and disease-free vessels are recreated virtually [58, 59]. Although this patient-specific approximation of the healthy vessel enables the anatomical variations among individuals to be taken into account, it can also be misleading due to the chance of reconstruction errors arising. Vertical studies following a population from healthy to diseased state are needed, together with better techniques for visualising atherisclerosis formations in-vivo, in order to conduct analysis for the successful identification of all the HWPs of interest for atherosclerosis formation [49].

1.2 Computational Modelling

One of the next challenges in medicine is the development of patient-specific diagnostic tools for a more targeted treatment and an improved quality of life (also called *"in silico"* medicine). Mathematical modelling has the potential to conduct "virtual experiments" that are patient-specific and non-invasive, providing an important tool to move closer towards a future of patient-specific diagnosis and prognosis. *In silico* medicine is very challenging as the incredible complexity of human pathophysiology makes it hard to conceptualise and translate into mathematical form[60].

As part of this chapter a review of the mathematical tools used in the study of cardiovascular diseases will be presented in the sections below. Mathematical models of the cardiovascular system can be broadly divided into three main categories[61], continuum mechanical models of the vascular soft tissue, fluid dynamical models describing the interaction between blood flow and vessel walls (also known as transport models) and mathematical models of biochemical properties of the vasculature (also known as biochemical models).

As atherosclerosis formation involves a complex interplay of mechanical and biochemical processes, a comprehensive model of atherosclerosis will require the integration of these various modelling approaches.

Although arterial tissue modelling corresponds to a large sub-section within this context[62–64], a review on the continuum mechanical models of vascular tissue will not be given as it is not relevant for the current work. The section

below will concentrate on the other two modelling approaches that are at the core of this thesis.

1.2.1 Transport models

The study of the transport of macromolecules (albumin, LDL) from the arterial lumen to the arterial wall has been the focus of a number of mathematical models[60, 65]. These models are usually classified according to the level of description of the fluid domain and the solid domain provided.

The simplest modelling approach used to model the arterial wall is the wall-free model approach, where the arterial wall is described as a simple boundary condition. The first application of a wall free model to LDL transport was developed by Wada et al.[66]. Because of the low amount of data handled, these models are easy to implement and to compute. As the wall domain is not modelled, important information for atherosclerosis modelling such as LDL concentration inside the arterial wall cannot be provided by these models.

A more detailed description of the arterial wall is given by the fluid-wall models. These models consider the arterial wall as a homogeneous layer, with uniform transport properties throughout; they can capture quantitative information inside the arterial wall, albeit, in a simplified way. The most refined modelling approach to the arterial wall is the multi-layer model. These types of model describe the arterial wall by considering its several heterogeneous layers. The multi-layer approach provides the most detailed information on the dynamics of macromolecules and other molecules, species or cells inside the wall[67, 68]. This model allows for a more detailed description of the artery, but requires a larger amount of parameters that are often difficult to estimate from experiments, source from the literature and implement.

To model the transport of molecules within the fluid domain, the simplest modelling approach is the so-called "lumen-free"[69]. In the lumen-free approach, the transport of macromolecules inside the lumen is not modelled, and the lumen is considered as a boundary with a constant concentration of macromolecules. In the case where the lumen is considered, the transport of macromolecules is modelled, allowing for a concentration profile of macromolecules inside the lumen

to be developed.

In the following sub-sections, a review of the various modelling approaches and techniques used to describe the fluid domain of the artery (the arterial lumen), the arterial fluid-solid interface (the arterial endothelium) and the arterial solid domain (the arterial wall) will be given (Figure 1.8).

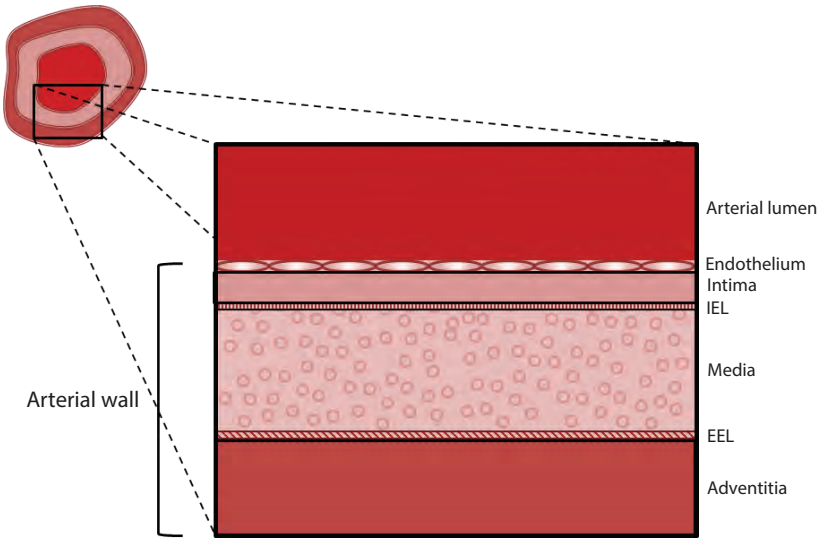

Figure 1.8: Transverse section of the computational domain considered. No differentiation among the components of the arterial wall is shown. The image is not shown to scale.

1.2.1.1 Lumen modelling

In atherosclerosis models, blood flow inside the lumen is usually modelled assuming blood as an incompressible Newtonian fluid obeying to the Navier-Stokes equations and the continuity equation[70, 71].

$$\rho \frac{\partial}{\partial t} \boldsymbol{u_l} = -\nabla p_l + \mu \nabla^2 u_l + \rho f \tag{1.5}$$

$$\nabla \cdot \boldsymbol{u_l} = 0 \tag{1.6}$$

Where $\boldsymbol{u}_l$ is the velocity vector field in the lumen, p_l is the blood pressure in

the lumen, f is the volume force vector, μ is the viscosity of the blood and ρ is the blood density[72].

These characteristics though, relate more to the behaviour of plasma alone, as blood shows a non-Newtonian behaviour known as shear thinning[73]. Shear thinning behaviour is caused by the cellular structure of blood. At very low shear rates red blood cells tend to aggregate more, leading to higher blood viscosity. On the other hand, at high shear rates, normal red blood cell aggregates are disrupted leading to a decreased viscosity. Other modelling approaches have assumed human blood to be a non-Newtonian fluid in order to study local haemodynamics and its role in the location of atherogenesis[74, 75]. Johnston et al. [76] considered different non-Newtonian models and a Newtonian model for the modelling of blood inside human right coronary arteries in a steady state regime. The WSS patterns were found to be consistent for both the Netwonian and the non-Newtonian flow [76]. Similarly, corresponding WSS values were predicted by all the models in areas of high to medium shear stress. Differences arised in the simulated areas of low shear stress, where the Newtonian model appeared to underestimate the value of local WSS [76, 77]. The importance of considering the non-Newtonian characteristics of blood is higher when modelling areas of low shear stress and small arterial vessels [76, 78]. For large to medium vessels (such as the aorta and the iliac arteries) [79], modelling the viscosity of blood as Newtonian can be considered a valid approximation [80].

The fluid environment is often modelled in steady state conditions. Short term variations in the flow patterns such as the pulsatile nature of blood velocity, can be averaged to a steady behaviour when considering long term processes like atherosclerosis. Some studies, however, have shown that the steady state assumption is inadequate in the presence of complex geometries generating modified flow patterns[69]. Furthermore, the steady state assumption would prevent the inclusion of time-dependent HWPs that, as already discussed, might play an important role in the identification of atherosclerosis-prone areas.

A study by Rappitsch et al.[81] investigated the influence of steady vs. pulsatile flow conditions on trans-endothelial flux of macromolecules. It was found that some features influencing endothelial transport could not be captured if flow pulsatility was neglected. Models coupling pulsatile flow with arterial wall mass

transport have been developed[71, 82], however difficulty arises when coupling transient flow simulations with macromolecule transport over a long period of time. Wood et al.[69] developed the lumen-free time-averaged (LFTA) approach, where the pulsatility effect is considered whilst keeping the steady state assumption. They coupled the transient blood flow with the wall domain using time-averaged values, allowing for different time definitions to be used in the different domains considered.

The transport of macromolecules inside the lumen can be modelled using a convection-diffusion equation[82–87]. The transient transport of macromolecules inside the arterial lumen would be given by:

$$\frac{\partial c_l}{\partial t} + \nabla \cdot (-D_l \nabla c_l + \boldsymbol{u_l} c_l) = 0 \tag{1.7}$$

where D_l is the macromolecule diffusion coefficient inside the arterial lumen, and c_l is the macromolecule concentration. As previously explained, a simplified approach to model plasma macromolecules is the "lumen free" approach[69, 72], where the concentration of macromolecules is kept constant throughout the fluid domain.

1.2.1.2 Endothelial modelling

The endothelium is usually only characterised in multi-layer models, where the different strata of the artery are modelled separately. An example of endothelium modelling in a simple model such the free-wall model is presented by Wada et al.[66]. In this free-wall model, the transport of macromolecules in the lumen is considered in both the axial and the radial direction, with the arterial endothelium as a boundary condition. At the blood-endothelium boundary, the steady state amount of LDL passing through the endothelium is modelled as the difference between the LDL that is carried to the wall and the LDL that diffuses back to the mainstream

$$\boldsymbol{\nu_w} c_w - D \left. \frac{\partial c}{\partial r} \right|_{r=r_0} = K c_w \tag{1.8}$$

where D is the LDL diffusivity and the total flux of LDL to the endothelium

can be expressed as:

$$Kc_w = n\boldsymbol{\nu_w}c_w + kc_w \tag{1.9}$$

with c_w as the wall macromolecule concentration, n as the fraction of LDL carried through the vessel wall by filtration flow, $\boldsymbol{\nu_w}$ as the filtration velocity of water through the arterial wall, and K as the endothelial uptake of LDL through both vesicular transport and receptor-mediated uptake (endocytosis).

A more complete description of the endothelial interface between the arterial wall and lumen was proposed using fluid-wall models and multi-layer models[84, 88]. The endothelium is modelled as a porous membrane where the macromolecule (solute) penetrates together with the macromolecule carrier (solvent). The transport of a solute and solvent through a membrane can be modelled with the Kedem-Katchalsky equations[60, 69, 83, 89]:

$$J_v = L_p(\Delta p_{end} - \sigma_{end}\Delta\Pi) \tag{1.10}$$

$$J_s = P_{end}\Delta c + (1 - \sigma_f)J_v c_{end} \tag{1.11}$$

Where J_v is the volume flux (solvent flux) and J_s is the solute flux through the membrane (the endothelium), L_p and P_{end} are the hydraulic conductivity and permeability of the endothelium, Δp is the pressure difference and Δc is the solute concentration difference across the endothelium, c_{end} is the mean solute concentration inside the endothelium, and $\Delta\Pi$ is the osmotic pressure with σ_{end} as the osmotic reflection coefficient. The net filtration pressure in Equation (1.10) is given by the term $\Delta p_{end}\sigma_{end}\Delta\Pi$, and it stands for the driving force of volume flux penetration. *In vitro* findings show that the LDL concentration in the arterial wall increases under elevated transmural pressure[90, 91]. In Equation (1.11) the term $(1-\sigma_f)$ represents the frictional reflection coefficient (or Staverman filtration coefficient); i.e. the extent to which the particles of LDL (the solute) are reflected by the endothelial membrane. The osmotic effect $\Delta\Pi$ is usually neglected when calculating the solvent flux as it is far below the hydraulic pressure gradient Δp_{end}[92]. Karner et al.[93] have investigated the influence of endothelial damage

and blood pressure on the distribution of albumin in the vascular wall, modelling the endothelium with the help of Kedem-Katchalsky equations. Their model showed that the main resistance to the macromolecule flux to the arterial wall is represented by the endothelium.

The properties of the endothelium have been shown *in vitro* to be linked to the local haemodynamics[90, 94, 95], as discussed in section 2.1.3. Sun et al.[88] developed an initial approach to model haemodynamic effects on the endothelium transport properties using a shear-dependent hydraulic conductivity (L_p) to calculate the volume flux through it (Equation (1.11)).

Factors that affect the permeability of endothelial cells are still not fully understood and they constitute an active field of research[41, 95]. Findings from Levesque et al. [32] show that in areas of flow recirculation the endothelial cells have a higher permeability to macromolecules. Some hypotheses attribute the change in endothelial permeability to the relaxation of the endothelial tissue leading to an increase in the endothelial clefts gap size[96]. Other experiments show that in areas of decreased blood flow, endothelial mitosis is stimulated and accelerated. These experiments suggest a new hypothesis that considers mitotic cells as "leaky cells" (meaning that the clefts surrounding these cells would no longer be the normal endothelial tight clefts) (Figure 1.9)[97, 98].

In order to account for this heterogeneous behaviour of the endothelium the three pores model[99] was created. The three pores model considers three pathways through which LDL can penetrate inside the endothelium (Figure 1.9):

Normal cell pathway Endothelial cells take up and metabolise plasma LDL macromolecules (endocytosis), no passage of LDL is allowed through intercellular clefts as the tight junctions block the passage of solutes with a radius greater than 2 nm (the average LDL radius is 11 nm).[83]

Vesicular pathway LDL macromolecules travel through the endothelial layer via vesicles (transcytosis) and are discharged in the arterial wall.

Leaky cell pathway Mitotic endothelial cells present leaky junction (the intercellular protein strands forming the tight junctions are broken down), these are 40 nm wide clefts that allow macromolecules such as LDL to pass through them.

Olgac et al.[83] linked the quantity of mitotic cells to local WSS values, with an inverse relationship between WSS and number of leaky cells sites. Modified versions of the Kedem-Katchalsky equations (Equations (2.8) and (2.9)) were used to include the three pores pathways [99] into their transport model of the endothelium.

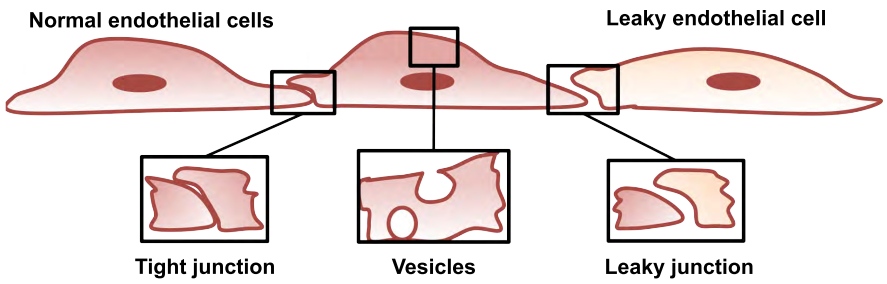

Figure 1.9: Diagram representing endothelium as described by the three pores model. Perpendicular cross section view showing two normal endothelial cells and a leaky endothelial cell. The three macromolecule transport pathways: tight junctions, vesicles and leaky junctions are shown.

Further extensions to this model included the heterogeneous endothelial transport properties and the glycocalyx layer[84]. Another approach to the Kedem-Katchalsky equations is to model the solvent flux through the endothelial clefts and the leaky junctions of the endothelium using the steady state Navier-stokes and continuity equations (Equations (1.5) and (1.6)) with the velocity $\boldsymbol{u}$ as the solvent velocity through the leaky clefts or junctions:

$$-\nabla p_{lj} + \mu \nabla^2 \boldsymbol{u_{lj}} = \rho (u_{lj} \cdot \nabla) \boldsymbol{u_{lj}} \tag{1.12}$$

where p_{lj} is the pressure in the corresponding leaky cleft or junction, and the material density and viscosity ρ and μ are taken for blood plasma.

The flux of solute (LDL) through the endothelial leaky junctions was coupled to the solvent flux with a convection-diffusion equation[87, 100] in a steady state environment:

$$\nabla \cdot (-D_{lj} \nabla c_{lj}) + \boldsymbol{u_{lj}} \cdot \nabla c_{lj} = 0 \tag{1.13}$$

where all the c_{lj} is the LDL concentration in the leaky junction and D_{lj} is the

diffusion coefficient of LDL through the leaky junction.

To account for the semi-permeable endothelial coating represented by the glycocalyx, Brinkman's equation for a porous medium was used:

$$\frac{\mu}{K_{pl}}\boldsymbol{u_l} = -\nabla p_l + \frac{\mu}{\epsilon_l}\nabla^2 u_l \tag{1.14}$$

$$\nabla \cdot \boldsymbol{u_l} = 0 \tag{1.15}$$

where ϵ_l and K_{pl} are the porosity and hydraulic permeability of the glycocalyx, p_l is the pressure and $\boldsymbol{u_l}$ is the superficial velocity vector of the glycocalyx.

Brinkman's equation (Equation (1.14)) was used to link the pressure drop with the velocity across the porous media[91]:

$$\boldsymbol{u_l} = -\frac{k}{\mu_l}\nabla p_l \tag{1.16}$$

Brinkman's equation (Equation (1.14)) allows a heterogeneous material with more than one pore size to be modelled, by adding a viscous term to Darcys Law (Equation (1.16)) (in order to account for the presence of a solid boundary, the glycocalyx).

Yang et al. [100] modelled transendothelial macromolecule transport using an extended version of the Brinkman's equation (accounting also for the temperature of the membrane) coupled with a convection-diffusion equation (Equation (1.13)) in a volume-averaged stationary form[91, 100]. The convection-diffusion equation was here improved by including the Staverman filtration and the osmotic reflection coefficient, to model the membrane pores behaviour in relation to the macromolecule penetrating them.

1.2.1.3 Arterial wall modelling

Characterisation of transport of macromolecules inside the arterial wall is at the centre of atherosclerosis models. The two main approaches characterising the wall beyond a boundary condition are the fluid-wall models and the multi-layer models. Fluid-wall models consider the arterial wall as a single layer composed of intima and media[82, 85–87]. Multi-layer models [84, 89, 100] differentiate

between the different arterial wall layers considering the intima, the IEL and the media (Figure 1.8) separately. The adventitia is usually treated as the arterial wall limiting boundary with a fixed macromolecule concentration value[88].

The arterial intima and media are usually modelled as porous layers with homogenous transport properties. In fluid-wall models, the concentration field of macromolecule in the arterial wall is computed with a convection-diffusion-reaction equation in steady state (Equation (1.17))[83, 88] or in transient conditions (Equation (1.18))[71]:

$$-D_w \Delta c_w + K_{sl} \nabla c_w \cdot \boldsymbol{u_w} = k c_w \tag{1.17}$$

$$\frac{\partial c_w}{\partial t} + \nabla c_w \cdot \boldsymbol{u_w} = D_w \Delta c_w + k c_w \tag{1.18}$$

where the transmural velocity $\boldsymbol{u_w}$ is described by Darcys Law[83, 89, 91, 100] or Brinkmans equation[82, 84]. D_w is the diffusivity of the macromolecule in the wall, K_{sl} is the solute lag coefficient[88], and k is the rate constant for chemical reaction of the macromolecule inside the arterial wall [71, 83, 88]. When modelling LDL transport, this reaction accounts for the degradation of the macromolecule and therefore has a negative sign, becoming a sink for LDL concentration. When intima and media are not differentiated, the transport constants used are usually values describing the behaviour of the media, this simplification is not far from reality as the media corresponds to 97% of the intima-media wall thickness[93]. In multi-layer models, a different equation would be used for each layer, with the transport coefficients changed accordingly[84, 93].

When considered, the IEL is usually modelled as a membrane with shear-dependent transport properties. The same approach used for the endothelial layer is used for IEL, where the leaky junctions are substituted by fenestrated pores. IEL is modelled using the Kedem-Katchalsky equations[89], or using Brinkman's equation for porous media[84], or by coupling the Brinkman's equation with convection-diffusion equations[71].

1.2.2 Biochemical models

Several models have tried to characterise the different bio chemical processes leading to atherosclerosis formation. Ross[101] defined atherosclerosis as a chronic inflammatory disease, different mathematical models have been developed[102, 103] based on this assumption. Ibragimov et al.[102, 104] proposed an initial approach for the modelling of this inflammatory process concentrating on intercellular interactions, such as chemotaxis (the movement of a cell along a chemical gradient). They created a system of partial differential equations(PDEs) that modelled the spatial distribution of the different species involved in atherosclerosis development; immune cells, SMCs, debris (dead cells, produced by degradation of immune cells or SMCs), chemoattractant (i.e. cytokines), native LDL and oxidised LDL. Their movement was considered to be due to purely diffusive behaviour and chemotaxis. The PDEs for the transient spatial concentration of immune cells (Equation (1.19)) and debris (Equation (1.20)) are shown below:

$$\frac{\partial n_1}{\partial t} = \nabla \cdot \left(\mu_1 \nabla n_1 - X_{11}^0 \frac{n_1}{c_1} \nabla c_1 - X_{13}^0 \frac{n_1}{c_3} \nabla c_3 \right) - d_1 n_1 \tag{1.19}$$

$$\frac{\partial n_3}{\partial t} = \nabla \cdot (\mu_3 \nabla n_3) + d_1 n_1 + d_2 n_2 - F(n_3, c_3) n_1 \tag{1.20}$$

Where X is the tactic sensitivity function, modelling the chemotactic motility as an advective term, μ_1 is the motility coefficient depending on the concentration of the chemical species or their density and their position, and μ_3 is the diffusion coefficient, depending on the species position. The parameters d_1 and d_2 are the degradation rates of immune cells and SMCs becoming debris, and F is the decrease in debris due to the immune response. The oxidation of LDL is modelled here as a single reaction, by simplification of the detailed model developed by Cobbold et al.[22]

Oxidation of LDL is considered to be a central event in atherosclerosis formation. Stanbro[105] first modelled the oxidation of a single LDL macromolecule by a free radical (Peroxonytrite) using an ordinary differential equation (ODE). LDL oxidation modelling was improved by Cobbold et al.[22] who proposed a mathematical model of $in - vitro$ LDL oxidation, using a system of time-dependent

ODEs. This model of oxidation is centred on the interaction of free radicals and the LDL protective layer of vitamin E (α-tocopherol). Each LDL particle with an intact layer of vitamin E would be protected from oxidation; however as a consequence of persistent residence of LDL inside a free-radical rich environment (the arterial wall) the protective layer would degrade and the LDL macromolecule would eventually oxidise. To model the interaction between LDL and free radicals a second order kinetic reaction was used:

$$LDL_n + R \xrightarrow{k} LDL_{n-1} \tag{1.21}$$

Applying the law of mass action, the transient change of concentration of LDL_{n-1} would be:

$$\frac{dLDL_{n-1}}{dt} = kLDL_nR \tag{1.22}$$

The subscript n belongs to the interval $[8, 0]$, meaning that there are eight possible states of LDL transformation/degradation, from LDL with six vitamin E (native LDL) to oxLDL (Figure 1.5). The depletion of the vitamin E layer leaves the LDL macromolecule prone to oxidation, with the final state of the chemical cascade being the oxLDL. To the authors' knowledge, this is the most detailed model of LDL oxidation that has been developed.

The oxidation of LDL was not modelled directly by El Khatib et al.[103, 106], but it was used as a tuning variable for the intensity of the inflammatory process. The model of atherosclerosis formation proposed was characterised by a system of reaction-diffusion equations describing M the density of immune cells (monocytes, macrophages) and A the density of the cytokines secreted by the immune cells:

$$\begin{cases} \frac{\partial M}{\partial t} = d_1 \frac{\partial^2 M}{\partial x^2} + f_1(A) - \lambda_1 M \\ \frac{\partial A}{\partial t} = d_2 \frac{\partial^2 A}{\partial x^2} + f_2(A)M - \lambda_2 A \end{cases} \tag{1.23}$$

Where the function f_1 represents the recruitment of monocytes as a consequence of oxLDL and the function f_2 models the cytokine production rate. A

traveling wave solution to the system as:

$$\begin{pmatrix} A(t,x) \\ M(t,x) \end{pmatrix} = W(x - ct) \tag{1.24}$$

represents the propagation of the chronic inflammatory reaction, where c is the speed of the wave. This modelling approach to atherosclerosis was further developed by Calvez et al.[107]. In this work, oxLDL, monocytes/macrophages and foam cells were considered. Their PDE for modelling the evolution of oxLDL (O_x) was:

$$\begin{cases} \partial_t O_x + div(\boldsymbol{v} O_x) = d_1 \Delta O_x - k_1 O_x \cdot M \\ \partial_{y=h} = \tau(x) C \\ \partial_{y=0} = 0 \end{cases} \tag{1.25}$$

where the second term on the right hand side of the PDE is the conversion of macrophages (M) into foam cells using a second order kinetic reaction. The diffusion of oxLDL in the domain is given by the first term on the right hand side. The second term on the left hand side models the lesion growth; it allows for the considered tissue to be displaced at speed $\boldsymbol{v}$ following the progression of plaque growth; the oxLDL is transported within it (transport of oxLDL in the lesion growth was neglected when computing the model). The boundary conditions for this PDE are 0 at the adventitial boundary ($y = 0$) and a concentration of native LDL (C) dependent on the WSS (τ) at the boundary with the lumen ($y = h$). The permeation of native LDL into the arterial wall was modelled as a function of local WSS, allowing the inflammatory model to be coupled with the blood flow[108]. The model of atherosclerosis was completed with the simulation of lesion formation:

$$\frac{dh}{dt} = \frac{k_1}{Ah} Q_{Ox} \cdot Q_M \tag{1.26}$$

The lesion growth (h) is modelled as vertical growth of the intima due to the formation of foam cells, given by the product of the quantity of oxLDL (Q_{Ox}) and macrophages (Q_M), calculated as the integral of the concentration over the height of the domain (for the 1D model). Study of the temporal development of

the inflammatory response was at the centre of the modelling approach proposed by Ougrinovskaia et al.[109] Here, the authors built a system of ODEs, representing the interactions between oxLDL and monocytes leading to the development of foam cells. Following the approach of Calvez et al.[107], they ignored the oxidation of LDL and the changing of monocytes to macrophages as the small time scale of these events (hours to days) can be considered negligible when compared to the time scale of atherosclerosis formation (months to years). Plaque growth was not directly modelled here, but foam cell accumulation was treated as characterisation of plaque growth behaviour.

A more advanced modelling of plaque growth was attempted by Zohdi et al.[62] The authors developed a model of arterial plaque growth and rupture, linking their plaque growth to the accumulation of monocytes in the arterial wall:

$$\dot{a} = K\eta \tag{1.27}$$

This is a standard growth equation[110] where $\dot{a}$ is the growing thickness of intima, K is the growth rate constant, and η is a function of monocytes accumulation.

This model represents what at the beginning of this section was defined as a continuum mechanical model of the vasculature soft tissue, and is included here to conclude this review on the modelling of the biochemical processes leading to plaque growth. The biochemical models of plaque development are not suitable for modelling the tissue changing properties typical of the evolution of the atheroma. To further model the atheroma and its rupture, the model will require a more detailed depiction of the arterial tissue, following the approach developed by Zohdi et al.[62]

As mentioned at the beginning of this section, a complete model of atheroma formation and evolution would need to combine all the different modelling branches briefly described and reviewed[61] here. Fluid dynamic models are needed to characterise the plaque location and evolution, biochemical models are needed to describe the processes leading to plaque formation and continuum mechanical models are needed to understand the evolution of the atheroma and to model the

impact of the disease on the arterial tissue.

1.2.3 Multiscale modelling

Complex biological processes, such as atherosclerosis occur at various levels of organisation (from the molecular and cellular scale, to the level of the whole organism)[111]. Modelling these processes requires us to take into consideration these various levels, which will lead to the creation of a multiscale model. Ingram et al.[112] identified three main tasks when creating a multiscale model. The first step is the identification of the different time and length scales, and the relative biological processes that they capture. This leads to the creation of a Scale Separation Map, as defined by Hoekstra et al.[113], where each area represents a submodel[111] with its definition of space and time. A scale separation map can be built with either a top-down or bottom-up approach. A middle-out approach can also be used: from the submodel that is the richest in terms of information or data, to the other levels[112, 114].

The second step is the development of a submodel for each level considered. The choice of the modelling technique depends on the biological system and on the type of behaviour to be recreated. A discrete approach is often used at the microscale (sub-cellular/cellular level). Modelling approaches such as agent based modelling (ABM)[115] and cellular automata (CA) [116] allow for the description of individual cells behaviour. These formalisms have been used to model SMCs proliferation during in-stent restenosis [115] and the reaction of the endothelial cells to the blood flow [117]. At the tissue level and organ level, the elements in the sub-model are usually considered as a continuum and a 3D spatial description is required. At this level, the submodel is usually described with mathematical approaches such as PDEs [118], or coupled ODEs [116]. The continuum spatial description can be reduced to a simpler a-dimensional representation. This type of reduction is called a lumped-parameter model, and it is often used to model arterial networks [119].

Moving from the micro scale to the macro scale, the modelling approach usually changes from discrete to continuum [120]. However, multiscale models that are discrete[117] or continuum across the different scales [118] can also be

found.

The last step is the integration of the different submodels in a coherent multiscale model, and the creation of a multiscale framework. This is perhaps the most challenging task, as the information flowing between the submodels is what would define the correct functioning of the whole multiscale model[112]. Generalised environments are being developed to handle and couple sub-models. One example of these environments is the Multi-scale Simulation Library (MUSCLE) developed by Sloot et al.[114]. This library would allow the implementation of CA, ABM and other formalisms across different scales [121]. Another effort has been made by the Physiome Project, developing an XML based service to integrate scales (ModelML), as well as for representing micro-scale (CellML) and macro-scale (FieldML) processes [122]. These multiscale frameworks or environments[114] have found a number of applications in cardiovascular modelling, such as modelling of the arterial wall evolution[115] and heart modelling [122].

1.3 Conclusion and key advantages of the proposed model

Atherosclerosis is the result of an intricate series of events. The triggering factor of this disease is the penetration of LDL inside the arterial wall, and its subsequent oxidation[101]. The immune system reacts to the presence of oxLDL initiating a chronic inflammatory response[101] that leads to plaque formation. *In vitro* experiments show a strong correlation between local haemodynamics and atherosclerosis formation, identifying arterial geometry as a risk factor[29]. *In silico* experiments have been developed to test the various hypotheses emerging from *in vivo* and *in vitro* studies and to gain a better understanding of the process of plaque formation[22, 58]. Mathematical models have described the process of atherosclerotic plaque formation from different perspectives, concentrating on different aspects of the disease. The interaction between local haemodynamics and arterial wall has been modelled primarily by fluid dynamic models, with shear-dependent endothelium transport properties[83, 84]and heterogenous characterisation of the different arterial wall layers[84]. Biochemical models mainly

address species interactions leading to the plaque formation. Characterisation of the arterial tissue properties is at the centre of continuum mechanical models, attempting to describe the structural changes due to atheroma development[62].

The main objective of this thesis is the development of a multiscale framework for the computational modelling of atherosclerosis at its early stage. This framework could be adapted according to patient-specific data and biomarkers, such as mean blood LDL levels, and the endothelial reaction to the local WSS.The main biochemical aspects of fatty streak formation are considered; from the LDL oxidation cascade[22] to plaque formation due to foam cell accumulation. The authors here developed a model linking the fluid dynamics with the biochemical processes in the atherosclerosis development, as already attempted by Calvez et al.[107]. Coupling a biochemical model with a fluid-wall transport model to describe plaque growth, will allow investigation of the influence of plaque formation on both the local haemodynamics and the progress of the overall disease. Details of this framework and the exemplars used to demonstrate its use will be presented in Chapters 2 – 5.

Chapter 2

Atherosclerosis Model

This chapter presents a detailed explanation of the atherogenesis model used as an example for the multiscale framework that is the focus of this thesis.

As described in the previous chapter, atherosclerosis is a complex disease involving the different strata of the arterial wall as well as the arterial lumen. In this model, the heterogeneous environment of the arterial domain was divided into different sub-domains, with homogeneous properties; the arterial lumen, the arterial endothelium and the arterial wall. Different modelling approaches were used to better describe each one of sub-domains and the dynamics taking place within them.

A chronic systemic disease like atherosclerosis spans from molecules to organs, and involves processes lasting from seconds to years. The use of a multiscale modelling approach with different spatial and temporal scales, allowed for a more targeted and feasible modelling of the atherosclerosis formation.

In the following section the fundamentals of the model are presented, with each sub-domain described separately. The multiscale modelling approach used will be explained in Section 2.2.

2.1 Model description

The governing equations of the atherosclerosis model are the subject of this first section. In order to explain the model, the "path" of a virtual LDL macromolecule

migrating from the blood stream and penetrating the arterial wall will be followed.

The first sub-domain to be described will be the arterial lumen. The arterial endothelium will be described next. Finally, the arterial wall model will be explained.

The disease formation is modelled as a continuum process.

A list of the variables used in this model (alongside a brief description) is presented in Table 2.1. These variables will appear throughout the rest of the chapter.

Figure 2.1 shows a simplified description of the arterial domain including the different sub-domains defined in this model. The different sub-domains presented in Figure 2.1 will be shown separately (Figure 2.3, Figure 2.9, Figure 2.10) within each of the following sections to provide a brief summary of the modelling approach used to model the biochemical and transport phenomena included in the model.

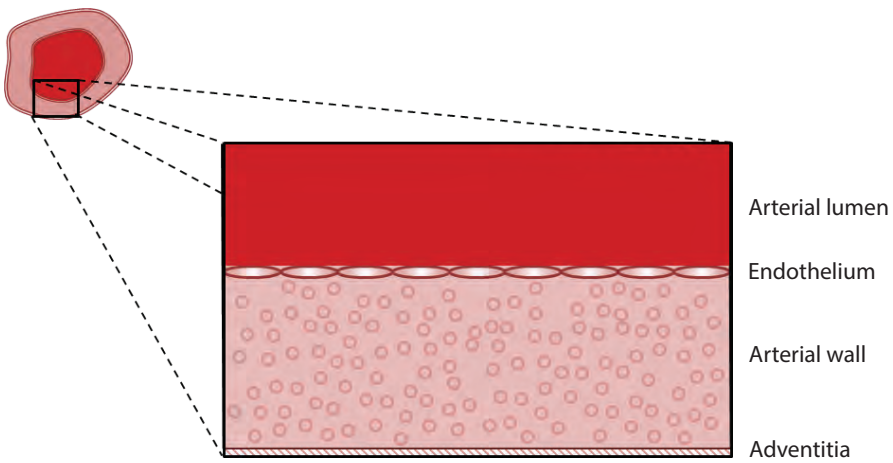

Figure 2.1: Transverse section of the modelled artery showing the different sub-domains considered.

Table 2.1: List of variables used in the governing equations of the atherosclerosis model.

Symbol	Quantity	Value	Ref
α	LDL Radius	11 nm	[83]
A_{tot}	Endothelial surface Area	0.015625 mm^2, mesh dependent	[83]
D_1	LDL diffusion coefficient in blood	5×10^{-12} m^2/s	[83]
D_w	LDL diffusion coefficient in the wall	8×10^{-13} m^2/s	[83]
D_m	Monocytes diffusion coefficient in the wall	1×10^{-3} mm^2/s	[108]
K	Darcys permeability of arterial wall	2.9×10^{-18} m^2	[83]
k_e	LDL oxidation constant	3 μM^{-1} s^{-1}	[22]
k_0	LDL oxidation constant for fully Vitamin E depleted LDL	6×10^{-5} μM^{-1} s^{-1}	[22]
k_m	Foam Cell formation constant	1×10^{-6} s^{-1}	*
K_5	Cytokine action	1×10^{-7} s^{-1}	*
l_{lj}	Length of leaky junction	2 nm	[83]
$L_{p,nj}$	Hydraulic conductivity of normal junctions	1.58×10^{-9} m(s $\cdot$ mmHg)	[123]
P_v	Diffusive permeability of vesicular pathway	1.92×10^{-11} m/s	[83]
R_{cell}	Radius of the endothelial cell	15×10^{-3} mm	[83]
r_w	LDL degradation rate	3×10^{-4} s^{-1}	[83]
σ	Solvent drag coefficient	Leaky cells: 0 Normal cells: 1	[124] [83]
w	Half-width of the leaky junction	20 nm	[83]
s_0	Scaling factor	0.5	*
Δp	Pressure difference across the endothelium	18 mmHg	[123]
μ_p	Plasma viscosity	0.001 Pa s	[83]

2.1.1 Arterial Lumen Model

The arterial lumen is considered as a fluid sub-domain. A description of the analytical tools used to characterise the haemodynamics and the transport of LDL and monocytes inside the arterial lumen is given and explained below.

2.1.1.1 Haemodynamics

Blood was modelled as a steady, homogeneous, incompressible fluid with constant viscosity. In our model, blood rheology was not considered and its properties were kept constant with a viscosity of $\mu = 0.0035$ Pa s and a density of $\rho = 1050$ kg/m^3 throughout the whole domain[83]. Although these assumptions are a simplification of reality, as mentioned in Section 1.2.1.1. of the previous chapter, a simple blood model was deemed enough for the exemplar multiscale application that is the object of this work [80]. The haemodynamics of the problem are calculated using the Navier-Stokes equations. Navier-Stokes equations are partial differential equations that describe mass, momentum and energy conservation in a fluid.

Continuity Equation:

$$\frac{\partial \rho}{\partial t} + \nabla \cdot (\rho \boldsymbol{U}) = 0 \tag{2.1}$$

Momentum Conservation Equation:

$$\frac{\partial (\rho \boldsymbol{U})}{\partial t} + \nabla \cdot (\rho \boldsymbol{U} \times \boldsymbol{U}) = -\nabla p + \nabla \cdot \tau + S_M \tag{2.2}$$

where p and τ are the pressure and stress tensor respectively, $\boldsymbol{U}$ is the flow velocity. The term S_M accounts for the momentum of forces external to the system.

The computational solution of this problem was performed in the Computational Fluid Dynamics Solver Ansys CfX v.14* (Ansys, Inc., Canonsburg, PA) (Figure 2.3).

Computational Fluid Dynamics is the computational implementation of nu-

*http://www.ansys.com/Products/Simulation+Technology/Fluid+Dynamics/Fluid+Dynamics+Products/ANSYS+CFX

merical methods and algorithms aimed at the characterisation and solution of fluid based problems. It allows for a fluid physical domain to be solved given its defining equations of state, boundary conditions and geometry. By dividing the domain of interest into primitive elements, a discrete solution of the problem can be found. The discretised form of the domain is called the computational mesh (or grid).

Ansys CfX v.14 uses a Finite Volume approach. In this technique the primitive elements consists of a discrete control volume (Figure 2.2). The equations of state are discretized over each control volume of the domain, leading to a system of linear conservative equations:

$$\sum_{nb_i} a_i^{nb} \varphi_i^{nb} = b_i \tag{2.3}$$

where for each control volume i, φ is the solution, a is the equation coefficient, b is the right hand side term, and nb is the neighbour of the control volume considered. This system of equations is solved all together, using a coupled solver approach.

Ansys CfX v.14 offers different numerical methods to solve the advection term, in this analysis the high resolution scheme was used. Shape functions are used to calculate the spatial derivative and the pressure gradient with second-order accuracy. To prevent pressure-velocity decoupling, the Rhie Chow correction term is applied to calculate pressure [125, 126]. The equations are solved in time with a fully implicit scheme. In steady state environment, the time-step of the time discretization acts as an "acceleration parameter", allowing for a quicker converging of the system to its steady state solution.

To solve the discrete system of linearized equations Ansys CfX v.14 uses an Algebraic Multigrid approach [127]. The solver virtually coarsen the grid during the solving iterations. This coarsen mesh imposes equations conservation over larger control volumes, improving the convergence rate. When approaching the end of the solving process the grid is re-refined to obtain the accurate solution.

For further information on Ansys CfX v.14, please see the user manual[128].

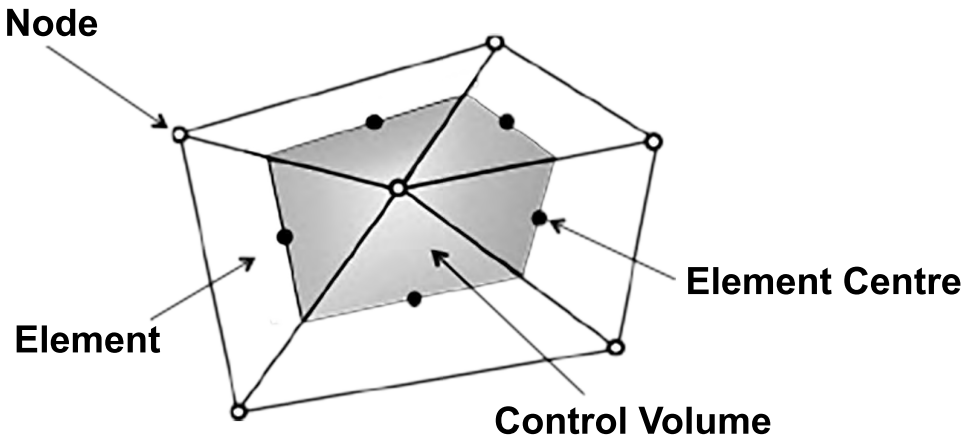

Figure 2.2: Control volume definition. The different elements forming the control volume, together with the mesh nodes and the elements centres are shown.

2.1.1.2 Description of the Lumen-Free Approach

Concentration inside the arterial blood was considered constant for both LDL and monocytes, following a lumen-free approach (Figure 2.3)[69].

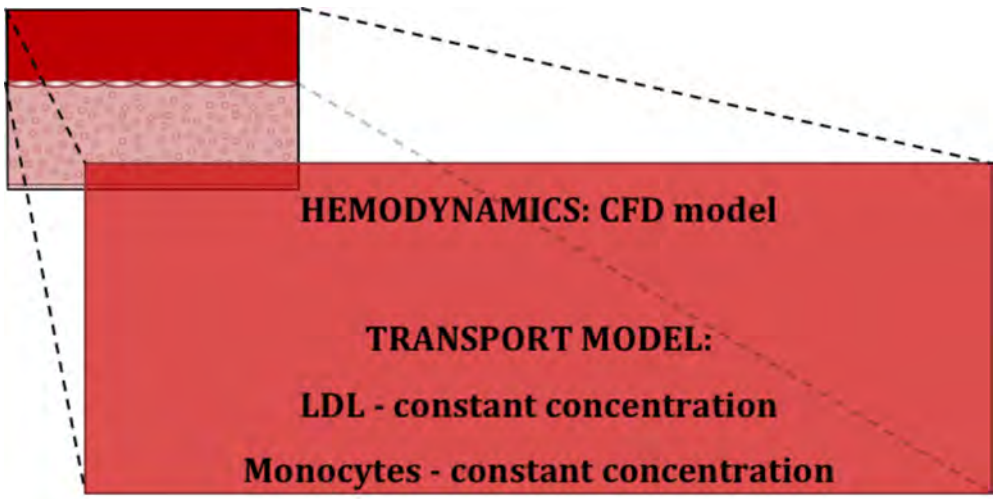

Figure 2.3: Detail of Figure 2.1 showing the model specifications for the arterial lumen.

The LDL concentrations (c_{lum}) implemented in the lumen correspond to the

mean LDL particle concentration (LDLp)[129].

Monocytes in the blood stream (M_{lum}) are considered to be in excess, following the assumption of an immune system that would provide constantly available monocytes, when required. As they are recruited by cytokine action, the controlling factor on the quantity of monocytes entering the arterial wall is represented by the severity of the cytokine stimuli.

The cytokines action will be further discussed in the section relative to the arterial wall (Section 2.1.3).

2.1.2 Endothelium Model

The model described in this section correlates the transport of macromolecules such as LDL *through the endothelium* as a result of the haemodynamic stimuli exerted *on the endothelium*.

Monocyte transport through the endothelium was not modelled. As a consequence to the activation of the immune system, it is assumed that monocytes can travel freely through the endothelium to reach the targeted macromolecules (oxLDL).

2.1.2.1 Correlation between Endothelial Shape Index and Wall shear stress (WSS)

As explained in the previous chapter, endothelial behaviour is heavily influenced by local haemodynamics (Section 1.1.4). The findings of *in vivo* experiment show that in presence of laminar flow, the endothelial cells appear as spindle-shaped and aligned in the direction of the flow [32, 130] (Figure 2.4a). In areas of altered haemodynamics they present differently [32]. When exposed to high WSS, endothelial cells tend to be very elongated and have a smaller surface area (Figure 2.4b), whilst in areas of low WSS they show a more circular shape [32] (Figure 2.4c). These more rounded shape endothelial cells (leaky cells) show an increased permeability, creating areas of higher macromolecular migration inside the arterial wall (Figure 2.5).

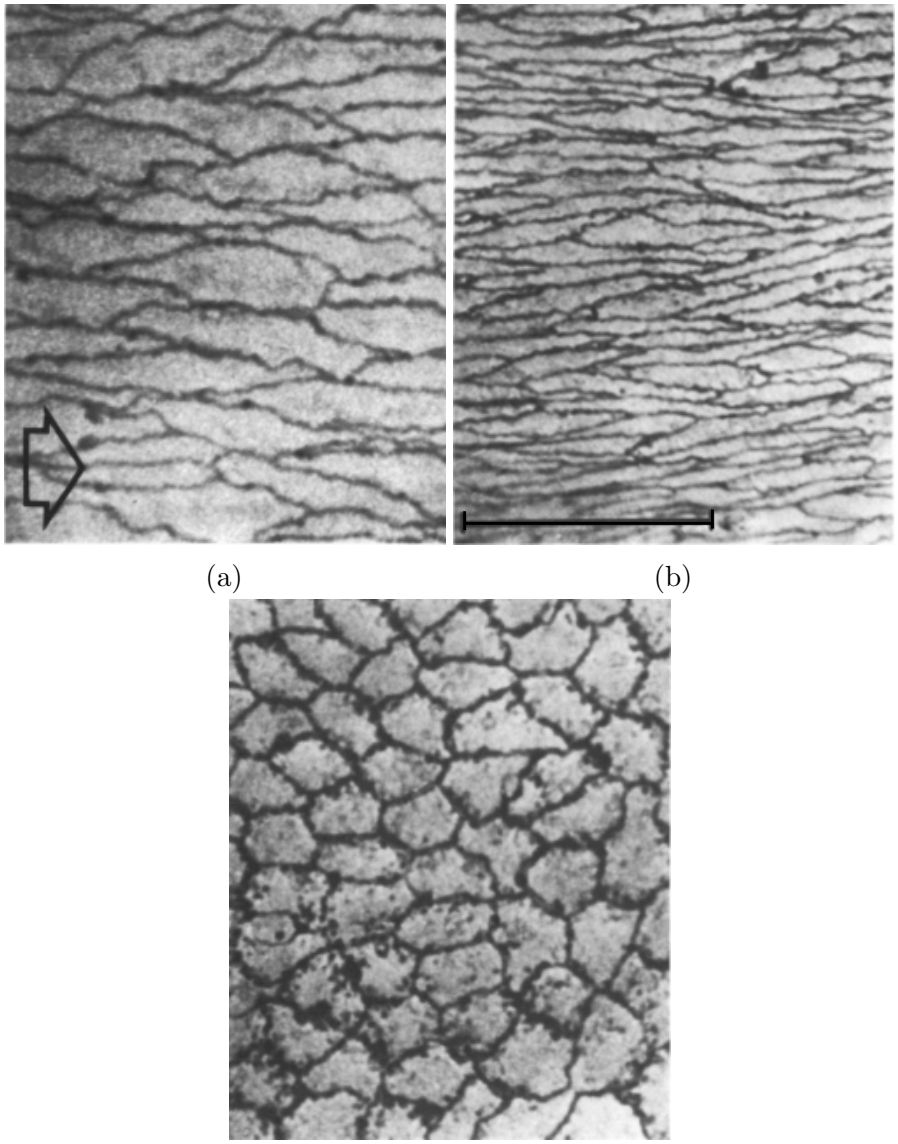

Figure 2.4: Light micrographs of endothelial cells. (a) Endothelial cells under laminar flow conditions, the cells are aligned in the flow direction (idicated with an arrow). (b) In areas of high shear the cells present as very elongated. (c) More circular cells with less evident alignment are observed in areas of low shear and high recirculation. Image bar = 100 μm(Images after [32]).

To relate endothelial permeability to local WSS, a relationship between WSS and endothelial cells Shape Index (SI) was taken from the experimental findings

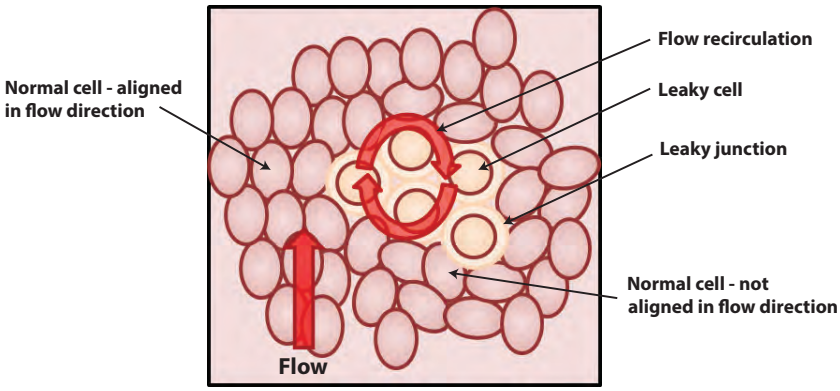

Figure 2.5: Pavement arrangement of the endothelial cells, showing cells alignment with flow direction. Leaky junctions surrounding the more circular cells (leaky cells), lead to an increased permeability to macromolecules.

of Levesque et al.[32] The Shape Index (SI) is a definition of the cellular shape, with a number going from one to zero; where a circle has a SI of one whilst a line has a SI of zero.

In their experiment, Levesque et al.[32] created an artificial stenosis in the aortas of ten mongrel dogs. Endothelial cell reaction to the modified haemodynamics caused by the stenotic neck can be seen in Figure 2.6, where the endothelial SI recordings together with the WSS values along the artery are plotted[32]. It can be observed that the maximum SI is located in the area immediately after the stenosis, highlighting an area of high haemodynamic disturbance[32]. From these data a direct relationship between endothelial SI and local WSS in the aorta emerges (Figure 2.7); where an increase in the SI is shown to be linked to a decrease in the local WSS.

To use this relationship in arteries other than the aorta, and considering the heterogeneity in the arterial haemodynamics, a generalised form of the SI function was developed.

It was assumed that a reasonable value of normal WSS for the aorta could be calculated using the Poiseuille law for laminar flow in a straight pipe[131]:

$$\tau = \frac{4 \cdot \mu \cdot Q}{\pi \cdot r^3} \tag{2.4}$$

where μ is the viscosity and was taken as the one of dog blood, 8.5 cen-

tipoise[32]. The radius r considered was the one of the cast model (5 mm) and the volumetric flow rate, Q, was fixed as to have a Reynolds Number of 450[32].

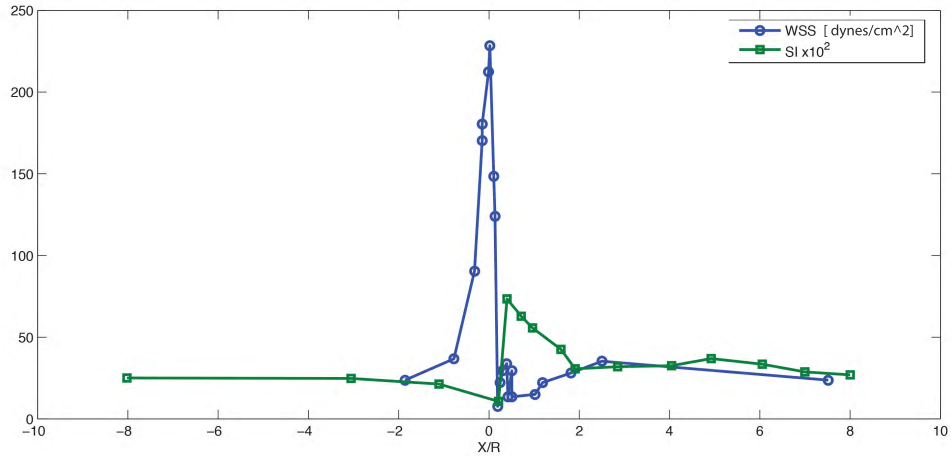

Figure 2.6: Variation of wall shear stress plot together with shape index function with position through the model. Experimental data from Levesque et al.[32]

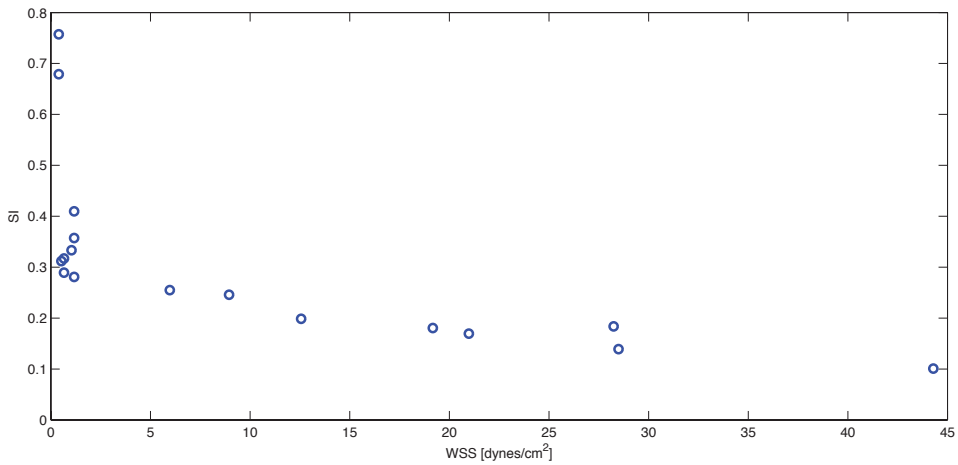

Figure 2.7: Shape Index as function of wall shear stress values. Experimental data from Levesque et al.[32]

From Equation (2.4) the normal value of WSS for the fluid domain in Levesque et al.[32] was $\tau_0 = 26$ dynes/cm^2. Linking SI to the ratio of local WSS to Poiseuille WSS (τ_0), rather than to the absolute value of local WSS recorded in Levesque et al.[32], allowed to generalise the relationship between SI and local WSS. The

data coming from Levesque et al.[32] normalised by τ_0 were represented by a continuous function, following the Olgac et al.[83] approach:

$$SI_2 = -0.2435 \cdot \frac{\tau}{\tau_0}^{0.3537} + 0.4025 \tag{2.5}$$

Where τ is the local WSS value, τ_0 is the Poiseuille WSS and 0.4025 is the maximum SI that an endothelial cell can assume. As it can be seen from Figure 2.8, experimental data show a linear relationship between the endothelial SI and WSS until the WSS has decreased by more than 95% of its normal value. This area, approaching the zero value for WSS is highly non-linear, with scattered values. The mean value among the scattered results for the SI function, calculated as 0.4025 was set as the maximum value.

The developed SI function, linking the local WSS normalised by the theoretical normal value of WSS (τ_0) for the artery in question, helped to obtain a more artery-specific model.

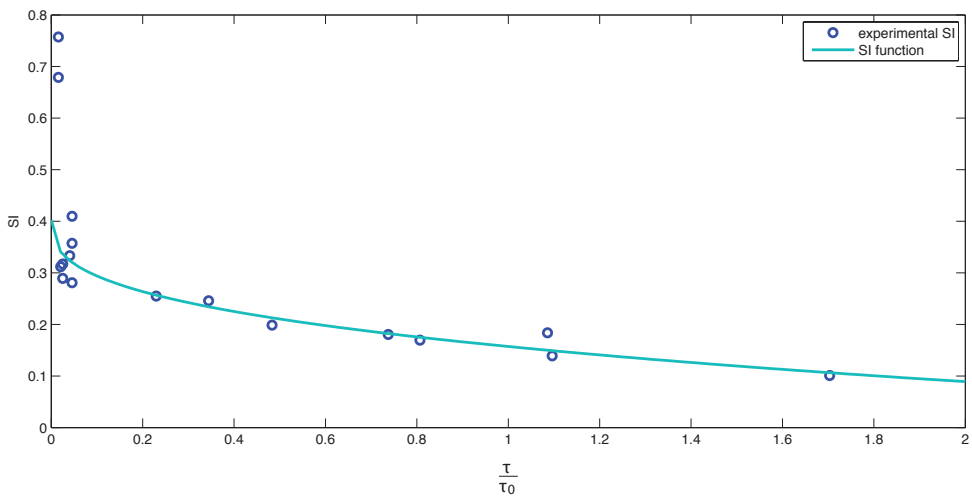

Figure 2.8: Shape Index as function of wall shear stress values normalised by $\tau_0 = 26$ dynes/cm^2. Experimental data from Levesque et al.[32]

2.1.2.2 Membrane Transport Model

To model the LDL passage through the endothelium, a modified version of the Kedem Ketchalsky's equations for membrane transport[83] was used (Figure 2.9):

$$J_v = L_p(\Delta p - \sigma_d \Delta\Pi) \tag{2.6}$$

$$J_s = P_i(c_{lum} - c_{w,end})\frac{Pe}{e^{Pe} - 1} + J_v(1 - \sigma)c_{lum} \tag{2.7}$$

where J_v is the volumetric flux through the endothelium, L_p is the hydraulic conductivity, Δp is the pressure difference through the endothelium, σ_d is the osmotic reflection coefficient and $\Delta\Pi$ is the osmotic pressure (negligible, when compared with the hydraulic pressure through the endothelium)[83]. The osmotic pressure is the pressure applied to the fluid that would offset migration through the membrane, and the osmotic reflection coefficient represents the ability of the membrane to discriminate between the solute and the solvent. J_s is the solute flux through the endothelium. The solute flux can be divided into a convective component entering the membrane $J_v(1 - \sigma)c_{lum}$ and a diffusive component represented by the first term of Equation (2.7), with P_i being its diffusive permeability, P_e the modified Peclet number[83], $c_{w,end}$ the LDL concentration in the arterial wall at the sub-endothelial layer and σ the solvent drag coefficient.

$$Pe = \frac{J_v(1 - \sigma)}{P_i} \tag{2.8}$$

The Peclet number* indicates the relative importance of convective and diffusive transport over the pore entrance.

As explained in the endothelium model section (Section 1.2.1) in Chapter 1, following the three pores approach[99], there are three main pathways through which macromolecule penetration can occur: leaky endothelial cell junctions, normal endothelial cell junctions and vesicular pathways. The vesicular pathway is not eligible for the case of volume flux transport, as vesicular exchange cannot produce a net volume flux[83], therefore the bulk of volume flux through the

*The standard Peclet number formula $Pe = \frac{Lv}{D}$, where L is the characteristic length, v is the velocity and D is the diffusion coefficient in the media.

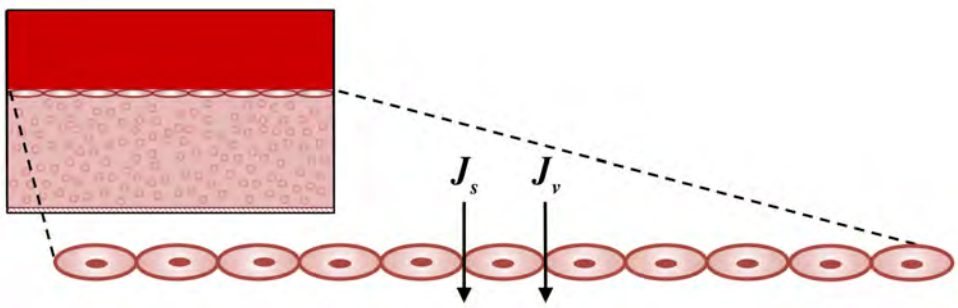

Figure 2.9: Details of Figure 2.1 showing the model specifications for the arterial endothelium.

endothelial membrane is given by:

$$J_v = J_{v,lj} + J_{v,nj} \tag{2.9}$$

where $J_{v,lj}$ is the flux through leaky junctions and $J_{v,nj}$ is the flux through normal junctions. Following the same approach of Olgac et al.[83], the arterial wall was modelled with the help of an electrical analogy, where the flow is driven by a pressure difference, analogous to the current driven by a difference in voltage, and the resistance to the flow entering the arterial wall is given by the endothelial layer.

$$J_v = \frac{\Delta p_{end}}{R_{end}} \tag{2.10}$$

where Δp_{end} is the pressure difference through the endothelium, taken from experimental values[123]. R_{end} is the resistance of the endothelium and it was calculated as the parallel sum of the resistance of leaky junctions and normal junctions[83].

$$\frac{1}{R_{end}} = \frac{1}{R_{lj}} + \frac{1}{R_{nj}} \tag{2.11}$$

where R_{lj} is the resistance through the leaky junction, and is calculated as:

$$R_{lj} = \frac{1}{L_{p,lj}} \tag{2.12}$$

and R_{nj} is the resistance through the normal junction pathway, calculated as:

$$R_{nj} = \frac{1}{L_{p,nj}} \tag{2.13}$$

To describe the LDL transport through normal junctions the hydraulic conductivity ($L_{p,nj}$) was taken from experimental results (Table 2.1). In the three pores theory[99], solute flux does not occur through normal endothelial cell junctions, but it only occurs through endothelial leaky cell junctions and vesicles:

$$J_s = J_{s,lj} + J_{s,v} \tag{2.14}$$

where the solute flux through the vesicular pathway ($J_{s,v}$) is calculated as 10% of the solute flux through the leaky junction pathway ($J_{s,lj}$)[18, 83]. Having defined the transport properties through both the vesicular pathway and the normal junction pathway (Table 2.1), the remaining transport properties to be defined are the ones describing the leaky junction pathway.

Leaky cells have an abnormally high permeability to macromolecules such as LDL, a factor which can be linked to magnitude of WSS acting on the endothelium. As shown in the previous chapter, experimental findings show that in areas of low WSS and high endothelial SI, the number of mitotic cells is increased[98], leading to the following relationship between endothelial SI and number of mitotic cells (MC)[83]:

$$MC = 0.003739e^{14.75} \cdot SI \tag{2.15}$$

For a given portion of endothelium, it has been shown that the quantity of mitotic cells that are leaky is approximately 80.5% and since these represent approximately 45.3% of the total number of leaky cells in that area[98], the number of leaky cells(LCs) can be calculated as:

$$LC = \frac{MC \cdot 0.805}{0.453} \tag{2.16}$$

The leaky junction is assumed to be twice the width of the normal cleft (i.e. 40 nm)[132], seeing it as a ring surrounding the endothelial cell (Figure 2.5), and treating the endothelial cell as spherical, the area of the leaky cell is calculated

as:

$$A_{lc} = (R_{cell} + 2w)^2\pi \tag{2.17}$$

Where R_{cell} is the radius of the endothelial cell (Table 2.1) and w is the half-width of the leaky cleft. The ratio of endothelium (ϕ) covered by leaky cells is then calculated:

$$\phi = \frac{MC \cdot A_{lc}}{A_{tot}} \tag{2.18}$$

Having defined the proportion of leaky cells over normal cells, and therefore the proportion of leaky junctions over normal junctions, the transport properties of the endothelium can be determined. The total hydraulic conductivity of the endothelial leaky junctions is defined as:

$$L_{p,lj} = \phi \cdot L_{p,slj} \tag{2.19}$$

where $L_{p,slj}$ is the hydraulic conductivity of a single leaky junction and is calculated as in Olgac et al.[83]

$$L_{p,sj} = \frac{w^2}{3\mu_p l_{lj}} \tag{2.20}$$

where w is the half-width of the leaky junction and l_{lj} is the length of the leaky junction (Table 2.1).

The diffusive permeability of a single leaky junction is:

$$P_{s,lj} = \frac{D_1}{l_{lj}} \tag{2.21}$$

with the total leaky junction diffusive permeability calculated as:

$$P_{t,lj} = P_{s,lj} \cdot \phi \cdot k_1 \tag{2.22}$$

where D_1 is the diffusion coefficient of LDL in blood and l_{lj} is the length of the leaky junction; k_1 represents the limited diffusivity of LDL through a pore

given its molecular radius[83] and is calculated as:

$$k_1 = 1 - \frac{\alpha}{l_{lj}} \tag{2.23}$$

with α being the radius of an average LDL particle (Table 2.1).

2.1.3 Arterial Wall Model

Once inside the arterial wall, the LDL and monocytes were characterised by means of their transport and chemical interactions (Figure 2.10). A monolayer approach was used, considering the arterial intima and media with IEL and EEL as forming one single layer. The adventitial layer was considered as the limiting boundary of the monolayer and neglected from the model, as it does not play an active role in the initial stage of atherosclerosis formation.

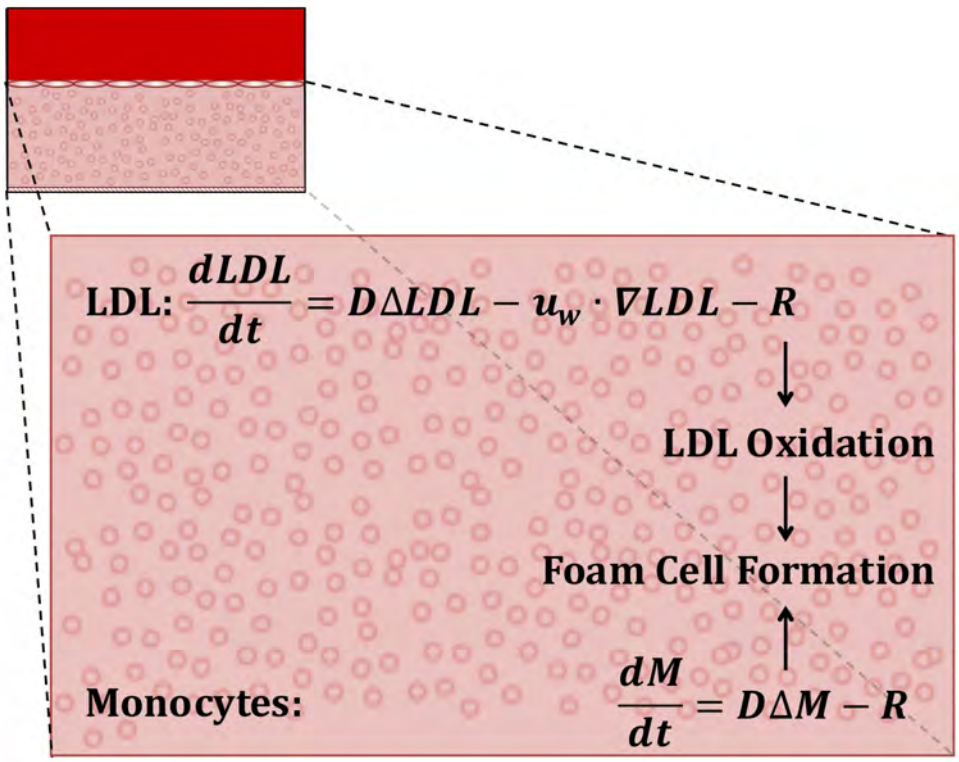

Figure 2.10: Details of Figure 2.1 showing the model specifications for the arterial wall.

2.1.3.1 LDL Transport

The transport of LDL inside the arterial intima-media layer has been modelled in the direction normal to the arterial lumen via a convection-diffusion-reaction equation[83]:

$$\frac{dc_w}{dt} = -\boldsymbol{u_w} \cdot \nabla c_w + D_w \Delta c_w - r_w c_w \tag{2.24}$$

The transmural velocity $\boldsymbol{u_w}$ is calculated using Darcys law:

$$\boldsymbol{u_w} = \frac{k}{\mu_p} \nabla p \tag{2.25}$$

where μ_p is the viscosity of plasma. The transport properties of the arterial wall with respect to LDL are described by the arterial wall Darcys permeability k and the diffusion coefficient D_w. The last term of Equation (2.24) is the degradation of the LDL particles, with r_w as the reaction coefficient.

The LDL fluxes (Equation (2.6) and Equation (2.7)) were imposed normal to the endothelium and they provided the sub-endothelial layer boundary value for $c_{w,end}$ (Equation (2.24)); a LDL value of $\frac{c_{w,adv}}{c_{w,end}} = 0.005$ as from experimental findings from Meyer et al.[90] was used at the boundary corresponding to the adventitia ($c_{w,adv}$) (Figure 2.11). The portion of reacting LDL ($r_w c_w$) is the quantity prone to degradation and it represents the source term for the LDL oxidation model which will be described in the next section.

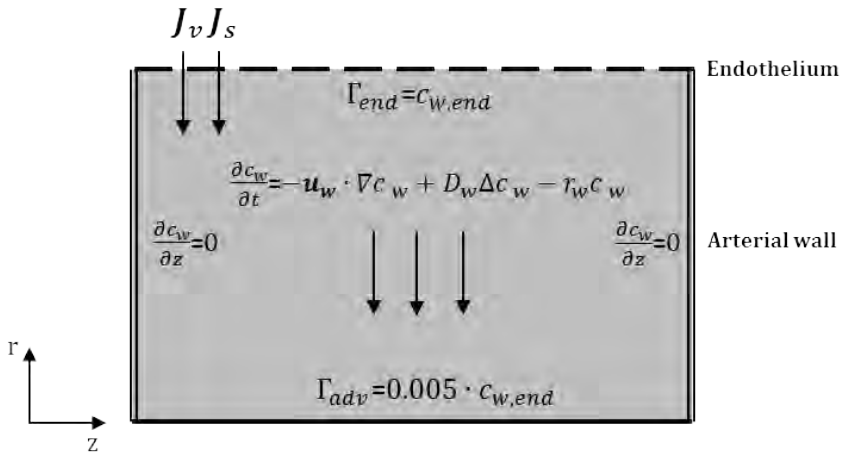

Figure 2.11: Macromolecule transport through the artery wall and endothelium; where c is the macromolecule concentration, Γ_{end} and Γ_{adv} are the boundary conditions at the endothelium and adventitia layer respectively.

2.1.3.2 LDL Oxidation

LDL oxidation is believed to be one of the triggering factors of atherosclerosis formation. As described in section 1.1.2.1 (LDL and its role in atherosclerosis), once inside the arterial wall the LDL will be exposed to oxidation by free radicals[22]. Its antioxidant defence, represented by the vitamin E contained in its outermost layer, will be depleted during the interaction between LDL and free radicals, leaving the LDL lipid core prone to oxidation.

On average six molecules of vitamin E are associated with an LDL molecule[11]; following the model developed by Cobbold et al.[22] each interaction with a free radical would deplete one of these vitamin E (Figure 1.5).

$$LDL_n + R \xrightarrow{k} LDL_{n-1} \tag{2.26}$$

where L_n represents the LDL particle with n vitamin E, R is the free radical and k_e is the kinetic constant for vitamin E oxidation. When the vitamin E is totally depleted, LDL will become prone to oxidation.

$$LDL_0 + R \xrightarrow{k_0} LDL_{ox} \tag{2.27}$$

L_0 is the vitamin E depleted LDL, L_{ox} is the oxidised LDL and k_0 is the LDL oxidation kinetic constant. The kinetic constant for oxidation of LDL k_0 is of a much lower rate than k_e, as the cholesterol core of LDL has a lower reactivity respect to the vitamin E[21].

As free radicals were assumed to be always available, their concentration variation in time was neglected and a fixed value was adopted. The chemical reactions of the oxidation cascade are considered to follow a first order reaction kinetics, the concentration of the reaction product depends solely on the concentration of the reactant.

Following the law of mass action, the concentration in time of the different LDL species in the oxidation cascade was:

$$\frac{dL_5}{dt} = r_w c_w - k_e R L_5 \tag{2.28}$$

$$\frac{dL_4}{dt} = k_e R L_5 - k_e R L_4 \tag{2.29}$$

$$\frac{dL_3}{dt} = k_e R L_4 - k_e R L_3 \tag{2.30}$$

$$\frac{dL_2}{dt} = k_e R L_3 - k_e R L_2 \tag{2.31}$$

$$\frac{dL_1}{dt} = k_e R L_2 - k_e R L_1 \tag{2.32}$$

$$\frac{dL_0}{dt} = k_e R L_1 - k_0 R L_0 \tag{2.33}$$

$$\frac{dL_{ox}}{dt} = k_0 R L_0 - k_m L_{ox} M_w \tag{2.34}$$

The native LDL particle with 6 Vitamin E (L_6) is represented here by the quantity of LDL prone to degradation ($r_w c_w$) coming from Equation (2.24).R represents the free radicals, modelled here as a fixed quantity of 1 μM. The last equation of the chemical cascade (Equation (2.34)) models the concentration of oxidised LDL. The second part of Equation (2.34) accounts for the degradation

of oxidised LDL by interaction with plasma macrophages (M_w).

Oxidised LDL is noxious to the body and its presence triggers an immune response[12]. Cytokines are secreted by the endothelial cells, leading to recruitment and migration of plasma monocytes into the arterial wall.

2.1.3.3 Monocytes Transport

Monocyte migration into the arterial wall is the body's immune response to oxidised LDL (Section 1.1.2.1 – From Monocytes to Foam Cells – The immune response to oxidised LDL). Once inside the arterial wall the assumption is made that all monocytes will differentiate into macrophages, neglecting the time needed for their differentiation. Their transport has been imposed in the normal direction to the arterial lumen and modelled with the following diffusion-reaction equation (Figure 2.10):

$$\frac{dM_w}{dt} = D_m \Delta M_w - k_m L_{ox} M_w \tag{2.35}$$

As a consequence of the activation of the immune system, monocytes were free to travel through the endothelial layer. Following the same principle, macrophages are also relatively free to travel inside the arterial wall, and show a high diffusion coefficient (D_m) (Table 2.1). The reaction term represents macrophages becoming foam cells after taking up oxLDL, with the kinetic constant k_m (Table 2.1) showing the rate of this reaction. The transport of monocytes-macrophages does not present an advection term. This term should represent the chemical force given by chemotaxis[102], and is in this case ignored; with the chemotaxis action represented merely by the activation of cytokines regulating the influx of monocytes in the arterial wall. The sub-endothelial interface boundary condition:

$$M_{w,end} = K_5 L_{ox} \tag{2.36}$$

shows a monocytes source proportional to the quantity of oxLDL (L_{ox}) by a factor K_5 (Table 2.1), representing the cytokines secreted by the endothelial cells in response to the oxLDL produced by the chemical cascade (Equations (2.28) to (2.34)). At the media-adventitia interface a constant concentration value as for the LDL model was used, $\frac{M_{w,adv}}{M_{w,end}} = 0.005$ (Figure 2.11).

The product of the interaction between oxLDL and macrophages is the formation of foam cells.

2.1.3.4 Foam cell formation and accumulations

Once a macrophage is filled up with oxLDL, it will become a lipid laden macrophage, also known as a foam cell. The interaction between oxLDL and macrophages has been modelled as a first order kinetic reaction:

$$LDL_{ox} + M_w \xrightarrow{k_m} F_w \tag{2.37}$$

giving the following change in foam cells concentration with time:

$$\frac{dF_w}{dt} = k_m L_{ox} M_w \tag{2.38}$$

F_w is the quantity of foam cells in the arterial wall and k_m is the kinetic constant for foam cells formation. Foam cells do not have any transport term in their equation as they are not "supposed" to move inside the arterial wall. Once created, they are unable to migrate out of the arterial wall and constrained in term of space, where they eventually form a stratified aggregation (Figure 2.12). Foam cell stratification is the basis of the fatty streak formation.

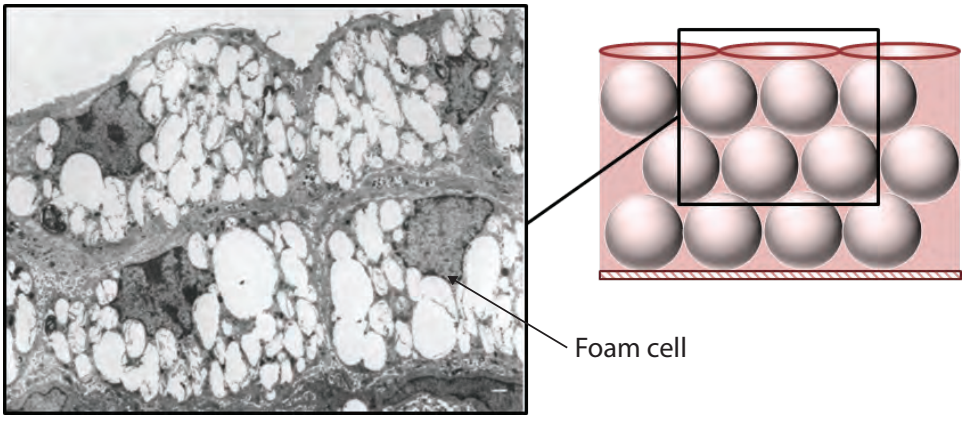

Figure 2.12: Electron micrograph of sub-endothelial fatty streak with two layers of foam cells (image bar = 1 μm). Lipid droplets can be visualised inside the foam cells. The figure on the right shows the close hexagonal packing technique used to approximate the foam cells stratification in the modelled arterial wall. Electron micrograph image from Faggiotto et al.[6].

To resemble the fatty streak structure, shown in Figure 2.12, foam cells were assumed to have a constant volume and spherical shape. Their quite regular pattern of stratification was modelled as following close hexagonal packing (Figure 2.12). The volume occupied by the foam cells would be:

$$V_F = \frac{F_{w,n} \cdot F_{w,V}}{0.7450} \tag{2.39}$$

with $F_{w,n}$ as the number of foam cells given by:

$$F_{w,n} = F_w \cdot N_A \tag{2.40}$$

where F_w is the foam cell concentration, N_A is Avogadro's number, and $F_{w,V}$ is the volume of a spherical foam cell with a radius of 20 µm[6]. V_F is the volume that the foam cells stratification formed in the model would occupy. At the early stage of formation this stratification of foam cells would be easily accommodated in the arterial wall portion considered, which has a volume (V) of:

$$V = A_{tot} \cdot IMT \cdot s_0 \tag{2.41}$$

with IMT being the intima-media thickness and A_{tot} the considered portion

of endothelium. The space available for the accommodation of new material without significant structural modification in the arterial wall is represented by the scaling factor s_0. When the volume represented by the accumulated foam cells is larger than V, the portion of arterial wall considered will start swelling:

$$\Delta h = \frac{V_F - V}{A_{tot}} \tag{2.42}$$

with Δh as the intima-media thickness (IMT) growth in the normal direction, leading to the initial stage of atherosclerotic plaque formation, the fatty streak.

2.2 Multiscale Modelling

Atherosclerosis is a lifelong systemic disease. From a modelling point of view the previous sentence can be loosely translated as, *"atherosclerosis is a biological process taking place over a wide spatial and temporal domain"*. In this chapter, the different processes occurring in the biological domain of the model have been described. This "biological domain" is the nutshell of the model, where all processes taking place are described in both the spatial and the temporal domain (Figure 2.13). The biological domain is very heterogeneous, spanning a range of timescales from quick molecular interactions to slow organ remodelling. These features make the biological domain extremely hard to characterise in terms of time and space, as there is a very large spatial and temporal span to cover. However, each of the biological processes has to be described in the most accurate way, so, difficulties arise in defining a level of characterisation and precision that are needed to satisfy each of them.

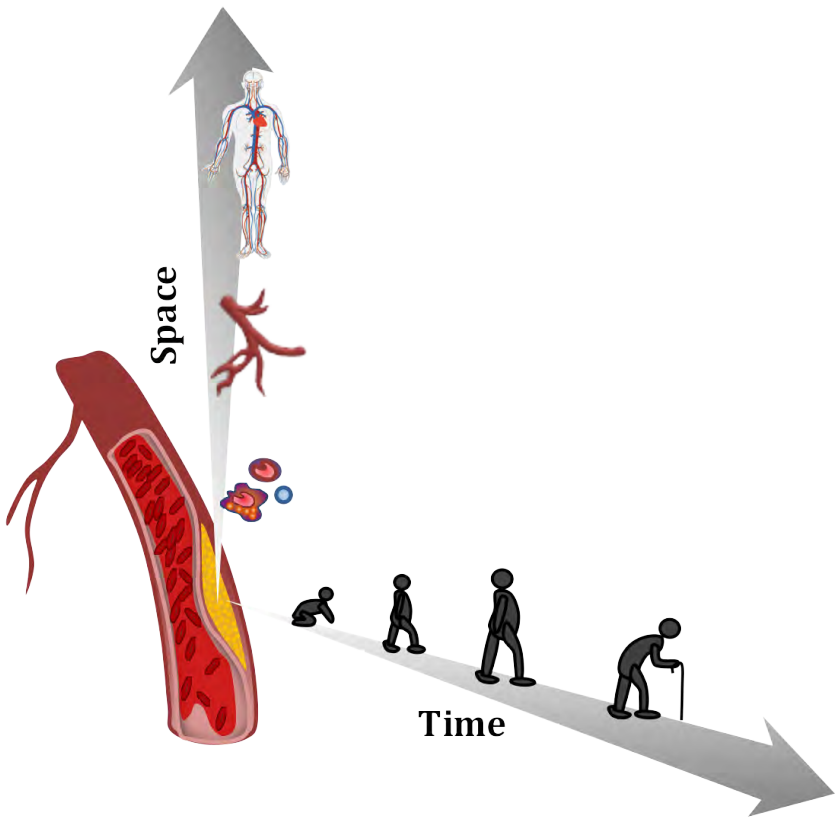

Figure 2.13: The biological domain (atherosclerosis) as a function of the time domain, represented by the life time of a human being, and the spatial domain, spanning from molecules, to tissues, to the whole organism.

One of the complexities of modelling a biological process lies in the choice of the right scale of definition. Choosing only one scale might be too coarse and lack definition in some processes, whilst a too fine scale would lead to over loading the model with data, making it very expensive or impossible to compute. This is the reason why it is important to choose the most appropriate scale for each domain, or sub-domain, using a multiscale modelling approach.

2.2.1 Spatial Scales

The three subdomains of this model have different spatial requirements. The fluid sub-domain, the arterial lumen, models the haemodynamics inside the artery. Its spatial scale needs to capture the fluid behaviour precisely, and it is represented by

the control volume in the computational fluid dynamics (CFD) mesh (Figure 2.14) (the choice of the optimal mesh for the computed domain will be discussed in the section relative to the Fluid Domain Discretisation in Chapter 4 and 5).

The surface area of endothelium and arterial wall considered (A_{tot}) was set accordingly to the CFD mesh element area (Table 2.1, Figure 2.14). Different spatial scales were used to model the endothelium and arterial wall sub-domains in the radial direction, as this is the direction of macromolecular transport. The endothelium was modelled as a membrane, where the transport of LDL was independent of its spatial discretisation. The spatial scale of the endothelium sub-domain in the radial direction was defined by the endothelium thickness[40].

In the arterial wall, a spatial scale of µmm was used. This scale allowed a precise definition of the distribution of macromolecules inside the arterial wall to be obtained that compares well with literature data[90], as will be shown in the following chapters.

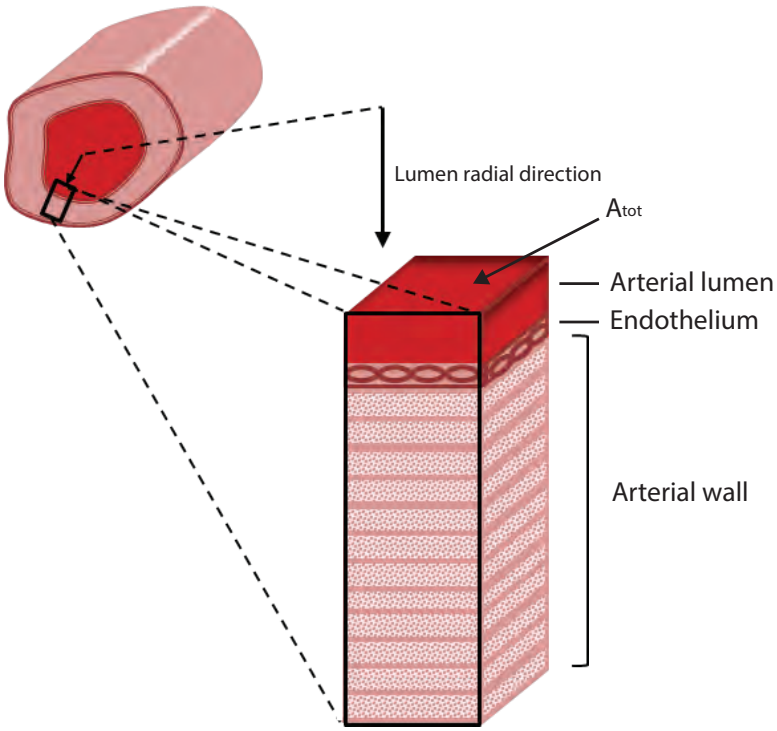

Figure 2.14: Slice of the model artery, showing: arterial lumen, endothelium and arterial wall and the considered endothelium and arterial wall surface area (A_{tot}). In the radial direction, the lumen is represented by a CFD mesh element, the endothelium by an element of its own thickness and the arterial wall discretised by elements on a scale of µm.

2.2.2 Temporal scale

The different processes involved in the modelling of atherosclerosis span from seconds to years. Among these different processes,biochemical interactions in the arterial wall, such as LDL oxidation chemical cascade, are the ones covering the shorter time span of action. Such processes need very short time scales in order to be properly characterised consequently, the time scale for the arterial wall, where these processes take place, was set to seconds.

The endothelium was modelled as a quasi-steady domain. Its transport properties are constant in time as long as the lumen haemodynamics are unchanged. Being the interface between the arterial wall (intima and media) and the blood flow (a domain modelled as steady state), the endothelium links information

coming from both sides, i.e., the arterial wall and the lumen. The change in LDL flux through the endothelium is dependent on its concentration gradient(Equation (2.7)), which is given by a difference in the LDL concentration between the arterial lumen and the arterial wall. The concentration gradient update happens in monthly intervals, as this is the time needed for the arterial wall model to reach a steady solution for the given boundary conditions. After stability in the arterial wall concentration is reached, the change in flux due to the concentration gradient can be calculated and the endothelium LDL solute flux changed accordingly. The update in the solute flux of LDL through the endothelium is entirely dependent on the change in LDL concentration in the wall so long as the haemodynamics are kept constant. A change in the haemodynamics would lead to a change in the whole transport properties of the arterial endothelium, and a change in the whole endothelial-arterial wall model behaviour.

The time definition of the model will be further discussed in Chapter 3.

2.3 Summary of model assumptions and limitations

This model is proposed as an exemplar application and represents an initial approach towards a more "integrated" modelling of atherosclerosis. Different aspects of atheroma formation, involving haemodynamics and the transport and biochemical interaction of species were considered, leading to a multiscale framework of the overall process.

The haemodynamics of the problem was solved with the help of finite volume computational fluid dynamics software, Ansys CfX v.14. In areas where WSS is extremely low (less than 5 dyn/cm^2)[36], the endothelial cells become "leaky" and show higher permeability to macromolecules. The endothelial layer was modelled as a membrane, where the membrane matrix is constituted by the endothelial cells and the pores of the membrane by the intra-cellular junctions, which would allow the passage of LDL through them when "leaky". Transport through this membrane was modelled with a shear-dependent modified version of the Kedem-Katchalskys equations.

Migration of LDL from the blood stream to the arterial wall leads to an accumulation of LDL macromolecules inside the intima-media. A Convection-Diffusion-Reaction equation models the transport of LDL inside the arterial wall. Interaction of LDL with ROS in the arterial wall leads to oxidation of LDL, marking the initial stage of atherosclerosis formation[133]. Once oxidised, LDL triggers the activation of cytokines and signalling proteins, recruiting blood-stream monocytes. These monocytes automatically become macrophages once inside the arterial wall and their distribution follows a Diffusion-Reaction equation. The final stage of this biochemical model is the interaction of macrophages with oxLDL, leading to the formation of foam cells.

Stratifications of foam cells are the core constituents of the initial atheroma. The growing atheroma has an impact on the overall model only when the swelling appears in the arterial wall. This swelling alters the haemodynamic patterns and redefines the behaviour of endothelial cells to LDL transport, initiating a new cycle with different transport boundaries and consequently different atheroma formation.

This integrated model allows description of the major phenomena that form the basis of atherosclerosis both separately, for a more detailed characterisation, and together to understand the dynamics of their interaction. As will be discussed further in the following chapter, great effort was devoted to make this model fast and versatile to implement, allowing for various hypotheses such as different model variables (i.e. different mean blood LDL concentrations) and arterial geometries (from idealised geometries to patient-specific geometries) to be easily tested.

Testing of various hypotheses was fundamental, as the information available in the literature (used to validate and test models of atherosclerosis) is often heterogeneous in terms of methods, quality and outcomes and often corresponds to simplified *in vitro* experiments when presenting only partial aspects of the problem. A valid example to illustrate this argument is the function linking endothelial cell Shape Index to local values of WSS[32, 83]. *In vitro* experiments on human endothelium show that the endothelial cells did not change their morphology for more than a shape index of 0.58 in post-stenotic areas[134]. The majority of experimental data is based on experiments on non-human endothelial

cells including dog endothelial cells[32]. The SI reaction shown by these cells in a similar haemodynamic environment is 18% more severe in comparison to human cells[134]. The difference in these results might arise from different experimental conditions and inter-species differences as, canine endothelial cells and human endothelial cells might react differently to given haemodynamic stimuli[35]. The issue raised by SI data could be applied to many of the values upon which this and the majority of models in the literature are calibrated. It is beyond the purpose of this thesis to discuss the validity of experiments done on non-human specimens in non-physiological environments, but is worth considering them among the limitations of this type of model.

2.4 Conclusion

A mathematical model of atherosclerosis formation was presented in this chapter. The model is based on a continuum, conservative approach. The artery modelled was divided into three sub-domains, arterial lumen, endothelium and arterial wall. Each of these sub-domains had their own spatial and temporal scale of definition. As the finer spatial scale adopted was deemed large enough with respect to the molecular size of the agents considered, the agents were treated macroscophically and described in terms of their concentration. Mass transport across the arterial wall was coupled to the fixed lumen concentration with the help of the semi-empirical relations of Kedem and Kaltchasky, for transport across the endothelium. The change in concentration inside the arterial wall over time was modelled with the help of diffusion-convection-reaction (LDL) and diffusion-reaction equations (monocytes/macrophages). The diffusion driven concentration gradient was modelled with the mathematical and observational Fick's law. When considered, the concentration change due to convection was driven by pressure gradient across the arterial wall following Darcy's law. The chemical reactions leading to LDL oxidation and foam cell formation were modelled using the law of mass action. Agents within the considered sub-domains were modelled with the help of these well understood and widely used formalisms, derived from experimental findings and in-vitro observations. Discretising the very heterogeneous arterial environment in homogeneous sub-domains and the complex phenomenon

of atherosclerosis in its core processes allowed for a more detailed modelling. As atherosclerosis is ultimately the product of these processes and their interactions, a holistic modelling approach was needed to create an integrated atherosclerosis model. The subject of the next chapter is this integrated atherosclerosis model called the *Atherosclerosis Remodelling Cycle*.

Chapter 3

Atherosclerosis Remodelling Cycle

Based on biological principles, key events and processes in the formation of plaque were identified for the development of a mathematical model (Chapter 2). Atherosclerosis is the result of interactions between these core processes, modelled here with the help of a workflow.

This workflow, created to model the development of early stage atherosclerosis formation *in silico* is called the *atherosclerosis remodelling cycle*. It consists of both a theoretical part devoted to the theoretical re-integration of the sub-processes, and a computational part, devoted to the computational implementation of the model, with the aim of creating a unique tool for the model of atherosclerosis. The two parts of the *atherosclerosis remodelling cycle* will be presented separately, as two workflows. As the computational workflow is the computational implementation of the theoretical workflow, it will be presented last.

3.1 Theoretical workflow

The *atherosclerosis remodelling cycle* defines the whole process of plaque formation, from capturing key haemodynamic variables that affect the permeability of the endothelium, to intima-media thickening and lumen remodelling as a conse-

quence of atherosclerosis formation. Figure 3.1 illustrates the theoretical workflow of the *atherosclerosis remodelling cycle*. The three arterial sub-domains defining the arterial lumen, endothelium and arterial wall are represented by the three white boxes. The orange coloured boxes (II, V, VIII, XI, and XIV) describe the LDL-related behaviour/processes within the three subdomains. The green coloured boxes define the monocyte-macrophage behaviour in the artery (III, XVI). The grey boxes are the initial (I) and final (XVIII) elements of this workflow. The arrows between boxes represent an exchange of information from one box (output) to another box (input). The information exchanged is represented in the workflow by the symbol next to the arrow.

The core elements of the model are presented in this workflow. These core elements can be a single or a series of model equations and variables. Table 3.1 lists the workflow entries including equations and variables.

The Navier-Stokes equations (I) are used to model the dynamics of blood flow inside the arterial lumen. The endothelial transport properties are influenced by haemodynamic variables, here characterised by WSS (IV). WSS values are input into the endothelium model and more precisely, to the shear dependent permeability part, represented by the Shape Index (SI) function (V).

Depending on the value of local WSS, the endothelium will have a proportion of cells that will behave as leaky (VII). The quantity of leaky cells (Φ) defines the permeability of the endothelium to the macromolecule of interest (LDL). The portion of leaky cells together with the quantity of LDL available for transport (VI), set as a fixed quantity in the lumen (II), defines the lumenal conditions for the three pores transport model (VIII), describing the different pathways through which LDL travels inside the endothelium.

The LDL solute and volume flux (X), having passed through the endothelium enters the arterial wall, where the LDL transport is characterised by a convection-diffusion-reaction equation (XI). As LDL accumulates inside the arterial wall, its concentration in the arterial wall subendothelial layer changes (XII), altering the transport of LDL through the endothelium (X). The reaction term ($r_w c_w$) in (XI) accounts for the different LDL degradation processes inside the arterial wall; representing the concentration of particles undergoing a chemical variation, this quantity (XIII) was considered as the concentration of native LDL particles

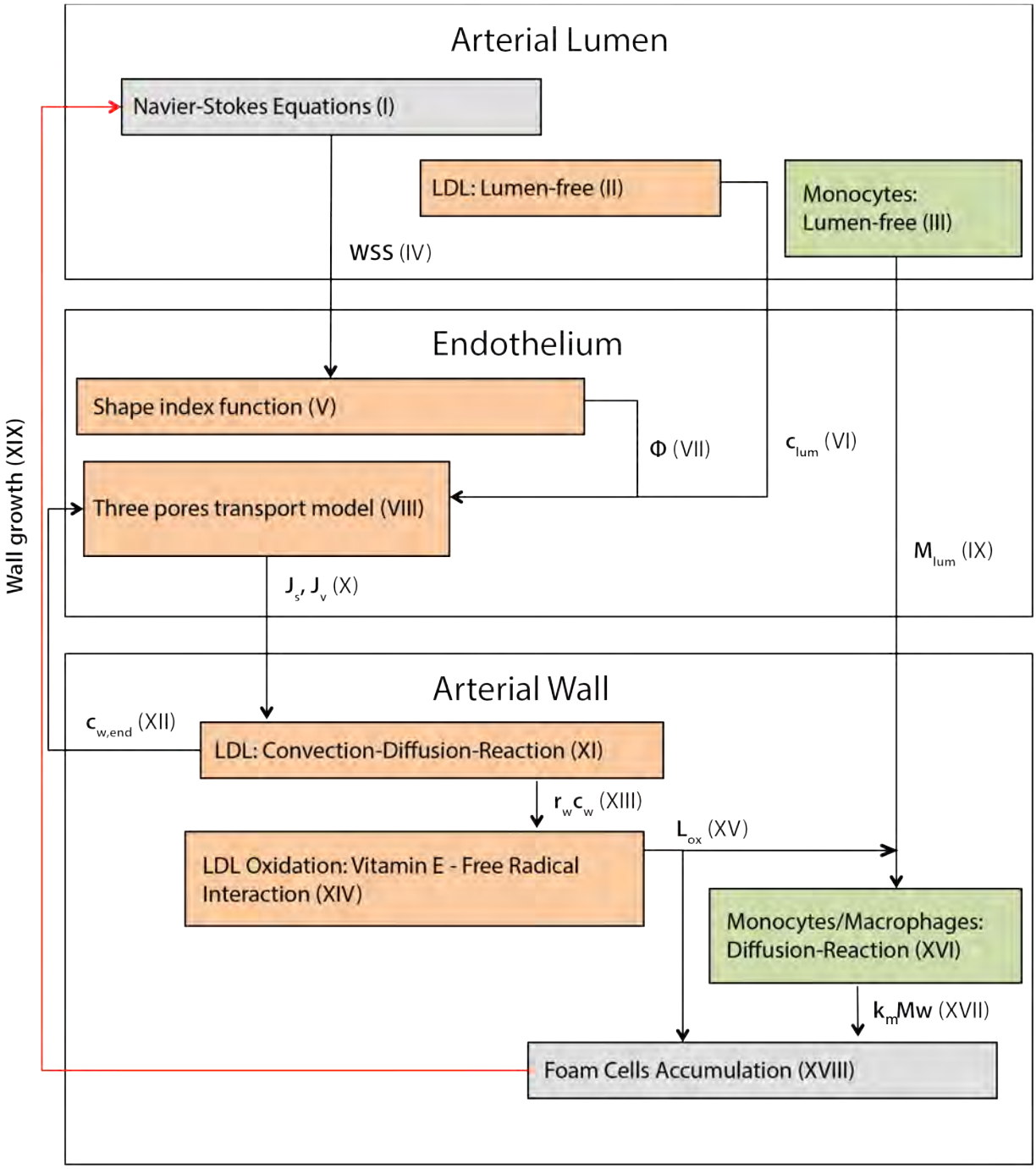

Figure 3.1: Theoretical workflow of the atherosclerosis model.

Table 3.1: Workflow (3.1, 3.2) entries with the corresponding set of equations or quantities that they represent

Flowchart	Equations	Variable	Units	Description
I	2.1, 2.2			Navier-Stokes equations
II, VI		c_{lum}	mol/m^3	Lumen-free approach – Mean blood LDL concentration
III, IX		M_{lum}	mol/m^3	Lumen-free approach – Blood monocytes concentration
IV		WSS	Pa	
V	2.4, 2.5			Shape Index Function
VII	2.15 - 2.18	Φ		Quantity of leaky cells
VIII	2.6 - 2.14, 2.19 - 2.23			Three Pores Transport Model
X		J_s, J_v	mol/m^{2}s, m/s	Solute Flux, Volume Flux
XI	2.24, 2.25			LDL Convection-Diffusion-Reaction equation
XII		$c_{w,end}$	mol/m^3	Sub-endothelial LDL concentration
XIII		$r_w c_w$	mol/m^{3}s	Degrading LDL concentration
XIV	2.28, 2.34			LDL Oxidation
XV		L_{ox}	mol/m^3	Oxidised LDL
XVI	2.35			Monocytes/macrophages Diffusion-Reaction equation
XVII		$k_m M_w$	mol/m^{3}s	Degrading macrophages
XVIII	2.38, 2.39			Foam cells formation and accumulation
XIX	2.41, 2.42		m	Arterial Wall Growth

in the oxidation cascade (XIV). The final product of the oxidation cascade is the arterial wall concentration of oxidised LDL (XV). Oxidised LDL (oxLDL) is one of the most important elements in this model as it is the triggering factor of the atherosclerosis inflammatory process.

OxLDL causes the recruitment of monocytes from the arterial lumen, a fixed and constantly available quantity (III) of immune cells. Monocytes are free to travel inside the arterial wall (IX) and are dependent on the quantity of oxidised LDL(XV). This defines the severity of the inflammation. Inside the arterial wall, monocytes turn into macrophages and their transport follows Diffusion-Reaction behaviour (XVI). The reaction term of (XVI) represents the concentration of macrophages that interacts with the oxLDL. The interaction between macrophages (XVII) and the quantity of oxLDL (XV) leads to the formation of fatty laden macrophages called foam cells (XVIII). Unable to leave the arterial wall, foam cells stratify, eventually leading to wall thickening and remodelling (XIX). Remodelling of the arterial wall is the result of the inflammatory process described herein, and marks the end of the *atherosclerosis remodelling cycle*.

Alteration of lumen geometry has an impact on haemodynamics, which influences the overall cycle, creating a feedback loop. After the lumen geometry has been altered, another *atherosclerosis remodelling cycle* can be initiated to simulate plaque progression further in time.

As explained in the previous chapter (Section 2.2.2), this model is defined by different temporal scales. Figure 3.2 shows a simplified version of the model theoretical workflow (Figure 3.1) where only the information exchanged between the various sub-processes of the model (white boxes) can be visualised together with the temporal setting of the model. The blue, orange and purple boxes show the different time domains used in this model. The two white boxes with the concentration of LDL (VI) and monocytes (IX) used in the lumen-free approach are fixed concentrations in this model, and are therefore not influenced by any time scale.

Starting from the centre, the innermost blue box shows the time domain of the arterial wall model. This is the smallest time domain, and it is set to accurately define the dynamics happening in the biochemical and transport processes happening in the arterial wall. The orange box is the time domain used to update

the endothelial transport model according to the concentration of LDL present in the arterial wall. The outermost time domain, the purple box is the time length of the whole *atherosclerosis remodelling cycle*, set to adjust the arterial lumen geometry according to the developing atherosclerosis plaque. When the calculations in the atheroma model produce a "growth", i.e., the arterial wall reaches a thickness of $\Delta h*$, it is considered that the impact of the change in geometry on the WSS pattern is not negligible, consequently the arterial geometry is updated to account for this change.

This $\Delta h*$ value is fixed as 1% of the radius of the artery in question. This threshold value was assumed as the maximum arterial deformation allowed, before the impact of the changing geometry on the haemodynamics had to be considered and a new *atherosclerosis remodelling cycle* started.

As previously mentioned, when this condition is met, the geometry of the artery is modified according to the arterial growth calculated in Equation (2.42), following a procedure that will be presented in the next section. Changing the arterial geometry will lead to a change in the haemodynamics and consequently a change in the local endothelium transport properties, leading to a whole system update. A second simulation cycle will now start to simulate growth further in time.

So far the theory behind the model and the integration of the various elements from a theoretical point of view have been described. In the following section, the computational implementation of this model will be discussed.

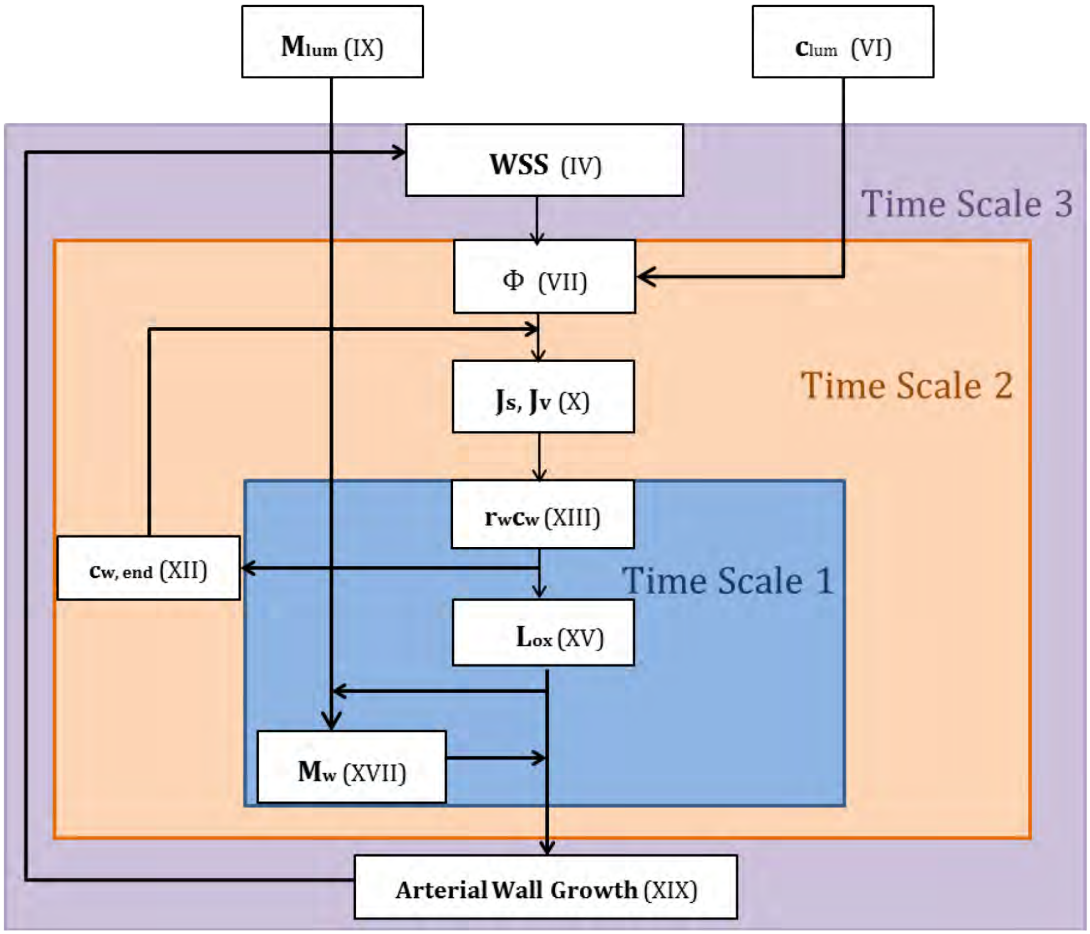

Figure 3.2: Theoretical Workflow of the atherosclerosis model. The inputs/outputs of fig. 3.1 are represented together with the model time scales.

3.2 Computational Workflow

Two different computational tools were used to model the different subdomains. A CFD software, Ansys CfX v.14, was used for the simulation of blood flow inside the lumen. The transport model and biochemical model of arterial endothelium and arterial wall was developed and implemented in Matlab* (The MathWorks, Natick, MA).

The computational workflow is shown in Figure 3.3. This workflow can be divided into two parts. The red borders represent the initialisation cycle, and the green borders characterise each cycle after the initialisation cycle. The black borders show the parts that are common to both.

The boxes filling in the workflow are of three colours. Each of the different colours represents the computational tool used to implement that part of the model: red colour is for Ansys CfX v.14 and blue colour for Matlab. Exchange between Matlab and Ansys CfX v.14 was done with the help of Microsoft Excel† (Microsoft Corporation, Redmond, WA), shown in the green colour boxes.

This workflow will be explained following the order of computational implementation. The initialisation cycle will be explained first, and then the other cycles will follow.

3.2.1 Atherosclerosis remodelling initialisation cycle

As already mentioned in the previous chapter, the Navier-Stokes equations, describing the haemodynamics in the arterial lumen for the given geometry and boundary conditions, are solved in Ansys CfX v.14. Once the solution for a given geometry has been computed, the variables of interest are extracted from the CFD model and saved in an Excel file. For a surface of n nodes, the data would

*`http://www.mathworks.it/products/matlab/`
†`http://office.microsoft.com/en-gb/excel`

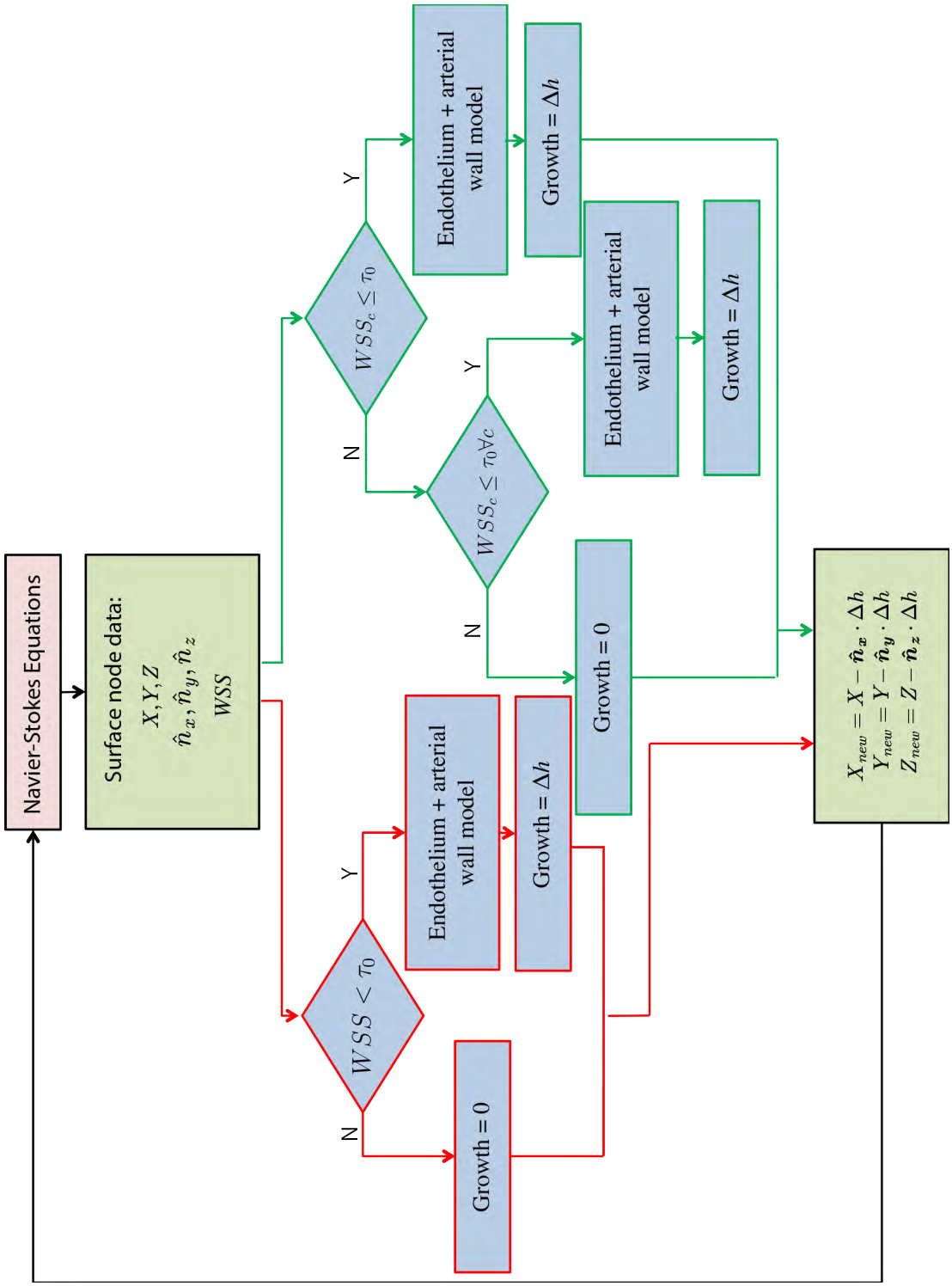

Figure 3.3: Computational workflow of the atherosclerosis model.

be exported in matrix form with each string representing a different variable:

$$\begin{bmatrix} N_1 & x_1 & y_1 & z_1 & \hat{\boldsymbol{n}}_{\boldsymbol{x_1}} & \hat{\boldsymbol{n}}_{\boldsymbol{y_1}} & \hat{\boldsymbol{n}}_{\boldsymbol{z_1}} & WSS_1 \\ N_2 & x_2 & y_2 & z_2 & \hat{\boldsymbol{n}}_{\boldsymbol{x_2}} & \hat{\boldsymbol{n}}_{\boldsymbol{y_2}} & \hat{\boldsymbol{n}}_{\boldsymbol{z_2}} & WSS_2 \\ N_3 & x_3 & y_3 & z_3 & \hat{\boldsymbol{n}}_{\boldsymbol{x_3}} & \hat{\boldsymbol{n}}_{\boldsymbol{y_3}} & \hat{\boldsymbol{n}}_{\boldsymbol{z_3}} & WSS_3 \\ & & & & \vdots & & & \\ N_n & x_n & y_n & z_n & \hat{\boldsymbol{n}}_{\boldsymbol{x_n}} & \hat{\boldsymbol{n}}_{\boldsymbol{y_n}} & \hat{\boldsymbol{n}}_{\boldsymbol{z_n}} & WSS_n \end{bmatrix} \tag{3.1}$$

where the first column is the node number, from second to the fourth column x, y and z coordinates of the node respectively, from the fifth to seventh column the projection of the normal vector in the x, y and z direction and the last column the WSS value at that nodal location.

Each variable stored in Equation (3.1) is individually processed in Matlab. The WSS nodal values are extracted from this matrix and selected following a specified criteria. The nodal number ($N_{1:n}$) is used as an identifying index for each of the extracted WSS values. If the WSS value at the nodal location is greater or equal to the Poiseuille WSS value for the given arterial branch as calculated in Equation (2.4), the node is discarded, and no arterial wall displacement (Δh, Equation (2.42)) is assigned to that node.

If the criterion is satisfied and the extracted WSS value is less than the calculated WSS Poiseuille value (Equation (2.4)), the node having that WSS value will be selected. This WSS value is used as the lumen side condition (IV in Figure 3.1) for the endothelium and the arterial wall model, implemented in Matlab.

Following the WSS selecting criteria, a new matrix of selected surface nodes are formed:

$$\begin{bmatrix} N_1 & 1 & x_1 & y_1 & z_1 & \hat{\boldsymbol{n}}_{\boldsymbol{x_1}} & \hat{\boldsymbol{n}}_{\boldsymbol{y_1}} & \hat{\boldsymbol{n}}_{\boldsymbol{z_1}} & WSS_1 \\ N_2 & 2 & x_2 & y_2 & z_2 & \hat{\boldsymbol{n}}_{\boldsymbol{x_2}} & \hat{\boldsymbol{n}}_{\boldsymbol{y_2}} & \hat{\boldsymbol{n}}_{\boldsymbol{z_2}} & WSS_2 \\ N_3 & 3 & x_3 & y_3 & z_3 & \hat{\boldsymbol{n}}_{\boldsymbol{x_3}} & \hat{\boldsymbol{n}}_{\boldsymbol{y_3}} & \hat{\boldsymbol{n}}_{\boldsymbol{z_3}} & WSS_3 \\ & & & & & \vdots & & & \\ N_n & n & x_n & y_n & z_n & \hat{\boldsymbol{n}}_{\boldsymbol{x_n}} & \hat{\boldsymbol{n}}_{\boldsymbol{y_n}} & \hat{\boldsymbol{n}}_{\boldsymbol{z_n}} & WSS_n \end{bmatrix} \tag{3.2}$$

where the first column is the node number, representing also the node index in the parent matrix (Equation (3.1)). The second column is the node positioning

index in the current matrix, the third to fifth column are the x, y and z coordinates of the node respectively, the sixth to eight column the projection of the normal vector in the x, y and z direction and the last column the WSS value on that surface node. Matrix (3.2) is a sub-matrix of (3.1), as it is the product of the element selection performed on the Matrix (3.1). WSS based node selective criteria, identifies the atherosclerosis-prone areas. Narrowing the area of interest allows for reduced data handling.

Once the lumen side boundary conditions have been set, the endothelium-arterial wall model can be implemented in Matlab. One of the assumptions of the model is that the transport of species occurs in the radial direction (direction normal to the lumen surface) only, hence, there is no exchange of information between neighbouring nodes (longitudinal direction) (Figure 2.11). The Matlab model of the endothelium and the arterial wall can be solved for each node separately. For increased computational efficiency, the selected surface nodes of the CFD model with their section of endothelium and arterial wall model are clustered in packages and solved in parallel. For parallelisation purposes a remote cluster (UCL Computer Science Cluster, total of 2500 cores, typical node with dual socket E5-2620, 48GB of memory and 128GB SSD (solid-state drive)) was used. The Matlab implementation would have to handle a much larger number of nodes at once without parallelisation. It follows that this parallelisation allows for a further decrease in the computational power required for this model.

The result of the endothelium and arterial wall model is an arterial wall growth value for each one of the CFD surface nodes considered. This growth value represents the thickening of the arterial wall and will result in a deformation of the arterial surface to accommodate the growth in IMT (Δh), as calculated from Equation (2.42). The displacement (Δh) value will be imposed on each of the surface nodes of the arterial lumen model. An increase in the arterial wall thickness would result in a displacement of the arterial lumen surface nodes towards the centre, as atherosclerosis formation leads to a decrease in the arterial lumen diameter.

Using the indexing number ($N_{1:n}$) the displacement (Δh) corresponding to each one of the surface nodes for both the pro-atherosclerotic areas and for areas where the displacement was imposed as zero, can be inserted in the original matrix

for the surface nodes. The following matrix will be created:

$$\begin{bmatrix} N_1 & x_1 & y_1 & z_1 & \hat{\boldsymbol{n}}_{\boldsymbol{x_1}} & \hat{\boldsymbol{n}}_{\boldsymbol{y_1}} & \hat{\boldsymbol{n}}_{\boldsymbol{z_1}} & WSS_1 & \Delta h_1 \\ N_2 & x_2 & y_2 & z_2 & \hat{\boldsymbol{n}}_{\boldsymbol{x_2}} & \hat{\boldsymbol{n}}_{\boldsymbol{y_2}} & \hat{\boldsymbol{n}}_{\boldsymbol{z_2}} & WSS_2 & \Delta h_2 \\ N_3 & x_3 & y_3 & z_3 & \hat{\boldsymbol{n}}_{\boldsymbol{x_3}} & \hat{\boldsymbol{n}}_{\boldsymbol{y_3}} & \hat{\boldsymbol{n}}_{\boldsymbol{z_3}} & WSS_3 & \Delta h_3 \\ & & & & \vdots & & & & \\ N_n & x_n & y_n & z_n & \hat{\boldsymbol{n}}_{\boldsymbol{x_n}} & \hat{\boldsymbol{n}}_{\boldsymbol{y_n}} & \hat{\boldsymbol{n}}_{\boldsymbol{z_n}} & WSS_n & \Delta h_n \end{bmatrix} \tag{3.3}$$

Where $N_{1:n}$ is the indexing number, the second to fourth entry are the node coordinates, the fifth to seventh entry are the nodes normal vector projections, and the last entry is the node displacement.

The information stored in Matrix (3.3) is used to calculate the nodal displacement to be imposed on the surface nodes of the CFD lumen geometry, using the point translation technique (Figure 3.4). For a single node, the new position coordinates X_{new}, Y_{new} and Z_{new} are given by:

$$X_{new} = X \pm \hat{n}_x \cdot \Delta h \tag{3.4}$$

$$Y_{new} = Y \pm \hat{n}_y \cdot \Delta h \tag{3.5}$$

$$Z_{new} = Z \pm \hat{n}_z \cdot \Delta h \tag{3.6}$$

Where X, Y, Z are the nodal coordinates of the initial geometry and $\hat{\boldsymbol{n}}_{\boldsymbol{x}} \cdot \Delta h$, $\hat{\boldsymbol{n}}_{\boldsymbol{y}} \cdot \Delta h$, $\hat{\boldsymbol{n}}_{\boldsymbol{z}} \cdot \Delta h$, are the displacement vectors with magnitude Δh and direction $\pm\hat{\boldsymbol{n}}_{\boldsymbol{x}}$, $\pm\hat{\boldsymbol{n}}_{\boldsymbol{y}}$, $\pm\hat{\boldsymbol{n}}_{\boldsymbol{z}}$. Applied to the Ansys CfX v14 model geometry surface, the new coordinates of the nodes are given by:

$$\begin{bmatrix} x_{1_{new}} & y_{1_{new}} & z_{1_{new}} \\ x_{2_{new}} & y_{2_{new}} & z_{2_{new}} \\ x_{3_{new}} & y_{3_{new}} & z_{3_{new}} \\ & \vdots & \\ x_{n_{new}} & y_{n_{new}} & z_{n_{new}} \end{bmatrix} = \begin{bmatrix} x_1 & y_1 & z_1 \\ x_2 & y_2 & z_2 \\ x_3 & y_3 & z_3 \\ & \vdots & \\ x_n & y_n & z_n \end{bmatrix} \pm \begin{bmatrix} \hat{\boldsymbol{n}}_{\boldsymbol{x_1}} & \hat{\boldsymbol{n}}_{\boldsymbol{y_1}} & \hat{\boldsymbol{n}}_{\boldsymbol{z_1}} \\ \hat{\boldsymbol{n}}_{\boldsymbol{x_2}} & \hat{\boldsymbol{n}}_{\boldsymbol{y_2}} & \hat{\boldsymbol{n}}_{\boldsymbol{z_2}} \\ \hat{\boldsymbol{n}}_{\boldsymbol{x_3}} & \hat{\boldsymbol{n}}_{\boldsymbol{y_3}} & \hat{\boldsymbol{n}}_{\boldsymbol{z_3}} \\ & \vdots & \\ \hat{\boldsymbol{n}}_{\boldsymbol{x_n}} & \hat{\boldsymbol{n}}_{\boldsymbol{y_n}} & \hat{\boldsymbol{n}}_{\boldsymbol{z_n}} \end{bmatrix} \cdot \begin{bmatrix} \Delta h_1 \\ \Delta h_2 \\ \Delta h_3 \\ \vdots \\ \Delta h_n \end{bmatrix} \tag{3.7}$$

Figure 3.4 shows the mesh deformation technique used for modelling lumen-imposed deformation caused by the arterial wall growth. A node (Figure 3.4a) is translated to a position at a distance Δh in the direction normal to the node (Figure 3.4b). Considering the node as part of the surface mesh (Figure 3.4c), the mesh deformation coming from the node translation can be visualised in Figure 3.4d.

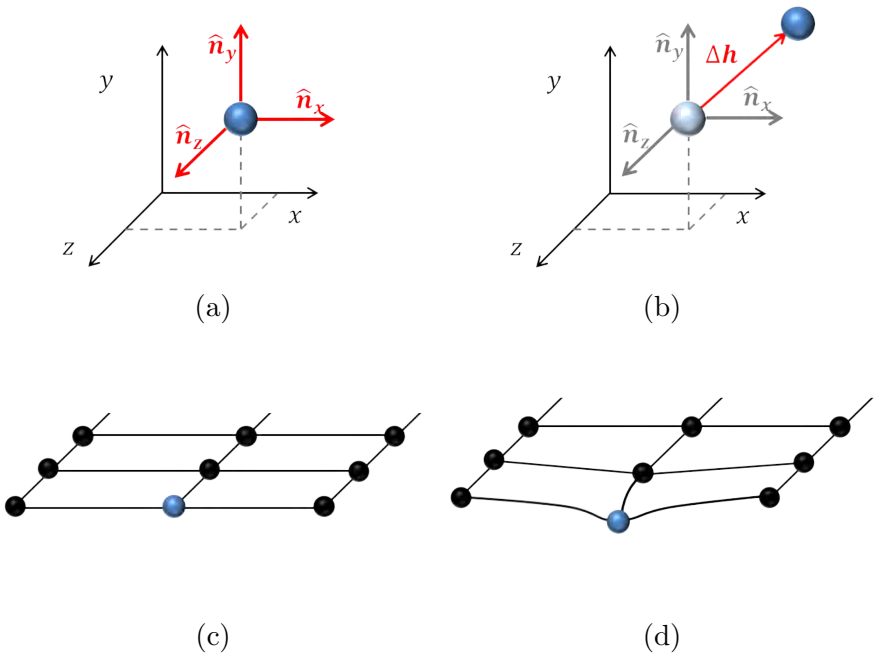

Figure 3.4: a. Node of the surface mesh represented in its x, y, z spacing with the projection of the normal vectors in the x, y and z directions. b. Translation of the node along a vector with magnitude Δh in the direction normal to its surface. c. Node located in a portion of the surface mesh grid. d. Displacement of that node downwards (towards the arterial lumen) and remodelling of the grid around it.

The node translation calculated can be imposed onto the surface nodes of the Ansys CfX v.14 model.

In order to instruct Ansys to perform the correct mesh deformation the fol-

lowing matrix needs to be utilised:

$$\begin{bmatrix} x_1 & y_1 & z_1 & x_{1_{new}} & y_{1_{new}} & z_{1_{new}} \\ x_2 & y_2 & z_2 & x_{2_{new}} & y_{2_{new}} & z_{2_{new}} \\ x_3 & y_3 & z_3 & x_{3_{new}} & y_{3_{new}} & z_{3_{new}} \\ & & & \vdots & & \\ x_n & y_n & z_n & x_{n_{new}} & y_{n_{new}} & z_{n_{new}} \end{bmatrix} \tag{3.8}$$

Where the first three entries are the nodal coordinates and the fifth to seventh column are the new x, y and z coordinates that the nodes will have after the translation has been performed.

As mentioned at the beginning of this section, the end of an *atherosclerosis remodelling cycle* is marked by the arterial wall deformation. In this case, the deformation marks the end of the first cycle, or initialisation cycle. To characterise the plaque development further in time, after the initialisation cycle has finished, another cycle will start. This is represented in Figure 3.3 by the green framed part of the workflow.

Once the *atherosclerosis remodelling cycle* has ended, the endothelium and arterial wall models are temporary interrupted as the wall growth threshold criterion (Δh^*) has been reached (Figure 3.1). Among the surface nodes, if at least one had a wall displacement value that satisfied the criteria:

$$\Delta h \cong \Delta h^* \tag{3.9}$$

where Δh^* is 1% of the artery radius. The developed growth threshold criterion has been satisfied and the CFD geometry is remodelled accordingly.

3.2.2 Atherosclerosis remodelling cycle

In order to continue calculating the arterial wall growth, the endothelium-arterial wall transport model had to be retrieved from the point where the simulation was interrupted. As this cycle is the continuation of the previous cycle, the transport model of the arterial wall is not re-initialised. The concentration value for each point in the discretised arterial wall at the time when the previous cycle was interrupted is utilised as the initialisation value for the current simulation cycle.

Because in certain areas the IMT increased due to plaque formation, the thickness of the arterial wall is not equal to the initially imposed IMT (used in Equation (2.42)) anymore. The new IMT thickness is given by:

$$IMT_c = IMT_{c-1} + \Delta h \tag{3.10}$$

Where IMT_c is the intima-media thickness at the current cycle, IMT_{c-1} is the intima media thickness of the previous cycle and Δh is the nodal displacement.

Because this cycle is the continuation of the previous cycle but with an updated geometry, the processes that started in the previous cycle must continue. Even in the case where the new value for WSS would allow for a normal endothelial behaviour to be restored, the previously triggered inflammatory process would not stop immediately and arterial swelling could still take place in these areas.

Preservation of the previously started inflammatory process will lead to a modification of the node-selective WSS threshold criteria, as shown in Figure 3.3.

To account for the modification of the pro-atherogenic area due to arterial change, nodal pre-selection represented by the WSS threshold criterion is now divided into two steps.

No displacement is assigned to the Ansys CfX v14 surface nodes if they do not belong to an area that was previously, or it is currently, identified as atherosclerosis-prone (the WSS at the current and previous time cycles is equal or more than the Poiseuille WSS value for the given geometry (Equation (2.4)). If the current WSS value is less than the Poiseuille value, those nodes are selected as belonging to the atherosclerosis-prone area. Finally, if the current WSS at the node is more than the Poiseuille value, but in the previous time cycles that node belonged to an atherosclerosis-prone area this would mean that some inflammatory process had been triggered there and can still continue. The node does not belong to an atherosclerosis-prone area anymore, as the endothelium recovered to a normal behaviour due to changes in the local haemodynamics. However, it did once belong to an atherosclerosis-prone area and the inflammatory process triggered could lead to further arterial wall deformation. It results that the endothelium and the arterial wall are modelled for both the case of WSS with a

lower value than the Poiseuille WSS at the current cycle and for the nodes that at least in one of the previous time cycles were part of an atherosclerosis-prone area.

As it can be seen from the workflow in Figure 3.3, the remaining part of the cycle does not differ from what was previously described. The result of this cycle, as it was for the initialisation cycle is a wall deformation value (Δh) to be imposed to the Ansys CfX v.14 model surface nodes.

3.3 Discussion

The *atherosclerosis remodelling cycle* was presented in this chapter. This workflow was developed to create a modelling tool that would consider the development of the initial state of atherosclerosis, from the penetration of LDL through the arterial wall to the formation of the atherosclerotic plaque. This tool was created integrating *in silico* the different sub-processes leading to atherosclerosis formation presented in the previous chapter.

The interactions between the different sub-processes were established with the help of a theoretical workflow that was then implemented computationally, using the most appropriate tools.

In this chapter, the *atherosclerosis remodelling cycle* workflow was divided into its theoretical part (theoretical workflow) and its computational part (computational workflow).

The theoretical part was presented in the first workflow, where the different core elements considered in the model were integrated together. Each of these core elements represent different parts (i.e. model equations and variables) of the theoretical model presented in Chapter 2 (Table 3.1).

A subset of the theoretical workflow, showing the time scales of the *atherosclerosis remodelling cycle* was presented in Figure 3.2. Following the multiscale modelling approach presented in the previous chapter, three different time scales were employed in this model. The first and smallest time scale are set to describe the arterial wall model. The second time scale is used to update the endothelium model accordingly to the change of LDL concentration inside the arterial wall. The third time scale is the time length of the entire *atherosclerosis remodelling*

cycle, the time needed by the modelled plaque to develop and reach a wall thickness of $\Delta h*$. At the end of the cycle, a value of arterial wall growth will be used to update the geometry of the artery considered. The WSS patterns will change accordingly, leading to a change in the penetration of macromolecules through the endothelium and, therefore, updating the whole *atherosclerosis remodelling cycle*. This will happen when the arterial wall growth developed in the model will have reached a certain threshold quantity (Δh^*, Equation (3.9)). As the arterial wall growth is the result of an accumulation process, it follows that this time will be of varying length, becoming shorter as the inflammatory process becomes more severe.

Modelling the atherosclerosis formation as a continuum process allowed capturing the dynamics of this complex systemic disease for years of development at a feasible computational cost.

The computational implementation workflow of the *atherosclerosis remodelling cycle* (Figure 3.3) was developed with the aim of producing a comprehensive tool for the multiscale modelling of atherosclerosis.

Different tools were used for the computational implementation of the model. The haemodynamics in the arterial lumen were modelled with the help of a CFD software Ansys CfX v.14. The arterial endothelium and arterial wall were modelled and implemented with the help of Matlab, using a coupled biochemical and transport model.

This computational workflow presents a valid alternative to patient-specific modelling and simulation of plaque, as it is separated into individual components and harnesses the power of parallel computing to perform computational tasks that would be otherwise intractable, in order to simulate long periods of time.

The endothelium-arterial wall model could be solved for each node independently as there is no data transfer in the nodal tangential direction (Figure 2.11). This allowed for easy parallelisation of the endothelium-arterial wall model, accelerating the computation speed. Furthermore, a pre-selection of the pro-atherogenetic areas in the arterial model, allowed for smaller set of the areas to be analysed within the geometry of interest (Figure 3.3) leading to a substantial decrease in the amount of information to be handled.

The *atherosclerosis remodelling cycle* can handle every geometry type and is

efficient in processing big data loads, making it an effective tool for the modelling of atherosclerosis.

Arterial lumen narrowing coming from atherosclerosis formation is modelled for each node on the wall surface of the modelled CFD domain. A point translation technique (Equations (3.4) to (3.6)) is used to displace the considered surface node in the normal direction at a distance Δh (Equation (2.42)) resulting from the arterial wall growth for that node. This localised nodal displacement allows for a greater versatility in the type of geometry that can be deformed and higher control on the type of deformation imposed, allowing for atherosclerosis formation to be modelled in irregular geometries like the anatomies of patient-specific arteries.

3.4 Conclusion

The *atherosclerosis remodelling cycle* presented here is a feedback loop model. The model cycle final output influences the model initial input in the next cycle.

Once a disease-prone environment has been identified (WSS low areas) a series of events causes the formation of an inflammation triggering factor (LDL oxidation) leading to the development of the disease. In the case of a chronic inflammatory disease such atherosclerosis, the disease cycle does not end with the formation of the plaque but keeps developing until the pro-atherogenic environment exists. This behaviour represents a feedback loop cycle, constantly repeating itself, until the pro-inflammatory condition is present. It is following this principle that the atherosclerosis model was developed.

In the following chapter, implementation results of this workflow will be presented. Two idealised geometries will be used in order to establish the validity of the method in a simplified setting.

Chapter 4

Atherosclerosis Modelling On Idealised Arterial Geometries

The implementation of the *atherosclerosis remodelling cycle* was first carried out on idealised arterial geometries and the results of this implementation is the subject of this chapter. As presented in Chapters 2 and 3, the model is highly dependent on the haemodynamics of the arterial model (via the WSS), so a first implementation using these idealised geometries allowed for easier testing in a controlled setting. This implementation, however, will be generalised and expanded and the study of a patient-specific case will be presented in Chapter 5.

First, the initial implementation of the atherosclerosis model was on a idealised, straight coronary artery with an axisymmetric geometry and in a steady state regime. At a second stage, the model was then improved to account for the formation of the atherosclerotic plaque in time (also defined as "evolution" in Chapters 4 and 5) and was finally generalised to accommodate the progression of plaque in any geometry. This transient model was tested on an axisymmetric idealised geometry similar to the geometry employed for the steady state model. Finally, a non-axisymmetric idealised artery was used to test the model and the methodology on a more complex geometry.

The simulation details of the atherosclerosis model implementations on the idealised arterial geometries will be presented in the first part of this chapter.

The second part of this chapter will be devoted to the presentation of the

results coming from these different implementations. The results will be presented in the same order used in the methodology section. First the steady state model (Section 4.1.1), then the transient model (Section 4.1.2). A discussion over the methodology and the results will follow (Section 4.2), to finish with the conclusion.

4.1 Methods

The steady state and transient models shown in this chapter are based on two arteries among the most common for atherosclerosis formation in the body[83, 131], i.e., the coronary artery and the femoral artery.*

4.1.1 Steady-state model

As previously discussed, the first implementation of this model was in steady state conditions, i.e., only location and severity of the formation were considered. This work is the subject of a published paper[135].

4.1.1.1 Idealised geometry of a coronary arterial stenosis

Computational Geometry

A straight axisymmetric geometry of a coronary artery was implemented (Figure 4.1) as in Olgac et al.[83]. The artery was modelled with a 40% stenotic reduction of the lumen. The stenotic neck was introduced as an element of haemodynamic disturbance to create a pro-atherogenic environment, as evidence in the literature suggests that geometry can be a risk factor for the development of atherosclerosis[29].

The arterial geometry is shown in Figure 4.1. The stenotic neck is 2 R_a long, and it is located 8 R_a downstream of the inlet. The artery has an un-stenosed radius $R_a = 1.85$ mm, and it is 60 R_a long.

*The choice of using two different arteries as exemplars came from the fact that through the development of the generalised model, the patient-specific available data was obtained from peripheral arteries, among which femoral arteries.

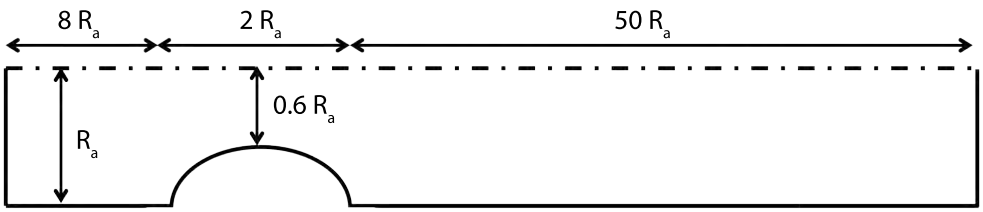

Figure 4.1: Axisymmetric straight idealised geometry of a coronary artery. Not shown to scale.

Boundary conditions and implementation setup

Each one of the arterial model sub-domains had specific boundary conditions and parameters for this implementation. These are described below.

Arterial Lumen

A parabolic velocity profile was imposed at the inlet [83] as described by Equation (4.1).

$$u(r) = 2U\left[1 - \left(\frac{r}{R_a}\right)^2\right] \tag{4.1}$$

where $u(r)$ is the velocity, U is the time averaged mean velocity of blood in the considered artery and was chosen as $U = 24$ cm/s for the carotid artery [83] and r is the radial location.

At the outlet, a constant pressure of 70 mmHg was used[90]. No slip conditions were set at the wall boundary.

A first analysis was carried out to analyse the impact of high levels of plasma lipids on plaque development. Two different mean blood LDL concentrations (c_{lum}) were considered as fixed values in the lumen: a moderately high value of mean blood LDL level of 5.5 mol/m^{3}and a more severe case of 7.77 mol/m^3[135]. These values were implemented as the LDL concentration in the lumen-free model, and correspond to a pathological state defined as LDL hyperlipoproteinemia, an abnormally high level of low density lipoproteins in blood[136], which could be linked with premature and severe atherosclerosis formation[137].

Arterial endothelium

The shape index function defining the relationship between WSS local values and endothelial cell shape explained in Chapter 2 is described by Equation (4.2) as follows:

$$SI_1 = 0.380e^{(-0.79WSS)} + 0.225e^{(-0.43WSS)} \tag{4.2}$$

As the geometry, parameters and boundary conditions of the coronary model were close to the *in silico* experimental settings of[83] the SI function in Equation (4.2) was considered suitable for this implementation.

Given the steady state regime, there was no time change in the solute flux through the endothelium. The concentration of LDL inside the arterial wall ($c_{w,end}$) was considered negligible as it is much smaller than the mean blood LDL concentration (c_{lum}). Equation (2.7) was simplified as:

$$J_s = P_i c_{lum} \frac{Pe}{e^{Pe} - 1} + J_v(1 - \sigma)c_{lum} \tag{4.3}$$

And can be arranged as:

$$J_s = P_{app} c_{lum} \tag{4.4}$$

Where the apparent permeability (P_{app}) represents the effects of traversing all the permeation pathways across the membrane and is defined as:

$$P_{app} = P_i \frac{Pe}{e^{Pe} - 1} + J_v(1 - \sigma) \tag{4.5}$$

Arterial Wall

The arterial wall was defined with an IMT = 0.34 mm, in accordance with the dimensions of a human coronary artery[138]. To solve for the transmural velocity (u_w) calculated using Darcys law (Equation (2.25)), a pressure boundary of p_{end} = 100 mmHg and p_{adv} = 17.5 mmHg was imposed at the sub-endothelial and adventitial boundary respectively[90].

Fluid domain descretisation

The lumen was meshed in Ansys Workbench v14. The mesh created was a structured mesh of 567800 quadrilateral elements and 1023455 tetrahedra. The total number of elements was 1691255. Five inflated boundary layers were used at the wall boundaries.

4.1.2 Transient Model

To simulate the development of the atherosclerosis formation in time, a transient model (as shown in Chapter 2) was developed. Peripheral arteries are among the most common locations for atherosclerosis formation. The artery used as a blueprint here was the common femoral artery. The fairly "straight" anatomy of this vessel allowed for a good test case, as the idealised case was close to the real one. Two different scenarios were considered as shown below.

4.1.2.1 Idealised Geometry of a Common Femoral Artery Stenosis

Computational geometry

A straight pipe with a stenotic neck was created (Figure 4.1). The measurement and physiological parameters were chosen as corresponding to a femoral artery, with R_a = 3 mm[131].

Boundary conditions and implementation setup

The boundary conditions for this implementation are described below.

Arterial lumen

A parabolic profile was imposed at the inlet of the fluid domain following Equation (4.1). The value for the time averaged mean velocity (U) was imposed as $U = 7.7$ cm/s. This velocity value was derived from the average WSS value in the common femoral artery (CFA), $WSS = 0.36$ Pa [39]. Although the mathematical model of lipoprotein accumulation and fatty streak formation was solved in time, the CFD model was solved for steady state conditions.

A stress free condition was used at the outlet[131]. No slip conditions were set at the wall boundary.

A mean LDL particle concentration of $c_{lum} = 1358$ nmol/L[129] was used as fixed value for mean blood LDL concentration in the lumen, to solve for the LDL transport model.

Arterial endothelium

Endothelial cell SI function was defined as the relationship between SI and local WSS normalised by the Poiseuille value of WSS for the considered artery, as explained in Chapter 2.

$$SI_2 = -0.2435 \cdot \frac{\tau}{\tau_0}^{0.3537} + 0.4025 \tag{4.6}$$

Where the Poiseuille WSS $\tau_0 = 0.36$ Pa. An artery-specific form of the SI function was implemented, as the artery does not have the same anatomical characteristics to match the experimental data presented in Levesque et al.[32].

Arterial wall

Consistent with the anatomy of the human femoral artery, the IMT was set as 0.562 mm[139]. The transmural velocity (u_w) was considered as homogeneous

throughout the arterial wall, and it was set to a value of $u_w = 1.78 \times 10^{-8}$ m/s[90].

Fluid domain discretisation

Ansys Workbench v14 was used to mesh the fluid domain. Only a quarter of the geometry for $0° \leq \Theta \leq 90°$ was meshed, the remaining geometry was simulated with the help of symmetry planes.

The mesh had a total of 3333998 elements among which 2961378 tetrahedra; the mesh was structured. Five inflated boundary layers were used at the wall boundaries.

4.1.2.2 Idealised Geometry of an S-shaped Common Femoral Artery

In the area just above the knee, the femoral artery shows a very mild S-shaped curvature. When the leg is flexed, a number of successive small short bends appear, giving the artery a wave-like appearance. In younger people these bends disappear when the leg is extended however, in older people they persist[131]. This sequence of bends could cause haemodynamic conditions leading to the creation of atherosclerosis-prone areas.

Computational geometry

An S-shaped femoral artery was built (Figure 4.2), following the same approach as in Hoogstraten et al.[131].

The artery has a radius $R_a = 3$ mm; both inlet and outlet are straight segments of 15 mm length and the two bends are both of 35°, with a radius of curvature of 39 mm[131].

Boundary conditions and implementation setup

As this implementation is for a common femoral artery, the boundary conditions and implementation settings are the same as the ones used for the previous case of the idealised geometry of a femoral artery stenosis.

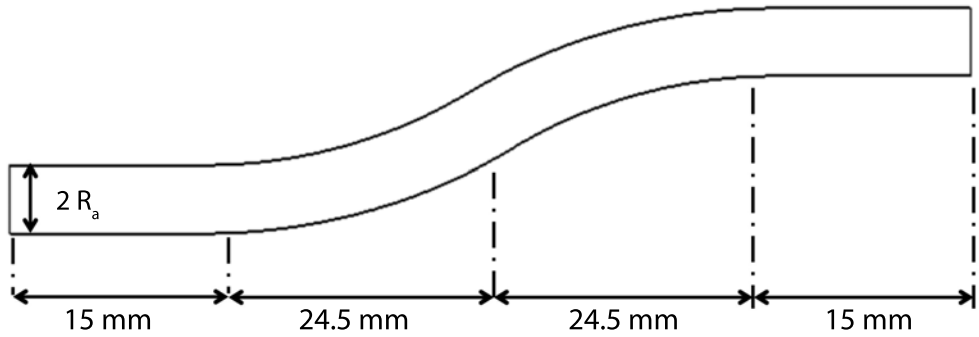

Figure 4.2: Geometry of an S-shaped femoral artery. Not shown to scale.

Fluid domain discretisation

An unstructured mesh was created in Ansys Workbench v14. The mesh had a total of 2551977 elements with 2123257 tetrahedral elements. Five inflated boundary layers were used at the wall for improved mesh structure. A grid independence study was used to choose the most adequate mesh for the current analysis, the details are shown in Appendix A.

4.2 Results

4.2.1 Steady-state Model

The wall shear stress distribution along the computational geometry has been compared with the analytical solution of WSS for a Poiseuille flow in a straight tube with the same radius (R_a), mean inlet velocity U and fluid density μ (Figure 4.3). The analytical solution corresponds to the WSS at the inlet and after the reattachment point at the outlet, showing that the mesh used is appropriate. A peak in the WSS value can be seen at the stenosis, due to flow acceleration (Figure 4.4) in the lumen narrowing. The fluid after the stenotic neck shows the *vena-contracta* behaviour, with decreased value of WSS and formation of recirculation zones near the wall boundaries, indicating possible atherosclerosis-prone areas.

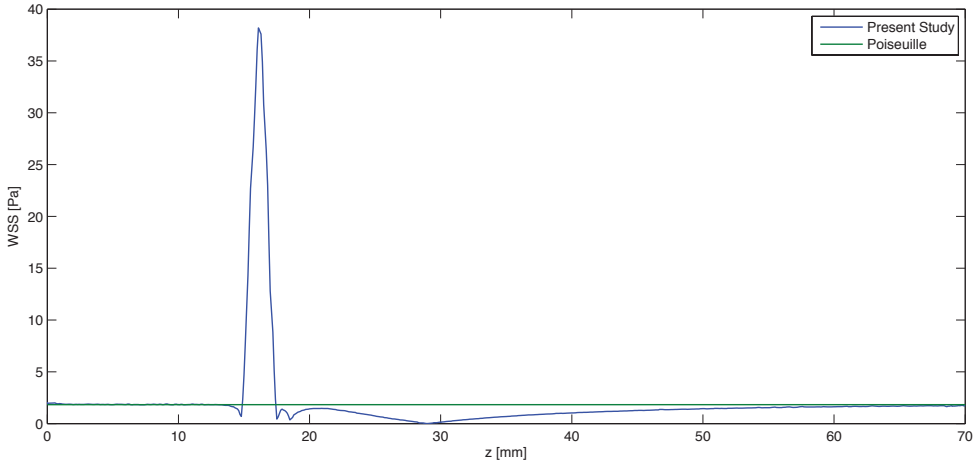

Figure 4.3: Local value of WSS as a function of the axial location z. The analytical solution of the Poiseuille flow is plotted here for comparison. Boundary conditions: inlet parabolic velocity profile (Equation (4.1)), outlet stress free.

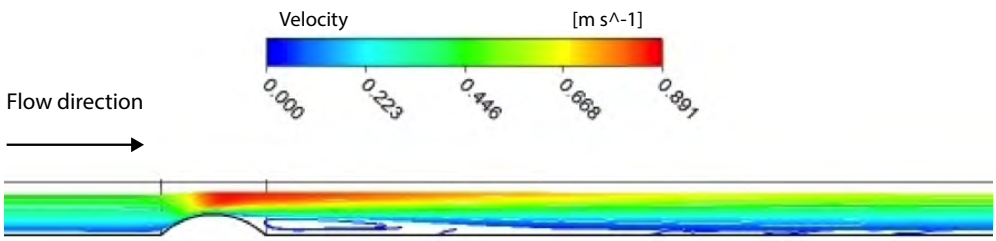

Figure 4.4: Velocity streamlines in the stenotic areas. The recirculation zone after the stenotic neck is shown.

The formation of areas with increased transport of plasma macromolecules and at higher risk of atherosclerosis can be visualised by looking at the endothelial apparent permeability (P_{app}) along the artery (Figure 4.5). The endothelial permeability has a steady value until approaching the stenotic area, where a first minor increase at the separation point is followed by a major increase in the area of highest flow recirculation. The point of minimum WSS (Figure 4.3) and maximum endothelial permeability is labelled in Figure 4.5 as z_0. After the reattachment point, the flow perturbation caused by the stenosis fades, leaving the

flow back to its normal dynamics (z_1).

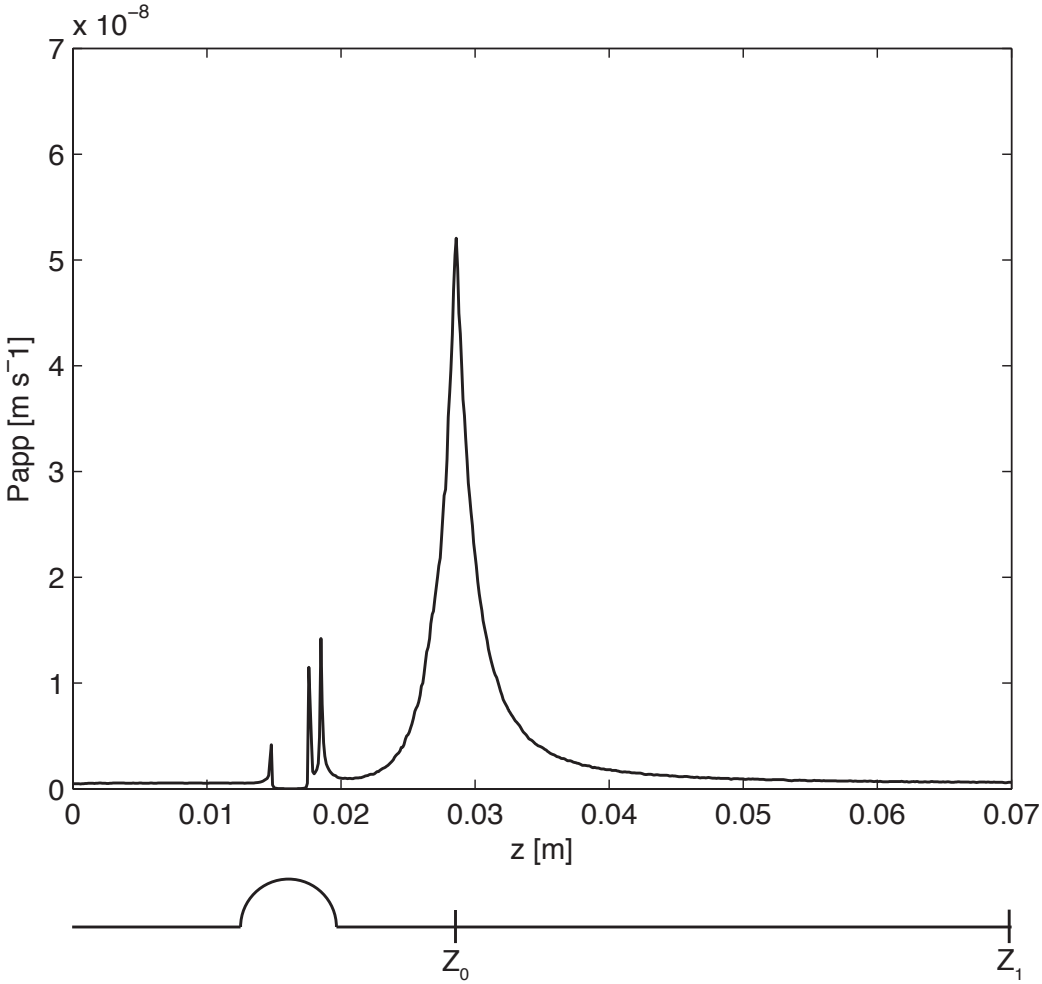

Figure 4.5: Apparent permeability (P_{app}) of endothelium as a function of the axial location z. The point of minimum WSS and maximum endothelial permeability (z_0) is shown, together with the point where normal haemodynamic conditions are regained (z_1).

Computations were performed for two different concentrations of mean blood LDL (c_{lum}); a moderately high concentration of 5.5 mol/m^3 and a more severe case with 7.7 mol/m^3.

The concentration distributions inside the arterial wall for the two different mean blood LDL concentrations implemented are shown in Figure 4.6. Here, the

LDL arterial wall values were taken at z_0 at the end of the first atherosclerosis cycle, before the lumen remodelling for plaque formation has occurred. The case of 7.7 mol/m^3 shows an almost 50% increase in LDL concentration inside the arterial wall compared with the less severe case (5.5 mol/m^3) of hyperlipoproteinemia. An increase in both the endothelial permeability and the concentration of mean blood LDL available in the lumen leads to a consistent increase in the flux of LDL penetrating inside the arterial wall, making the high permeability areas more susceptible to atherosclerotic growth.

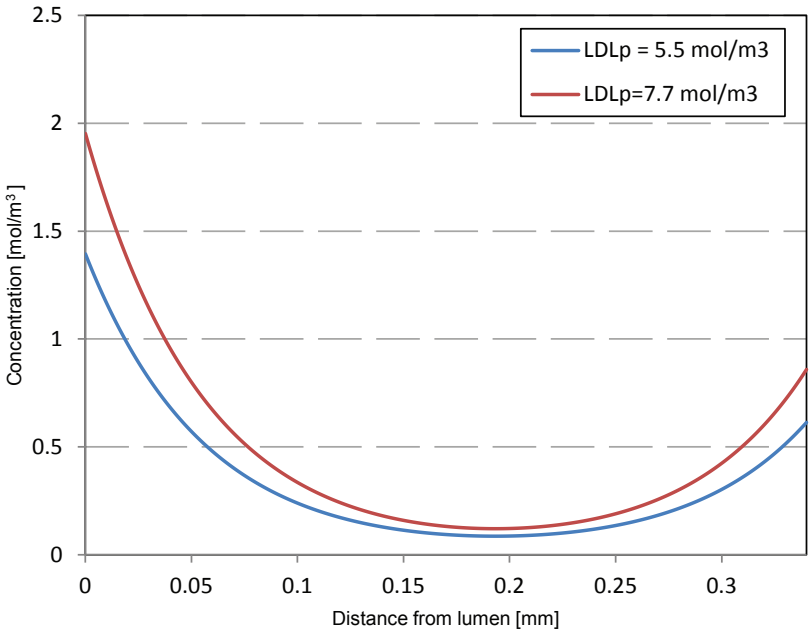

Figure 4.6: LDL arterial concentration profiles taken at point z_0 along the vessel length. The two profiles corresponding to the different LDL mean blood concentration implemented are shown.

Figure 4.7 shows the WSS pattern and geometry outline for the most severe case of hyperlipoproteinemia (7.7 mol/m^3) at the beginning and at the end of the first *atherosclerosis remodelling cycle*. Plaque formation is shown at the end of the first atherosclerosis cycle (Figure 4.7b) in the area of low WSS (Figure 4.7a) where the endothelial permeability was shown to be high (Figure 4.5).

Two *atherosclerosis remodelling cycles* were performed in steady state for the two different mean blood LDL concentrations. Plaque development was present in both cases as shown in Figure 4.8.

At the end of the first atherosclerosis cycle, hyperlipoproteinemia caused plaque development to occur in the post-stenotic area. Figure 4.9 shows (a) LDL endothelial apparent permeability at the end of the first atherosclerosis model cycle for a mean blood LDL level of 5.5 mol/m^3 (b) and a mean blood LDL level of 7.7 mol/m^3. Comparing the endothelial permeability before (Figure 4.5) and after plaque formation (Figure 4.9), changes in the endothelial local transport properties can be visualised. The permeability in the recirculation zone for a mean blood LDL level of 5.5 mol/m^3 (Figure 4.9a) shows two peaks in value with a drop in the middle, created by the newly formed plaque. Figure 4.9b also shows two value increases in the endothelial permeability. The first increase corresponds to the flow separation point, the second increase is in the recirculation zone caused by the initial stenosis, where the permeability appears majorly modified from its behaviour in the initial geometry configuration (Figure 4.5). The drop in permeability distal to the plaque is much more developed for the most severe case of hyperlipoproteinemia (7.7 mol/m^3) (Figure 4.9b) than for 5.5 mol/m^3 (Figure 4.9a), showing that the newly formed plaque has enough of an impact on the flow to bring the endothelial permeability back to normal values. This plaque generates also a new recirculation zone downstream (Figure 4.9b), leading to another increase in the endothelial permeability and creating a new atherosclerosis-prone area. At the end of the second *atherosclerosis remodelling cycle* (Figure 4.8b) in agreement with the endothelial apparent permeability behaviour in Figure 4.9b, a second plaque forms downstream from the first plaque.

Information on the severity of the simulated lesion, such as plaque size and number of plaques is summarised in Table 4.1. For the mean blood LDL level of 5.5 mol/m^3 there was an atherosclerotic formation in the post stenotic branch; this plaque grew in size but did not initiate the formation of another plaque. Conversely, from the implementation of a 7.7 mol/m^3 mean blood LDL level a fairly large atherosclerotic formation was present after the first *atherosclerosis remodelling cycle* (plaque cross sectional area of 0.588 mm^2). During the second *atherosclerosis remodelling cycle*, the first plaque grew in size and another plaque

formed.

Table 4.1: Simulation Results

LDL Mean Blood Concentration (mol/m^3)	5.5		7.7	
	Plaque number	Plaque cross sectional area (mm^2)	Plaque number	Plaque cross sectional area (mm^2)
1st Simulation	1	0.147	1	0.588
2nd Simulation	1	0.366	1	0.8
			2	0.56

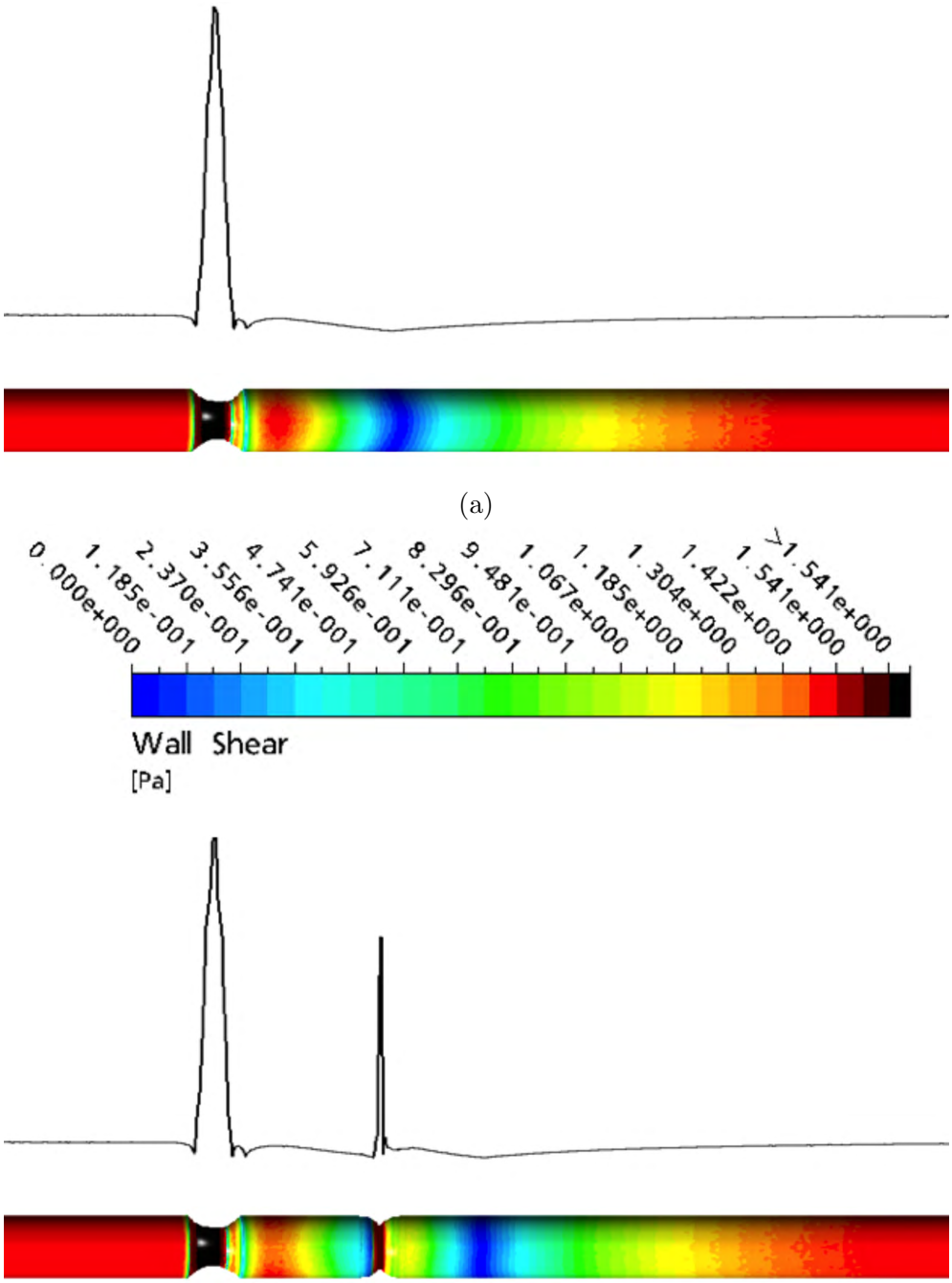

Figure 4.7: Wall Shear Stress contour plot and pattern along the vessel length for the most severe hyperlipoproteinemic case (7.7 mol/m^3) taken at : (a.) the beginning of the *atherosclerosis remodelling cycle* and (b.) the end of the *atherosclerosis remodelling cycle*. Notice that the maximum value showed on the contour plot is for the range of WSS going from 1.541 Pa s to the peak value.

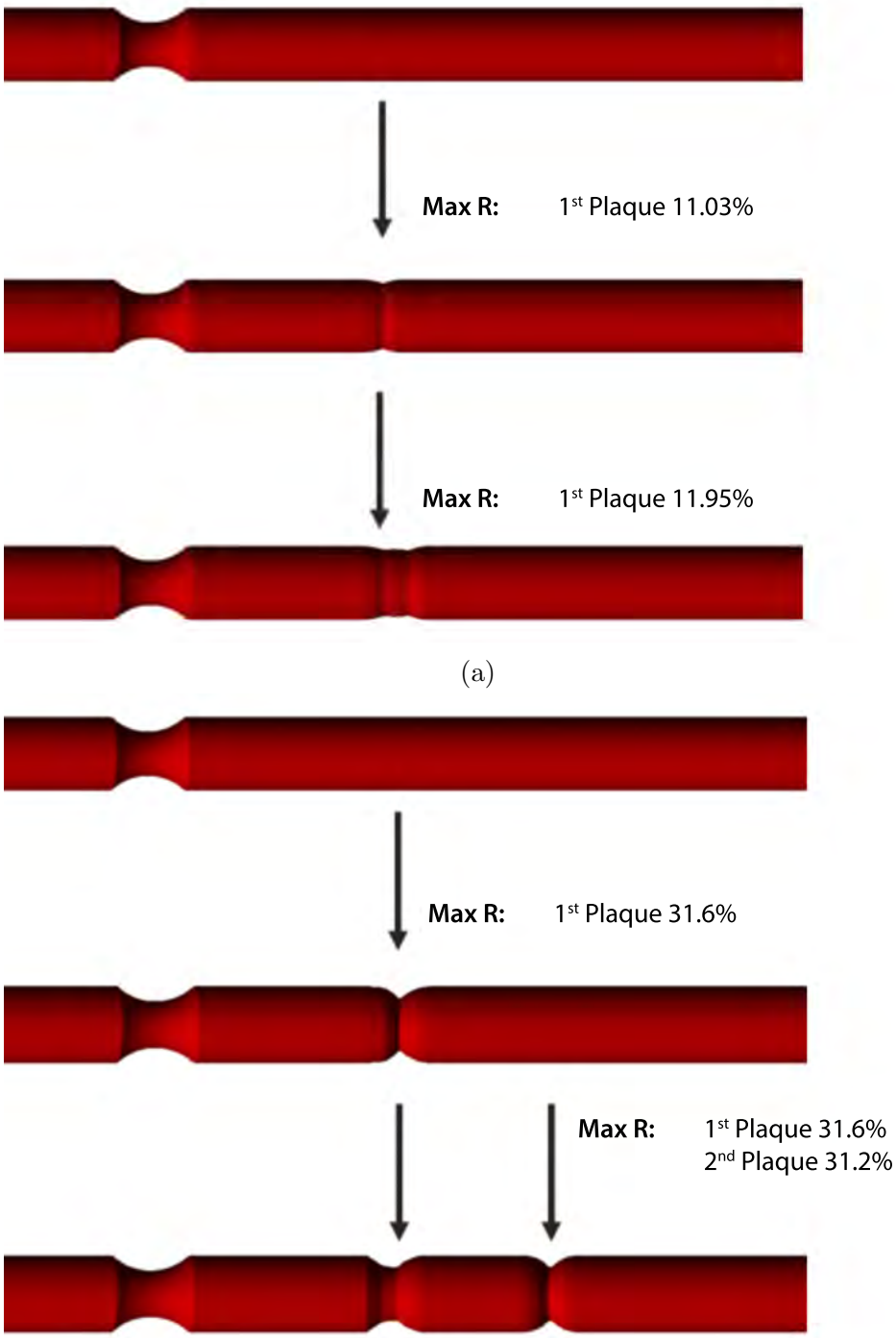

Figure 4.8: Atherosclerotic formation with percentage of maximum normalised radial reduction (R). $R = \frac{r_0}{R_0}$, where r_0 is the radial reduction at the time step. A. Lesion growth for a mean blood LDL level of 5.5 mol/m^3. B. Lesion growth and second lesion formation for a mean blood LDL level of 7.7 mol/m^3.

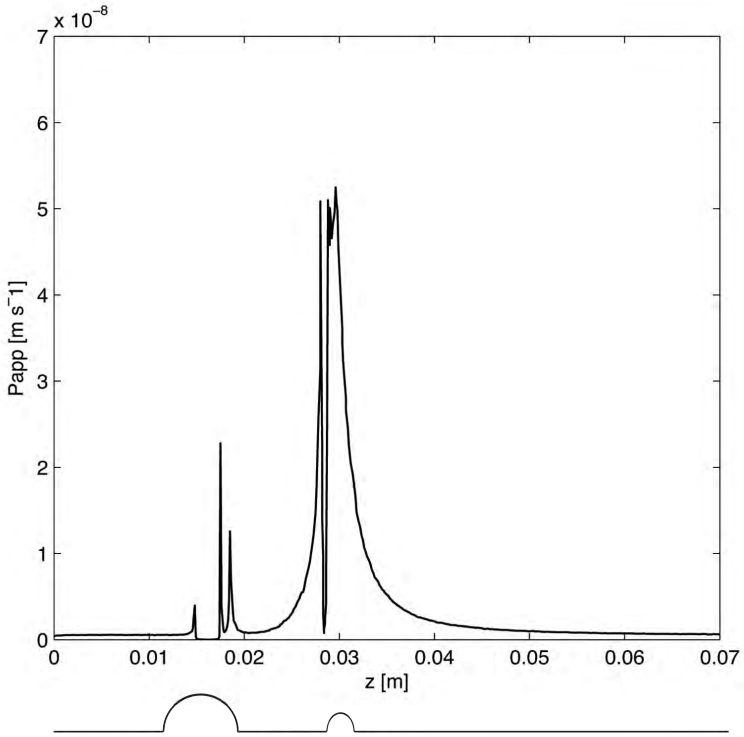

(a)

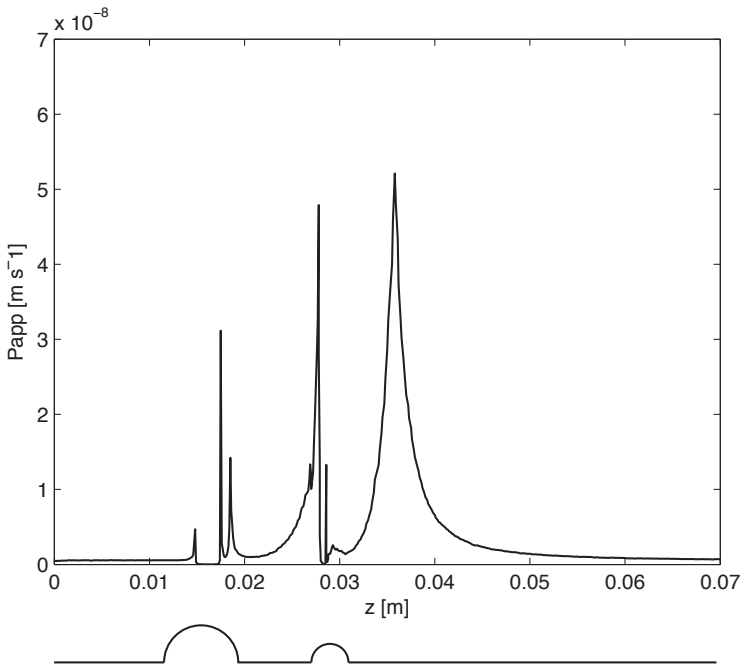

(b)

Figure 4.9: LDL endothelial apparent permeability (P_{app}) as a function of the axial location z. Endothelial transport property taken at the end of the first atherosclerosis cycle for a mean blood LDL level of (a) 5.5 mol/m^3 and a mean blood LDL level of (b) 7.7 mol/m^3

4.2.2 Transient Model

4.2.2.1 Idealised geometry of a common femoral artery stenosis

The computational mesh used shows a WSS that corresponds well with the analytical solution of WSS for a Poiseuille flow in a straight tube with same radius (R_a), flow mean velocity U and fluid density μ (Figure 4.10).

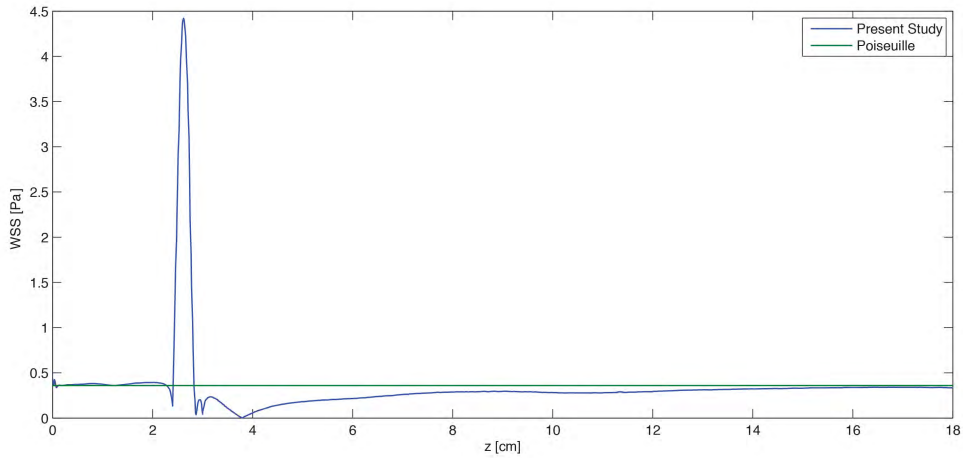

Figure 4.10: Local value of WSS as a function of the axial location z. The analytical solution of the Poiseuille flow is here plot for comparison. Boundary conditions: inlet parabolic velocity profile (Equation (4.1)), outlet stress free.

The haemodynamic patterns are qualitatively similar, hence, the apparent permeability (P_{app}) taken at the beginning of the initialisation cycle plotted along the stenotic common femoral artery (Figure 4.11) and the apparent permeability for the stenotic coronary artery (Figure 4.5) show the same trend; highlighting similar atherosclerosis-prone areas. The endothelial response to WSS is defined by an artery-specific SI function Equation (4.6), derived from the experimental results of Levesque et al.[32] tuned for the artery in question, as shown in Section 2.1.2, Chapter 2.

In areas of high endothelial permeability, LDL penetration would occur. Once inside the arterial wall, interaction of LDL with free radicals would initiate a chemical cascade, leading to the formation of oxidised LDL and foam cells. An illustration of the behaviour of the different reactants in the modelled chemical cascade is given in Figure 4.12.

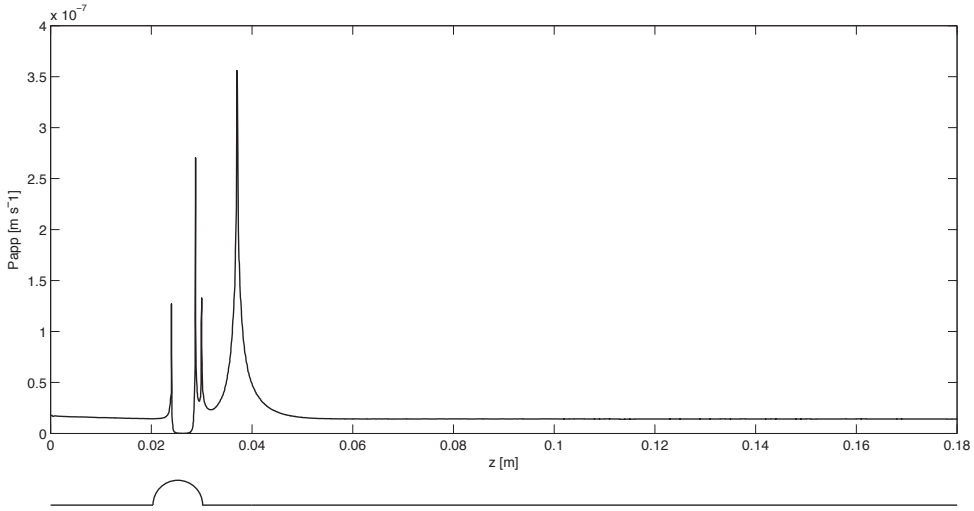

Figure 4.11: Apparent permeability (P_{app}) of endothelium as a function of the axial location z.

Figure 4.12a shows the chemical cascade leading to the oxidation of LDL. A fixed concentration of 1.323 nmol/L corresponding to the subendothelial LDL concentration at the global WSS minima after 6 years of simulation time was imposed as the initial concentration of native LDL (LDL with 6 vitamin E). The behaviour of the LDL oxidation cascade is in agreement with Cobbold et al.[22]. However, as the change in concentration of the free radicals due to the kinetic reaction was neglected and free radicals were assumed constant, there is a different time response in the LDL oxidation process compared to the results shown in Cobbold et al.[22]. The interaction between wall monocytes/macrophages and oxidised LDL leading to the formation of foam cells is shown in Figure 4.12b. Foam cell formation and accumulation indicates presence of an inflammatory process. The consequence of this inflammatory process would be the formation of atherosclerotic plaque.

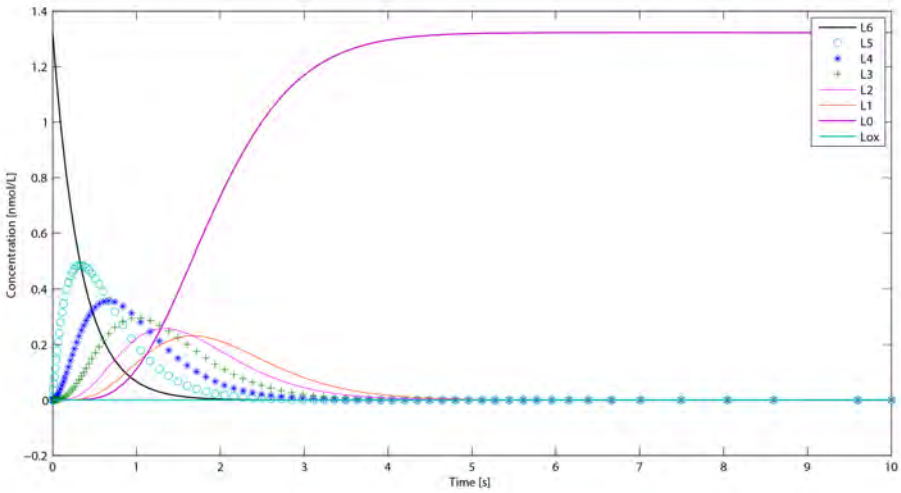

(a)

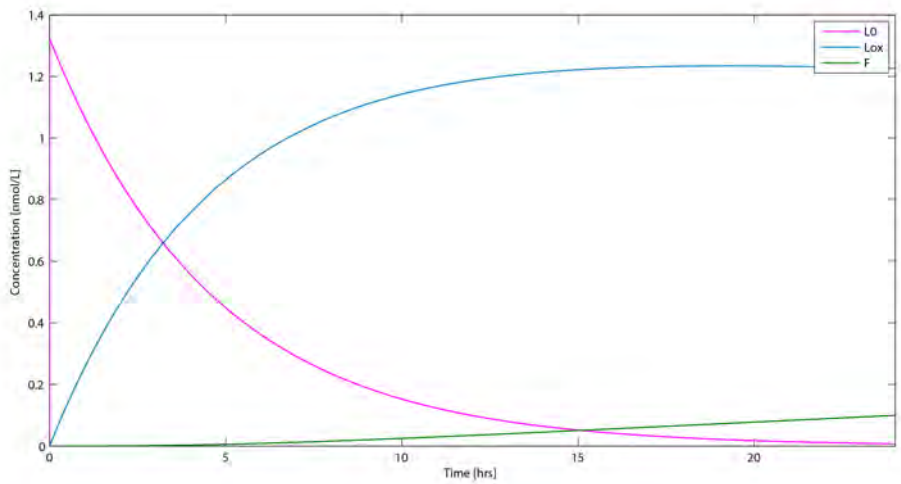

(b)

Figure 4.12: (a) Temporal profile of the LDL oxidation cascade. A fixed concentration of 1.323 nmol/L was imposed as the initial concentration of LDL with 6 Vitamin E (L_6). (b) Temporal profile of foam cell formation; the oxidised LDL and LDL prone to oxidation are included.

In the presence of a stenosis (40% radial reduction of lumen), the model predicts that an initially healthy artery would develop a plaque of maximum thickness of $\approx \Delta h*$ after 6 years (where $\Delta h*$ is equal to 1% of the artery radius). The deformation imposed on the CFD mesh to account for plaque formation is shown in Figure 4.13. The relative error in the mesh displacement was calculated as:

$$e = \frac{\epsilon_{p^I} - \epsilon_{p^{II}}}{\Delta h} \tag{4.7}$$

Where p^I is the position where the mesh node p was displaced to by Ansys CfX v14., p^{II} is the analytical displacement that node p should have had following equations (Equations (3.4) to (3.6)) and Δh is the displacement in the normal direction. The minimum error was found to be zero, with a maximum error of 9% for the node where the maximum displacement was applied. This error does not only arise from computational inaccuracy, but it can be attributed to the passive displacement of the node considered due to the surrounding nodes being displaced.

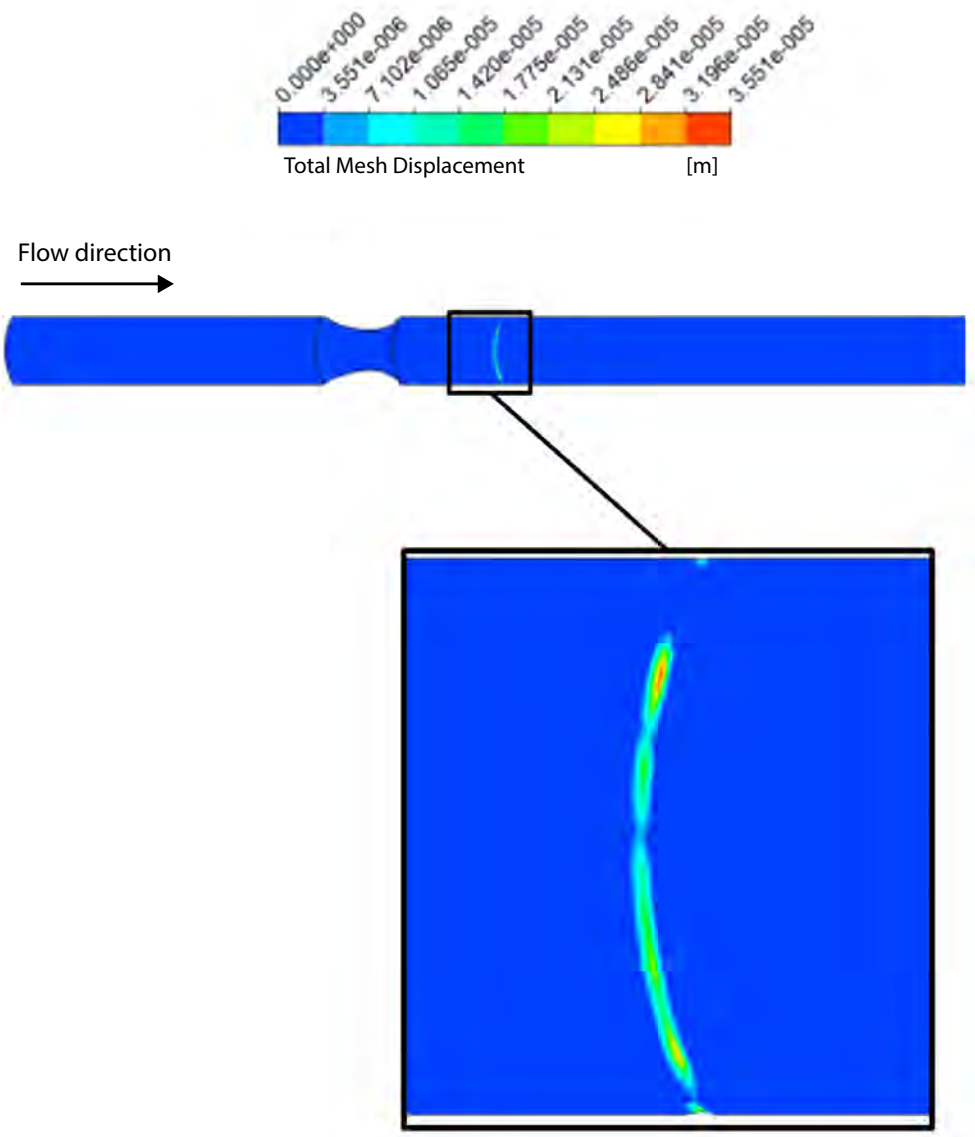

Figure 4.13: Contour plot of a total mesh displacement showing the plaque formation after 6 years. Part of the side view is shown. A zoomed detail of the geometry side view shows the plaque. The mesh displacement contour plot is not symmetric. This is most likely due to a non-uniform mesh. Other factors influencing mesh displacement could be numerical artifacts linked to mesh-displacement errors and/or problems related to local minima and differences in the mesh elements. The flow in the post-stenotic area is not at levels of global linear instability, as the Reynolds Number never reaches the critical value of 722 [140, 141].Although, a transient to turbulent behaviour is still present, leading to local flow perturbations and differences in the local minima [141].

4.2.2.2 Idealised geometry of S-shaped common femoral artery

The haemodynamics for this case can be visualised from the velocity contour plot in Figure 4.14.

Flow detachment areas are minimal in the lower wall distal and proximal to the S-shaped curvature, and more prominently in the upper wall, in the area between the first bend and the second bend. These flow detachment areas generate a local decrease in the fluid velocity and recirculation areas and local changes in the endothelial transport properties (Figure 4.15). This is different to the case discussed previously, where a sharp cross-sectional narrowing in the arterial lumen generated large areas of flow recirculation, the flow recirculation is less severe.

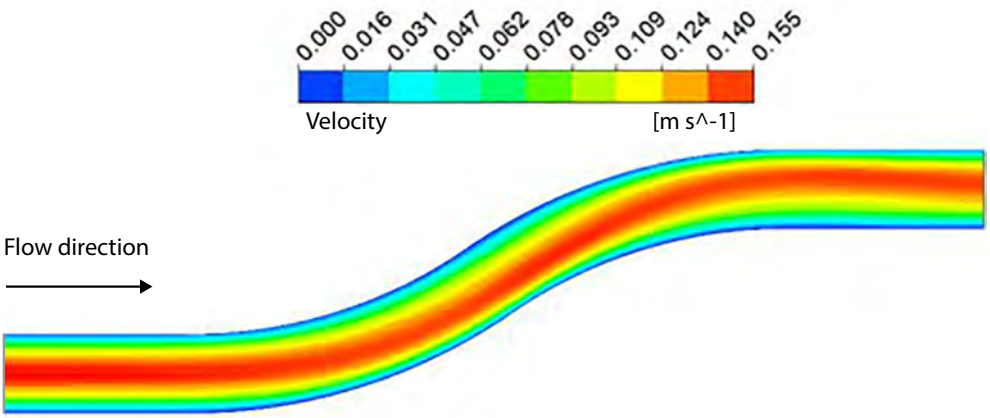

Figure 4.14: Velocity contour plot for a mid plane. Flow detachment is present in areas proximal and distal to the double bend in the lower wall. Flow detachment to the upper wall is present at the end of the first bend and at the beginning of the second bend. Boundary conditions: inlet parabolic velocity profile Equation (4.1), outlet stress free.

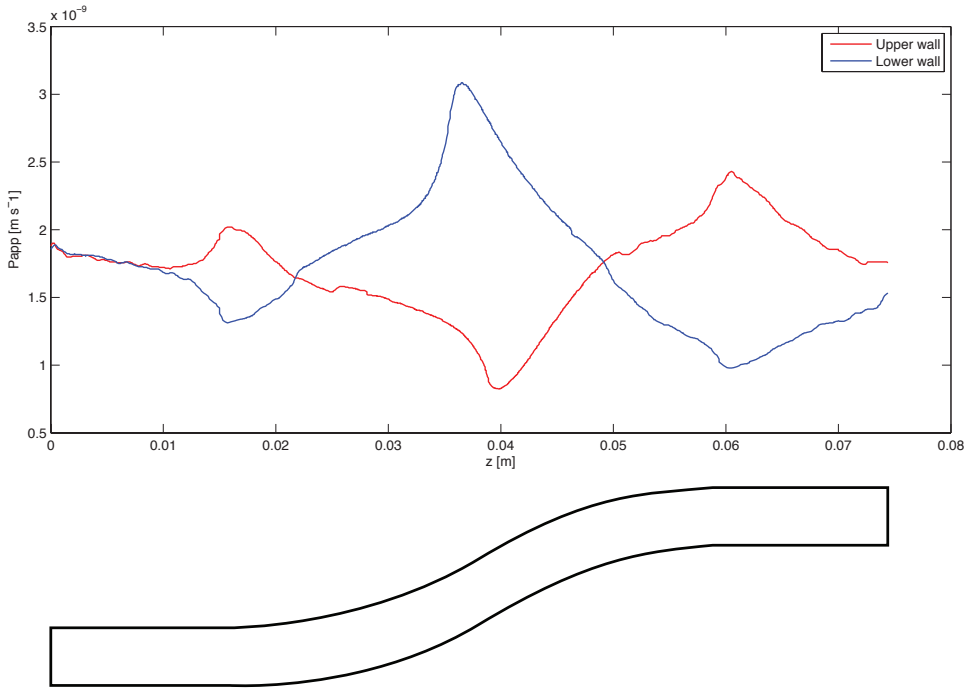

Figure 4.15: Apparent endothelial permeability (P_{app}) taken at the beginning of the initialisation cycle as a function of the axial location. The apparent permeability in the upper wall (blue) shows an increase in the area between the two bends. Two minor increases can be seen in the lower wall (red), in the area distal and proximal to the double bend. These peaks show areas of local increase in the endothelial permeability, which can be considered atherosclerosis-prone areas.

For a case in which there are mild changes in the endothelial transport properties from the normal endothelial behaviour, the simulated atherosclerosis formation would take longer to develop. Starting from a healthy artery, this model predicts that after 17 years of simulated time, plaque development would occur.

Atherosclerosis formation was modelled further in time and a second *atherosclerosis remodelling cycle* computed. The contour plot of total mesh displacement after 17 years and 6 months is visualised in Figure 4.17.

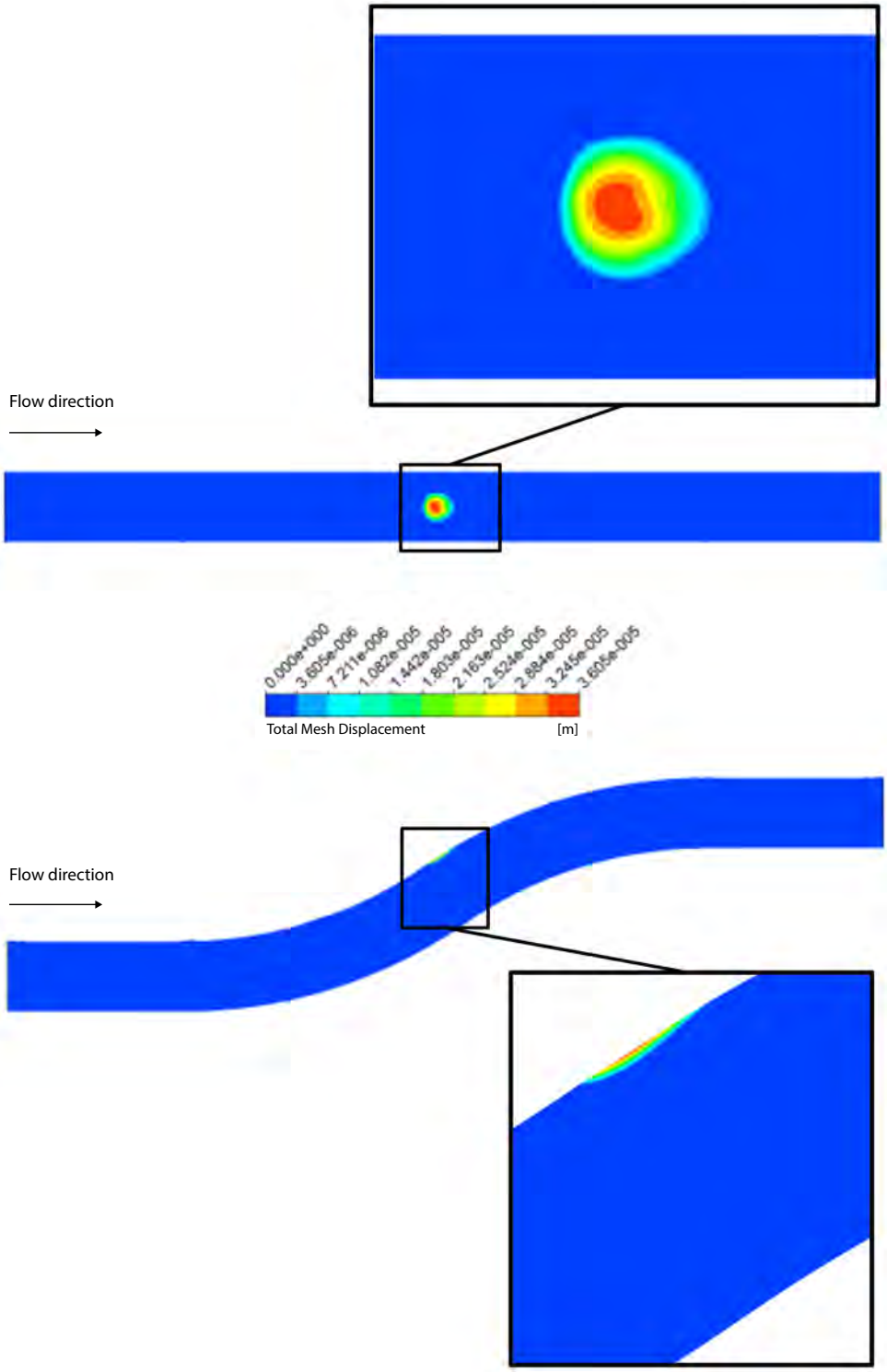

Figure 4.16: Contour plot of a total mesh displacement showing the plaque formation after 17 years. Top view and side view are shown. A zoomed detail of the geometry side view shows the plaque.

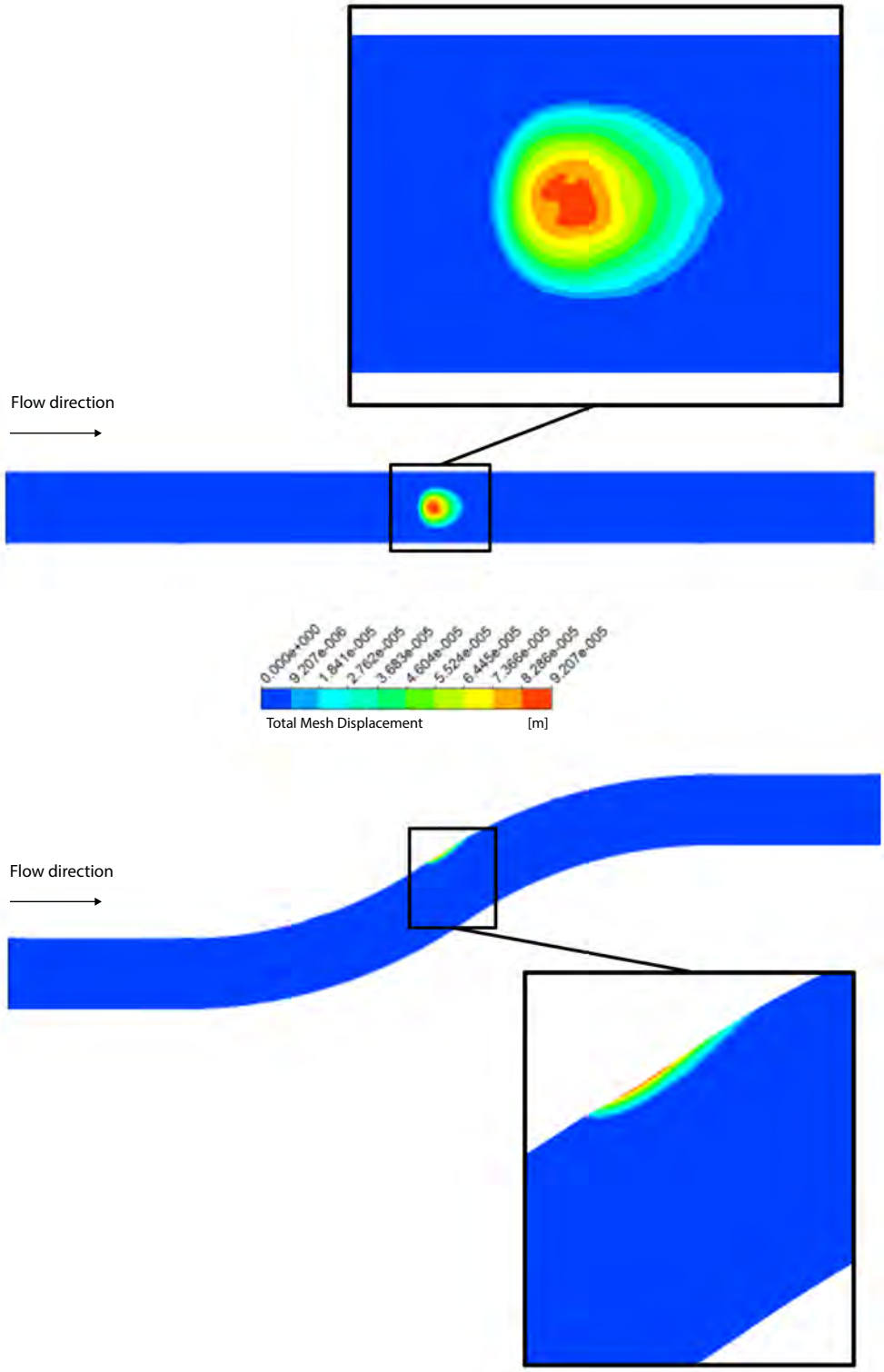

Figure 4.17: Contour plot of a total mesh displacement showing the plaque formation after 17 years and 6 months. Top view and side view are shown. A zoomed detail of the geometry side view shows the plaque.

4.3 Discussion

The model and workflow presented in this thesis show initial concrete steps towards a more ambitious target of developing a patient-specific predicting tool for atherosclerosis plaque formation and development. To achieve this goal, the atherosclerosis modelling framework needs to characterise appropriately the process of formation of plaque. Disease location, severity and rate of progression are the three issues central to this study.

Initially, the computational framework was developed for steady-state simulations. Neglecting the transient aspect of atherosclerosis allowed a simplified testing model able to link the haemodynamics to the processes behind the formation of plaque in the arterial wall to be built. The haemodynamics of an idealised stenotic coronary artery geometry were modelled following the approach of Olgac et al.[83]. The variation of the local endothelium transport properties were made dependant on the local haemodynamics. The *vena-contracta* led to the creation of larger endothelial permeability areas after the stenotic narrowing and subsequent plaque formation in these areas. This compares well with literature findings in the literature which show that atherosclerosis formation usually occurs downstream of a stenosis[95].

A constant mean blood LDL concentration value was used for each simulation, neglecting local variations in concentration[142].

Two different hyperlipoproteinemic blood LDL levels were implemented. Arterial wall concentration profiles were taken at the point of highest endothelial permeability (z_0) to analyse the effect of different mean blood LDL concentrations (Figure 4.6). A higher concentration of LDL in the arterial wall would trigger a more acute inflammatory process, leading to a more severe atherosclerosis formation[143]. The distribution of LDL inside the arterial wall was consistent with *in vivo*[90] experimental results.

Development of atherosclerotic plaque was modelled for the two different mean blood LDL levels. Differences in plaque formation for the cases analysed show the dependency of atherosclerosis severity on mean blood LDL levels (Figure 4.8). The plaques developed in the tract downstream of the stenosis caused a local variation in the endothelial transport properties. In the initial geometry the

maximum local permeability was at the recirculation area caused by the stenosis (Figure 4.7a and Figure 4.5).As a consequence of plaque formation, haemodynamics and the endothelial permeability in the location of the newly formed plaque changed (Figure 4.9). Endothelial permeability to macromolecules also appeared to have increased further downstream of the plaque formation in the most severe hyperlipoproteinemia case (Figure 4.9b). This new high endothelial permeability location is linked to the formation of a new local WSS minima (Figure 4.7b) caused by the plaque formation. To analyse how the atherosclerosis would progress given the change in the haemodynamic environment, a new simulation was performed. There was a further development in size for the first plaque formation for both of the hyperlipoproteinemia cases (Table 4.1). As already shown by the local increase in endothelial transport properties, a second plaque developed in the most severe hyperlipoproteinemia case. This result (multiple stenosis) mimics the several subsequent plaque formations that can be found in arteries such as the common femoral artery and the popliteal[95].

The development of atherosclerosis with time was modelled in a stenotic common femoral artery. The relationship between endothelial transport properties and haemodynamics was represented by a normalised Shape Index Function Equation (4.6). This SI function allows for a more artery-specific description of the endothelial behaviour.

Once inside the arterial wall, the LDL starts interacting with free radicals until full oxidation occurs. The chemical cascade shown in Figure 4.12a shows the temporal degradation of LDL from its native form (L_6) to its fully oxidized state (L_{ox}). Foam cells start forming after 3 hours from the start of the process (Figure 4.12b), and are still forming throughout the first day of the inflammatory process. An *in vitro* experiment showing the time it takes for the lipids to metabolise inside the macrophage foam cells shows that lipid accumulation is carried out mainly in the first 24 hours[144]. This model does not analyse the lipid accumulation in the macrophages. However, by showing that foam cells start forming in the first 24 hours, it indicates a behaviour that is in agreement with that observed *in vitro*[144].

A sensitivity analysis was carried out on the parameters involved in the modelling of cytokine activity and foam cell formation rate. The model plaque growth

was relatively sensitive to these parameters, as shown Appendix B. Further analyses must be conducted on these parameters for validation purposes.

The first signs of atherosclerosis in the stenotic common femoral artery developed after 7 years of simulated time (Figure 4.13). The plaque location is in the area of increased endothelial permeability to macromolecules (Figure 4.11) and is coherent with the results for the stenotic coronary artery. To the best of the authors' knowledge, there is no available data in the literature to validate plaque development for a stenosis of 40% radial reduction, in which a severe haemodynamic disturbance is present. The same parameters and boundary conditions were used for the case of the S-shaped geometry. Geometry can be identified as one of the main risk factors for atherosclerosis[29], as the creation of atherosclerosis-prone areas is highly dependent on the local haemodynamics. Arterial tortuosity is among the most common causes of atherosclerosis formation in the peripheral arteries[145]. For arterial single curvatures, it has been observed that there is likelihood for atherosclerosis to form in the inner curvature of the vessel[146, 147]. For a more complex tortuosity like S-shaped curvatures (formed by two subsequent single bends, as shown in Figure 4.2), different haemodynamic patterns from a single curvature would develop, as already investigated in Hoogstraten et al.[131].

The flow velocity pattern (Figure 4.14) compares well with the study of Hoogstraten et al.[131]. Analysing the behaviour of the endothelial transport properties (P_{app}), there is indication of atherosclerosis-prone areas. These areas coincide with the inner curvature of the first bend, comparing well with the findings by Wood et al.[146] and Smedby et al.[147]. The area of the inner curvature for the second bend also shows the formation of another, milder, atherosclerosis-prone area. As previously mentioned, atherosclerosis formation would become evident in this geometry after 17 years (Figure 4.16). Evidence suggests that for subjects with no atherosclerotic predisposition, fatty streak formation can be detected in adolescents and young adults[148, 149].

Another atherosclerosis model cycle was carried out, to follow the atherosclerosis development further in time. The threshold IMT growth ($\Delta h*$, Equation (3.9)) was reached for this second cycle after 6 months. Whilst the results are in good agreement with evidence from the literature with regards to the time of develop-

ment of the first formation of plaque and for the location of the plaque, the rate of growth of the plaque developed (corresponding to the time length of the second atherosclerosis model cycle) appears to be too fast. Measurements of plaque thickness from CT scan images taken at periodic time intervals have been carried out to assess the rate of growth, showing a linear behaviour[150, 151]. This rate of growth is measured on plaques that are far more developed than the initial fatty streak formation, with a calcified formation, implying that other factors such as smooth muscle cells migration might have already played a role[8]. As only the mechanisms at the base of initial atherosclerosis formation[133] have been considered in this study, the focus was on producing a proof of concept, i.e., multiscale computational framework able to simulate the initial stages of plaque formation. Other mechanisms would have to be introduced to model the development of the plaque more accurately. Improvements are discussed in the last chapter of this thesis.

4.4 Conclusion

An initial implementation of the atherosclerosis formation model was carried out on three different idealised geometries roughly corresponding to the characteristics of human arteries of interest. The effect of local haemodynamics on endothelial transport was first observed in a stenotic coronary artery in a steady state regime. Different levels of mean blood LDL were introduced in the simulation, to observe the role played by LDL as a risk factor. Location of plaque development was found to be entirely dependent on the haemodynamic pattern; whilst severity of formation was influenced by the concentration of LDL in the lumen. Further analysis was carried out for a transient case and implemented in two different types of common femoral arteries; a stenotic common femoral artery and an S-shaped common femoral artery. The mean blood concentration of LDL was kept constant in this analysis. The plaque development in the stenotic common femoral artery developed much faster than in the latter case, showing how the disturbance in the haemodynamics influences both the location of the plaque and the pace of growth. The haemodynamic behaviour in the S-shaped femoral artery was more physiological than the stenotic artery, as it was closer to conditions found

in healthy arteries. The fatty streak in this artery developed at a slower pace than in the stenotic artery, and it was in good agreement with *in vivo* observations of fatty streak formation in young adults[148, 149].

The atherosclerosis plaque development will be implemented in real patient geometries in the next chapter.

Chapter 5

Patient Specific Modeling of Atherosclerosis Formation

The aorta and peripheral arteries are among the prevalent sites for atherosclerosis formation in the human body[152]. Currently, clinical assessment of peripheral artery disease (PAD) is based on criteria such as walking distance and Ankle Brachial Pressure Index (ABPI)[153]. Further investigations that confirm the diagnosis on patients that showed positive responses to those examinations include Doppler ultrasound imaging, or more invasive imaging techniques such as Magnetic Resonance Angiography (MRA) and Computed Tomography Angiography (CT Angiography). Usually the patient has to undergo these semi-invasive procedures at regular time intervals, to monitor the disease progression.

A tool able to predict the prevalence and severity of the disease with only one initial invasive procedure required would improve the patients' quality of life, and provide a useful prognostic tool for clinicians.

In this chapter, patient-specific simulations of atherogenesis achieved via implementing the *atherosclerosis remodelling cycle* (Chapter 3) for one patient are presented. Different locations on the same patient were analysed and are described below. Studying only one patient enabled the impact on the model of other atherosclerosis factors such as genetic predisposition or inter-patient variability and life-style contrasts between patients to be neglected, and is a useful proof-of-concept for the methodology and hypotheses proposed in this thesis.

To describe the haemodynamics of the arterial flow appropriately, anatomical details and velocities used for the different arterial branches were specific for the patient. Other data, such as mean blood LDL particles and IMT were taken from gender specific population-averaged data [129, 139, 154].

The patient-specific anatomical geometry data was acquired from multi-slice computed tomography (MSCT) images obtained from University College London Hospital (UCLH). Informed consent and approval from the ethical committee were obtained by the managing clinician (Ethics number: 13/EM/0143). An approximation of the patient's healthy anatomical state was obtained through segmentation of the vessel lumen, including the detected calcified plaques. Three different Cases were analysed, each one considering a different segment of the arterial tree (Figure 5.1). Case 1 modelled atherosclerosis in a portion of the descending aorta together with the two common iliac arteries (CIAs), the external iliac arteries (EIAs) and internal iliac arteries (IIAs). Case 2 and 3 considered atherosclerosis in the right and left CFAs respectively, with their descending branches, the deep femoral arteries (DFAs) and the superficial femoral arteries (SFAs).

The methodology behind the patient-specific data processing and the simulation setup will be presented here. Results coming from the implementation of the atherosclerosis model with the real patient data showed formation of atherosclerosis in the segments of the arteries under study. Comparison between the model identified atherosclerosis-prone areas, the computed atherosclerosis formations and the calcified plaques detected from MSCT observation showed good agreement. This will be further discussed in the sections below. A brief conclusion will follow.

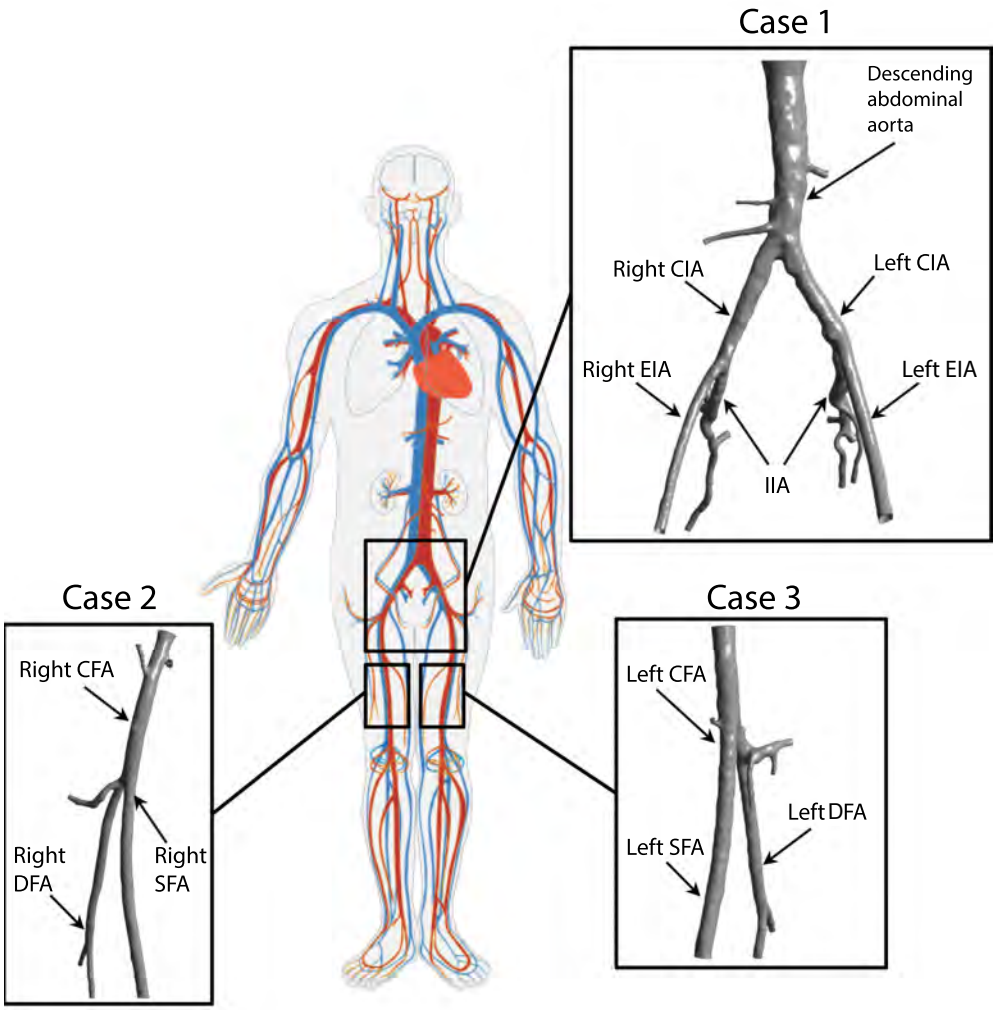

Figure 5.1: Diagram of the human circulatory system, with the three arterial segments considered in the modelled Cases highlighted. The geometries obtained from MSCT images segmentation are shown together with the names of the different branches.

5.1 Methods

5.1.1 Image acquisition and processing

A 50 year old male patient was selected for this study. The study was carried out retrospectively on data stored in the UCLH and the UCL Medical School database. Two sets of contrast enhanced MSCT angiograms were selected. The first set of contrast enhanced MSCT was performed on the abdomen and peripheral arteries with a SOMATOM Sensation Siemens 64 CT-system* (Siemens Medical Solutions, Forchheim, Germany). An initial non-contrast enhanced scan was carried out for calcium scoring and plaque detection (Figure 5.2a). The parameters of the scan were: slice thickness 5 mm for the non-contrast and 1 mm for the contrast, KVP 120, zero gantry/detector tilt, exposure time 500 ms, x-ray tube current of 305 mA for the non-contrast and 325 mA for the contrast, rotation direction CW, patient position FFS, convolution Kernel B30f for the non-contrast and B31f for the contrast. The second set of MSCT angiogram was performed 13 months later on the abdomen and peripheral arteries of the patient for follow up. The second set of contrast enhanced MSCT was performed with a SOMATOM Sensation Siemens 16 CT-system† (Siemens Medical Solutions, Forchheim, Germany). Only the non-contrast scan was analysed for calcium scoring in comparison with the first set. The parameters of the non-contrast scan were: slice thickness 5 mm, KVP 120, zero gantry/detector tilt, exposure time 500 ms, x-ray tube current of 37 mA, rotation direction CW, patient position FFS, convolution Kernel B30f. The smooth Kernel filtering used (B30f) allowed for a smaller attenuation of calcium within the tissue, simplifying plaque scoring[155]. A sample slice of the first set of MSCT showing vessel lumen resolution with application of contrasting agent (a) and without contrast (b) is shown in Figure 5.2.

The data coming from the MSCT Angiography was stored following Digital Imaging and Communication in Medicine (DICOM) standards and image processing was carried out with the help of the image processing software ScanIP‡

*http://www.healthcare.siemens.co.uk
†http://www.healthcare.siemens.co.uk
‡http://www.simpleware.com/software/scanip

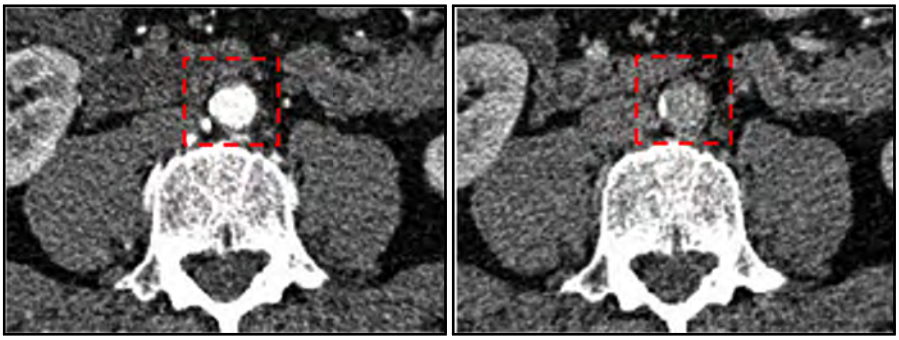

(a) (b)

Figure 5.2: MSCT angiogram transverse slice of the same section taken with (a) contrasting agent and (b) no contrasting agent. The descending aorta can be visualised (red square). The lumen is highlighted with white colour (contrasting agent) in slice (a). The lumen is still visible when no contrasting agent is present but is not differentiated from the surrounding tissue. A calcified plaque of the descending aorta can be visualised in slice (b). The plaque is shown as a white formation on the left hand side of the lumen. The calcified plaque can be visualised clearly when no contrasting agent is present (b), the plaque is not detectable in slice (a).

(Simpleware Ltd, UK). ScanIP is image processing software designed for visualising and segmenting MSCT angiogram images (and other types of medical images supported by the software) to create 3D representations of the regions of interest.

The image processing carried out in Scan IP to obtain a 3D reconstruction of the geometries used in this study is described in the following section, together with a brief introduction to MSCT angiogram imaging.

5.1.1.1 Image processing

Computed tomography is a medical imaging technique used to generate three-dimensional (3D) images of internal body structures. To generate the images the patient is exposed to a series of x-ray beams. These rays are detected by a digital x-ray detector. The x-ray source and detector are placed on the diametrically opposite sides of the device (Figure 5.3b) and the patient is placed in the centre. In conventional CT scanning, the source and the detector are rotated around the body and for each gradient of rotation an x-ray image is generated and stored. In MSCT, also known as helical (spiral) CT scanning, the x-ray beam rotates

tracing a helix of raw data. Each rotation generates data specific to an angled plane of section. The data is interpolated to give the estimated value in the axial plane[156].

As different materials absorb the x-rays differently, based on x-ray absorption the scanner can differentiate among different materials in the body such as calcium and soft tissue. This differentiation is however less clear when capturing similar materials like different tissue types, making arterial anatomy within the body difficult to detect. An intra-arterial contrast agent is used to highlight the arterial lumen and to visualise the arterial anatomy of interest.

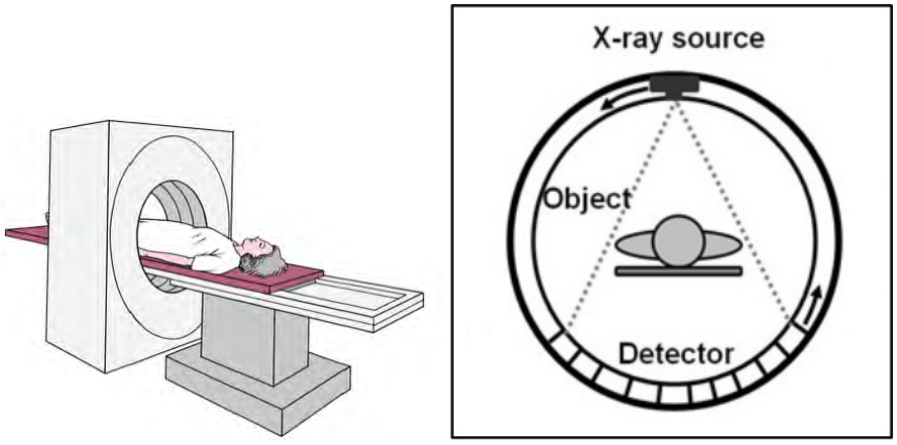

(a) (b)

Figure 5.3: (a) Computer tomography machine (Image after: `http://www.merckmanuals.com/home/special_subjects/common_imaging_tests/computed_tomography.html`). (b) The patient is in a supine position and is passed through a circular hollow section, where the x-ray source and x-ray detector are located (Image after Zhang et al.[157]).

The projected x-ray image represents a very thin transverse slice of the body scanned. As the CT image corresponds to a thickness, the pixel used to represent the image has a thickness as well, becoming a volumetric element. The elements composing a CT image are volumetric pixels, also called voxels.

A CT slice image is pictured in a grey-scale (Figure 5.2) with different colour intensity corresponding to different materials detected inside the scanned body.

5.1.1.2 Image segmentation

An initial selection of the images to be processed in ScanIP for further analysis was performed on the contrast MSCT slices at hand. The stack of images corresponding to the area of interest (from the kidneys to the femoral heads) was cropped and selected. This initial data selection was performed to ease data handling by neglecting the regions of no interest.

A threshold segmentation algorithm was used on the selected stack of images to create a mask. A mask reconstructs the 3D geometry of the object represented in the MSCT angiogram. The threshold segmentation is achieved based on the greyscale intensity. The greyscale intensity is a defining criterion that allows different objects to be identified and selected separately, based on their shade of grey. As the grey-scale intensity selected was for a pixel close to white colour, the bones and the arterial lumen (where the contrast agent is located, showed in white in the MSCT), together with the calcified portion of the arterial lumen, are selected on the MSCT images. These elements now belong to the same mask, as opposite to the rest of the elements in the MSCT scan that belong to the background data.

After the first segmentation, the MSCT image is processed further. The arterial lumen of interest is selected by applying the *flood fill* segmentation tool (ScanIP, Simpleware Ltd., UK) on a pixel belonging to the arterial lumen. This is a region growing algorithm* that selects the areas to fill on a similarity and connectivity based criterion. The flood fill would select all the pixels connected to the selected one (seed point) with the same grey-scale intensity. A mask with one continuous structure of the arterial lumen is created (Figure 5.4). Morphological filters and cavity fill filters are applied to the new mask to delete object mistakenly captured by the flood fill segmentation, and to fill up the internal gaps that might be present in the arterial lumen mask.

To reduce image noise and remove artefacts from the handled data, a recursive Gaussian smoothing filter[158] is applied to the mask. The result of these mask manipulations is a smooth uniform and homogeneous representation of the 3D geometry of the arterial tree segment of interest(Figure 5.5a).

*Region growing algorithm is a region-based segmentation method. The region to be segmented is defined through the selection of an initial "seed point" within it.

To create the geometry of Case 1 (Figure 5.1); the descending aorta with the two CIAs, EIAs and IIAs, a further geometry manipulation was needed. The descending aorta was affected by atherosclerosis formation proximal to the right CIA, preventing the contrast agent from highlighting this segment (Figure 5.4). In order to re-create the arterial geometry before the occurrence of any disease, and as a first approximation for this proof-of-concept, this tract of the iliac artery was reconstructed manually. Reconstruction of the right common iliac was performed using the *paint* tool (ScanIP, Simpleware Ltd., UK) in ScanIP. This tool allows individual voxel handling on each slice of the MSCT scan. Manual voxel selection was done on each MSCT slice following the boundary of what was identified to be the right CIA lumen. Figure 5.4a shows a CT angiogram transverse slice of the right and left CIAs (Figure 5.1). The lumen of the left CIA is shown in golden colour. This is the mask created with the flood fill threshold segmentation. The red mask in the MSCT image is the lumen of the right CIA. This was the lumen reconstructed using the paint tool. The entire anatomy of the patient descending aorta with the two CIAs, EIAs and IIAs was reconstructed (Figure 5.4b).

The three geometries obtained from the processed MSCT images are reconstructions of the arterial lumen anatomies before the development of the atherosclerosis formation. An approximation of the geometry of the patent lumen is attained by including the portion of the lumen with the calcified plaque in the geometry reconstruction. It is acknowledged that there are limitations to this approach and these will be discussed in this chapter.

The geometries are exported from ScanIP and meshed in Ansys ICEM CFD software* (Ansys, Inc., Canonsburg, PA) for 3D flow simulation.

5.1.1.3 Generation of a Computational Mesh for a Real Patient Geometry

Ansys ICEM CFD is a mesh generator and mesh optimisation tool that allows the acquisition and processing of very complex geometries. The geometries generated in ScanIP were edited in Ansys ICEM CFD to optimise mesh creation for the CFD analysis.

*`http://www.ansys.com/Products/Other+Products/ANSYS+ICEM+CFD`

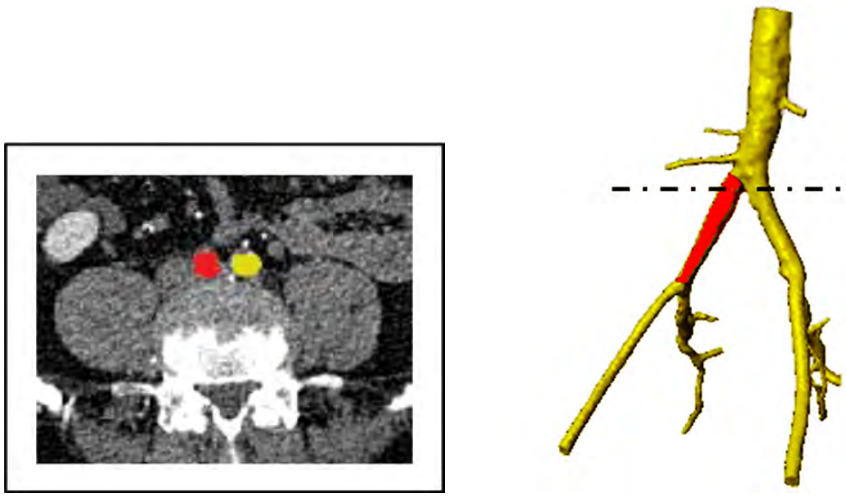

(a) (b)

Figure 5.4: (a) MSCT angiogram transverse slice showing the two CIA lumen. Coloured in golden colour is the mask given by the region growing threshold. The red lumen was manually selected as no contrast agent was present in this portion of the artery. (b) The 3D geometry of the mask is shown. The red portion is the right CIA manually added. The dashed line shows the position of the MSCT slice.

The geometry had to be modified to apply flow boundary conditions. The edges representing the final tract of the different branches did not originally have sharp edges suitable for imposing flow boundary conditions. Using Ansys ICEM CFD cutting tools, surfaces normal to the flow were generated at the inlet and outlets of the geometry.

In the atherosclerosis model developed, the endothelial transport changes to the local WSS is artery-specific, as explained in Chapter 2, Section 2.1.2. The endothelial reaction to the local WSS was tuned according to the artery haemodynamics, given its lumen diameter and mean blood velocity. The different arteries in the anatomical section considered were selected allowing for the application of artery-specific transport properties. Cutting tools were used to separate each branch from the rest of the geometry (Figure 5.5b). Geometry selection of the individual arterial branches allows an artery-specific approach.

As the inlet boundary profile did not present a regular circular surface, an

artificial inlet was created to impose parabolic flow velocity at its boundary. A circular surface normal to the inlet was created upstream from the real inlet. The *loft surface over several curves* (ScanIP, Simpleware Ltd., UK) tool was used to create a surface linking the circular surface and the real inlet. This inlet pipe created would gently modify its cross section from the perfectly circular profile of the circular surface to the irregular profile of the real inlet (Figure 5.5c). The circular surface was used as the new inlet of the arterial geometry. The same approach of creating a cylindrical prolongation to the arterial inlet has been used in Antiga, Selimovic et al.[159, 160].

An initial volumetric robust Octree* mesh of the geometry was created. Prism layers† were added at the wall boundary for a refined mesh structure. A tetrahedral mesh was then generated with the Delaunay‡ method. This type of algorithm requires a parent mesh to generate a new mesh. The new mesh retains the same characteristics imposed to the parent mesh. The Delaunay is a robust and fast method to generate high quality meshes.

The Delaunay mesh was processed for quality checking and smoothing.

5.1.1.4 Plaque scoring and segmentation

Plaque scoring was performed on non-contrast MSCT slices in conjunction with Mr O. Agu, consultant general vascular and endovascular surgeon at UCL Hospitals. The first set of MSCT angiogram showed relatively patent common femoral arteries with atherosclerosis formation in the descending aorta and left and right CIAs. The records show that the second set of MSCT angiograms were performed 13 months later on the abdomen and peripheral arteries of the patient for follow up. There was no evidence of newly formed calcified lesions. The calcified plaques detected were segmented manually (Figure 5.6a) and highlighted with a mask of contrasting colour(Figure 5.6b). The 3D geometry of the lumen appears then

*The Octree mesh method is a meshing algorithm allowing for faster computation. The mesh is not uniformly refined, larger elements are maintained, and refinement is performed only where necessary[161]

†Prism layers are added at the boundaries to improve mesh quality near the walls.

‡The Delaunay method is a mesh generating algorithm needing an existing surface mesh. Based on Delaunay tetra mapping, this algorithm increases the mesh refinement maintaining a high speed of computation[161]

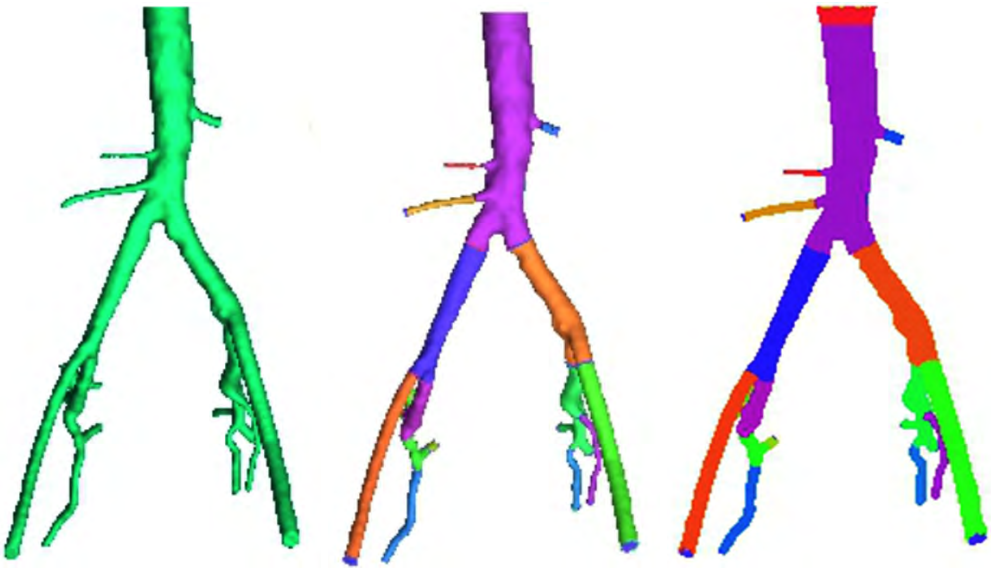

(a) (b) (c)

Figure 5.5: Geometry of the descending aorta with the two CIAs, EIAs and IIAs showing the meshing process in Ansys ICEM CFD (Ansys, Inc., Canonsburg, PA). (a) The geometry coming from CT segmentation is cut at the extremities to create inlet/outlet boundaries. (b) The different arterial branching are then selected. (c) An artificial inlet of circular cross section is added upstream of the geometry inlet, and a volumetric mesh of the geometry is created.

with plaques of contrasting colour, allowing for better visualisation of the disease (Figure 5.6c). The 3D geometry of the artery (with the highlighted plaques) for each one of the arterial segments considered will be shown in the results section of this Chapter.

5.1.1.5 Velocity data acquisition and processing

The velocities shown in the patient's records were taken with Doppler echocardiography at the time of the second MSCT angiogram and these were used for the simulations as there are no velocity recordings for the patient's first check-up. Being a retrospective study, only data already available were used. To obtain an approximation of the mean velocities values, the velocity profile images for the arteries of interest were selected from the Doppler echocardiography report.

Extraction of data from the images was carried out using Image J*, an open source tool for the analysis of scientific images, and MATLAB. The velocity profile was extracted from the Doppler echocardiography report using the Image J plot analysis tool *plot profile*. The coordinates of the different points of the velocity function were extracted; conversion was applied to express the grey-scale intensity in terms of velocity value and the distance (in pixels) in terms of the time period. The extracted velocity curve was then processed in MATLAB. The mean velocity was obtained by integrating the velocity curve over its time period. Figure 5.7 shows the process of the velocity profile acquisition performed from the Doppler echocardiography images.

Having introduced the general methodology employed for real patient data acquisition and processing, the patient-specific atherosclerosis modelling cases developed in this study (Figure 5.1) will be presented in more detail.

For the three patient-specific atherosclerosis simulations (Cases 1-3, Figure 5.1), the boundary conditions and implementation settings for the CFD arterial lumen model, the transport model and the biochemical model are the same as the ones used for the transient simulation of the idealised common femoral artery (Chapter 4, Section 4.1.2).

*http://rsb.info.nih.gov/ij/

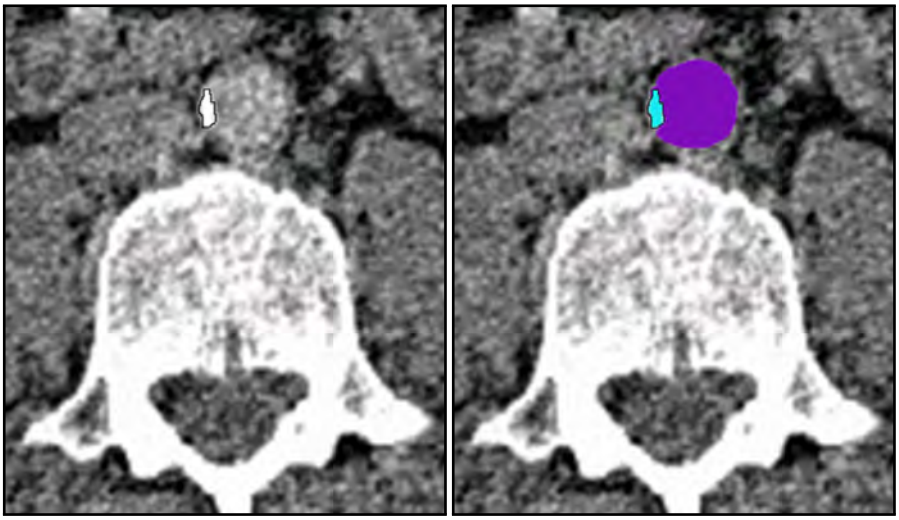

(a) (b)

(c)

Figure 5.6: Plaque scoring. Detail of a MSCT slice of the descending aorta (already shown in Figure 5.2). (a) The calcified plaque contour is highlighted with a black line. (b) The plaque is painted with a contrasting colour (light blue) from the arterial lumen (purple). (c) Geometry of the descending aorta with the two CIAs, EIAs and IIAs showing segmented plaques in contrasting colour.

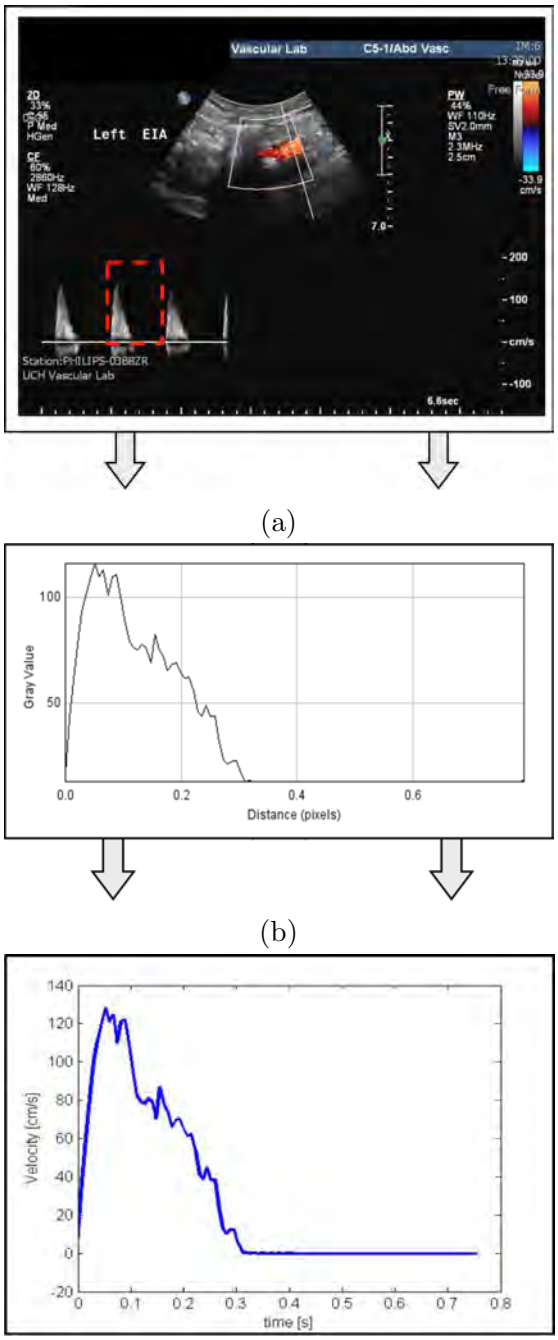

Figure 5.7: Velocity profile acquisition from Doppler echocardiography images. The velocity profile, shown in the red box (a) was extracted with ImageJ (b) and then processed in Matlab (c).

5.1.2 Case 1: Model of the Descending Abdominal Aorta with the two common iliac arteries (CIAs), the external iliac arteries (EIAs) and internal iliac arteries (IIAs)

5.1.2.1 Geometry specifications and computational implementation

The geometry of the descending aorta with the two common iliac arteries, the external iliac and internal iliac arteries created from the segmentation of the first set of MSCT scan is shown in Figure 5.8.

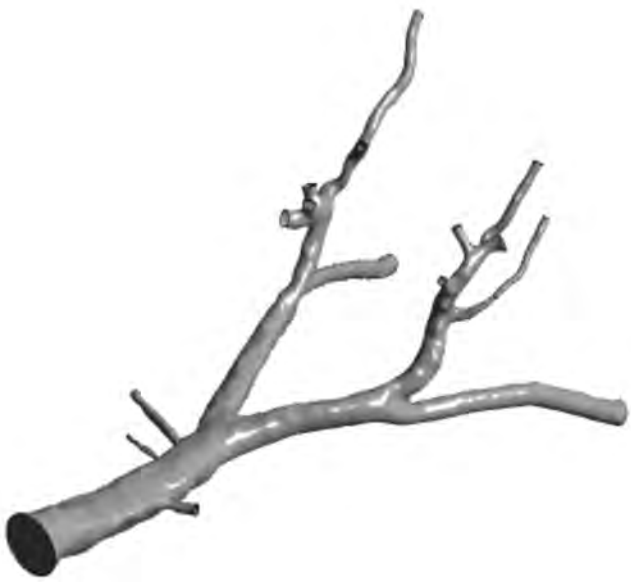

Figure 5.8: Geometry of the descending aorta with the two common iliac arteries, the external iliac and internal iliac arteries.

The geometry encloses the patent lumen and the calcified plaques. The right common iliac artery has been artificially re-created to simulate a virtually disease-free vessel. The area of the real inlet of the descending aorta is $A_0 = 2.96 \times 10^{-4}$ m^2 and the area of the added inlet pipe is $A_{inlet} = 4.522 \times 10^{-4}$ m^2. A parabolic velocity profile (Equation (4.1)) was imposed at the inlet of the aorta. The mean velocity for the descending aorta extracted from velocity recording taken with Doppler echocardiography at the time of the second MSCT angiogram was used. The mean velocity for the descending aorta was $U_0 = 24.574$ cm s^{-1}. The mean

velocity imposed at the inlet of the added pipe (U) was calculated according to the radial dimension of the added inlet pipe using flow conservation law:

$$U = U_0 \frac{A_0}{A_{inlet}} \tag{5.1}$$

Three segments of the geometry were considered for atherosclerosis modelling, i.e., the descending aorta and the left and the right common iliac arteries. From MSCT plaque scoring these segments emerged to be the ones with atherosclerosis formations(Figure 5.9). Simulations were carried out separately on each of the different segments. To use an artery-specific approach, the Poiseuille wall shear stress was calculated for each segment (Equation (2.4)). The left common iliac and right common iliac inlet cross sectional areas were measured to be $A_{0,leftCIA} = 5.47 \times 10^{-5}$ m^2 and $A_{0,rightCIA} = 9.95 \times 10^{-5}$ m^2. The mean flow velocities for these two branches could not be retrieved from the Doppler echocardiography data available, as the lumen occlusion in the right common iliac branch disturbed the haemodynamics, making the velocity recordings not fit for purpose. The left common iliac and right common iliac mean flow velocities were approximated using Ansys CfX Post v.14 as $U_{0,leftCIA} = 0.267$ m s^{-1} and $U_{0,rightCIA} = 0.354$ m s^{-1}. The inlet information such as cross sectional area and mean velocity allowed for the Poiseuille WSS for each of the considered arterial segments to be calculated. The resulting Poiseuille WSS was $\tau_0 = 0.3553$ Pa for the descending aorta, $\tau_0 = 0.683$ Pa for the left common iliac artery and $\tau_0 = 0.88$ Pa for the right common iliac artery. This Poiseuille WSS was used as τ_0 in Equation (2.5) allowing for the endothelial response to local WSS to be artery-specific (Chapter 2, Section 2.1.2.1).

5.1.2.2 Fluid domain discretisation

The Ansys ICEM CFD mesh for Case 1 was a Delaunay unstructured mesh with prismatic layers at the wall boundary for increased resolution. A grid independence study showed that a mesh with 6,972,969 elements was suitable to accurately describe the fluid dynamics in the portion of the artery considered. The difference in the computed WSS values between meshes was calculated as a

relative error (e):

$$e = \left| \frac{\boldsymbol{WSS}_{finer}(z) - \boldsymbol{WSS}_{coarser}(z)}{\boldsymbol{WSS}_{finer}(z)} \right| \tag{5.2}$$

where $\boldsymbol{WSS}$ is the local value of WSS , z is the spatial location and $finer$ and $coarser$ is the coarsness of the meshes compared. Between the finest considered grid (10 million elements) and the chosen grid the calculated maximum relative error was 2.4%. Details of the grid independence study carried out using Equation (5.2) are shown in Appendix C.

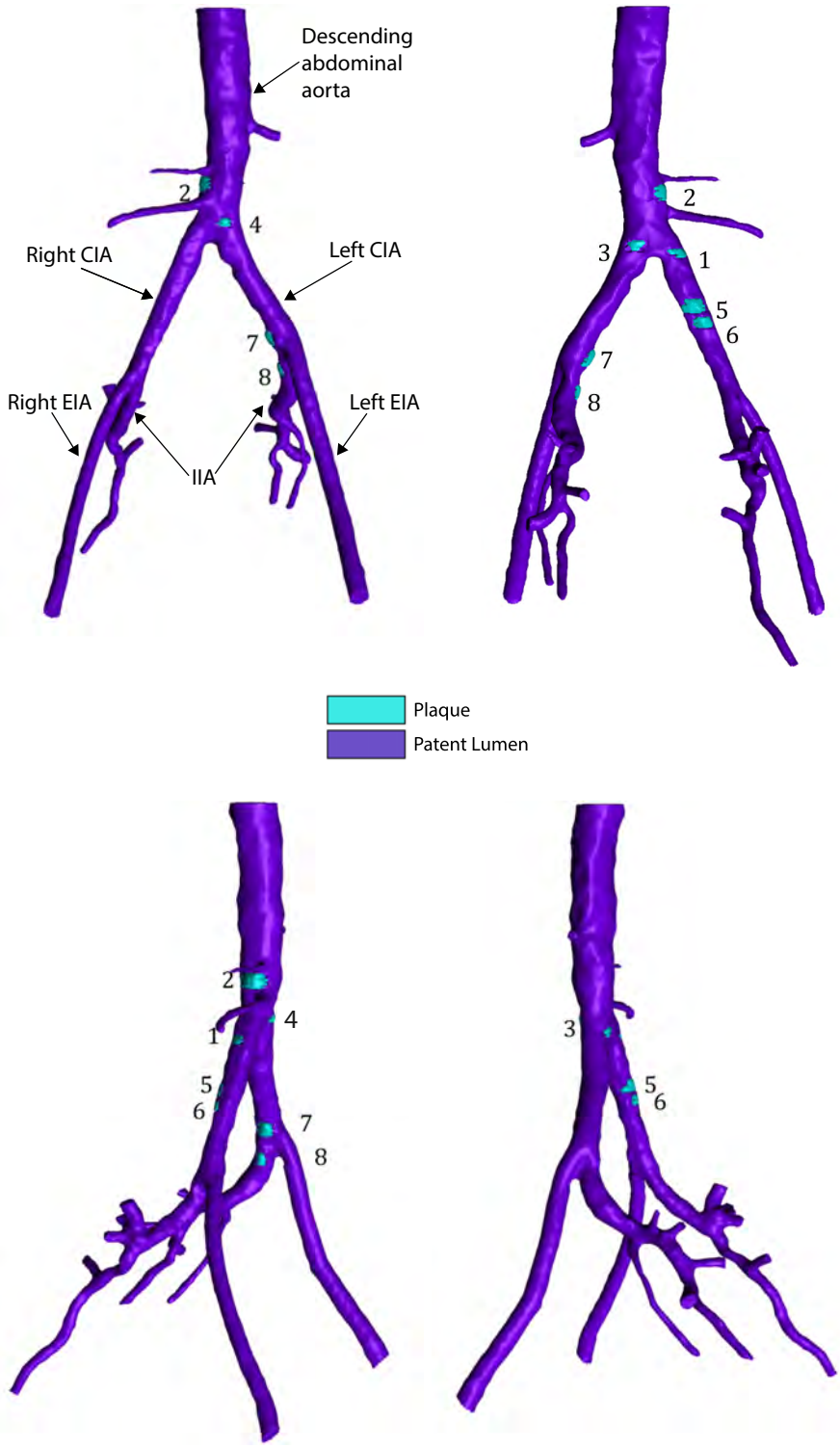

Figure 5.9: MSCT segmented geometry of the Model of the descending aorta with the two common iliac arteries, the external iliac and internal iliac arteries. The atherosclerotic plaques are segmented in contrasting colour (light blue) from the patent lumen (purple). The detected plaques are numbered.

5.1.3 Case 2: Model of the Right Common Femoral Artery (CFA), with the Deep Femoral Artery (DFA) and the Superficial Femoral Artery (SFA)

5.1.3.1 Geometry specifications and computational implementation

The segmented patent lumen geometry of the right common femoral artery, with the deep femoral artery and the superficial femoral artery is shown in Figure 5.10.

Figure 5.10: Geometry of the right common femoral artery, with the deep femoral artery and the superficial femoral artery.

The area of the CFA inlet was $A_{0,rightCFA} = 3.6 \times 10^{-5}$ m^2 and the area of the inlet added pipe was $A_{inlet} = 5.67 \times 10^{-5}$ m^2. Mean velocity for the right CFA as extracted from Doppler echocardiography velocity recordings was $U_0 = 0.3516$ m s^{-1}. Flow continuity was applied to calculate the mean velocity at the added inlet pipe.

MSCT plaque scoring was carried out on the right CFA, with the DFA and the SFA. As shown in Figure 5.11, a plaque formation was detected at the initial segment of the deep femoral artery. The reduced dimensions of the vessel considered and the low level of calcification in the arterial wall among other factors, made the plaque scoring results uncertain. For comparison with *in vivo* observations, a simulation of atherosclerosis formation was performed in the deep femoral artery.

For the artery-specific endothelial transport model, the mean flow velocity $U_{0,rightDFA} = 0.104$ m s^{-1} and the cross sectional area $A_{0,rightDFA} = 1.27 \times 10^{-5}$ m^2 for the deep femoral artery were extracted from CfX Post v.14. The calculated Poiseuille WSS was $\tau_0 = 0.724$ Pa.

5.1.3.2 Fluid domain discretisation

The Ansys ICEM CFD mesh for Case 2 was a Delaunay unstructured mesh with prismatic layers at the wall boundary for increased resolution. The mesh chosen for this study was of 1,215,885 elements, as there were negligible differences in the haemodynamics solution when compared with a finer grid. There was a maximum error of 3% between the computed WSS in the finest considered grid (1.9 million elements) and the chosen grid calculated using Equation (5.2). The grid independence study is shown in Appendix C.

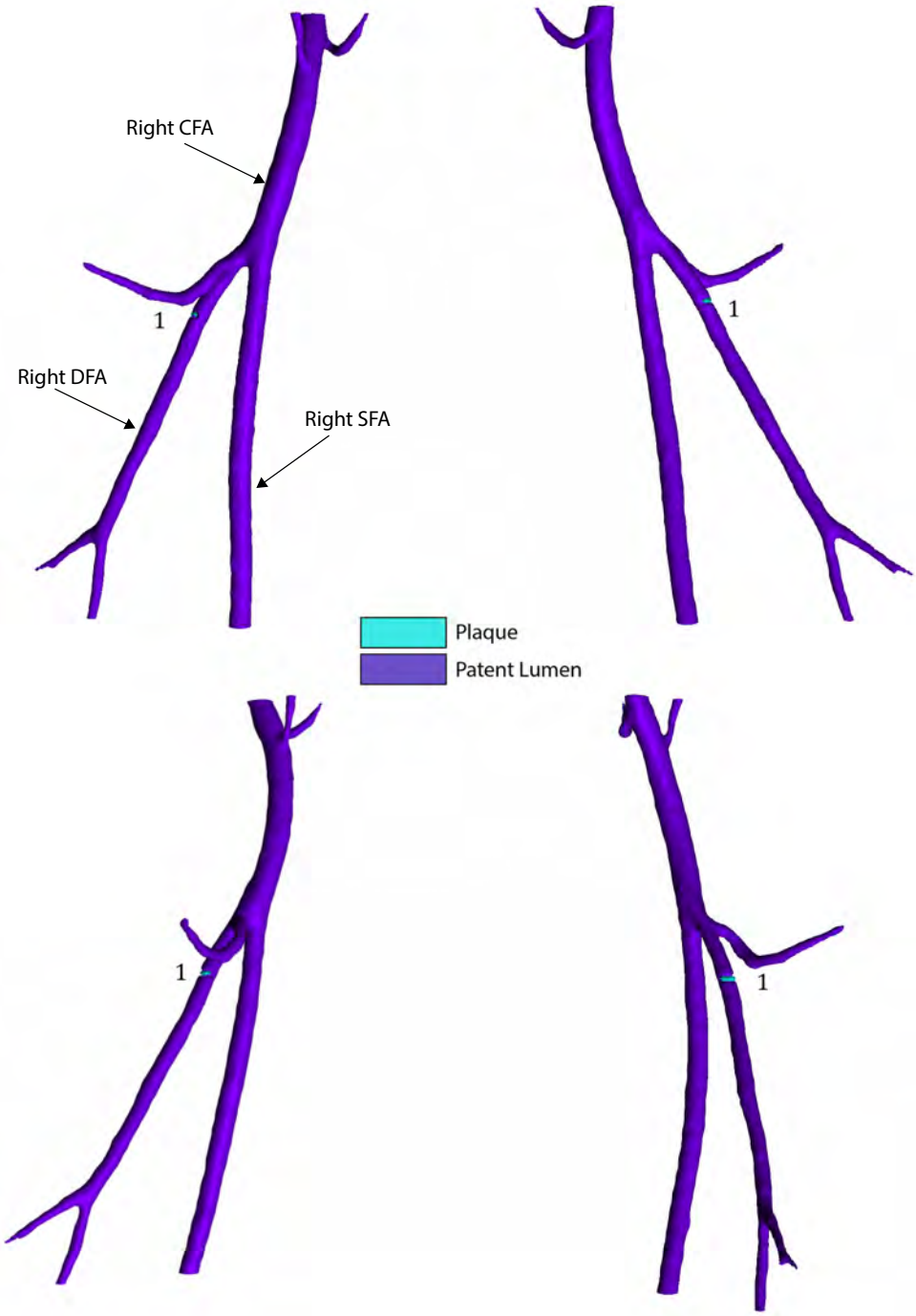

Figure 5.11: MSCT segmented geometry of the model of the right common femoral artery, with the deep femoral artery and the superficial femoral artery. The atherosclerotic plaque is segmented in contrasting colour (light blue) from the patent lumen (purple). The detected plaque is numbered.

5.1.4 Case 3: Model of the Left Common Femoral Artery (CFA), with the Deep Femoral Artery (DFA) and the Superficial Femoral Artery (SFA)

5.1.4.1 Geometry specifications and computational implementation

The geometry of the disease-free segmented lumen of the left common femoral artery, with the deep femoral artery and the superficial femoral artery is shown in Figure 5.12.

Figure 5.12: Geometry of the left common femoral artery, with the deep femoral artery and the superficial femoral artery.

The inlet area of the left CFA was $A_{0,leftCFA} = 6.09 \times 10^{-5}$ m^2, with a surface area of the inlet added pipe of $A_{inlet} = 7.84 \times 10^{-5}$ m^2.

The mean velocity for the left CFA as extracted from Doppler echocardiography recordings was $U_0 = 0.207$ m s^{-1}. Flow continuity (Equation (5.1)) was applied to calculate the mean velocity at the inlet of the added pipe. The endothelial response to the local WSS values was tuned with the calculated Poiseuille law WSS for the left CFA, given the inlet radial dimension and the mean flow velocity. The Poiseuille WSS was calculated to be $\tau_0 = 0.657$ Pa.

MSCT plaque scoring was carried out on the arterial segment of the left CFA with the DFA and the SFA as shown in Figure 5.13. The lesions identified were in the left CFA. As for Case 2, given the small extent of calcification detectable in the MSCT images, there is uncertainty in the plaques detected and segmented. Atherosclerosis formation was analysed in the model of the left CFA.

5.1.4.2 Fluid domain discretisation

The fluid domain of the left CFA, with the DFA and the SFA was meshed with Ansys ICEM CFD. The mesh created was a 1,111,901 elements Delaunay unstructured mesh with prismatic layer at the wall boundary for increased resolution. The difference (Equation (5.2)) in the calculated WSS between the finest considered grid (1.9 million elements) and the considered grid was 3.1%. The grid independence study for this geometry is showed in Appendix C.

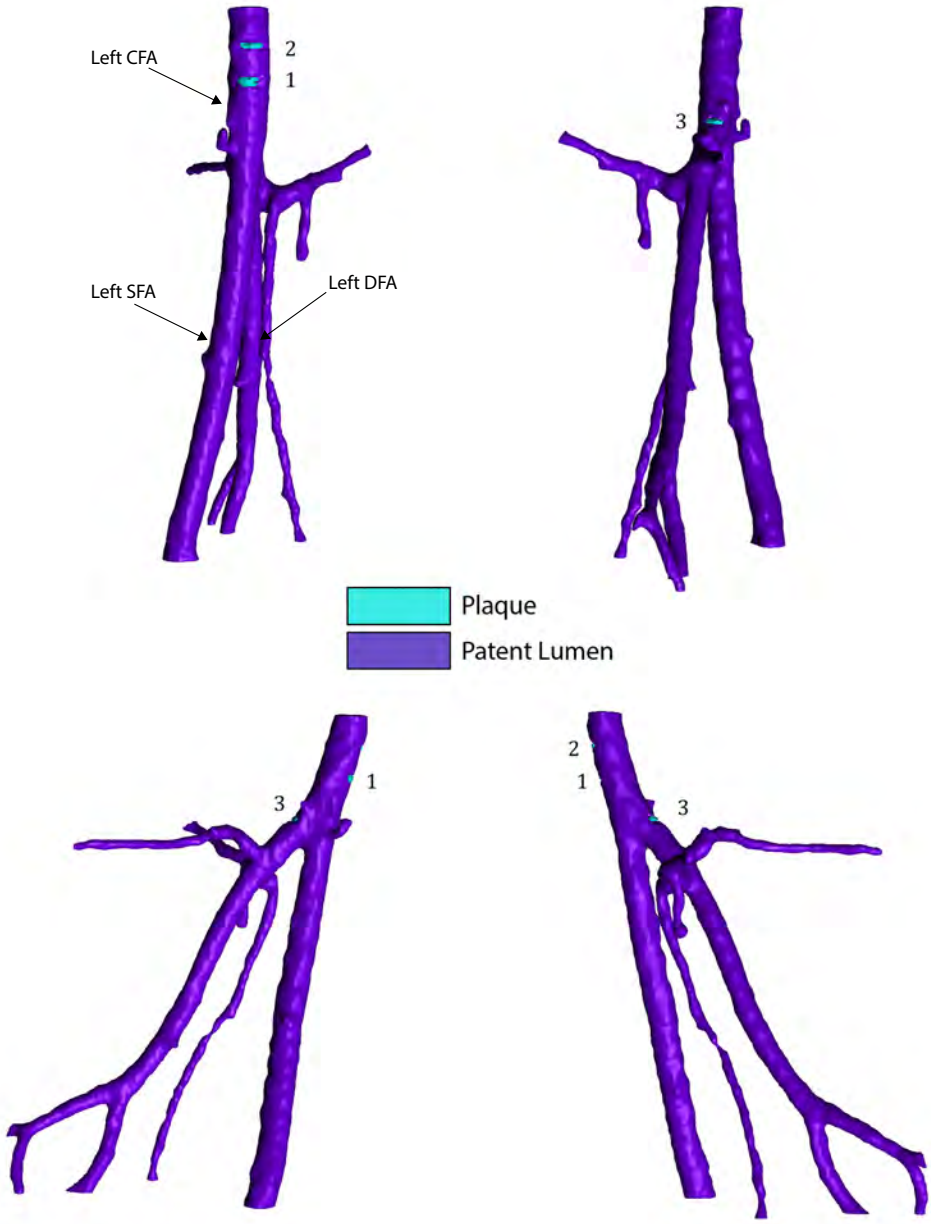

Figure 5.13: Geometry of the model of the left common femoral artery, with the deep femoral artery and the superficial femoral artery. The atherosclerotic plaques are segmented in contrasting colour (light blue) from the patent lumen (purple). The detected plaques are numbered.

5.2 Results

5.2.1 Case 1: Simulation Results

As discussed in Chapter 2, WSS governs the endothelial transport property of macromolecules in this model. The WSS pattern for Case 1 is shown in Figure 5.14. Whilst areas of high WSS are evident, areas of interest for atherosclerosis formation are not highlighted. A rescaled plot of the WSS in the descending aorta, aiming to better differentiate the areas of low WSS is shown in Figure 5.15. The maximum limit of this re-scaled plot is set as the Poiseuille WSS value for a pipe with the same radial dimensions and flow inlet velocity of the descending aorta (Table 5.1). The areas of WSS equal or above the Poiseuille value are not differentiated as these are the areas with normal endothelial behaviour. On the contrary, areas below the Poiseuille WSS value are visible and local minima of WSS are highlighted, showing potential pro-atherogenic areas. To highlight the artery-specific pro-atherogenic areas, a re-scaled WSS contour was plot for each artery separately (Figures 5.15 to 5.17). For each artery the Poiseuille WSS value (Table 5.1) was set as the maximum value in the corresponding re-scaled contour plot.

The most severe atherosclerosis formation in the descending aorta would reach the threshold level of $\Delta h*$ (equal to 1% of the considered artery radius) after 16 years and 8 months, concluding the first *atherosclerosis remodelling cycle* for the descending aorta. Careful consideration must be given to the meaning of the time indication of atherosclerosis formation in these simulations. The anatomical features were extracted from an adult patient and it was assumed that the arterial tree of the patient would reach full anatomical development in 18 years, without presenting any atherosclerosis formation, and with arterial lumen and an arterial wall fully patent. Following this, the model estimates the patient will have early atherosclerosis lesion formation in around 34 years and 8 months. The most severe atherosclerosis formation for the left common iliac and the right common iliac would reach the respective threshold value $\Delta h*$ after 16 years and 11 months and 16 years and 10 months, also corresponding to 34 years and 11 months and 34 years and 10 months respectively. The plaque formation in the

Table 5.1: Case 1 summary. The results of MSCT plaque scoring segmentation for each modelled artery, together with the mean blood velocity (U_0) and the calculated Poiseuille WSS (τ_0) are given.

Case 1	*In vivo* detected plaques	U_0 [ms^{-1}]	τ_0 [Pa]
Descending Abdominal Aorta	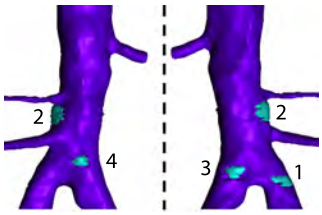	0.24574	0.3553
Left CIA		0.267	0.683
Right CIA		0.354	0.88

descending aorta, the left common iliac artery and the right common iliac artery can be visualised in Figures 5.18 to 5.20. Here the mesh displacement contour plots are shown, indicating areas where the mesh nodes were displaced to account for plaque formation. Plaque development corresponds to areas of local haemodynamic perturbations. Figure 5.21 shows the flow velocity cross sectional contour plots before the atherosclerosis formation at the location where the plaque will develop. The contour plots are numbered and are shown inside the geometry and zoomed-in on the side of the geometry. The plaque formations (Figures 5.18 to 5.20) correspond to the areas of local flow velocity decrease. Comparison between modelled atherosclerotic formations (Figures 5.18 to 5.20) and the plaques observed *in vivo* (Figure 5.9) shows partial agreement. Some of the plaques developed in the model were not detected from MSCT plaque scoring. Furthermore some of the plaques shown in the MSCT plaque scoring were not developed

during the simulation. However, as shown in the re-scaled WSS contour plots for the three different arteries (Figures 5.15 to 5.17), all the plaques found in the MSCT plaque scoring would correspond to areas that were highlighted as atherosclerosis-prone.

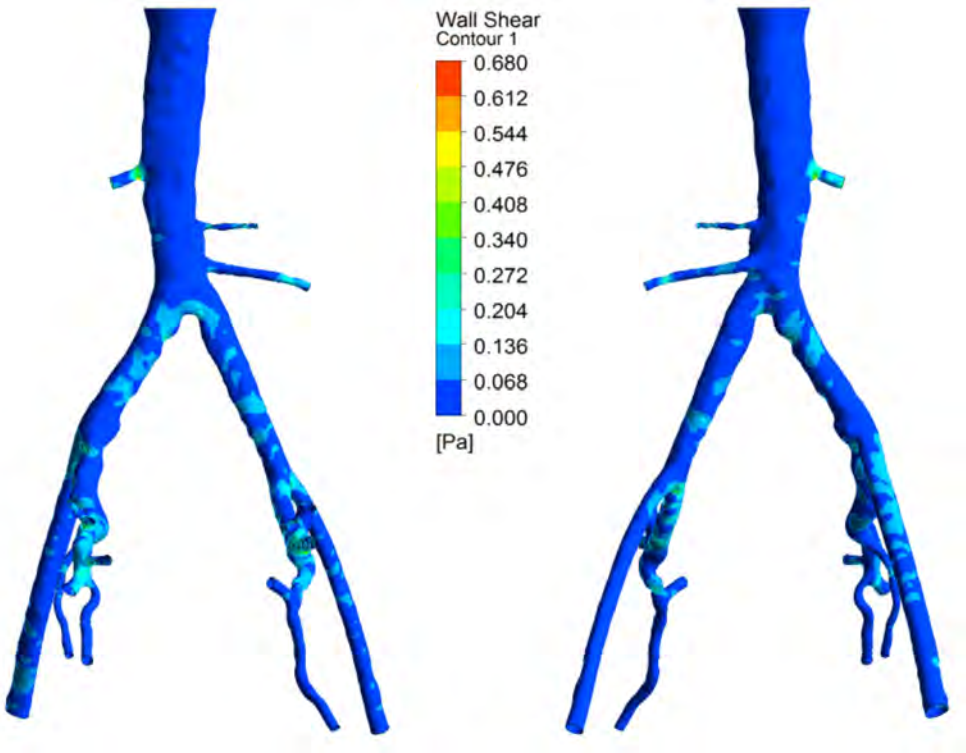

Figure 5.14: Model of the descending aorta with the two common iliac arteries, the external iliac and internal iliac arteries global WSS contour plot.

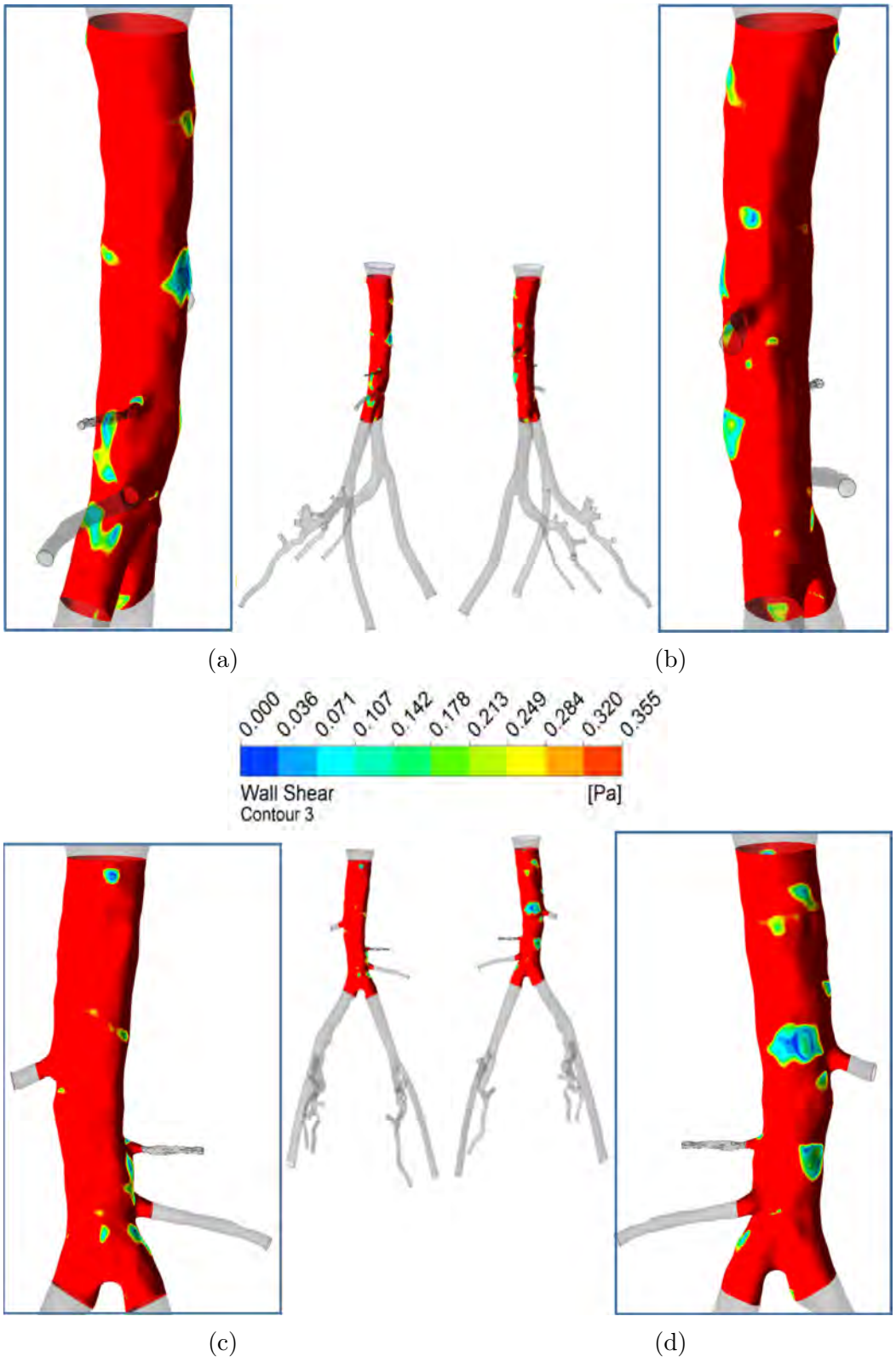

Figure 5.15: Re-scaled WSS contour plot of the descending aorta. The plot maximum WSS detectable is the Poiseuille WSS for the descending aorta $\tau_0 = 0.3554$ Pa.

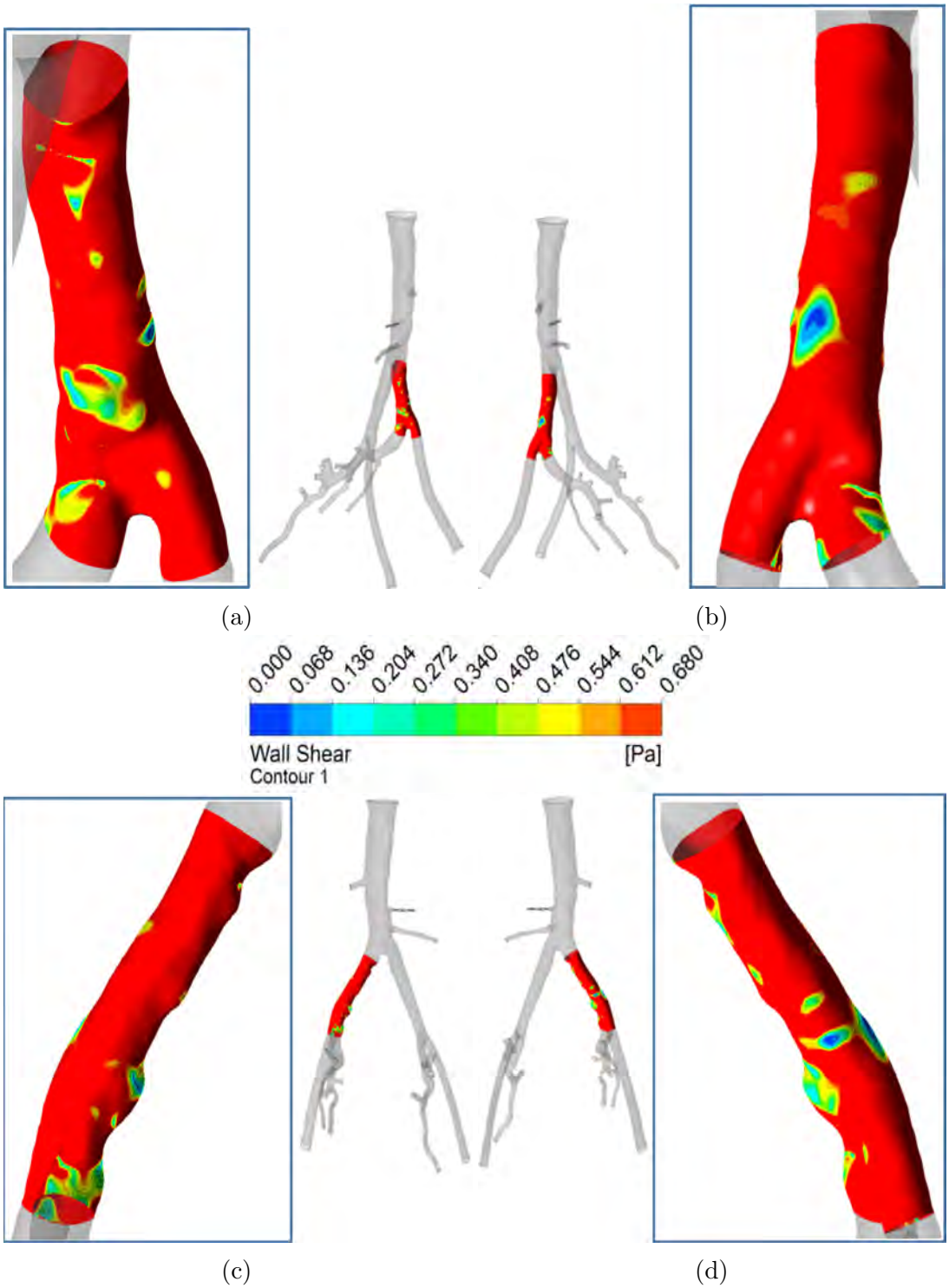

Figure 5.16: Re-scaled WSS contour plot of the left common iliac artery. The plot maximum WSS detectable is the Poiseuille WSS for the right common iliac artery $\tau_0 = 0.68$ Pa.

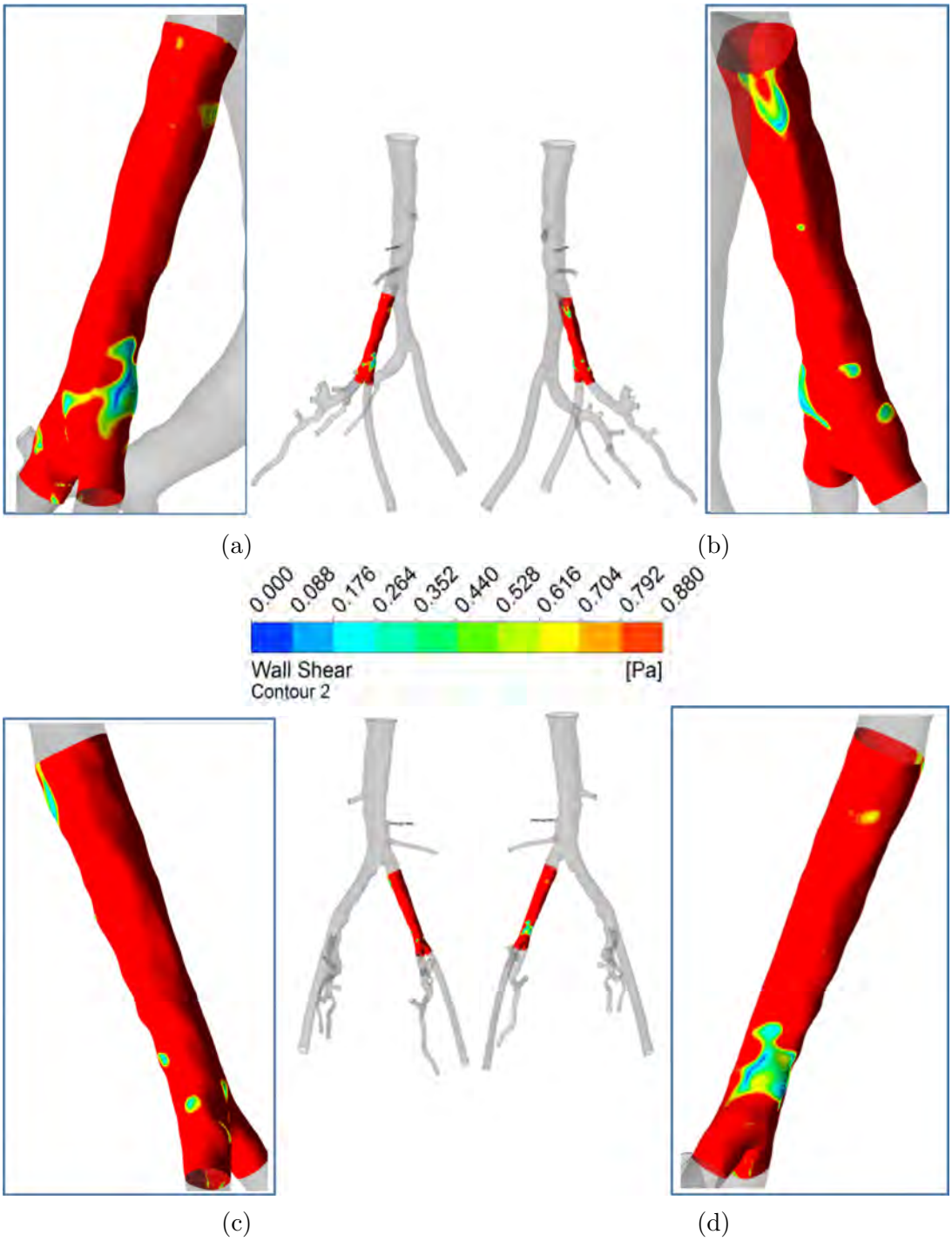

Figure 5.17: Re-scaled WSS contour plot of the right common iliac artery. The plot maximum WSS detectable is the Poiseuille WSS for the left common iliac artery $\tau_0 = 0.88$ Pa.

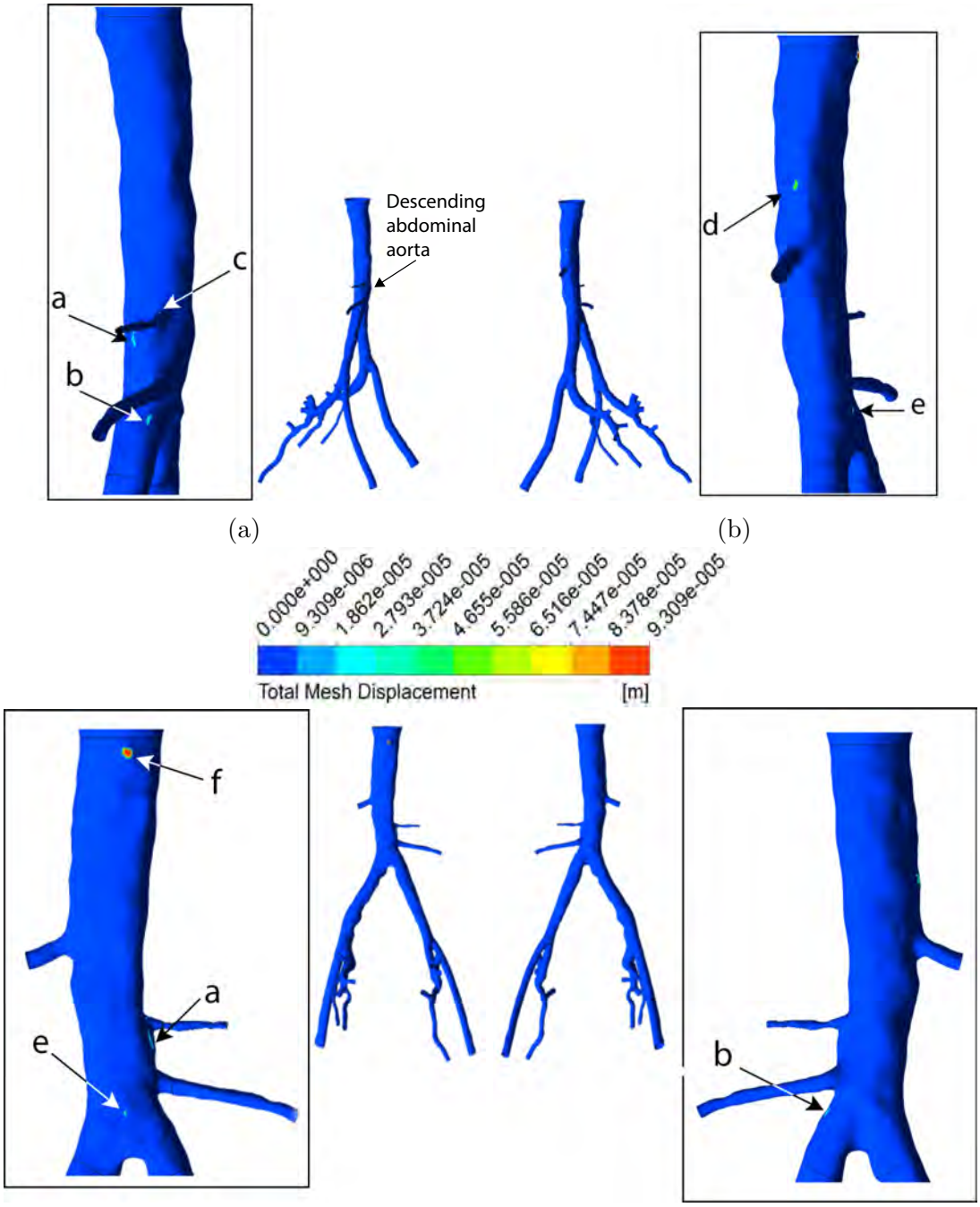

Figure 5.18: Mesh deformation contour plot for the descending aorta with the two common iliac arteries, the external iliac and internal iliac arteries. Plaques occurrence was modelled solely in the descending aorta. Areas of mesh displacement indicate plaque formation.

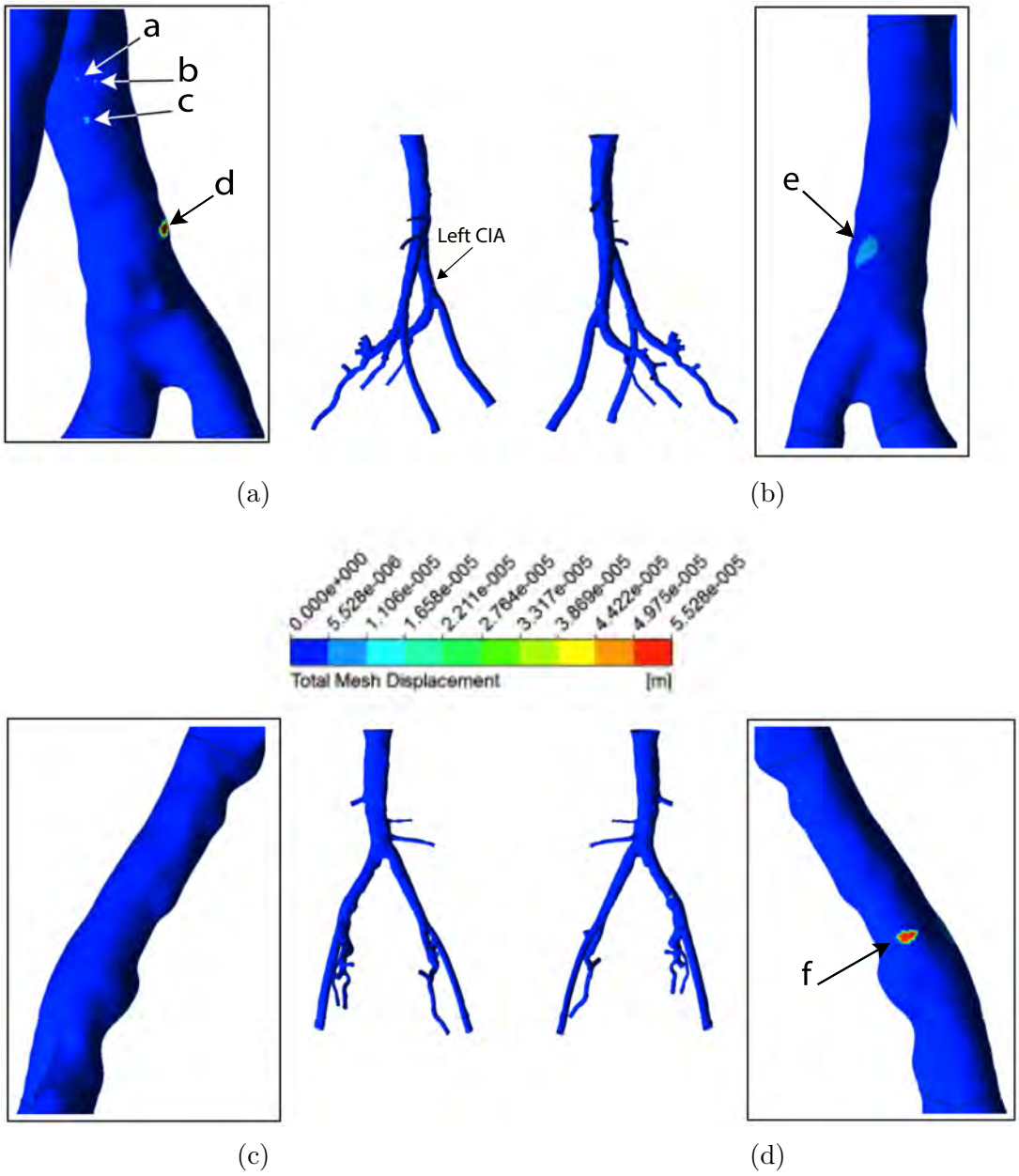

Figure 5.19: Mesh deformation contour plot for the descending aorta with the two common iliac arteries, the external iliac and internal iliac arteries. Plaques occurrence was modelled solely in the left common iliac artery. Areas of mesh displacement indicate plaque formation.

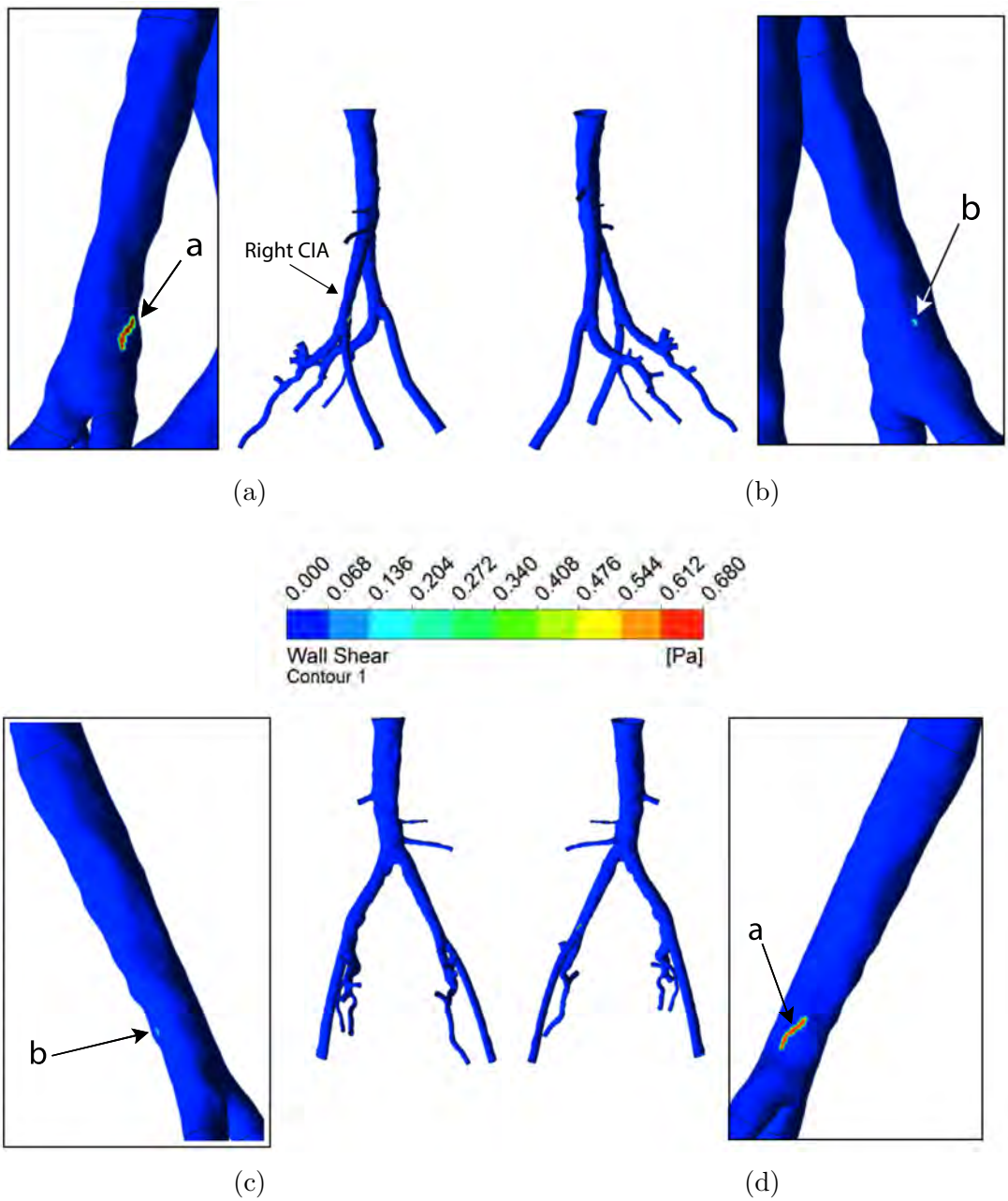

Figure 5.20: Mesh deformation contour plot for the descending aorta with the two common iliac arteries, the external iliac and internal iliac arteries. Plaques occurrence was modelled solely in the right common iliac artery. Areas of mesh displacement indicate plaque formation.

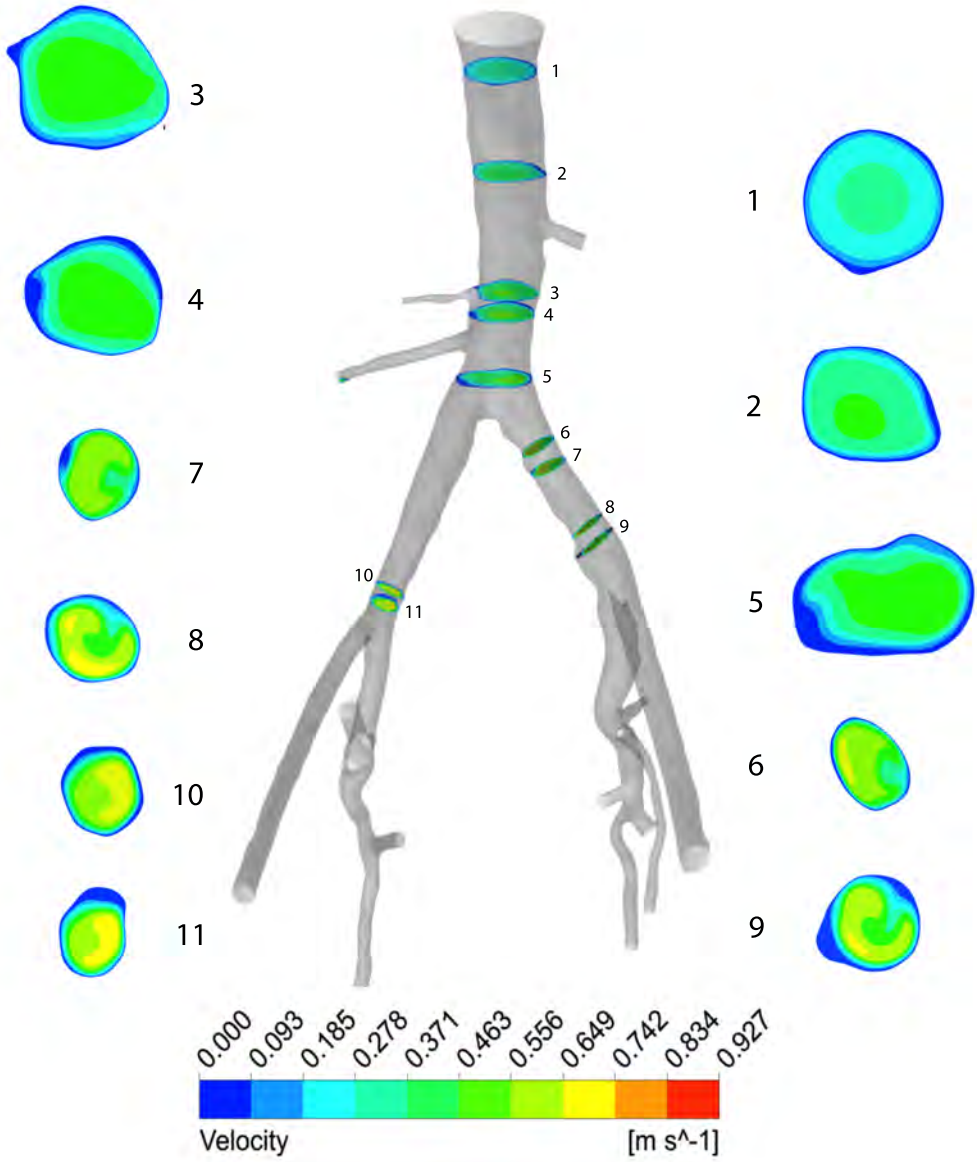

Figure 5.21: Surface velocity contour plots at the location of plaque development for the descending aorta with the two common iliac arteries, the external iliac and internal iliac arteries. The contour plots are shown in the geometry, and their enlarged cross-section view is showed separately. The numbers link the contour plots in the geometry with the separate cross section view. The picture is not shown not to scale.

5.2.2 Case 2: Simulation Results

The velocity streamlines for blood flow in the right CFA and its branching arteries are shown in Figure 5.22. There is a large difference in the volumetric blood flow and local flow velocity between the DFA and SFA. This difference in the haemodynamics between the branches arteries underlines the need for an artery-specific endothelial response to local WSS. A globally defined endothelial response to local WSS would lead to consider the entirety of the DFA as atherosclerosis-prone, given the lower flow velocity detected here. The global WSS contour plot is shown in Figure 5.23. The re-scaled WSS plot for the deep femoral artery, using the Poiseuille WSS value (Equation (2.4) and table 5.2) for a straight pipe with the same inlet velocity and radial dimensions of the artery is shown in Figure 5.23. The identified plaque in the MSCT plaque scoring (Figure 5.11 and table 5.2) is identified in the contour plot as an area of low WSS.

Table 5.2: Case 2 summary. The results of MSCT plaque scoring segmentation for the modelled artery, together with the mean blood velocity (U_0) and the calculated Poiseuille WSS (τ_0) are given.

Case 2	*In vivo* detected plaques	U_0 [ms^{-1}]	τ_0 [Pa]
Right SFA		0.104	0.724

The simulation shows that the patient would develop atherosclerosis in the DFA after 20 years and 5 months, starting from a point in which the anatomical characteristics of the patient would not in principle change in time (as discussed for Case 1). Figure 5.24 shows the mesh deformation contour plot for the deep femoral artery showing plaque formation. Only one plaque is present in the seg-

ment proximal to the artery bifurcation. From MSCT observation (Figure 5.11), a plaque formation in this area was not evident.

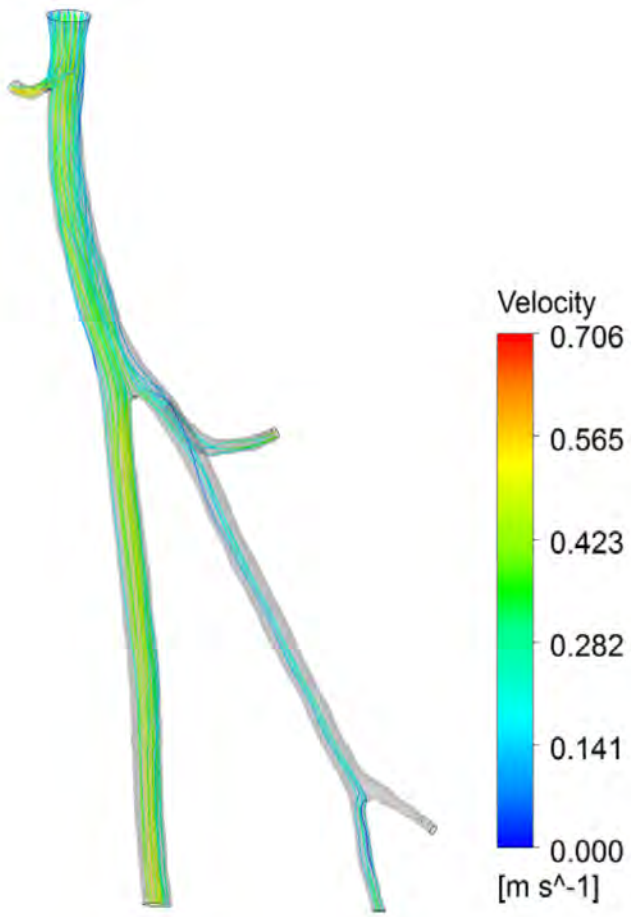

Figure 5.22: Velocity streamlines for the model of the right common femoral artery, with the deep femoral artery and the superficial femoral artery.

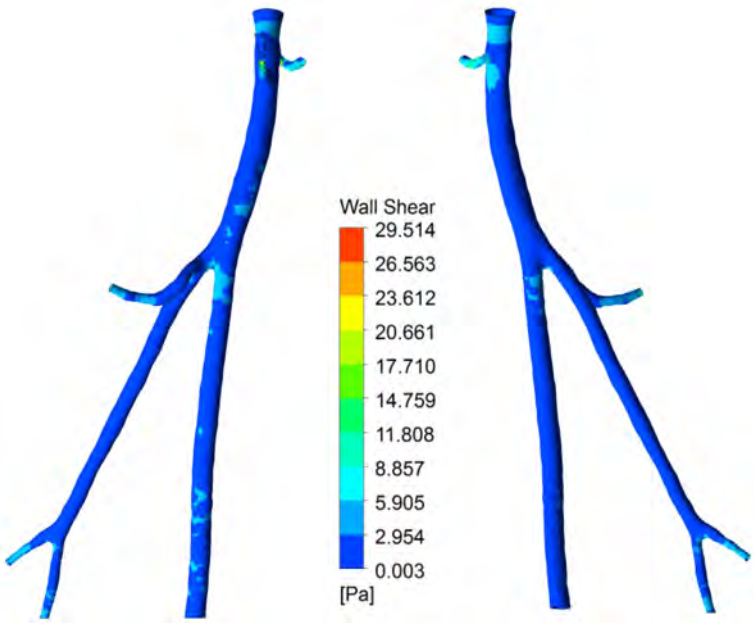

Figure 5.23: Global WSS contour plot for the model of the right common femoral artery, with the deep femoral artery and the superficial femoral artery.

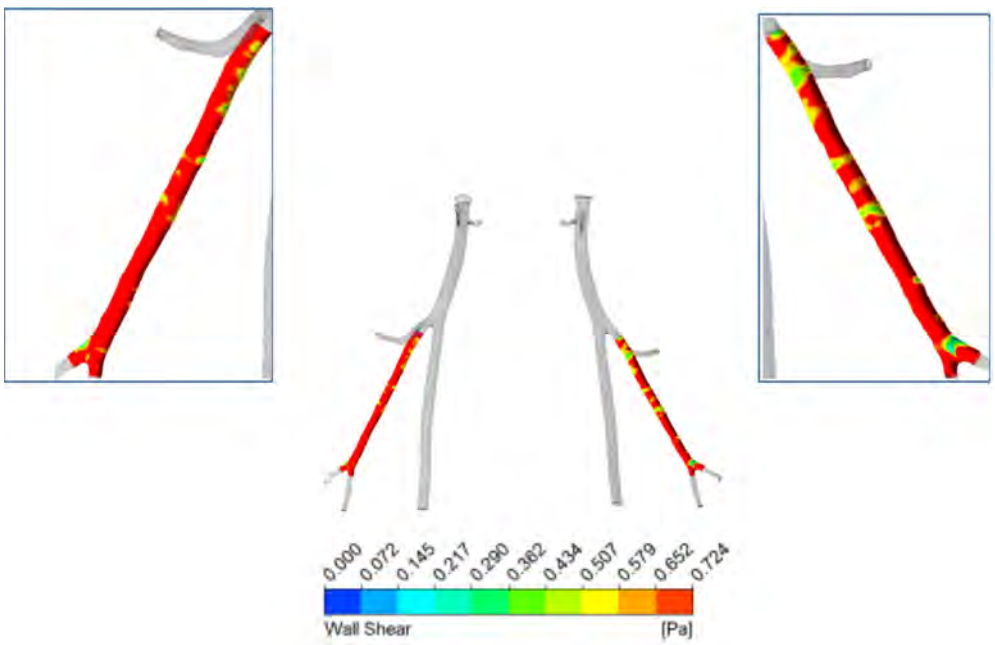

Figure 5.24: Re-scaled WSS contour plot of the right deep femoral artery. The plot maximum WSS detectable is the Poiseuille WSS for the right deep femoral artery $\tau_0 = 0.724$ Pa

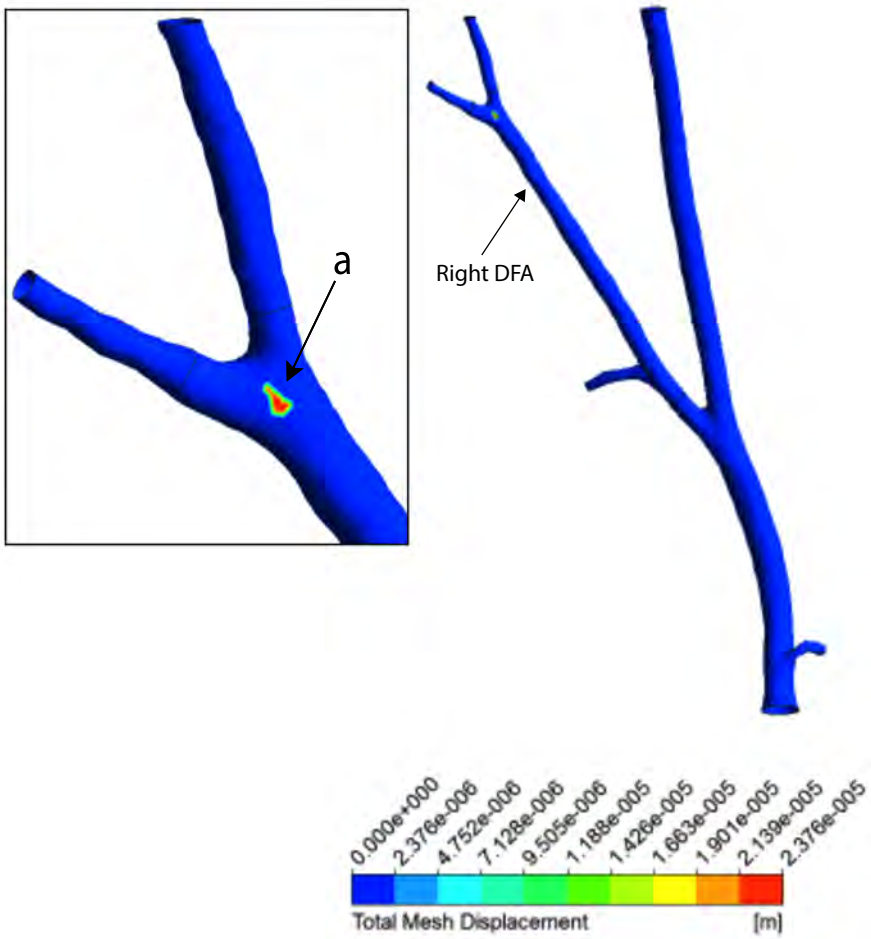

Figure 5.25: Mesh deformation contour plot for the right common femoral artery, with the deep femoral artery and the superficial femoral artery. Plaques occurrence was modelled solely in the deep femoral artery. The contour plot of mesh displacement indicates the area where the nodes were displaced to model the plaque formation.

5.2.3 Case 3: Simulation Results

Velocity streamlines are shown in Figure 5.26. The area of the common femoral artery (Figure 5.1 and table 5.3) proximal to the bifurcation with the deep femoral artery shows flow detachment. Plaque 3 observed *in vivo* (Figure 5.13) is located in this area of flow detachment. The re-scaled WSS plot for the common femoral artery, scaled with the maximum WSS as the Poiseuille WSS value (Table 5.3) for the same radial dimension and mean inlet flow velocity is shown in Figure 5.27. The small artery branching out of the CFA was not considered in the simulation. From this plot, two main atherosclerosis-prone areas emerge in the CFA, the area distal to the DFA and an area distal to the small artery branching out of the CFA.

Table 5.3: Case 3 Summary. The results of MSCT plaque scoring segmentation for the modelled artery, together with the mean blood velocity (U_0) and the calculated Poiseuille WSS (τ_0) are given.

Case 3	*In vivo* detected plaques	U_0 [ms^{-1}]	τ_0 [Pa]
Left CFA	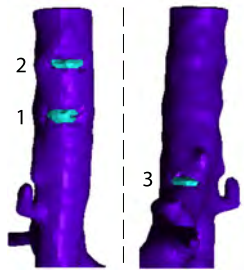	0.207	0.657

Atherosclerosis growth was simulated for the CFA, and after 20 years and 9 months (starting from the developed artery), an atherosclerosis formation was shown. This can be seen in the mesh deformation contour plot Figure 5.28. The simulated atherosclerotic plaque formed in one of the areas that the re-scaled WSS contour plot showed as pro-atherogenic. This plaque does not precisely correspond to what was detected from MSCT plaque scoring; however, it could be representing plaque 1 (Figure 5.13) in a more distal location.

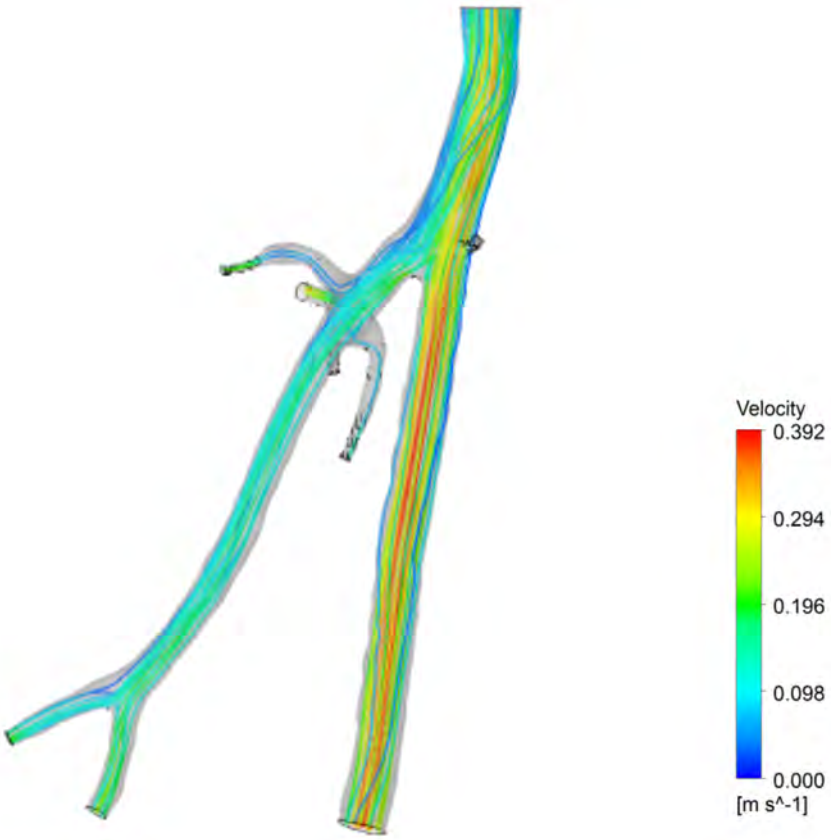

Figure 5.26: Velocity streamlines for the model of the left common femoral artery, with the deep femoral artery and the superficial femoral artery.

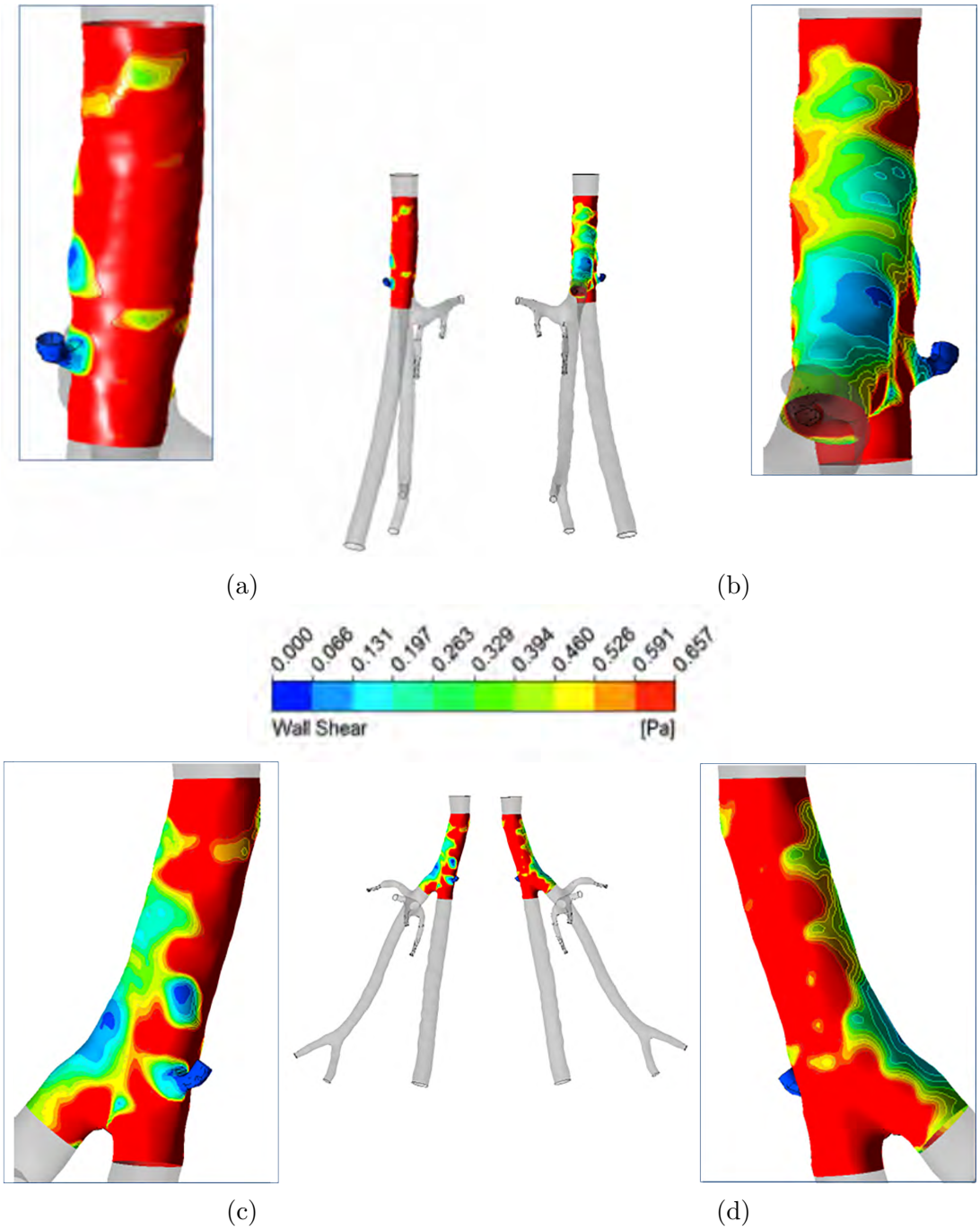

Figure 5.27: Re-scaled WSS contour plot of the left common femoral artery. The plot maximum WSS detectable is the Poiseuille WSS for the left common femoral artery $\tau_0 = 0.6572$ Pa.

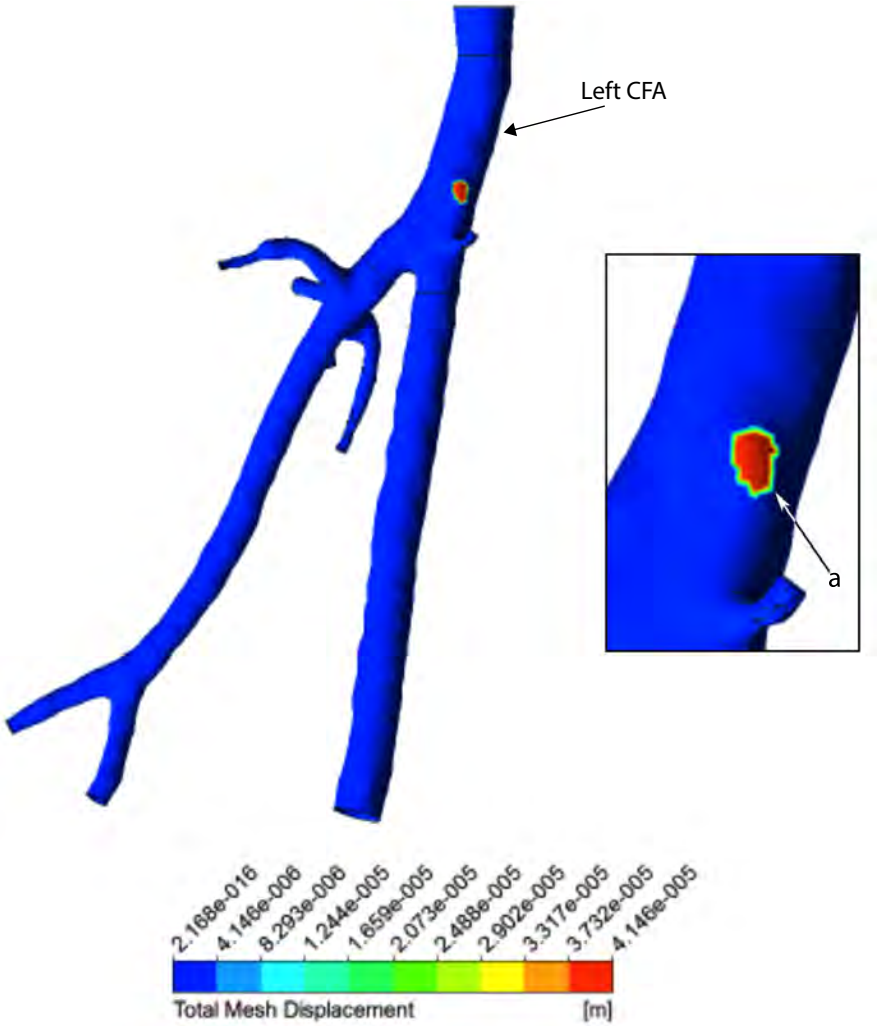

Figure 5.28: Mesh deformation contour plot for the left common femoral artery, with the deep femoral artery and the superficial femoral artery. Plaques occurrence was modelled solely in the left common femoral artery. The area of mesh displacement indicates the plaque formation.

5.3 Discussion

The *in silico* atherosclerosis formation framework developed in this thesis and described in Chapters 2-4 was used to simulate patient-specific plaque formation in a proof-of-concept model. The patient-specific anatomical data were obtained from MSCT angiogram images. Doppler echocardiography images were used to calculate flow time-averaged mean velocities. The patient selected for this study had atherosclerosis formations in the peripheral arteries. Having a patient that already had developed the disease allowed for comparison between the simulations and *in vivo* observations in order to test the framework, establish its viability and qualitatively validate the results.

Three cases with different sections of the patient's arterial tree were considered and arterial lumen geometries were segmented from MSCT images. To obtain the characteristics of the lumen geometry before disease occurrence, the plaques detected were segmented together with the free lumen. In Case 1, the right common iliac artery was artificially re-created as stenosis blockage prevented the MSCT contrast agent from identifying it.

An artery-specific approach was used to model the endothelial transport response to local WSS. Two different types of WSS contour plots were used to analyse the haemodynamics in the modelled arteries. The areas of high WSS could be analysed with a global WSS contour plot (Figures 5.14 and 5.23). However, this plot would not highlight the areas of low WSS (of more interest for this analysis as potentially prone to atherosclerosis). An artery-specific WSS contour plot was developed re-scaling the global WSS contour plot, by setting the maximum WSS as the calculated Poiseuille WSS value for a pipe with the same cross sectional dimension and mean flow velocity of the artery considered (Tables 5.1 to 5.3).

The geometries of the three sections with highlighted segmented plaques (Figures 5.9, 5.11 and 5.13) show a good agreement with the pro-atherosclerosis areas highlighted by the WSS re-scaled contour plots (Figures 5.15 to 5.17, 5.24 and 5.27) as shown in Table 5.4. All the plaques detected in the MSCT correspond to areas of low WSS with the exception of plaque 2 (Figure 5.13) in the left common femoral artery (Figure 5.27).

Table 5.4: Summary of the *in vivo* observed plaques together with the model diagnostic indices (the MSCT images with the segmented plaques are Figure 5.9 for Case 1, Figure 5.11 for Case 2 and Figure 5.13 for Case 3). Two diagnostic atherosclerosis indices were used to assess the agreement with in-vivo observations : plaque in highlighted atherosclerosis-prone areas (the modelled WSS pattern showed atherosclerosis-prone areas corresponding to the location of the in-vivo observed plaque) and plaque simulated by the model (a modelled plaque developed in the location of the in-vivo observed plaque).

Case	Artery	Plaque observed in MSCT images	Plaque in highlighted atherosclerosis-prone areas	Plaque simulated by the model
Case 1	Descending abdominal aorta	1,2,3	✓	✓
		4	✓	✓
	Left CIA	7	✓	✓
		8	✓	×
	Right CIA	5,6	✓	×
Case 2	Right DFA	1	✓	×
Case 3	Left CFA	1	✓	✓
		2	×	×
		3	✓	×

As already discussed in the previous chapter, areas of low WSS are caused by a local decrease in the flow velocity (Figure 5.21), leading to a local increase in the transport properties of the endothelium and the creation of pro-atherogenic areas. Velocity Contour Plots 1 and 4 (Figure 5.21), show the velocity behaviour and arterial cross section at the location of Plaque f (Figure 5.18) that did not correspond to the observations *in vivo* (Contour Plot 1) and Plaque a (Figure 5.18) that did correspond to a plaque observed *in vivo* (Contour Plot 4) (Plaque 2, Figure 5.9). A local decrease in the flow velocity caused by the distal bifurcation, leads to the formation of Plaque a (Contour Plot 4, Figure 5.21). On the contrary, Contour Plot 1 shows a local velocity decrease caused by an irregularity in the artery cross sectional shape. Errors in the segmentation of MSCT geometry can lead to the creation of geometric artefacts, altering the haemodynamics in the artery simulated. Atherosclerotic Plaque f (Figure 5.18) occurred in the location corresponding to velocity Contour Plot 1 (Figure 5.21), possibly generated

by poor resolution in the MSCT images of the contrast lumen. As WSS values are dependent on both haemodynamics and lumen geometry, poor image quality can lead to the creation of "artificial" plaques. Together with the geometry, mesh quality has a large impact on the plaque formation. In case of the highly irregular patient-specific geometries, the impact that sharp differences in the local WSS minima and the effect that mesh elements have on the mesh deformation have been addressed up to a point; they have been minimised using WSS averages within the considered pro-atherogenic areas.

The simulation results of Case 1 show six plaques in the descending aorta, five plaques in the left CIA and two plaques in the right CIA. Of the plaques developed, three plaques in the descending aorta (a, b and e. Figure 5.18) closely correspond to Plaques 1, 2 and 3 observed *in vivo* (Figure 5.9). Plaque f (Figure 5.19) developed in the left CIA approximately corresponds to Plaque 7 (Figure 5.9). None of the plaques developed in the recreated right CIA correspond to the plaques observed *in vivo*. For this artery, the WSS pattern does not show atherogenic areas precisely in the location where the plaques are observed *in vivo*. The area of low WSS appears at the same longitudinal location but more towards the inner side of the bifurcation. A WSS pattern difference due to boundary conditions and simulation settings might cause this error. Furthermore, as the right CIA artery lumen was manually reconstructed, it is possible that the segmentation could not precisely capture the anatomy of the artery leading to an incorrect reproduction of the artery patent lumen.

Case 2 showed the development of a plaque in the right DFA in the tract proximal to the bifurcation (Plaque a, Figure 5.25). This result does not correspond to *in vivo* observations. The plaque detected from MSCT observation of the right SFA (Figure 5.11) is located more proximally, and it is in an area detected as low WSS area (Figure 5.24). Case 3 developed one plaque in the left CFA (Plaque a, Figure 5.28). Plaque a developed in the left CFA could correspond to Plaque 1 observed *in vivo* (Figure 5.13), but more distally and internally located than the segmented plaque. Areas of low WSS are highlighted in the area proximal to the bifurcation with the left DFA (Figure 5.27), showing a pro-atherogenic area where *in vivo* observation shows a plaque formation (Plaque 3). There is no low WSS area corresponding to Plaque 2 in the left CFA (Figure 5.28). As shown in

Table 5.2, there is a good agreement between atherosclerosis-prone areas and developed plaques in the model and the *in vivo* observations. 91.7% of the plaques observed *in vivo* were identified by the model as atherosclerosis-prone areas, and 41.7% of the plaques observed in-vivo were developed in the model. There was an over prediction in the model, with plaques developed and atherosclerosis-prone areas highlighted by the low WSS not having a correspondence with the *in vivo* analysis results.

Wall shear stress is the determining factor in this model for both the location of the atherosclerosis-prone area and possible atherosclerotic formation, when other factors such as mean blood LDLp levels are kept constant.

A time-averaged blood flow rate based on the pulsatile velocity profiles extracted from Doppler echocardiography data, was imposed at the inlet of each of the different arterial tree sections considered. *In silico* experiments carried out by Wood et al.[69] showed that the WSS local minima was located more distally when a pulsatile velocity was considered. Furthermore, time averaged WSS (TAWSS) is found to differ in value from steady state WSS in large arterial branches such the aorta[162], indicating the importance of considering a transient flow. A steady state flow environment was considered for this first implementation, following the same approach used for the modelling of atherosclerosis on idealised arterial geometries. The application of a pulsatile velocity at the inlet will require more detailed Doppler echocardiography data than the ones available for this study, and will be considered among the future improvements for this modelling of patient-specific atherosclerosis formation. The endothelial response to WSS has a much longer time frame than the temporal variations in the haemodynamics, making the steady flow approximation a valid one up to a point; however, transient flow will be considered among the possible future implementations and will be further discussed in the next chapter. Simply considering WSS as a tuning factor for endothelial response to local haemodynamics might be the cause of the observed over-prediction in the model. It emerged from Levesque et al.[32] that the maximum deformation in the endothelial cells shape would occur in areas where a local WSS maxima would be followed by a local WSS minima. Spatial Wall Shear Stress Gradient (WSSG) could, therefore, play a role in defining the local intensity of flow disturbance, becoming an added selective

criterion in the detection of atherosclerosis-prone areas.

Not only the inlet conditions but the conditions at the other boundaries influence the haemodynamics. A stress free outlet boundary was used in this implementation, neglecting the flow resistance represented by the downstream vasculature. A resistive outlet boundary would be expected to change the haemodynamics in the domain, possibly changing the location of the atherosclerosis-prone areas[163]. The implementation of resistive outlet boundaries are considered as future improvements to this model and will be discussed in the following chapter.

The assumption of a rigid wall is not expected to influence the results as a steady state simulation is performed. In large arteries such as the aorta, the vessel compliance should be considered; however, in a steady-state simulations the role played by compliant walls can be neglected [164]. The rigid-wall assumption can be considered acceptable also in transient scenarios. In a study on the haemodynamics of the mesenteric artery by Jeays et al. [165], they showed that difference in average wall shear stress value between rigid and moving wall models was less than 2.1%.

From *in vivo* observations, it emerged that the majority of plaques would develop in areas close to arterial bifurcations and this has been already reported numerous times in the literature[29, 166]. It would be, therefore, necessary to segment every different branch, even the minor ones, to accurately model the artery haemodynamics. In absence of the two minor right hand side branches of the descending aorta (Figure 5.21), there would not be flow detachment (Figure 5.21, Plane 4) leading to no plaque development (Figure 5.18, Plaque *a*). As the haemodynamics is highly geometry sensitive, it is necessary to accurately segment the real healthy state anatomy of the artery considered. The patent lumen was here obtained by artifically removing the atherosclerotic plaque from the diseased vessel [50, 51, 58]. One of the limitations of this approach is the assumption that the vessel would retain its initial anatomy after plaque development [49]. The lumen compensatory enlargement due to plaque formation [167] could lead to an overestimation of the diameter of the initial disease-free vessel [51]. Achenbach et al. [168] considered different degrees of atherosclerotic lumen narrowing, up to a maximum of 75% stenotic diameter reduction, and reported that the arterial remodelling cause by lumen stenosis is negligible. In Case 1

the right CIA presented with a severe blockage of the lumen. Even though from MSCT observation the calcified plaque does not appear as obstructing the entirety of the lumen, the total absence of contrast agent within the arterial lumen suggests a complete lumen obstruction. This observation leads to the second limitation of the artificial creation of the patent lumen, the assumption that the patent lumen could be segmented by removal of the calcified plaque [49]. The atherosclerosis plaque obstructing the left CIA could be a plaque mostly made of lipids, which are not identified during MSCT plaque scoring. This would justify the absence of flow in an artery not showing an extensively calcified lumen. As the calcified plaque does not correspond to the entirety of the plaque, its artificial removal could lead to a false representation of the initial lumen diameter [51]. The segmentation error introduced by an imprecise plaque removal to recreate the patent lumen has to be considered. A prospective study following the disease development starting from an healthy artery could help to overcome this limitation and further validate the model [50, 51].

5.4 Conclusion

To the authors knowledge, this is the first time the transport and biochemical interaction between LDLp and monocyte/macrophages have been linked to plaque growth and wall remodelling in a 3D patient-specific multiscale model of atherosclerosis [118][58]. It is also the first model to propose a more artery-specific approach to shear-dependent transport properties. Novelty of the model proposed here is the creation of a workflow, the *atherosclerosis remodelling cycle*, a workflow that includes the core processes behind the formation of atherosclerosis at its early stage and that can constitute the "skeleton" for further development towards a more detailed and sophisticated atherosclerosis model. The method developed in this study was able to capture key features of atherogenesis such as the location of pro-atherogenic areas as also shown by Olgac et al.[58], and to reproduce the formation of plaques detectable from *in vivo* observations[149].

From comparison with *in vivo* observations, it emerged that the model would identify 91.7% of the locations where atherosclerotic plaque was present if the artery-specific WSS plots are used. Furthermore, the model managed to simulate

almost half of the plaques detected from *in vivo* observation. The majority of plaques that were successfully modelled were in the descending aorta segment of Case 1, where the model reproduced 4 plaques out of the observed 8. The model was less precise in the modelling of plaque development for the two other Cases, the right DFA and the left CFA. However, the plaques observable from MSCT for these two sections of the arterial tree were not as visible as the extensively calcified plaques detained in the descending aorta and the right and left CIA, leaving a large margin of error in the reported observations. It has emerged that local decrease in the WSS is a reasonable initial approximation for identifying plaque location, but other factors must be considered. The model tends to over-predict the areas at risk of atherosclerosis, suggesting the need of other factors, such as WSSG to better modulate the endothelial reaction to haemodynamics. As the haemodynamics is heavily influenced by arterial lumen geometry, an accurate geometry segmentation of MSCT images is needed. It was observed here that atherosclerosis-prone areas also developed where there was a poor image segmentation.

Further developments are necessary in order to overcome the current limitations and to improve the accuracy of the results. The limitations and improvements will be discussed in the following chapter.

Chapter 6

Conclusion and Future Work

6.1 Atherosclerosis Model

In Chapter 2, *Atherosclerosis Model*, the mathematical model of atherosclerosis formation was presented. The model developed integrated a transport model with a biochemical model approach in order to better characterise the dynamics of the initial state of atheroma, the fatty streak formation. Starting from a healthy arterial wall, the model considered the immune system reaction to the oxidised LDL leading to foam cell accumulation and fatty streak formation. Following the three pores model developed by Curry[99] and the work of Olgac et al.[83] the penetration of LDL inside the arterial wall was linked to the haemodynamic stimuli exerted on the arterial endothelium. Experimental findings were used to relate the endothelial permeability with the ratio of local WSS[32] to the normal WSS for the artery, calculated as Poiseuille WSS[131]. Use of the ratio of local WSS to the "ideal" artery WSS, allowed the experimentally derived endothelial response to WSS to be tuned according to the artery considered, making the endothelial transport properties artery-specific. This initial approach towards a fully artery-specific model, allowed different arterial segments of the human arterial tree to be modelled, without neglecting their heterogeneity[35].

WSS should be considered along with other haemodynamic stimuli, in this model. As already presented in the first chapter of this thesis (Section 1.1.3), experimental findings suggest that various Haemodynamic Wall Parameters(HWPs)

play an important role in characterising the endothelial transport properties[33]. Together with the HWPs, intraluminal pressure and consequently arterial wall transmural pressure are also of importance. In this model transmural pressure was kept constant, following the experimental procedures by Meyer et al.[90]. Their experimental findings[90] showed that for higher intraluminal pressure, the penetration of plasma macromolecule such as albumin through the arterial wall is enhanced, suggesting an important contribution when modelling macromolecular transport. Furthermore, an increase in interluminal pressure has been proven to be linked to an increase in the permeability of IEL[132]. In this model the IEL was not differentiated from the arterial wall, with the exception of the endothelium, as the arterial wall was modelled as a single layer. When modelling a more advanced stage of atherosclerosis, smooth muscle cell migration from the media to the intima layer will have to be considered[8] leading to a more detailed multi-layer approach. Differentiation of the different layers of the arterial wall, will lead to a more refined modelling of the transport properties of IEL. This fenestrated membrane will be modelled following the same approach of the endothelium model presented here, with its permeability to macromolecules linked to the transluminal pressure, as shown in Huang et al.[132].

As this model concentrated on the initial stage of atherosclerosis formation, only LDL and monocytes/macrophages were considered in the transport model. LDL inside the arterial wall was modelled with a convection-diffusion-reaction equation (Equation (2.24)) and the transport of monocytes/macrophages was modelled with a diffusion-reaction Equation (2.35), where the reaction term represents the degradation of the native species. The quantity of migrating monocytes inside the arterial wall was made dependent from the concentration of oxidised LDL inside the arterial wall. Linking the immune response of the body to the concentration of oxidised LDL, is a simplified approach to the characterisation of cytokine action[25].

Degradation of LDL inside the arterial wall was modelled following the approach of Cobbold et al.[22], where the oxidation of LDL is the product of the interaction between native LDL and free radicals. Monocytes, once inside the arterial wall, instantly differentiate into macrophages and start reacting with oxidised LDL to degrade into lipid laden macrophages, the foam cells. Foam cell

accumulation was modelled as stratification following close hexagonal packing and was the basis of plaque formation[6]. Plaque phase of growth is usually modelled using *in vivo* observations[150, 151]. Clinical validation of the developed plaque growth was not achieved and future work will be devoted to perfecting the wall growth function, in order to characterise better the atheroma formation over time.

Arterial wall inward swelling alters haemodynamics, leading to a change in the endothelial transport properties, changing the whole cycle of atherosclerosis formation. Very heterogeneous spatial and temporal dimensions are involved in a complex biological process like atherosclerosis, where very fast molecular interactions impact on the organ functioning over the years. The interaction of such different dimensions or scales in the process modelled requires the creation of a multiscale model. A model where the best spatial and temporal characterisation for each sub-process is attained, maintaining an integrity in the whole model thanks to the interplay of the different scales considered.

The main objective of this work was to develop a mathematical model that would integrate the key factors to early stage plaque formation, using different modelling approaches and techniques. This model was developed to describe the whole early atherosclerosis cycle, from the formation of atherosclerosis-prone areas, to the initiation of the lesion, ending with the impact of the lesion on arterial haemodynamics and the progression of the disease. A workflow was proposed as a basis of this model, that enabled the various sub-domains and scales of definition of the model to function together and to create this integrated modelling approach of atherosclerosis, the *Atherosclerosis Remodelling Cycle*.

6.2 Atherosclerosis Remodelling Cycle

Chapter 3 presented the workflow created for the implementation of the atherosclerosis model, the *atherosclerosis remodelling cycle*. The atherosclerosis sub-processes modelled mathematically were first integrated together with the help of a theoretical workflow. The workflow was modelled as a feed-back loop, that follows the events leading to the atherosclerosis plaque formation. Once the disease has formed the haemodynamic patterns would change accordingly, thus creating a

new environment for the disease formation and development. Final information on the initial *atherosclerosis remodelling cycle* (geometry update because of plaque formation) would be used to initiate the new *atherosclerosis remodelling cycle*. Each of these cycles define the development of the disease in a given haemodynamic environment.

The temporal development of the *atherosclerosis remodelling cycle* was defined using a multiscale approach, as already presented in Chapter 2 (Section 2.2.2). The smallest time-scale follows the progression of inflammatory disease, modelling the biochemical processes happening within the arterial wall. The second time-scale updates the endothelial transport model according to the disease progression inside the arterial wall. The third, and longest, time-scale is the time length of the whole *atherosclerosis remodelling cycle*, at the end of which a new cycle starts. Each time the developed disease produces a plaque of given size, the haemodynamics are updated leading to the initiation of a new loop.

Ansys CfX v14 was used to describe the lumen fluid sub-domain, whilst the solid sub-domain of the endothelium and arterial wall were described using Matlab. A computational workflow was created to computationally implement the theoretical workflow and to link the different softwares used within it. The tool produced aimed to deliver high feasibility and computational efficiency. The atherosclerosis model functioning was not geometry dependent, as each different surface node of the geometry was solved separately. A pre-selection of the atherosclerosis-prone areas allowed the computational cost of the whole geometry processing to be reduced with a more targeted choice of input data.

The computational workflow was structured as to reduce the cost of implementation. Solving for the CFD model and biochemical model separately, allowed savings as the computational cost of a constant interaction between the CFD sofware (Ansys CfX v14.) and the biochemical model software (Matlab) was reduced. The multiscale time setting allowed a steady-state environment in the CFD model whilst keeping a fully transient biochemical model, updating the CFD model only for plaque accurance. Furthermore, the inflammatory process for each CFD surface node could be solved separately from the neighbouring nodes allowing for an easy parallelisation and subsequent reduction in the computational time.

6.3 Atherosclerosis Modelling on Idealised Arterial Geometries

In Chapter 4 an initial implementation of the atherosclerosis formation model was carried out on three different idealised geometries of human arteries. The effect of local haemodynamics on endothelial transport was first observed in a stenotic coronary artery with a steady-state transport-biochemical model of the arterial wall and endothelium. To observe the role played by LDL as a risk factor different levels of high mean blood LDL were introduced in the model. LDL confirmed its role as risk factor, making the atherosclerosis formation more severe in the case of a higher severity of hyperlipoproteinemia. Observing the behaviour of endothelial apparent permeability, it emerged that the location of plaque formation was entirely dependent on the local haemodynamics. From studies on endothelial behaviour to haemodynamic disturbance cause by stenotic narrowing[32] it emerged that high permeability areas were not only located at the global WSS minima, but in the areas where there was an high WSS level followed by a low WSS level. Levesque et al.[32] finding suggests that, for highly disturbed geometries, the endothelial behaviour is highly dependent on the WSS spatial gradient (WSSG). This HWP[33] will be included in future modelling of endothelial behaviour.

To describe better atheroma development, a transient time regime was introduced for the transport-biochemical model. Following the Hoogstraten et al.[131] model, an idealised common femoral artery presenting two successive bends was implemented as a geometry at high risk for atherosclerosis formation[29]. Together with the S-shaped anatomy, an idealised stenotic common femoral artery was implemented. To model shear dependent endothelial transport properties in arteries anatomically different from the aorta studied by Levesque et al.[32] an artery-specific endothelial SI function was developed.

Plaque development in the stenotic artery had a faster phase than in the S-shaped artery. This finding suggests that, for the same mean blood cholesterol conditions, geometry plays an important role as risk factor[29], showing the role played by the arterial haemodynamics in defining both the location of the disease and the severity of the disease developed.

6.4 Patient Specific Modelling of Atherosclerosis Formation

In Chapter 5 atherosclerosis formation on patient-specific arteries was modelled. Arterial lumen anatomy of a patient with atherosclerosis formations in his peripheral arteries was extracted from MSCT angiogram images and processed in Scan IP. In order to produce the anatomy of the disease free arterial lumen the atherosclerosis plaques visible were segmented as part of the lumen and a tract where atherosclerosis formation prevented lumen enhancement with contrasting agent was artificially recreated. Three different segments of the arterial tree were considered as different modelling cases. Patient-specific mean blood velocity data were extracted from Doppler Echocardiography data.

An artery-specific endothelial transport behaviour was implemented for each one of the arteries considered. Defining the transport for each artery following its specific haemodynamics allowed the WSS atherosclerosis-prone areas to be highlighted better. It would have not been appropriate to define a global endothelial transport function for the different cases considered, as within them the haemodynamics of the various arteries were very heterogeneous. The arteries were defined separately using cutting and selecting tools in Ansys ICEM v14. The selection of an area belonging to the parent artery or the branching artery was done arbitrarily; the criterion followed was to define a cutting edge from one artery to the other that would not coincide with the location of any of the *in vivo* observed plaques, in order not to alter the modelled results. Refinement on the branch selection criterion will be considered as part of improvements to this model.

To the author's knowledge, this is the first model implementing a generalised artery-specific approach for the prediction of atherosclerosis-prone areas in different patient-specific anatomies. It is also the first 3D patient-specific atherosclerosis model characterising plaque development.

The model reproduced the occurrence of almost half of the plaques (41.7%) detected from *in vivo* observation and highlighted the majority of the atherosclerosis-prone areas (91.7%). The most precise results in plaque occurrence was in the descending aorta segment (Case 1), where three of the 4 plaques detected from

in vivo observation were reproduced by the model. All of the plaques of Case 1 observed *in vivo* were highlighted in the model as atherosclerosis prone-areas. This high accuracy in the results could be due to the bigger anatomical size of the segment considered, allowing for a more precise image segmentation and an higher precision in the plaques detected from *in vivo* observations.

As the location of atherosclerotic plaques is in this model defined by the haemodynamic behaviour, error in the location of plaque formation is linked to errors in the modelling of the exact haemodynamics. High quality MSCT images, with low levels of artefacts is important for the correct modelling of haemodynamics, as haemodynamics are heavily influenced by the arterial lumen geometry.

Together with the lumenal geometry, the fluid domain boundary conditions play an important role in the definition of the haemodynamics. The current boundary conditions are; parabolic time-averaged velocity at the inlet, rigid walls, and a stress free condition at the outlets. The location of local WSS minima may alter if pulsatile velocity is applied at the inlet boundary, as shown in an *in silico* experiment by Wood et al.[69]. Together with a transient velocity, the WSS would be influenced by factors describing the blood rheology. It will be worth considering the shear-thinning behaviour of blood, in order to better simulate the haemodynamics in the fluid domain. The arterial wall was here assumed as rigid, not allowing for any compliant behaviour. This assumption will play a major role when considering the blood pulsatile behaviour. Future improvements might include a fluid-structure interaction model (FSI) to analyse the impact that a compliant wall would have on the haemodynamics and ultimately on the atherosclerosis development (currently being investigated at the Multiscale Cardiovascular Engineering Group of UCL).

A resistive outlet condition could be implemented to account for the flow resistance given by the downstream branching arteries. In a study by Stergiopulos et al.[169] the author created a one-dimensional mathematical representation of the whole circulatory system. The flow resistance values for the main arterial segments were calculated thanks to this analogical model. These data can be used for an initial implementation of more physiological boundary conditions. Differences in the model haemodynamics given by stress free outlet condition and

resistive outlet condition will be among the future investigations to be considered. Implementing the new boundary conditions and comparing the atherosclerosis-prone areas coming from this implementation with the *in vivo* observed plaque formation will allow assessing their importance in this simulation domain.

More patients should be selected for further developing this initial approach to patient specific modelling of atherosclerosis. For each patient, plaque measurements on MSCTs at follow up times will be used to more precisely tune the plaque growth function.

The aim of this work was to produce an effective tool for the modelling of atherosclerosis plaque formation, the *atherosclerosis remodelling cycle*. At the basis of this tool is a multiscale model considering some of the main fluid dynamics, biochemical and transport processes leading to the formation of atherosclerosis. A workflow was created to achieve integration between the different processes modelled and to implement them computationally. The reduced computational cost and data handling allowed to model plaque formation and development for years of computational time. The *atherosclerosis remodelling cycle* was able to handle highly irregular geometries, making its implementation on patient-specific geometries possible. Together with the anatomy, the *atherosclerosis remodelling cycle* can consider other patient-specific factors such as mean blood velocity and mean blood LDL concentration.

The *atherosclerosis remodelling cycle* presented here is an initial step towards the goal of producing an in-silico tool for the clinical management of atherosclerosis.

Bibliography

1. Iaizzo P. Handbook of Cardiac Anatomy, Physiology, and Devices (Current Clinical Oncology). Humana Press, 2009.
2. Levick JR. An introduction to Cardiovascular Physiology. Hodder Arnold, 2003.
3. Reitsma S, Slaaf DW, Vink H, Zandvoort MA van, and Egbrink MG ounde. The endothelial glycocalyx: composition, functions, and visualization. Pfungers Arch 2007;454:345–359.
4. Huang AL, Jan KM, and Chien S. Role of intercellular junctions in the passage of horseradish peroxidase across aortic endothelium. Lab Invest 1992;67:201–209.
5. Henriksen RC, Kaye GI, and Mazurkiewicz JE. Histology. 1997.
6. Faggiotto A, Ross R, and Harker L. Studies of hypercholesterolemia in the nonhuman primate. I. Changes that lead to fatty streak formation. Arteriosclerosis 1984;4:323–340.
7. Faggiotto A and Ross R. Studies of hypercholesterolemia in the nonhuman primate. II. Fatty streak conversion to fibrous plaque. Arteriosclerosis 1984;4:341–356.
8. Gerthoffer WT. Mechanisms of vascular smooth muscle cell migration. Circulation research 2007:607–621.
9. Betteridge DJ, Illingworth R, and Shepherd J. Lipoproteins in Health & Disease. London: Arnold, 2000.
10. Esterbauer H, Gebicki J, Puhl H, and Jurgens G. Review Article: The role of lipid peroxidation and antioxidants in oxidative modification of LDL. Free Radic. Biol. 1992.
11. Stocker R. The ambivalence of vitamin E in atherogenesis. Trends in biochemical sciences 1999;24:219–223.

12. Cox DA and Cohen ML. Effects of oxidised low-density lipoprotein on vascular contraction and relaxation: clinical and pharmacological implications in atherosclerosis. Pharmacological Reviews 1996;48:3–19.

13. Vasile E, Simionescu M, and Simionescu N. Visualization of the binding, endocytosis, and transcytosis of low-density lipoprotein in the arterial endothelium in situ. The Journal of Cell Biology 1983;96:1677–1689.

14. Brown MS and Goldstein JL. Receptor-mediated endocytosis: insights from the lipoprotein receptor system. Proceedings of the National Academy of Science 1979;76:3330–3337.

15. Vasile E, Simionescu M, and Simionescu N. Visualization of the Binding, Endocytosis, and Transcytosis of Low-density Lipoprotein in the Arterial Endothelium in Situ. J Cell Biol 1983;96:1677–1689.

16. Hajjar DP and Haberland ME. Lipoprotein trafficking in vascular cells Molecular Trojan horses and cellular saboteurs. Journal of Biological Chemistry 1997;272:22975–22978.

17. Wiklund O, Carew TE, and Steinberg D. Role of the low density lipoprotein receptor in penetration of low density lipoprotein into rabbit aortic wall. Arteriosclerosis, Thrombosis, and Vascular Biology 1985;5:135–141.

18. Cancel L, Fitting A, and Tarbell JM. In vitro study of LDL transport under pressurized (convective) conditions. American journal of physiology. Heart and circulatory physiology 2007;293:H126–H132.

19. Mugge A. The role of reactive oxygen species in atherosclerosis. Z Kardiol. 1998;87:851–864.

20. Hodis HN, Kramsch DM, Avogaro P, et al. Biochemical and cytotoxic in vivo circulating oxidized (LDL-). The Journal of Lipid Research 1994;35:669–677.

21. Upston JM, Terentis AC, and Stocker R. Tocopherol-mediated peroxidation of lipoproteins: implications for vitamin E as a potential antiatherogenic supplement. FASEB J. 1999;13:977–994.

22. Cobbold CA, Sherratt JA, and Maxwell SRJ. Lipoprotein oxidation and its significance for atherosclerosis: a mathematical approach. Bulletin of mathematical biology 2002;64:65–95.

23. Esterbauer H, Dieber-Rotheneder M, Waeg G, Striegl G, and Juergens G. Biochemical structural and functional properties of oxidized low-density lipoprotein. Chemical research in toxicology 1990;3:77–92.

24. Pocock G and Richards CD. Human Physiology - the Basis of Medicine. Oxford University Press, 2006.

25. Glass C. The macrophage foam cell as a target for therapeutic intervention. Vol. 8. Nat Med, 2002.

26. Gerrity RG. The role of the monocyte in atherogenesis: I. Transition of blood-borne monocytes into foam cells in fatty lesions. The American journal of pathology 1981;103:181.

27. Howard G, Wagenknecht LE, Burke GL, et al. Cigarette Smoking and Progression of AtherosclerosisThe Atherosclerosis Risk in Communities (ARIC) Study. JAMA 1998;279:119–124.

28. Williams CL. Cardiovascular Health in Childhood: A Statement for Health Professionals From the Committee on Atherosclerosis, Hypertension, and Obesity in the Young (AHOY) of the Council on Cardiovascular Disease in the Young, American Heart Association. Circulation 2002;106:143–160.

29. Friedman MH, Deters OJ, Mark FF, Bargeron CB, and Hutchins GM. Arterial geometry affects hemodynamics. A potential risk factor for atherosoclerosis. Atherosclerosis. 1983;46:225–231.

30. Silkworth JB, Stehbens WE, and Phil D. The shape of endothelial cells in en face preparations of rabbit blood vessels. Angiology 1975;26:474–487.

31. Flaherty JT, Pierce J, Ferrans VJ, Patel D, TUCKER W, and FRY DL. Endothelial nuclear patterns in the canine arterial tree with particular reference to hemodynamic events. Circulation research 1972;30:23–33.

32. Levesque MJ, Liepsch D, Moravec S, and Nerem RM. Correlation of endothelial cell shape and wall shear stress in a stenosed dog aorta. Arteriosclerosis, Thrombosis, and Vascular Biology 1986;6:220–229.

33. Buchanan JR, Kleinstreuer C, Hyun S, and Truskey GA. Hemodynamics simulation and identification of susceptible sites of atherosclerosis lesion formation in a model abdominal aorta. J Biomech 2003;36:1185–1196.

34. Cunningham KS and Gotlieb AI. The role of shear stress in the pathogenesis of atherosclerosis. Lab Invest 2005;85:9–23.

35. Cheng C, Helderman F, and Tempel D. Large variations in absolute wall shear stress levels within one species and between species. Atherosclerosis. 2007;195:225–235.

36. Sakamoto N, Ohashi T, and Sato M. Effect of shear stress on permeability of vascular endothelial monolayer cocultured with smooth muscle cells. Jsme Int J C-Mech Sy 2004;47:992–999.

37. Sill HW, Chang YS, Artman JR, Frangos JA, Hollis TM, and Tarbell JM. Shear -stress increases hydraulic conductivity of cultured endothelial monolayers. Am J Physiol Heart Circ Physiol 1995;268:H535–H543.

38. Dai G, Kaazempur-Mofrad MR, and Natarajan S. Distinct endothelial pheno-types evoked by arterial waveforms derived from atherosclerosis-susceptible and -resistant regions of human vasculature. Proc Natl Acad Sci U S A 2004;101:14871–14876.

39. Kornet L, Hoeks AP, Lambregts J, and Reneman RS. In the femoral artery bifurcation, differences in mean wall shear stress within subjects are associated with different intima–media thicknesses. Arterioscler Thromb Vasc Biol 1999;19:2933–2939.

40. Florian JA, Kosky JR, Ainslie K, Pang Z, Dull RO, and Tarbell JM. Heparan sulphate proteoglycan is a mechanosensor on endothelial cells. Circ. Res. 2003;93:E136–E142.

41. Cecchi E, Giglioli C, Valente S, et al. Role of hemodynamic shear stress in cardiovascular disease. Atherosclerosis. 2011;214:249–256.

42. Hyun S, Kleinstreuer C, and Archie Jr JP. Computational particle-hemodynamics analysis and geometric reconstruction after carotid endarterectomy. Computers in Biology and Medicine 2001;31:365–384.

43. Lei M, Kleinstreuer C, and Truskey GA. A focal stress gradient-dependent mass transfer mechanism for atherogenesis in branching arteries. Medical Engineering & Physics 1996;18:326–332.

44. Ku DN, Giddens DP, Zarins CK, and Glagov S. Pulsatile flow and atherosclerosis in the human carotid bifurcation. Positive correlation between plaque location and low oscillating shear stress. Arteriosclerosis, Thrombosis, and Vascular Biology 1985;5:293–302.

45. Moore JJ, Xu C, Glagov S, Zarins CK, and Ku DN. Fluid wall shear stress measurements in a model of the human abdominal aorta: oscillatory behavior and relationship to atherosclerosis. Atherosclerosis. 1994;110:225–240.

46. He X and Ku DN. Pulsatile flow in the human left coronary artery bifurcation: average conditions. Journal of Biomechanical Engineering 1996;118:74–82.

47. Malek AM, Alper SL, and Izumo S. Hemodynamic Shear Stress and Its Role in Atherosclerosis. The Journal of the American Medical Association 1999;282:2035–2042.

48. Niwa K, Kado T, and Sakai J. The effects of a shear flow on the uptake of LDL and acetylated LDL by an EC monoculture and an EC-SMC coculture. Ann Biomed Eng 2004;32:537–543.

49. Peiffer V, Sherwin SJ, and Weinberg PD. Does low and oscillatory wall shear stress correlate spatially with early atherosclerosis? A systematic review. Cardiovascular research 2013.

50. Knight J, Olgac U, Saur SC, et al. Choosing the optimal wall shear parameter for the prediction of plaque location—A patient-specific computational study in human right coronary arteries. Atherosclerosis 2010;211:445–450.

51. Rikhtegar F, Knight JA, Olgac U, et al. Choosing the optimal wall shear parameter for the prediction of plaque location—A patient-specific computational study in human left coronary arteries. 2012;222:432–437.

52. Hoi Y, Zhou YQ, Zhang X, Henkelman RM, and Steinman DA. Correlation Between Local Hemodynamics and Lesion Distribution in a Novel Aortic Regurgitation Murine Model of Atherosclerosis. 2011;39:1414–1422.

53. Gijsen FJH, Wentzel JJ, Thury A, et al. A new imaging technique to study 3-D plaque and shear stress distribution in human coronary artery bifurcations in vivo. Journal of biomechanics 2007;40:2349–2357.

54. Augst AD, Ariff B, McG Thom SA, Xu XY, and Hughes AD. Analysis of complex flow and the relationship between blood pressure, wall shear stress, and intima-media thickness in the human carotid artery. 2007:H1031–H1037.

55. Krams R, Wentzel J, Oomen JA, Vinke R, Schuurbiers JC, and Feyter PJ de. Evaluation of endothelial shear stress and 3D geometry as factors determining the development of atherosclerosis and remodeling in human coronary arteries in vivo. Combining 3D reconstruction from angiography and IVUS (ANGUS) with computational fluid dynamics. Arterioscler Thromb Vasc Biol. 1997:2061–2065.

56. Koskinas KC, Feldman CL, Chatzizisis YS, et al. Natural History of Experimental Coronary Atherosclerosis and Vascular Remodeling in Relation to Endothelial Shear Stress: A Serial, In Vivo Intravascular Ultrasound Study. Circulation 2010.

57. Chatzizisis YS, Jonas M, Coskun AU, et al. Prediction of the Localization of High-Risk Coronary Atherosclerotic Plaques on the Basis of Low Endothelial Shear Stress: An Intravascular Ultrasound and Histopathology Natural History Study. Circulation 2008.

58. Olgac U, Poulikakos D, Saur SC, Alkadhi H, and Kurtcuoglu V. Patient-specific three-dimensional simulation of LDL accumulation in a human left coronary artery in its healthy and atherosclerotic states. American journal of physiology. Heart and circulatory physiology 2009;296:H1969–H1982.

59. Olgac U, Kurtcuoglu V, Saur SC, and Poulikakos D. Identification of atherosclerotic lesion-prone sites through patient-specific simulation of low-density lipoprotein accumulation. Med Image Comput Comput Assist Interv. 2008:774–781.

60. Prosi M, Zunino P, Perktold K, and Quarteroni A. Mathematical and numerical models for transfer of low-density lipoproteins through the arterial walls: a new methodology for the model set up with applications to the study of disturbed lumenal flow. Journal of biomechanics 2005;38:903–917.

61. Ritter LR, Ibragimov A, Walton JR, and McNeal CJ. Illuminating Atherogenesis Through Mathematical Modeling. In: *Atherogenesis*. Ed. by Parthasarathy PS. Intech, 2012.

62. Zohdi T, Holzapfel GA, and Berger SA. A phenomenological model for atherosclerotic plaque growth and rupture. Journal of theoretical biology 2004;227:437–443.

63. Holzapfel GA, Gasser T, and Ogden RW. A new constitutive framework for arterial wall mechanics and a comparative study of material models. J. Elast 2000;61:1–48.

64. Gasser TC, Ogden RW, and Holzapfel GA. Hyperelastic modelling of arterial layers with distributed collagen fibre orientations. Journal of the royal society interface 2006;3:15–35.

65. Tarbell JM. Mass transport in arteries and the localization of atherosclerosis. Annual Review of Biomedical Engineering 2003;5:79–118.

66. Wada S and Karino T. Theoretical study on flow-dependent concentration polarization of low density lipoproteins at the luminal surface of a straight artery. Biorheology 1999;36:207–223.

67. Fry D. Mathematical models of arterial transmural transport. American Journal of Physiology 1985;248:H240–H263.

68. Fry D. Mass transport, atherogenesis, and risk. Arteriosclerosis 1987;7:88–100.

69. Wood NB, Hughes AD, Thom S, Xu XY, and Sun N. Influence of Pulsatile Flow on LDL Transport in the Arterial Wall. Annals of biomedical engineering 2007;35:1782–1790.

70. Sun N, Torii R, Wood NB, Hughes AD, Thom SA, and Xu XY. Computational modeling of LDL and albumin transport in an in vivo CT image-based human right coronary artery. Journal of Biomechanical Engineering 2009;131:021003–021003.

71. Yang N and Vafai K. Modeling of low-density lipoprotein (LDL) transport in the artery-effects of hypertension. Int. J. Heat Mass Transfer 2006;49:850–867.

72. Bird RB, Stewart WE, and Lightfoot EN. Transport Phenomena. John Wiley & Sons, 2007.

73. Anand M and Rajagopal KR. A shear-thinning viscoelastic fluid model for describing the flow of blood. International Journal of Cardiovascular Medicine and Science 2004;4:59–68.

74. Shibeshi S and Collins WE. The rheology of blood flow in a branched arterial system. Appl. Rheol. 2005;15:398–405.

75. Chen J and Lu XY. Numerical investigation of the non-Newtonian blood flow in a bifurcation model with a non-planar branch. Journal of biomechanics 2004;37:1899–1911.

76. Johnston BM, Johnston PR, Corney S, and Kilpatrick D. Non-Newtonian blood flow in human right coronary arteries: steady state simulations. J Biomech. 2004;37:709–720.

77. Cho YI and Kensey KR. Effects of the non-Newtonian viscosity of blood on flows in a diseased arterial vessel. Part 1: Steady flows. Biorheology. 1991;28:241–262.

78. Ballyk PD, Steinman DA, and Ethier CR. Simulation of non-Newtonian blood flow in an end-to-side anastomosis. Biorheology. 1994;31:565–586.

79. Canic S, Mikelic A, and Tambaca J. A two-dimensional effective model describing fluid–structure interaction in blood flow: analysis, simulation and experimental validation. Fluidsolid interactions: modeling, simulation, bio-mechanical applications 2005;333.

80. Quarteroni A, Tuveri M, and Veneziani A. Computational vascular fluid dynamics: problems, models and methods. Computing and Visualization in Science 2000;2:163–197.

81. Rappitsch G and Perktold K. Pulsatile albumin transport in large arteries: a numerical simulation study. ASME J. Biomech. Eng. 1996;118:511–519.

82. Stangeby DK and Ethier CR. Coupled computational analysis of arterial LDL transport – effects of hypertension. Comput. Methods Biomech. Biomed. Eng. 2002;5:233–241.

83. Olgac U, Kurtcuoglu V, and Poulikakos D. Computational modeling of coupled blood-wall mass transport of LDL: effects of local wall shear stress. American journal of physiology. Heart and circulatory physiology 2008;294:H909–H919.

84. Dabagh M, Jalali P, and Tarbell JM. The transport of LDL across the deformable arterial wall: the effect of endothelial cell turnover and intimal deformation under hypertension. American journal of physiology. Heart and circulatory physiology 2009;297:H983–H996.

85. Koshiba N, Ando J, Chen X, and Hisada T. Multiphysics simulation of blood flow and LDL transport in a porohyperelastic arterial wall model. Journal of Biomechanical Engineering 2007;129:374–385.

86. Ethier CR. Computational modeling of mass transfer and links to atherosclerosis. Annals of biomedical engineering 2002;30:461–471.

87. Ai L and Vafai K. A coupling model for macromolecule transport in a stenosed arterial wall. International journal of heat and mass transfer 2006;49:1568–1591.

88. Sun N, Wood NB, Hughes AD, Thom SA, and Xu XY. Fluid-wall modelling of mass transfer in an axisymmetric stenosis: effects of shear-dependent transport properties. Annals of biomedical engineering 2006;34:1119–1128.

89. Sun N, Wood NB, Hughes AD, Thom SA, and Xu XY. Effects of transmural pressure and wall shear stress on LDL accumulation in the arterial wall: a numerical study using a multilayered model. American journal of physiology. Heart and circulatory physiology 2007;292:H3148–H3157.

90. Meyer G and Tedgui A. Effects of pressure-induced stretch and convection on low-density lipoprotein and albumin uptake in the rabbit aortic wall. Circulation research 1996;79:532–540.

91. Vafai K and Tien CL. Boundary and inertia effects on flow and heat transfer in porous media. Int. J. Heat Mass Transfer 1981;24:195–203.

92. Huang ZJ and Tarbell JM. Numerical simulation of mass transfer in porous media of blood vessel walls. American journal of physiology. Heart and circulatory physiology 1997;273:H464–H477.

93. Karner G and Perktold K. Effect of endothelial injury and increased blood pressure on albumin accumulation in the arterial wall: a numerical study. Journal of biomechanics 2000;33:709–715.

94. Lin SJ, Jan KM, Weinbaum S, and Chien S. Transendothelial transport of low density lipoprotein in association with cell mitosis in rat aorta. Arteriosclerosis, Thrombosis, and Vascular Biology 1989;9:230–236.

95. Himburg HA, Grzybowski DM, Hazel AL, LaMack JA, Li XM, and Friedman MH. Spatial comparison between wall shear stress measures and porcine arterial endothelial permeability. American journal of physiology. Heart and circulatory physiology 2004;286:H1916–H1922.

96. Minshall RD and Malik AB. Transport across the endothelium: regulation of endothelial permeability. In: *The Vascular Endothelium I*. Springer Berlin Heidelberg, 2006.

97. Lin SJ, Jan KM, and Chien S. Role of dying endothelial cells in transendothelial macromolecular transport. Arteriosclerosis, Thrombosis, and Vascular Biology 1990;10:703–709.

98. Chien S. Molecular and mechanical bases of focal lipid accumulation in arterial wall. Progress in biophysics and molecular biology 2003;83:131–151.

99. Curry FE. Mechanics and thermodynamics of transcapillary exchange. In: *Handbook of Physiology, The Cardiovascular System, Microcirculation*. Ed. by Bethesda. Am Physiol Soc, 1984:309–374.

100. Yang N and Vafai K. Low-density lipoprotein (LDL) transport in an artery–A simplified analytical solution. International journal of heat and mass transfer 2008;51:497–505.

101. Ross R. Atherosclerosis—an inflammatory disease. New England journal of medicine 1999;340:115–126.

102. Ibragimov AI, McNeal CJ, Ritter LR, and Walton JR. A mathematical model of atherogenesis as an inflammatory response. Mathematical Medicine and Biology 2005;22:305–333.

103. El Khatib N, Genieys S, and Volpert V. Atherosclerosis initiation modeled as an inflammatory process. Mathematical Modelling of Natural Phenomena 2007;2:126–141.

104. Ibragimov V, Ritter L, and Walton JR. Stability analysis of a reaction diffusion system modeling atherogenesis. SIAM Journal on Applied Mathematics 2010;70:2150–2185.

105. Stanbro WD. Modeling the interaction of peroxynitrite with low-density lipoproteins. II: reaction/diffusion model of peroxynitrite in low-density lipoprotein particles. Journal of theoretical biology 2000;205:465–471.

106. El Khatib N, Genieys S, Kazmierczak B, and Volpert V. Mathematical modelling of atherosclerosis as an inflammatory disease. Philosophical Transactions of the Royal Society A: Mathematical, Physical and Engineering Sciences 2009;367:4877–4886.

107. Calvez V, Houot JG, Meunier N, Raoult A, and Rusnakova G. Mathematical and numerical modeling of early atherosclerotic lesions. In ESAIM: Proceedings. EDP Sciences. 2010;30:1–14.

108. Calvez V, Ebde A, Meunier N, and Raoult A. Mathematical modelling of the atherosclerotic plaque formation. In ESAIM: Proceedings. EDP Sciences. 2009;28:1–12.

109. Ougrinovskaia A, Thompson RS, and Myerscough MR. An ODE model of early stages of atherosclerosis: mechanisms of the inflammatory response. Bulletin of mathematical biology 2010;72:1534–1561.

110. Fontana M. Corrosion Engineering. New York: McGraw-Hill, 1986.

111. Southern J, Pitt-Francis J, Whiteley J, et al. Multi-scale computational modelling in biology and physiology. Progress in biophysics and molecular biology 2008;96:60–89.

112. Ingram GD, Cameron IT, and Hangos KM. Classification and analysis of integrating frameworks in multiscale modelling. Chemical engineering science 2004;59.

113. Hoekstra AG, Lorenz E, Falcone JL, and Chopard B. Towards a Complex Automata Framework for Multi-scale Modeling: Formalism and the Scale Separation Map. Computational ScienceICCS 2007 2007;4487:922–930.

114. Sloot PMA and Hoekstra AG. Multi-scale modelling in computational biomedicine. Briefings in bioinformatics 2010;11:142–152.

115. Evans DJW, Lawford PV, Gunn J, et al. The application of multiscale modelling to the process of development and prevention of stenosis in a stented coronary artery. Transactions of the Royal Society A: Mathematical, Physical and Engineering Sciences 2008;366:3343–3360.

116. Fishwick PA. Handbook of Dynamic System Modeling. CRC Press, 2007.

117. Halliday I, Atherton M, Care CM, et al. Multi-scale interaction of particulate flow and the artery wall. Medical engineering & physics 2011:1–9.

118. Parodi O, Exarchos TP, Marraccini P, et al. Patient-specific prediction of coronary plaque growth from CTA angiography: a multiscale model for plaque formation and progression. IEEE Trans Inf Technol Biomed 2012;16:952–965.

119. Liang F, Takagi S, Himeno R, and Liu H. Multi-scale modeling of the human cardiovascular system with applications to aortic valvular and arterial stenoses. Medical & biological engineering & computing 2009;47:743–755.

120. Weinan E, Engquist B, Li X, Ren W, and Vanden-Eijnden E. Heterogeneous Multiscale Methods: A Review. Communications in computational physics 2007;2:367–450.

121. Hoekstra AG, Falcone JL, Caiazzo A, and Chopard B. Multi-scale Modeling with Cellular Automata: The Complex Automata Approach. Cellular automata 2008;5192:192–199.

122. Hunter PJ, Crampin EJ, and Nielsen PMF. Bioinformatics, multiscale modeling and the IUPS Physiome Project. Briefings in bioinformatics 2008;9:333–343.

123. Tedgui A and Lever MJ. Filtration through damaged and undamaged rabbit thoracic aorta. American journal of physiology. Heart and circulatory physiology 1984;247:H784–H791.

124. Whale MD, Grodzinsky AJ, and Johnson M. The effect of aging and pressure on the specific hydraulic conductivity of the aortic wall. Biorheology 1996;33:17–44.

125. Rhie CM and Chow WL. A numerical study of the turbulent flow past an isolated airfoil with trailing edge separation. AIAA journal 1983;21.

126. Majumdar S. Role of underrelaxation in momentum interpolation for calculation of flow with nonstaggered grids. Numerical Heat Transfer 1988;13:125–132.

127. Raw M. Robustness of coupled Algebraic Multigrid for the Navier-Stokes equations. AIAA journal 1996;96.

128. Ansys. Ansys Users Manual. Ansys, 2000.

129. Mora SS, Szklo MM, Otvos JDJ, et al. LDL particle subclasses, LDL particle size, and carotid atherosclerosis in the Multi-Ethnic Study of Atherosclerosis (MESA). Atherosclerosis. 2007;192:7–7.

130. Malek AM and Izumo S. Mechanism of endothelial cell shape change and cytoskeletal remodeling in response to fluid shear stress. J Cell Sci. 1996;109:713–726.

131. Hoogstraten HW, Kootstra JG, Hillen B, Krijger JKB, and Wensing PJW. Numerical simulation of blood flow in an artery with two successive bends. Journal of biomechanics 1996;29:1075–1083.

132. Huang Y, Rumschitzki D, Chien S, and Weinbaum S. A fiber matrix model for the growth of macromolecular leakage spots in the arterial intima. Journal of Biomechanical Engineering 1994;116:430–445.

133. Berliner JA, Navab M, Fogelman AM, et al. Atherosclerosis: basic mechanisms oxidation, inflammation, and genetics. Circulation 1995;91:2488–2496.

134. Barakat AI and Lieu DK. Differential responsiveness of vascular endothelial cells to different types of fluid mechanical shear stress. Cell biochemistry and biophysics 2003;38:323–343.

136. Fredickson DS and Levy RL. Familial hyperlipoproteinemia. In: *The Metabolic Basis of Inherited Disease*. Ed. by Stanbury JB, Wyngaarden JB, and Fredrickson DS. New York: McGraw-Hill, 1972.

137. Kane JP, Malloy MJ, Ports TA, Phillips NR, Diehl JC, and Havel RJ. Regression of coronary atherosclerosis during treatment of familial hypercholesterolemia with combined drug regimens. JAMA: the journal of the American Medical Association 1990;264:3007–3012.

138. Dodge JT, Brown BG, Bolson EL, and Dodge HT. Lumen diameter of normal human coronary arteries. Influence of age, sex, anatomic variation, and left ventricular hypertrophy or dilation. Circulation 1992;86:232–246.

139. Cheng KS, Mikhailidis DP, Hamilton G, and Seifalian AM. A review of the carotid and femoral intima-media thickness as an indicator of the presence of peripheral vascular disease and cardiovascular risk factors. Cardiovascular research 2002;54:528–538.

140. Sherwin SJ and Blackburn HM. Three-dimensional instabilities and transition of steady and pulsatile axisymmetric stenotic flows. J. Fluid Mech. 2005;533:297–327.

141. Mao X, Blackburn HM, and Sherwin SJ. Optimal inflow boundary condition perturbations in steady stenotic flow. J. Fluid Mech. 2012;705:306–321.

142. Li H, Cybulsky MI, Gimbrone MA, and Libby P. An atherogenic diet rapidly induces VCAM-1, a cytokine-regulatable mononuclear leukocyte adhesion molecule, in rabbit aortic endothelium. Arteriosclerosis and thrombosis : a journal of vascular biology / American Heart Association 1993;13:197–204.

143. Steinberg D. Atherogenesis in perspective: Hypercholesterolemia and inflammation as partners in crime. Nature Medicine 2002;8:1211–1217.

144. Mori M, Itabe H, Higashi Y, et al. Foam cell formation containing lipid droplets enriched with free cholesterol by hyperlipidemic serum. Journal of lipid research 2001;42:1771–1781.

145. Smedby OO and Bergstrand LL. Tortuosity and atherosclerosis in the femoral artery: what is cause and what is effect? Annals of biomedical engineering 1996;24:474–480.

146. Wood NB, Zhao SZ, Zambanini A, et al. Curvature and tortuosity of the superficial femoral artery: a possible risk factor for peripheral arterial disease. Journal of Applied Physiology 2006;101:1412–1418.

147. Smedby OO, Johansson JJ, Mlgaard JJ, Olsson AGA, Walldius GG, and Erikson UU. Predilection of atherosclerosis for the inner curvature in the femoral artery. A digitized angiography study. Arteriosclerosis, Thrombosis, and Vascular Biology 1995;15:912–917.

148. Strong JP and McGill Jr. HC. The pediatric aspects of atherosclerosis. Journal of Atherosclerosis Research 1969;9:251–265.

149. Strong JP, Malcom GT, McMahan CA, et al. Prevalence and Extent of Atherosclerosis in Adolescents and Young AdultsImplications for Prevention From the Pathobiological Determinants of Atherosclerosis in Youth Study. JAMA 1999;281:727–735.

150. Tang DD, Yang CC, Mondal SS, et al. A negative correlation between human carotid atherosclerotic plaque progression and plaque wall stress: In vivo MRI-based 2D/3D FSI models. Journal of biomechanics 2008;41:10–10.

151. Groot E de, Hovingh GK, Wiegman A, et al. Measurement of arterial wall thickness as a surrogate marker for atherosclerosis. Circulation 2004;109:III33–8.

152. Pentecost, Criqui, Dorros, et al. Guidelines for Peripheral Percutaneous Transluminal Angioplasty of the Abdominal Aorta and Lower Extremity Vessels. Journal of Vascular and Interventional Radiology 2003;14:–.

153. McDermott MM, Mehta S, Liu K, et al. Leg symptoms, the ankle-brachial index, and walking ability in patients with peripheral arterial disease. Journal of general internal medicine 1999;14:173–181.

154. Elbasan Z, Sahin DY, Gur M, et al. Aortic Distensibility and Aortic Intima-Media Thickness in Patients without Clinical Manifestation of Atherosclerotic Cardiovascular Disease. Echocardiography 2012:n–a.

155. Cademartiri FF, Runza GG, Mollet NRN, et al. Influence of increasing convolution kernel filtering on plaque imaging with multislice CT using an ex-vivo model of coronary angiography. Radiologia Medica 2005;110:234–240.

156. Goldman LW. Principles of CT: multislice CT. Journal of nuclear medicine technology 2008;36:pages.

157. Zhang J, Yang G, Lee Y, Chang S, Lu J, and Zhou O. MO-E-L100J-07: Multiplexing Radiography for Ultra-Fast Computed Tomography: A Feasibility Study. Med Phys 2007;34:2527–2527.

158. Young IT and Vliet LJ van. Recursive implementation of the Gaussian filter. Signal processing 1995;44:139–151.

159. Antiga L. Patient-Specific Modeling of Geometry and Blood Flow in Large Arteries. PhD thesis. Politecnico di Milano.

160. Selimovic A, Ventikos Y, and Watton PN. Growth and Remodelling Hypotheses for Patient-specific Models of Cerebral Aneurysm Evolution. In: *8th European Solid Mechanics Conference*. University of Oxford. 2012.

161. Schroeder WJ and Shephard MS. A combined octree/delaunay method for fully automatic 3-D mesh generation. Int. J. Numer. Meth. Engng. 1990;29:37–55.

162. Loudon CC and Tordesillas AA. The Use of the Dimensionless Womersley Number to Characterize the Unsteady Nature of Internal Flow. Journal of theoretical biology 1998;191:16–16.

163. Vignon-Clementel IE, Alberto Figueroa C, Jansen KE, and Taylor CA. Outflow boundary conditions for three-dimensional finite element modeling of blood flow and pressure in arteries. Computer methods in applied mechanics and engineering 2006;195:3776–3796.

164. Lantz J, Renner J, and Karlsson M. Wall shear stress in a subject specific human aorta - Influence of fluid-structure interaction. International Journal of Applied Mechanics 2011;03:759–778.

165. Jeays AD, Lawford PV, Gillott R, et al. Characterisation of the haemodynamics of the superior mesenteric artery. J Biomech. 2007;40:1916–1926.

166. Nakazawa G, Yazdani SK, Finn AV, Vorpahl M, Kolodgie FD, and Virmani R. Pathological Findings at Bifurcation Lesions. Journal of the American College of Cardiology 2010;55:9–9.

167. Glagov S, Weisenberg E, Zarins CK, Stankunaviciu R, and Kolettis GJ. Compensatory enlargement of human atherosclerot... [N Engl J Med. 1987] - PubMed - NCBI. N Engl J Med. 1987;316:1371–1375.

168. Achenbach S, Ropers D, Hoffmann U, et al. Assessment of coronary remodeling in stenotic and nonstenotic coronary atherosclerotic lesions by multidetector spiral computed tomography. J Am Coll Cardiol. 2004;43:842–847.

169. Stergiopulos N, Young DF, and Rogge TR. Computer simulation of arterial flow with applications to arterial and aortic stenoses. Journal of biomechanics 1992;25:1477–1488.

Personal Publications

Di Tomaso G, Diaz-Zuccarini V, and Pichardo-Almarza C. A multiscale model of atherosclerotic plaque formation at its early stage. Biomedical Engineering, IEEE Transactions on 2011;58:3460–3463.

DiTomaso G, Diaz-Zuccarini V, and Pichardo-Almarza C. A coupled Biochemical-CFD Multi-scale Model of Atherogenesis. Proceedings of ESB2012, Journal of Biomechanics 2012;45.

Diaz-Zuccarini V, Di Tomaso G, Agu O, and Pichardo-Almarza C. Towards personalised management of atherosclerosis via computational models in vascular clinics: a technology based on a patient-specific simulation approach. IEEE Healthcare Technology Letters 2014;1:13–18.

Diaz-Zuccarini V, Di Tomaso G, Agu O, and Pichardo-Almarza C. A Multi-Scale and Patient-Specific Computational Framework of Atherosclerosis Formation and Progression. To be submitted for publication.

Appendix A

Mesh sensitivity analysis of an idealised geometry of an s-shaped common femoral artery.

A grid independence study was performed for the idealised geometry of a femoral artery. As this geometry could not be fully compared with the analytical solution for a Poiseuille flow for a straight pipe, the most suitable mesh was chosen by comparison among different meshes. Three sets of uniform unstructured grids consisting of 1M, 2.5M and 4.5M elements were built. The converged results for the WSS magnitude taken on a longitudinal cut of the upper wall of the geometry were chosen for comparison (Figure A.1). The lower wall area was chosen, as this is the area where the WSS global minima is located and where the atherosclerosis plaque formed (Figure A.2).

The relative error (e) in computing the local WSS value is calculated as in Olgac et al.[129]:

$$e = \left| \frac{\boldsymbol{WSS}_{finer}(z) - \boldsymbol{WSS}_{coarser}(z)}{\boldsymbol{WSS}_{finer}(z)} \right| \tag{A.1}$$

where $\boldsymbol{WSS}$ is the local value of WSS, z is the spatial location and $finer$ and $coarser$ refers to the quality of the grid being compared. The highest computed error between the chosen mesh (2.5M) and the finest mesh considered is of 6%. Figure A.2 shows the global minima of the three meshes considered. As the grid refinement increases a converging trend can be seen, with the relative error between 2.5M and the finest mesh being of 1.2%.

The chosen mesh is acceptable, as the maximum value in the relative error is

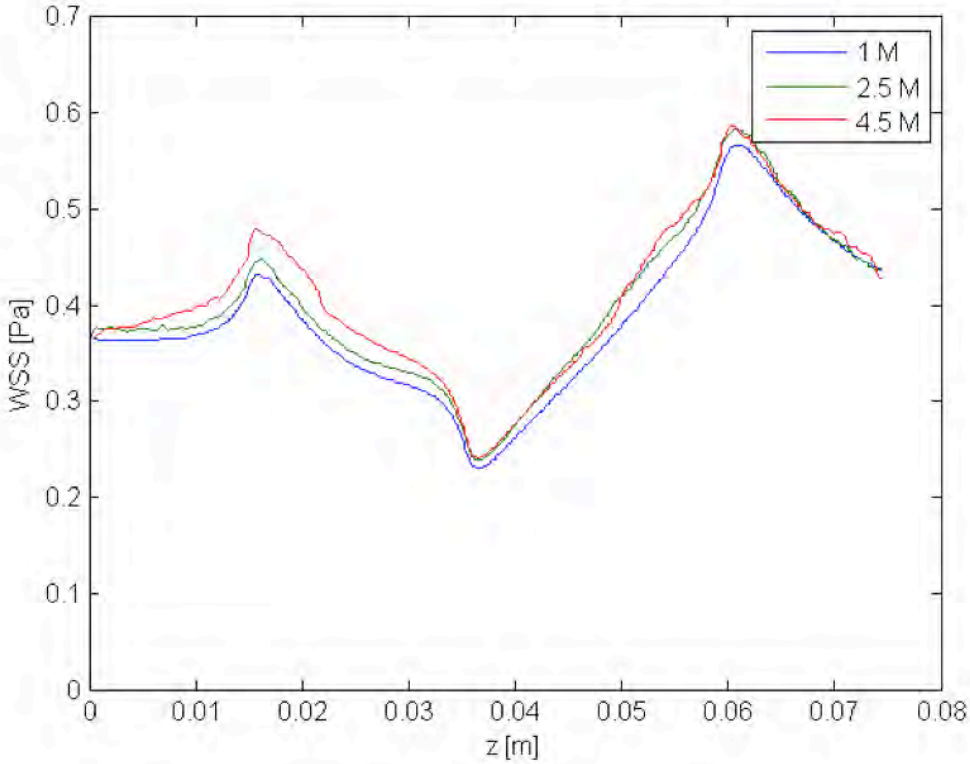

Figure A.1: Local value of WSS as a function of the axial location z for three different grids were considered for comparison, a 1 million elements grid (1M), a 2.5 million elements grid (2.5M) and a 4.5 million elements grid (4.5M). Boundary conditions: inlet parabolic velocity profile (equation 43), outlet stress free.

located in areas of high WSS, that are of no interest in the current model, and the discrepancy in the computed local WSS is much lower in areas of low WSS, of higher interest in this contest.

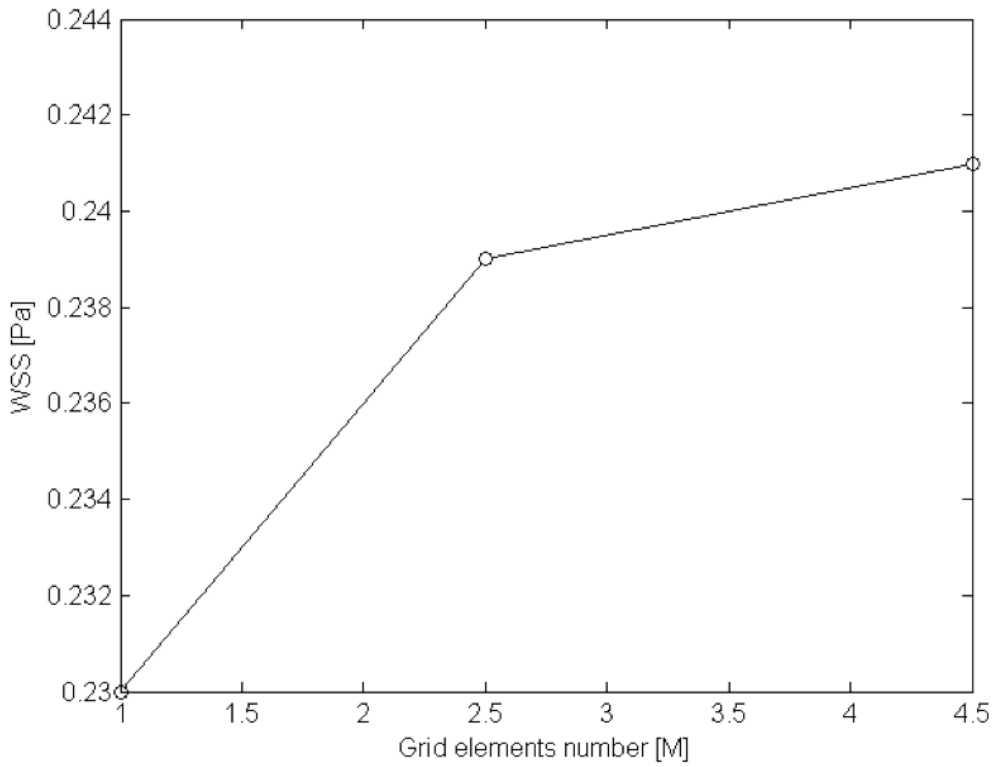

Figure A.2: Global minima of WSS as a function of grid elements number.

Appendix B

Sensitivity analysis of foam cell formation rate and cytokines action parameters.

Impact of the parameters for foam cell formation (k_m) and cytokine action (K_5) on the time of growth was here analysed, where the time of growth is the time needed for the artery to reach the thickness Δh (Equation (2.42)).

Figures B.1 to B.4 show how the time of growth varies with k_m and K_5. The parameters were altered of 10%, 20% and 30%. The percentage change of the different parameters is calculated as:

$$\%k_m = \frac{k_m - k_m*}{k_m*} \cdot 100 \tag{B.1}$$

$$\%K_5 = \frac{K_5 - K_5*}{K_5*} \cdot 100 \tag{B.2}$$

Where k_m* and K_5* are the kinetic rates of cytokines action and foam cell formation rate used in the model (Table 2.1). The percentage change in the time of growth is calculated as:

$$\%\text{Time of Growth} = \frac{\text{Time of Growth} - \text{Time of Growth}*}{\text{Time of Growth}*} \cdot 100 \tag{B.3}$$

where the Time of Growth$*$ is calculated with the kinetic rates of cytokines action and foam cell formation rate used in the model (Table 2.1).

The two different kinetic constants appear to influence the time of growth in

the same way. There is an inverse relationship between the change in the kinetic constants (K_5 and k_m) and the change in the time of growth $\Delta h*$.

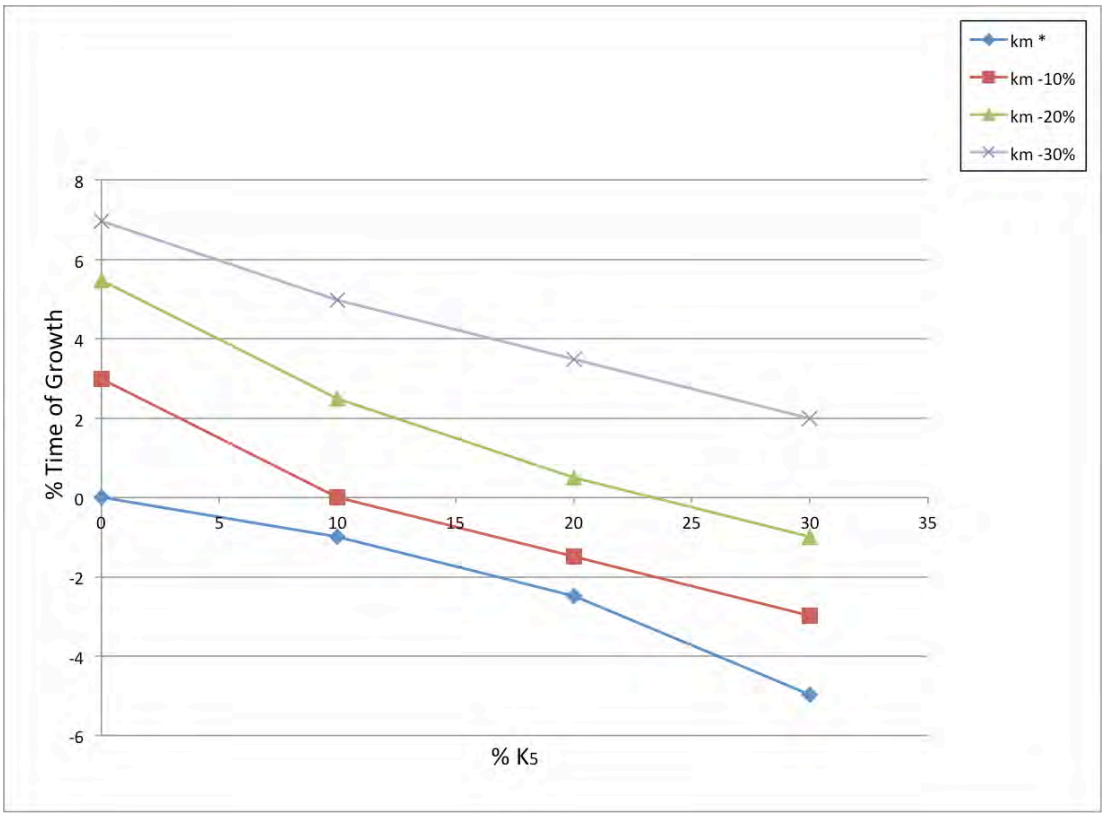

Figure B.1: Impact of the change in k_m and K_5 on the time of growth. The impact on the time of growth given by an increase of 0%, 10%, 20% and 30% in K_5 and a decrease of 0%, 10%, 20% and 30% in k_m is here plotted. The k_m parameter is kept constant at a different percentage for each line in the graph, the variation in the K_5 parameter is represented by the x-axis.

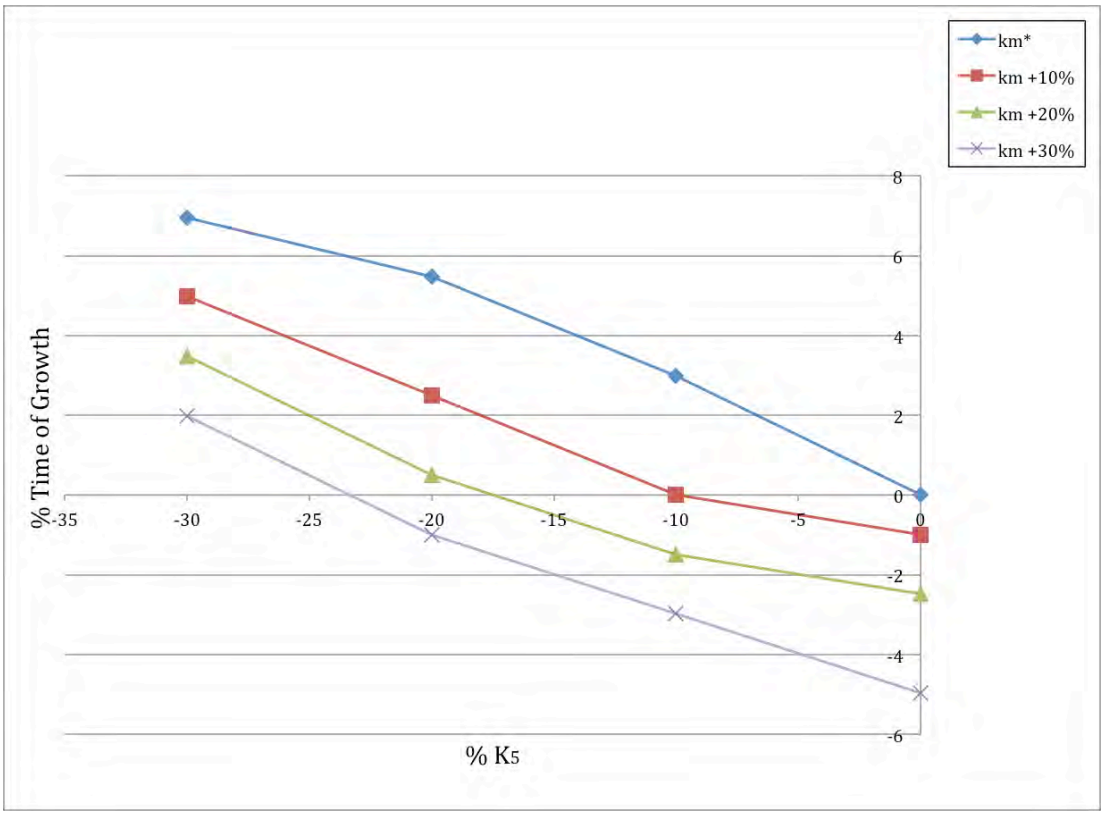

Figure B.2: Impact of the change in k_m and K_5 on the time of growth. The impact on the time of growth given by a decrease of 0%, 10%, 20% and 30% in K_5 and an increase of 0%, 10%, 20% and 30% in km is here plotted. The k_m parameter is kept constant at a different percentage for each line in the graph, the variation in the K_5 parameter is represented by the x-axis.

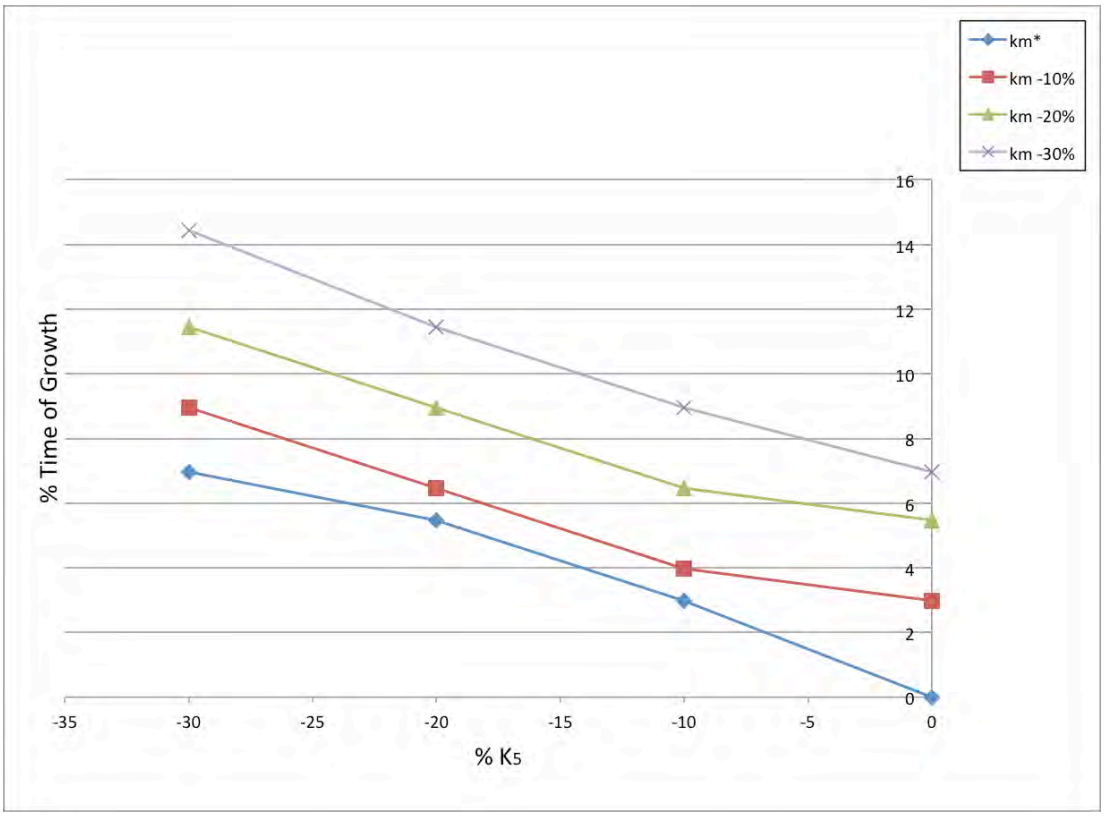

Figure B.3: Impact of the change in k_m and K_5 on the time of growth. The impact on the time of growth given by a decrease of 0%, 10%, 20% and 30% in K_5 and a decrease of 0%, 10%, 20% and 30% in k_m is here plotted. The k_m parameter is kept constant at a different percentage for each line in the graph, the variation in the K_5 parameter is represented by the x-axis.

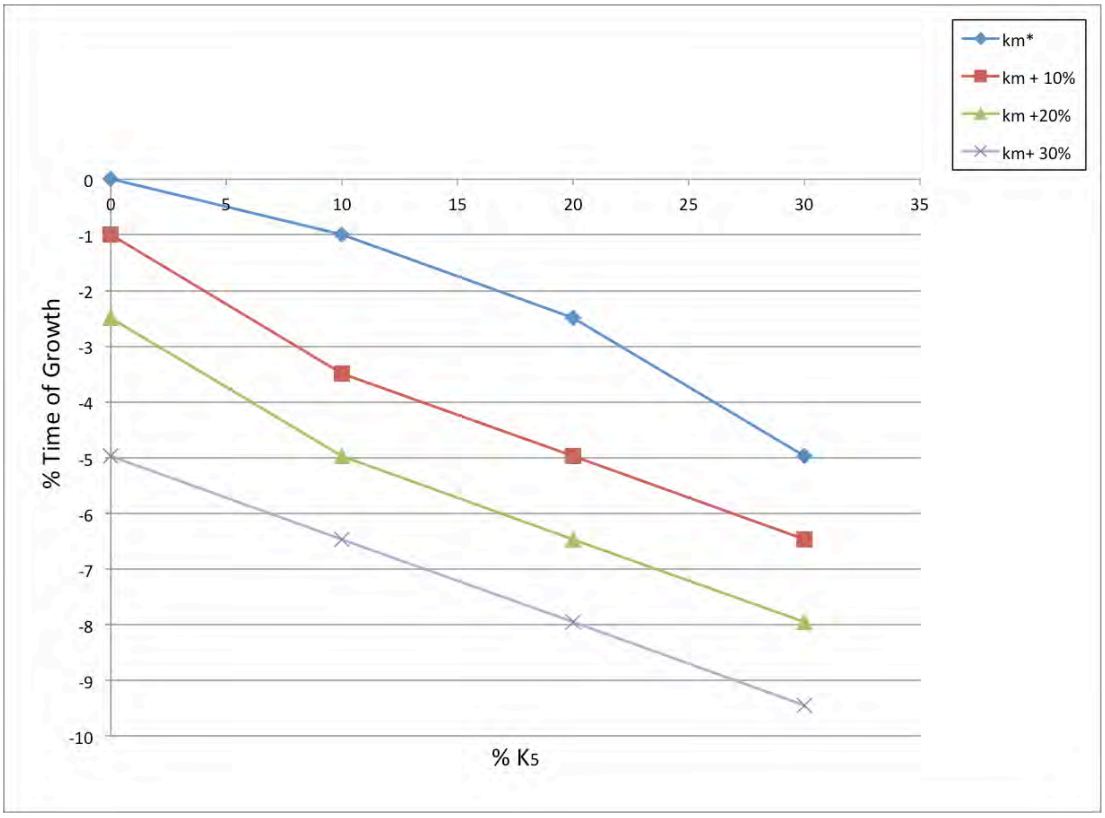

Figure B.4: Impact of the change in k_m and K_5 on the time of growth. The impact on the time of growth given by an increase of 0%, 10%, 20% and 30% in K_5 and an increase of 0%, 10%, 20% and 30% in k_m is here plotted. The k_m parameter is kept constant at a different percentage for each line in the graph, the variation in the K_5 parameter is represented by the x-axis.

Appendix C

Mesh sensitivity analysis for the three patient-specific cases.

Grid independence study was performed for the patient specific geometries of the three cases considered. For Case 1, four sets of unstructured mesh of 3 million elements, 6.6 million elements, 7.8 million elements and 10 million elements were considered. A cloud of points over the surface mesh was used as a probing function for local WSS values extraction. The converged results for the local WSS magnitude probed at the points locations for the four different cases analysed is plot in Figure C.1 along the z-axis.

The maximum relative error between the finest grid (10 million elements) and the chosen grid (6.6M elements) calculated with Equation (A.1) was 2.4%.

Three sets of unstructured grids were considered for Case 2: 0.8 million elements, 1 million elements and 1.9 million elements. The converged results for the local WSS magnitude probed at different geometry locations for the three different cases analysed is plotted in Figure C.2 along the z-axis. The maximum relative error in WSS calculation between the finest considered grid and the chosen grid (1 million elements) was 3%.

The three different grids considered for grid independence study on Case 3 were a 0.8 million elements grid, a 1.2 million elements grid and a 1.9 million elements grid. The converged results for the local steady WSS values at different locations in the geometry for the three different grids are plot in Figure C.3. The maximum relative error between the chosen grid (1 million elements) and the finest grid (1.9 million elements) was 3.2%.

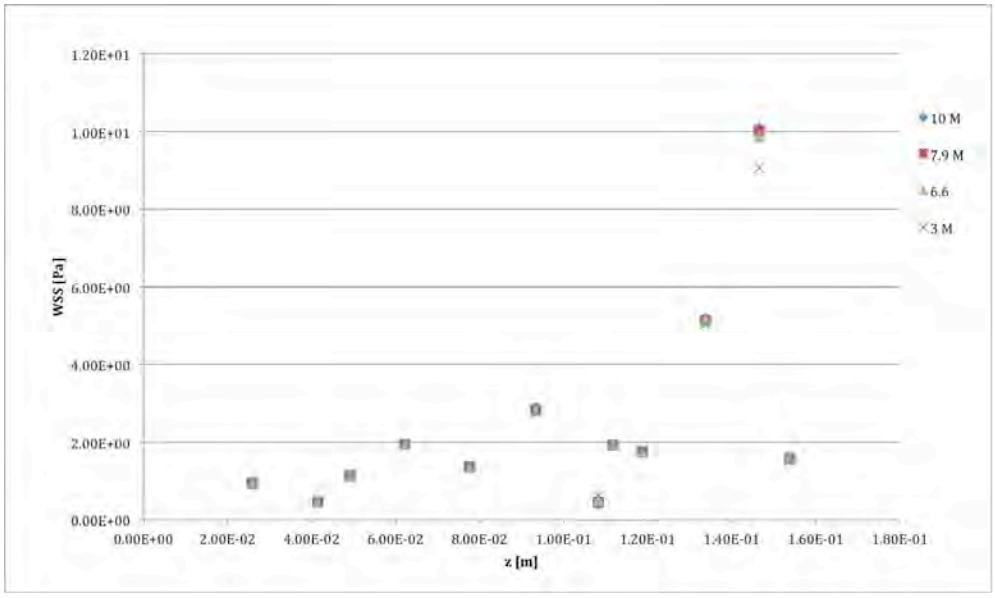

Figure C.1: Local value of WSS as a function of the axial location z for the four different grids were considered for comparison, a 3 million elements grid (3M), a 6.6 million elements grid (6.6M), a 7.9 million elements grid (7.9M) and a 10 million elements grid (10M). Boundary conditions: inlet parabolic velocity profile (equation 43), outlet stress free.

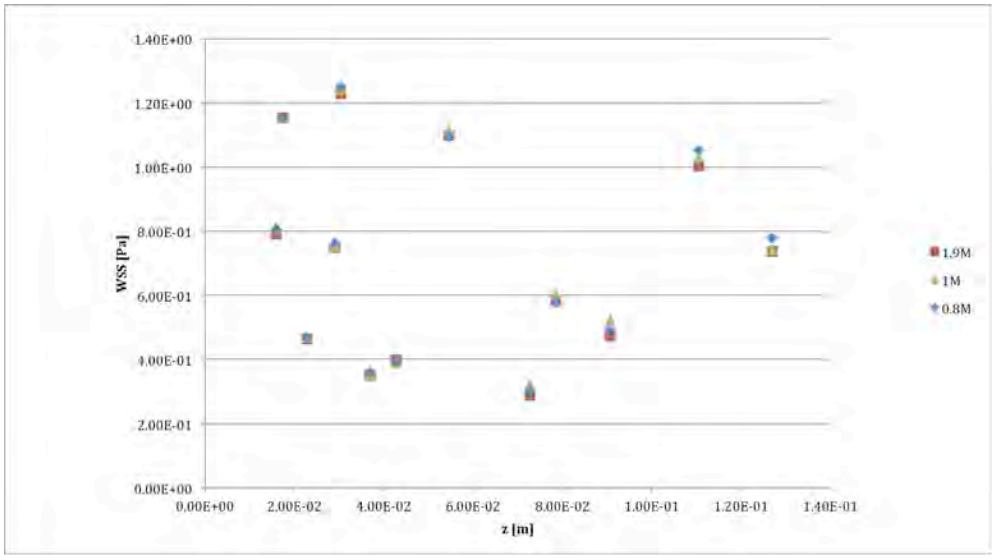

Figure C.2: Local value of WSS as a function of the axial location z for the three different grids considered for case 2, a 0.8 million elements grid (0.8M), a 1 million elements grid (1M) and a 1.9 million elements grid (1.9M). Boundary conditions: inlet parabolic velocity profile (equation 43), outlet stress free.

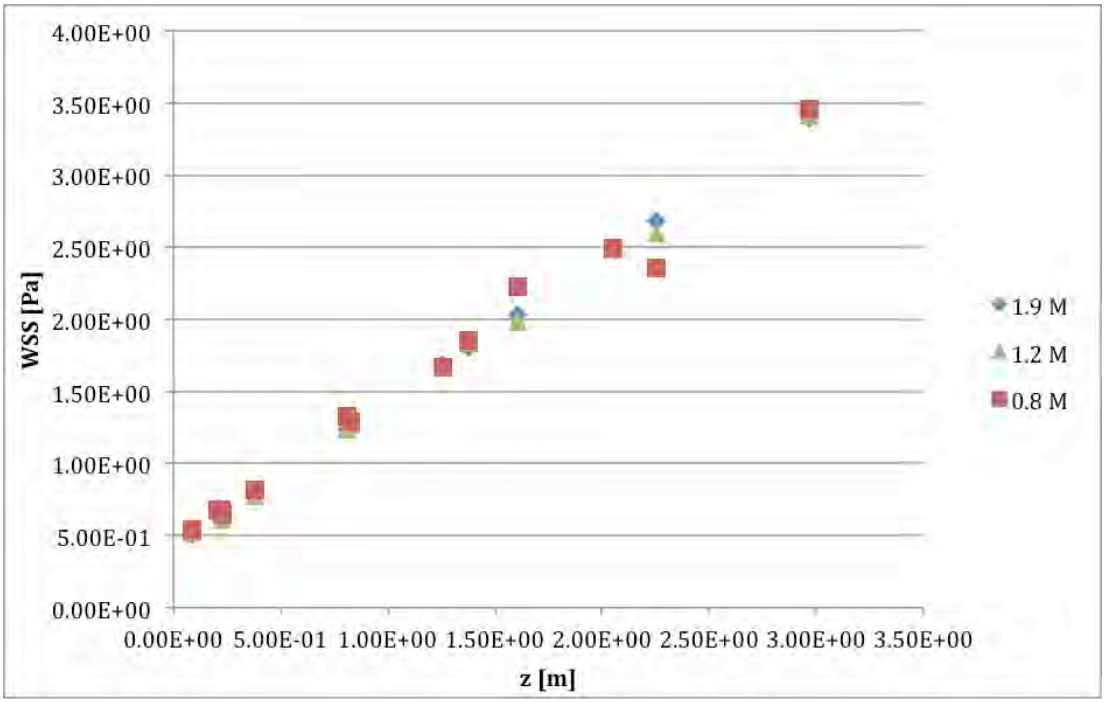

Figure C.3: Local value of WSS as a function of the axial location z for the three different grids considered for case 2, a 0.8 million elements grid (0.8M), a 1.2 million elements grid (1.2M) and a 1.9 million elements grid (1.9M). Boundary conditions: inlet parabolic velocity profile (equation 43), outlet stress free.

Fine